Università degli Studi di Napoli "Federico II"

PhD Thesis
in
Novel Technologies for Materials, Sensors and Imaging

XXII cycle

Single Photon Counting X-Ray Micro-Imaging of Biological Samples

Paola Maria Frallicciardi

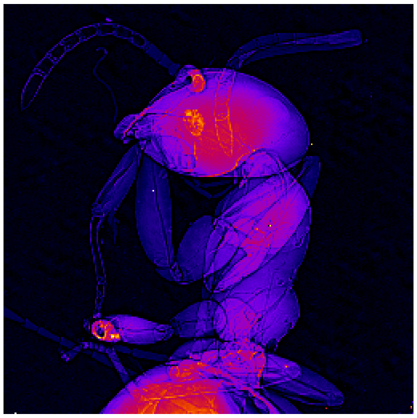

Supervisor:

Prof. Paolo Russo

Academic Year 2009–2010

O Rose, thou art sick!

The invisible worm

That flies in the night,

In the howling storm,

Has found out thy bed

Of crimson joy:

And his dark secret love

Does thy life destroy.

William Blake

Index

Introduction

In this thesis, performed in the framework of the interdisciplinary research of the Italian National Institute of Physics (INFN) and within a collaboration with Prof. S. Pospisil at Czech Technical University in Prague, Institute of Experimental and Applied Physics, we compared the experimental technique of Single Photon Counting (SPC) imaging to the charge integrating Flat Panel (FP) detector imaging, for X-ray biomedical imaging applications. In particular, we investigated the application of SPC detector for the X-ray micro-imaging and X-ray volumetric Computed Tomography (CT) technique.

The motivation for such a research arises from the potential advantages of the single photon counting technology. In fact, this detection modality allows to have an efficient suppression of the electronic noise, scatter radiation rejection and immunity for afterglow effect of scintillator-based detectors, thanks to a read-out scheme able to discriminate photons with energy above a chosen threshold. This means that, during the exposure, the signal increases but not the noise, leading to excellent values of the image quality parameters such as the Signal-to-Noise Ratio (SNR) and the Contrast-to-Noise Ratio (CNR). In SPC imaging, each interacting photon is counted as one single event, independently of its energy, so that soft X-rays are equally weighted compared to the harder ones. This results into a high Contrast (C) also for low attenuating objects, such as soft tissues in an organism or small biological samples. On the contrary, charge integrating detectors (and FP detector among this class of devices) integrate both signal and noise, and high energy photons bring a larger weight than low energy ones. These high energy photons, however, contribute less to the detectability (SNR) and to the visibility (C) of low contrast samples, since material attenuation generally decreases with increasing energy.

Theoretical models and computer simulations [1]-[3] show that energy sensitive detectors - and SPC detectors as particular representatives of this class of devices - may perform better than charge integrating systems in terms of SNR, for X-ray 2D and 3D imaging. The significance of such result is also related to the possibility of a high image quality for a satisfactory visualization of the sample with a lower radiation dose, because the same image SNR can be achieved with a lower exposure level.

The above described aspects of the SPC technology are most important in medical imaging, where the patient absorbed dose and the low contrast image quality for the soft tissues detection are the fundamental parameters to take into account. In fact, the harder task in X-rays imaging is to visualize small and low-attenuating structures in an organism, using X-rays of energies neither too low (because they result in a high absorbed dose) or too high (because they result in loss of contrast for softer tissues).

SPC detectors may provide an accurate representation of the beam hardening effect with compared to charge integrating devices [4]. In fact, charge integration decreases the relative weight of the low energy part of the spectrum thus giving less importance to the loss of the soft photons as the beam is transmitted through the sample. On the other hand, SPC devices assign the same weight to all the detected photons, leading to a higher but more correct expression of the beam hardening effect.

The aim of this thesis is to experimentally demonstrate the feasibility of planar, real-time and tomographic X-ray imaging utilizing an SPC detector in the field of Medical Physics. Since the use of this technology is regarded as an alternative to the more commonly employed charge integrating systems, a comparison with an FP detector, in terms of image quality parameters (SNR, C, CNR) evaluation has also been done.

The thesis is organized as follows.

In the first chapter, the basic concepts of the SPC technology are described, with a particular attention to the analysis of advantages and drawbacks of its use in Medical Imaging. The CT technique and the more common reconstruction algorithms have also been described in their general features. Finally, an overview of the state of the art of the SPC application in CT is presented.

In the second chapter, the experimental systems employed for the experimental part of this work are described, with particular attention to the SPC detector used: the Medipx2 SPC hybrid pixel detector, developed within the Medipix2 European Collaboration (designed at CERN, Geneva, Switzerland) to which University & INFN Napoli belong [5]. The characterization of the measurements setups is presented. Moreover, two kinds of detector pixels efficiency equalizations have been described: the standard Flat Field Correction (FFC) and the Signal-to-Thickness Calibration (STC) [6] [7].

In the third chapter are reported the experimental tests and images relative to the application of the Medipix2 SPC detector for planar, tomographic and real-time X-ray imaging of small biological samples. Then, its performance in terms of image quality parameters has been compared to a commercially available FP charge integrating detector used in the same experimental conditions. Moreover, two kinds of detector pixels efficiency equalizations have been compared in terms of image parameters, on images of both phantoms and biological samples.

References

[1] R. N. Cahn, *et al.*, “Defective quantum efficiency dependence on X-ray energy weighting in mammography”, Med. Phys., vol.26, No. 12 (1999);

[2] J. Giersch, *et al.*, “The influence of energy weighting on X-ray imaging quality”, NIM A, vol.531, pp. 68-74 (2004);

[3] P. M. Shikhaliev, *et al.*, “Photon counting computed tomography: concept and initial results”, Med. Phys., vol. 32 (2), pp. 427-36 (2005);

[4] P. M. Shikhaliev, “Beam hardening artefacts in computed tomography with photon counting, charge integrating and energy weighting detectors: a simulation study”, Phys. Med. Biol., vol. 50, pp. 5813-27 (2005);

[5] Medipix collaboration at *www.cern.ch/medipix*;

[6] J. Jakubek, “Data processing and image reconstruction methods for pixel detectors”, NIM A, vol. 576, 164-170, (2003);

[7] J. Jakubek, *et al.*, “Quality of X-ray transmission radiography based on single photon counting device”, NIM A, vol.546, pp. 113-117 (2005).

Chapter 1. Application of a Single Photon Counting (SPC) detector in the medical imaging field

In this chapter we introduce the concept of the Single Photon Counting (SPC) detector and we examine its usage in the field of medical imaging as an alternative to the commonly used charge integrating detectors. In particular, we investigate its application for the Computed Tomography (CT) technique.

The chapter is divided into 3 paragraphs:

1.1 SPC: how it works, advantages and drawbacks
1.2 Computed Tomography
1.3 SPC and CT: state of the art

1.1 SPC: how it works, advantages and drawbacks

Most radiological imaging systems consist of direct or indirect digital detector CCD or, screen-films. This class of devices works via a charge integrating principle: the sum of the charge accumulated in a pixel corresponds to the total X-ray energy absorbed in that pixel in the image. Therefore the contribution of the converted photons is weighted by their energy. Image contrast is generated by the absorption of photons in different parts of the object. Since the low energy photons are attenuated more strongly in the object, they carry more information than the high energy ones; for this reason, weighting the photon by its energy implies that image contrast carried by low energy photons has a weaker weight and the Poisson noise contributions from high energy photons are enhanced. The result is a decrease in the image Signal-to-Noise ratio (SNR).

The alternative is the photon counting mode that performs counting of single events. Quantum imaging has become possible due to the advances in microelectronics, which allows for design and fabrication of pixellated chips with pulse processing front-end electronics in each cell. In this way a particle signal can be distinguished from the background noise and the discrimination is implemented using a noise reducing pre-amplifier circuit and a discriminator in every read-out channel to set, when possible, the detecting level safely above the noise. The measured charge pulse defines the energy of the absorbed photon, and it is possible to perform spectroscopic discrimination in each pixel. Furthermore, is possible to use a few thresholds to select an energy window in a continuous spectrum to provide the so-called “colour” X-ray imaging.

The main advantage of photon counting noise suppression is the resulting large and linear dynamic range that improves the image quality for low-contrast objects and allows to lower the patient dose [8]. Hence, it is possible to use long continuous data acquisition times to improve the image contrast for applications with low photon flux. A photon counting detector would also provide immunity from the afterglow effect, present in scintillator based detector, which causes image blurring and degradation of spatial resolution for CT [13].

In the medical X-ray imaging field an important requirement is a high count rate capability and a fast digital data storage. This necessity has been met thanks to the employment of Application Specific Integrated Circuit (ASIC) technologies, able to accommodate the high counting and data transfer rates required.

The density of electronic components per unit area exponentially increases with time, thanks to the reduced feature size, allowing increased functionality per unit area and/or reduced pixel size. On the other hand, the smaller the pixel area the higher the probability of the charge sharing effect (the signal charge from one particle shared between several pixels[1]) that leads to a loss of registered hits and, for medical imaging applications, this is turned into a higher patient dose [14]. A number of solutions have been studied to overcome this problem, like summing up the charge fractions belonging to the charge deposition of one particle and comparing the summed charge to a threshold [15].

When comparing the integrating technology with the SPC one in the case of a polychromatic X-ray source, one can find that the SNR is improved due to the fact that an SPC detector assigns an optimal energy-weighting factor *w* (equal to 1) to the detected photons, as opposed to the charge integrating detector, where the energy factor is approximately proportional to the energy of the photon (*w* ~ E), favouring high energy photons.

In fact, by appropriately selecting the weighting factor *w*, as a function of the photon energy E, the image SNR can be optimized. For a photon energy spectrum passing through two adjacent regions, 1 and 2, with different absorption coefficients (different transmission T), the SNR can be defined as the difference of the means of two intensity distributions S_1 and S_2, divided by their standard deviations σ^2_1 and σ^2_2 [16]:

$$SNR = \frac{|< S_1 > - < S_2 >|}{\sqrt{(\sigma_1^2 + \sigma_2^2)}},$$

from which one can write [1]:

$$SNR = \frac{\int_E w(E)(< n_1(E) > - < n_2(E) >)}{\sqrt{(w_1^2(< n_1 > + < n_2 >)}},$$

where n_1 and n_2 denote the number of photons recorded in the two adjacent regions. It has been shown [1] that the optimal weighting function is given by:

---

[1] The photon interaction with the detecting medium convoluted with diffusion gives rise to an extended cloud of charge, whose lateral dimension might reach a size comparable to the pixel pitch [15].

$$W_{opt}(E) = \frac{T_1(E) - T_2(E)}{T_1(E) + T_2(E)}$$

with T_1 and T_2 the transmission through region 1 and region 2 respectively. This optimal weight function can only be calculated if the exact composition and thicknesses of the object are already known. It can be seen that, in the region dominated by the photoelectric effect (10 - 40) keV, the energy weighting, using a weighting factor of $1/E^3$, can result in an SNR[2] enhancement compared to the integrating and the SPC modality. Moreover, with the energy weighting mode it is possible to get images with the same quality but with less photons, reducing the dose by a factor of 2.5 [2]. In Tab. 1-1a, Tab. 1-1b and Tab. 1-1c we report some Monte Carlo simulated results from ref. [1] in which the performances in terms of SNR of the three possible detection modalities have been compared: the charge integration, the energy weighting and the single photon counting. Three phantoms have been simulated: a low contrast one, a high contrast breast calcifications one and a computed tomographic one (see caption relative to Tab. 1-1 for details). As one can see from the SNR evaluation, the higher image quality is recovered from the energy weighting modality, followed by the single photon counting detection.

Fig. 1-1 reports the behaviour of the theoretical weighting function, as evaluated from ref. [1], for two material combinations and the plot of $1/E^3$, compared to the plot for an integrating detector (~ E) and a counting detector (const.). A further consideration must be done on the improvements accomplished with optimum energy weighting on single photon counting mode as well as with the single photon counting mode on energy integrating mode for two different energy spectra [1]: one can see that the SNR enhancements are larger for a molybdenum spectrum than for a tungsten spectrum. In fact, the Mo spectrum shows stronger variations with energy, especially in the low energy region where the relative differences between the weight factors are larger, therefore the gain in weighting the spectrum is larger for molybdenum compared to tungsten. The found results are fairly similar for tumours and for micro-calcifications.

It is worth paying attention also to an important effect of X-ray computed tomography that is the "beam hardening". This effect is caused by the higher absorption from the sample of X-rays with lower energy, so that the spectrum traversing the sample looses a huge fraction of its soft component, resulting "harder" than the original one. It is interesting to note how different types of detector face with this phenomenon.

---

[2] The Signal-to-Noise ratio as defined in ref. [2] is: SNR = $\frac{\tilde{S}}{\sigma_{\tilde{S}}}$, where $\tilde{S}$ is the sum of the signals of each channel of an energy sensitive detector multiplied for an individual weighting factor w_i and $\sigma_{\tilde{S}}$ is the noise obtained from the error propagation (assuming that the noise is Poisson distributed).

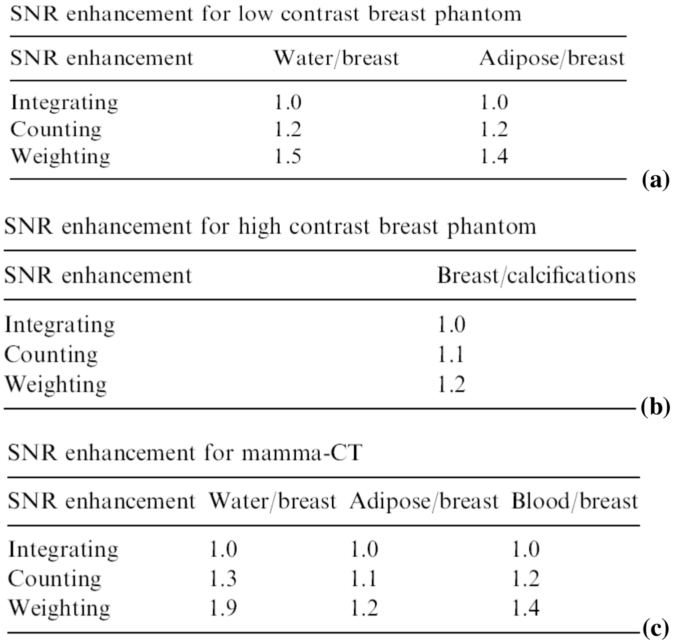

SNR enhancement for low contrast breast phantom

SNR enhancement	Water/breast	Adipose/breast
Integrating	1.0	1.0
Counting	1.2	1.2
Weighting	1.5	1.4

(a)

SNR enhancement for high contrast breast phantom

SNR enhancement	Breast/calcifications
Integrating	1.0
Counting	1.1
Weighting	1.2

(b)

SNR enhancement for mamma-CT

SNR enhancement	Water/breast	Adipose/breast	Blood/breast
Integrating	1.0	1.0	1.0
Counting	1.3	1.1	1.2
Weighting	1.9	1.2	1.4

(c)

Tab. 1-1 Results from SNR evaluation on Monte Carlo simulated data relative to a low contrast phantom (a cylinder consisting of breast tissue including five cylinders of adipose tissue and five cylinders of water) (a), a breast calcification phantom (a cylinder consisting of 30 mm thick breast tissue, including 35 breast calcification of different thicknesses and diameters) (b) and a computed tomography phantom (a phantom 56 mm diameter including eight low contrast objects: one adipose and one water object and six objects of blood with different diameters) (c). The evaluations have been done simulating an integrating detector, a single photon counting detector and a weighting detector. [1]

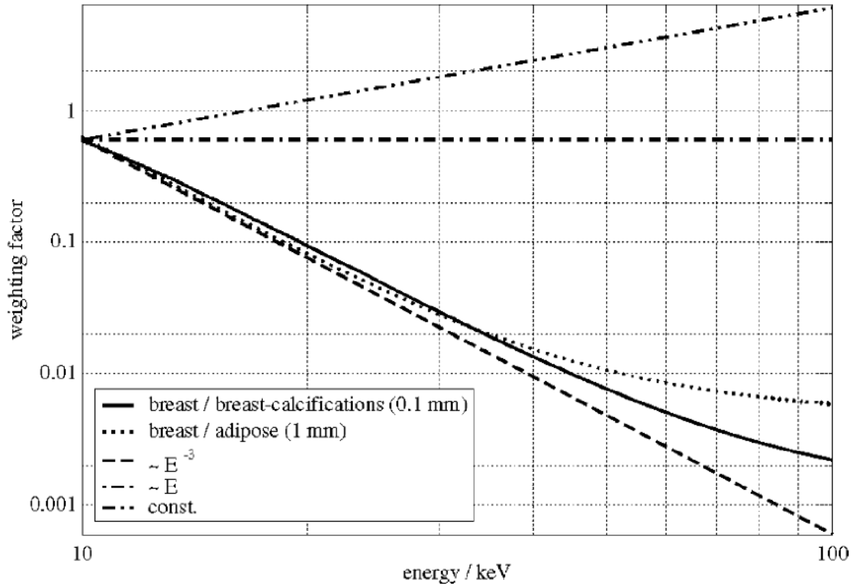

Fig. 1-1 Weighting functions for two material combinations and the plot for 1/E^3, resulting in the best approximation. For comparison also the plot for an integrating detector (~ E) and a counting detector (const) are shown. [2]

It has been shown [4] from a simulation study that a charge integrating detector results in 1.8 % less beam hardening artefacts from bone insert in a 20 cm diameter water phantom compared to a photon counting[3]. On the other hand optimal energy weighting, providing the highest SNR, results in 7.7 % higher beam hardening artefacts from the same bone insert, compared to the SPC detector. These values can be explained as follows: the energy weighting detectors score the detected photons with the factor proportional to E^{-3}, so that the lower energy photons are scored higher than high energy photons; therefore, energy weighting detectors overestimate the beam hardening effect. On the other hand, for the same reason, the charge integrating devices underestimate this effect. Only the photon counting technology provides an accurate representation of the phenomenon because of its flat energy weighting.

1.2 Computed Tomography

Among the high number of medical imaging techniques, X-ray Computed Tomography (CT) holds, nowadays, the most important role for 3-D morphological investigation of organs and tissues both in the human and in the animal diagnostic field. This non-invasive method, in fact, allows to visualize the anatomical internal structures of a body and it is commonly combined with a functional diagnostic technique (as SPECT, PET or MRI) to get a global functional knowledge of the organism.

The physical principle exploited in CT is the X-ray penetrative nature and the attenuation which they undergo when passing through the body. X-rays of given energy are differently attenuated from different tissues (soft tissues or bone structures), giving rise to a three-dimensional map of the attenuation coefficient of the body. In this way it is possible to get information on anatomical structures, on their morphology and position and, consequently, to find anomalies, diseases and structural changes.

The potential of the CT technique has been exploited not only in the diagnostic medical field but also in several other applications, like diagnostic of materials, investigation of microelectronics components, biology, geophysics, archaeology, cultural heritage, safety in public places or with controlled-door (airports, military zones, prisons, etc.) and in all the sectors in which an internal and non-destructive investigation of opaque objects is necessary. All the CT systems realized for non-clinical purposes go under the definition of "industrial CT".

An X-ray CT system is realized by means of three principal components: an X-ray source (typically tube), the sample to be analysed and a detection system of the transmitted radiation. Moreover, it is necessary to use a mechanical rotation arrangement for the sample or, alternatively, for the source-detector system. The image acquisition process consists of the detection of the X-rays beam exting from the sample and interacting with a detector placed in the downstream. The images

---

[3] The beam hardening has been evaluated as the relative percentage of the average pixel values in the shadow of the bones compared to the average pixel values over the periphery of the image [4].

(projections) are acquired at different angular positions of the sample compared to the source-detector system, at least, 180° + α (depending on the geometry and on the beam angle), where α is the fan angle (aperture angle of the beam). In this way, each angular view corresponds to a bi-dimensional projection of the tri-dimensional attenuation properties of the sample. There are four generations for the CT geometry, as depicted in Fig. 1-2 (a - d): in the first generation (a) the detector-source pair translates through the object's whole dimension at each angular view; the geometry and scanning modality for the second generation (b) is the same as the first, but the beam has a given fan angle while the single detector is substituted by a linear array of several detectors to increase the sampling. In the third generation (c) the fan beam is wider as well as the detectors array so as to avoid the translation. Finally, in the fourth generation (d) only the tubes rotate and the fan beam is recorded by an array of static detectors placed all around the sample. Alternatively to these geometries, the source-detector couple stands fixed in one position, while the sample rotates.

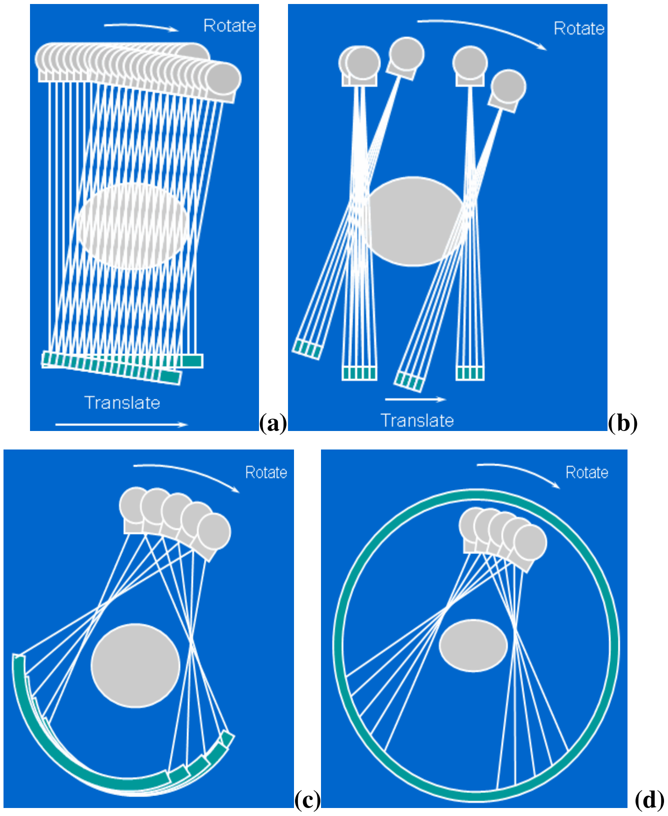

Fig. 1-2 First (a), second (b), third (c) and fourth (d) generation of CT depicted in a schematic way [8]. As described in the text, in the first generation (a) the detector-source couple translates through the whole object's dimension at each angular view; the geometry and scanning modality for the second generation (b) is the same as the first, but the beam has a fan aperture angle while the single detector is substituted by an array of several linear or bent detectors to increase the sampling. In the third generation (c) the fan beam is wider as well as the detectors array so as to avoid the translation. Finally, in the fourth generation (d) only the tubes rotate and the fan beam is recorded by an array of static detectors placed all around the sample.

The projection of an object at a given angle φ is made up of a set of line integrals, representing the total attenuation of the X-ray beam traversing the whole object in a straight line. The simplest and easiest way to model the phenomenon is by considering the data collected as a series of parallel rays, at position ξ, across a projection angle φ and for various angles.

Attenuation occurs exponentially in tissue:

$$I = I_0 \exp(-\int \mu(x,y)d\xi)$$

where μ(x) is the attenuation coefficient at position x along the ray path. Therefore, generally, the total attenuation p of a ray at position ξ, on the projection angle φ is given by the line integral:

$$p(\xi,\varphi) = \ln(I/I_0) = -\int \mu(x,y)d\xi), \ (1)$$

and because in polar coordinate the value of ξ onto which the point (x, y) will be projected at angle φ can be written as:

$$\xi = x\cos\varphi + y\sin\varphi$$

equation (1) can be rewritten as:

$$p(\xi,\varphi) = \int f(x,y)\delta(x\cos\varphi + y\sin\varphi - \xi)dxdy,$$

where f(x, Y) represents μ(x, y), δ is the Dirac delta function and the coordinates x, y, ξ and φ are defined in Fig. 1-3.

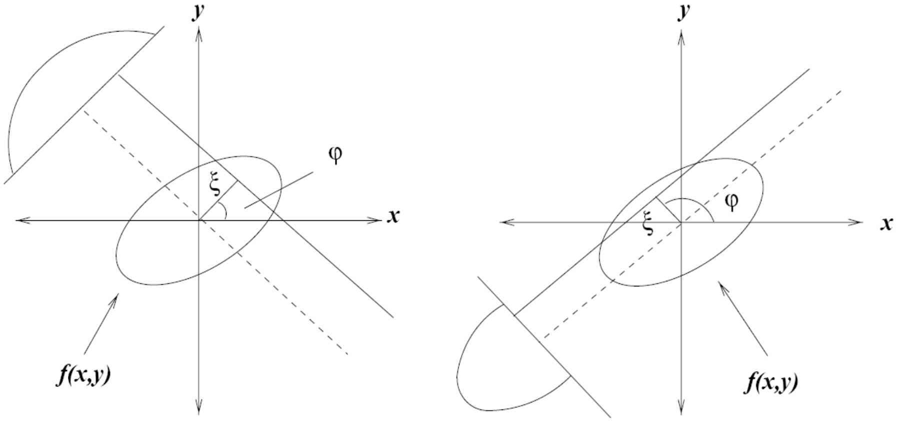

Fig. 1-3 Coordinate system for the Radon transform [9]

The function p(ξ, φ) is the so-called "Radon transform" of the 2-D object and it is often referred to as "sinogram" because for an off-center point source it is a sinusoid. A typical slice image and its Radon transform are shown in Fig. 1-4.

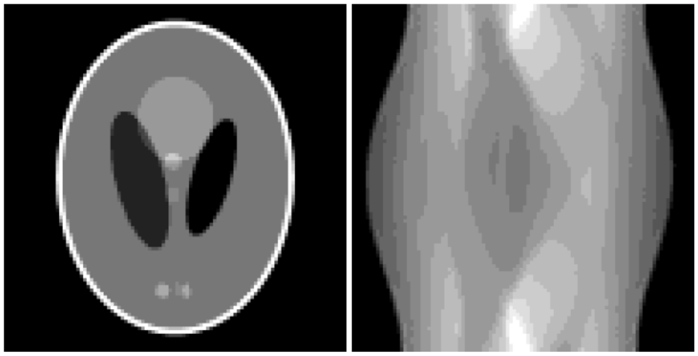

Fig. 1-4 Shepp-Logan phantom and its Radon transform (sinogram) [8]

The task of tomographic reconstruction is to find f(x, y) for given knowledge of p(ξ, φ). Mathematically, a backprojection operation defined as:

$$f_{BP}(x, y) = \int p(x\cos\varphi + y\sin\varphi, \varphi)d\varphi$$

is calculated to bring the measured sinogram back into the image space along the projection path. Fig. 1-5 shows the backprojection image of the Shepp-Logan phantom of Fig. 1-4.

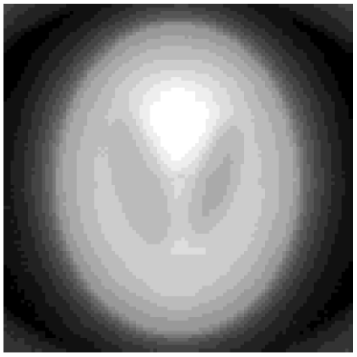

Fig. 1-5 The backprojection image of the Shepp-Logan phantom. [8]

The solution to the inverse Radon transform is based on the "central slice theorem" (CST), wich relates $F(\nu_x, \nu_y)$, that is the 2D Fourier transform (FT) of f(x, y), and $P(\nu, \varphi)$, that is the 1D FT of p(ξ, φ). Matematically:

$$P(\nu, \varphi) = F(\nu\cos\varphi, \nu\sin\varphi)$$

and it states that the value of the 2D FT of f(x, y) along a line at the inclination angle φ is given by the 1D FT of p(ξ, φ), the projection profile of the sinogram acquired at angle φ. From the draw of Fig. 1-6one can deduce that with enough projections, $P(\nu, \varphi)$ can fill the ν_x - ν_y space to generate $F(\nu_x, \nu_y)$.

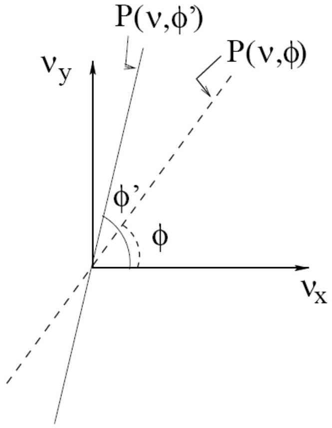

Fig. 1-6 Central slice theorem [9]

Once $F(\nu_x, \nu_y)$ is obtained from $p(\xi, \varphi)$ using the CST, $f(x, y)$ can be obtained by applying the inverse FT to $F(\nu_x, \nu_y)$ that converts data back from frequency domain to spatial domain (Fig. 1-7).

$$\begin{tikzcd}
f(x,y) & F(\nu_x,\nu_y) \arrow[l, "2\text{D FT}^{-1}"'] \\
p(\xi,\phi) \arrow[r, "1\text{D FT}"'] & P(\nu,\phi) \arrow[u, "\text{CST}"']
\end{tikzcd}$$

Fig. 1-7 Flow of direct Fourier reconstruction [9]

The simple backprojection has the problem of the “pattern” artefacts caused by radiation from adjacent areas resulting in the blurring of the object. Since the blurring decreases with the distance r from the object of interest, it can be described by a 1/r function and can be minimized by applying a filter to the acquisition data. Such method is called the filtered backprojection (FBP) and the applied filter is the” ramp filter” drawn in Fig. 1-8. The filtered projections are backprojected to produce an image that is more representative of the original object: once the Fourier transform $F(\nu_x, \nu_y)$ of each row in the sinogram of the 2-D projection data is taken and added together, the ramp filter $H(\nu)$, in the frequency domain is applied to each profile data:

$$F'(\nu) = H(\nu) \cdot F(\nu),$$

where $F'(\nu)$ is the filtered backprojection which is obtained as the product of $H(\nu)$ and $F(\nu)$. Finally, the inverse Fourier transform is performed to recover the filtered projection data, which are then backprojected in the same way as in the simple backprojection.

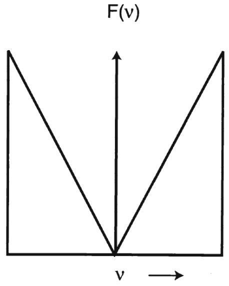

Fig. 1-8 The typical high-pass ramp filter in frequency domain [10]

An undesirable effect of the ramp filter is the amplification of the noise associated with high spatial frequencies in the images. To overcome this effect, other types filters can be used.

The FBP algorithm is an analytic method, but, on the other hand, the reconstruction is actually exact only when the noise influence is negligible and when the number of projections is infinite. Moreover, it is not an easy task to implement the algorithm taking into account the different experimental conditions like the geometry, the presence of scattering radiation or fluorescence from the sample, the beam hardening, the phase contrast effect. This limitation leads to the manifestation of artefacts in the tomographic slices lowering the image quality. To overcome this problem the class of iterative reconstruction algorithms based on the Expectation Maximization (EM) can be seen as a good alternative. Their main benefit lies in the possibility of more realistically modelling the physics of the data acquisition process, including non-linear detector response compared to attenuation line integral caused by beam hardening and scatter, as well as the stochastic properties of the measured data. Other advantages include the ease with which they can be adapted to specific detector-response models, robust performance in the presence of incomplete data and the possibility of incorporating arbitrary constraints.

Among the iterative algorithms based on the expectation maximization method the more widely used ones are the maximum expectation maximization (MLEM) algorithm and the Ordered Sub-set Expectation Maximization (OSEM) algorithm. The first one works as follows: the projections of the sample are computed by means of a physical model and then compared to the measured ones. From the comparison the trial model of the object is updated to recover projections closer to the experimental ones. The iterative nature of the algorithm stands in the repetition of these steps (Fig. 1-9) – simulation of projections from a trial object, comparison with acquired projections and modifications of the trial object to get a new set of projections – until the perfect convergence of the simulated and experimental data producing the tri-dimensional image of the object. The main disadvantage of the MLEM iterative method is the long computational time.

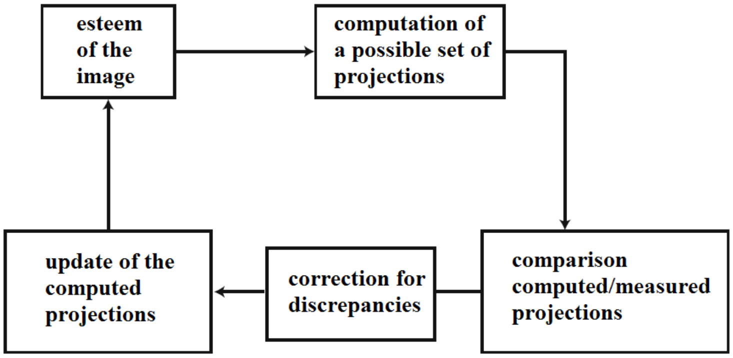

Fig. 1-9 Schematic diagram of the iterative reconstruction methods.

To accelerate the convergence speed of iterative algorithms the technique of Ordered Subsets (OS) has been introduced, which, combined with the EM method, takes the name of OSEM. The OSEM algorithm splits each iteration in several sub-iterations and, in each sub-iteration, just a selected subset of all projections is used for trial object modification. The subsequent sub-iteration uses a different subset of projections and so on. One single full iteration is complete when all the projections have been exploited. The number of projections in each subset can be as low as three or four and the speed of an iterative process results approximately increased by the number of subsets used. OSEM algorithm includes the standard EM as a particular case when a single sub-set, including all the projection, is used. [11]

Finally, when the reconstruction is complete, visualization softwares (*ImageJ, MicroView,* etc.) allow to overlap the tomographic slices in a way to recover a tri-dimensional image in which the internal sample's characteristics and their placement in the space are clearly distinguishable.

1.3 SPC: state of the art

Nowadays, all of the major imaging systems manufactures (*Canon, GE, Hologic, Philips, Siemens, Toshiba, Varian*) offer Flat Panel based Detectors (FPD), employing indirect or direct conversion technology. The pixel sizes of these detectors range from 70 µm x 70 µm to 200 µm x 200 µm, in arrays up to 14 million pixels and active areas up to 43 cm x 43 cm [18]. The alternative SPC technology, although it may show a better image quality than the charge integrating one [1], is still not largely spread in laboratories and in clinical systems because of limitations as the small sensitive areas and the high costs of production and testing. Anyway, as one can find in literature, photon counting imaging has been approached adapting detectors based on Si [19] [20], CZT [21] [22], Xe based gas avalanche detectors [23] and Micro-Channel Plate (MCP) detectors [24] [25]. Thus, in the medical physics panorama we can find some examples of SPC detectors employed for X-ray imaging; in the following we present a short *excursus* of such devices.

1.3.1 XPAD2 and XPAD3 photon counting chip for X-ray PIXSCAN CT scanner

An example of SPC detector employment in CT comes from the collaboration between the *Centre de Physique des Particules de Marseille* (Marseille, France), the *Laboratoire de Cristallographie* (Grenoble, France) and *SOLEIL Synchrotron* (St. Aubin, France). The CT scanner developed by this collaboration employs the X-ray Pixel Chip with Adaptable Dynamics (XPAD3) circuit, a photon counting chip, newer version of a XPAD2 [26] [27]. This device is a hybrid detector in which the chip is connected to the sensor (Si or CdTe) using the bump bonding and flip-chip technologies. The circuit is designed in IBM 0.25 μm technology and contains 9600 square pixels, 130 μm x 130 μm in size, arranged in a matrix of 80 x 120 elements. It provides a count rate higher than 10^9 ph/pixel/mm^2, a high dynamic range higher than 60 keV, a noise detection level of 100 $e^{-/}$rms, the possibility of an energy window selection and an image read-out lower than 2 ms/frame. Each pixel of the chip contains a charge sensitive preamplifier, an operational transconductance amplifier followed by a set of current comparators for energy selection. The selected pulses feed a 12 bits counter associated with an overflow mechanism. Nine configuration bits are available in each pixel for control. The newer version has not yet been tested for tomographic acquisition, differently from the older one, XPAD2. This chip includes 600 pixels of 330 μm x 330 μm. It includes a charge amplifier, a discriminator and a 15 bits counter. Eight XPAD2 are bump-bonded on a 65 mm x 8 mm x 0.5 mm silicon sensor. Thanks to a fast read-out system, the full detector can be read in less than 2 ms. A table with all the specifications of the two chip versions is shown in Tab. 1-2.

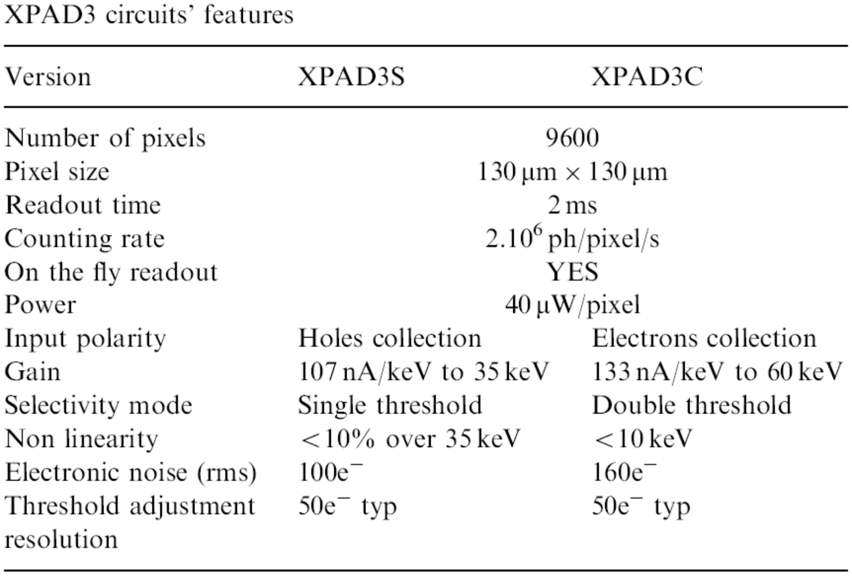

XPAD3 circuits' features

Version	XPAD3S	XPAD3C
Number of pixels	9600	
Pixel size	130 μm × 130 μm	
Readout time	2 ms	
Counting rate	2.10^6 ph/pixel/s	
On the fly readout	YES	
Power	40 μW/pixel	
Input polarity	Holes collection	Electrons collection
Gain	107 nA/keV to 35 keV	133 nA/keV to 60 keV
Selectivity mode	Single threshold	Double threshold
Non linearity	<10% over 35 keV	<10 keV
Electronic noise (rms)	$100e^-$	$160e^-$
Threshold adjustment resolution	$50e^-$ typ	$50e^-$ typ

Tab. 1-2 XPAD2 and XPAD3 chip's features. "S" stands for "Si", "C" stands for "CdTe" [27]

The CT scanner employing the XPAD2 detector is named PIXSCAN (a photo is shown in Fig. 1-10). Tomographies of an anesthetized mouse, placed into a Plexiglas cylinder, were performed using a wide conic beam aperture X-ray source (30 W, 60 kV, 0.8 mA; *Rontgentek, SEPH, France*) with an emission spot of 50 µm x 50 µm. Also several black calibration images (no object and fixed source) were acquired and averaged to obtain the map of unstable oscillating pixels. Similarly several white calibration images (no object but open source) were used to map non-working pixels with constant output. All defective pixels (oscillating and non-counting) were masked for the tomographic reconstruction calculation.

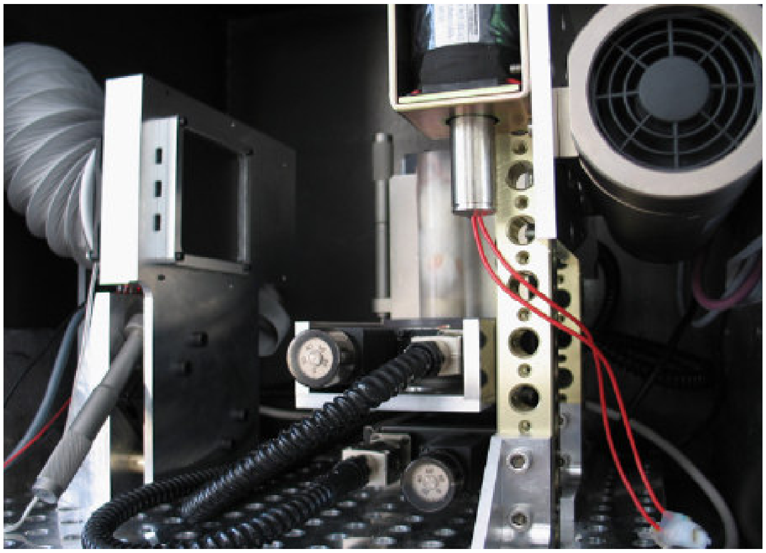

Fig. 1-10 PIXSCAN tomograph, employing the hybrid SPC detectorXPAX2 [26]

Even though 400 cone beam projections were required to get the best possible spatial resolution for the tomographic reconstruction of the mouse body, given the detector pixel size, only one image per degree (360 images per scan) has been acquired. These images have then been processed using a Feldkamp-based reconstruction algorithm for cone beam tomography provided by *CREATIS* (*RecFDK*). Examples of both one projection and of the resulting mouse tomographic images are presented in Fig. 1-11. Although images are still preliminary and can still be improved in different ways, a high absorption contrast can be seen between the air-filled lungs (dark) and the dense spine and rib bones (white) on the horizontal and coronal slices.

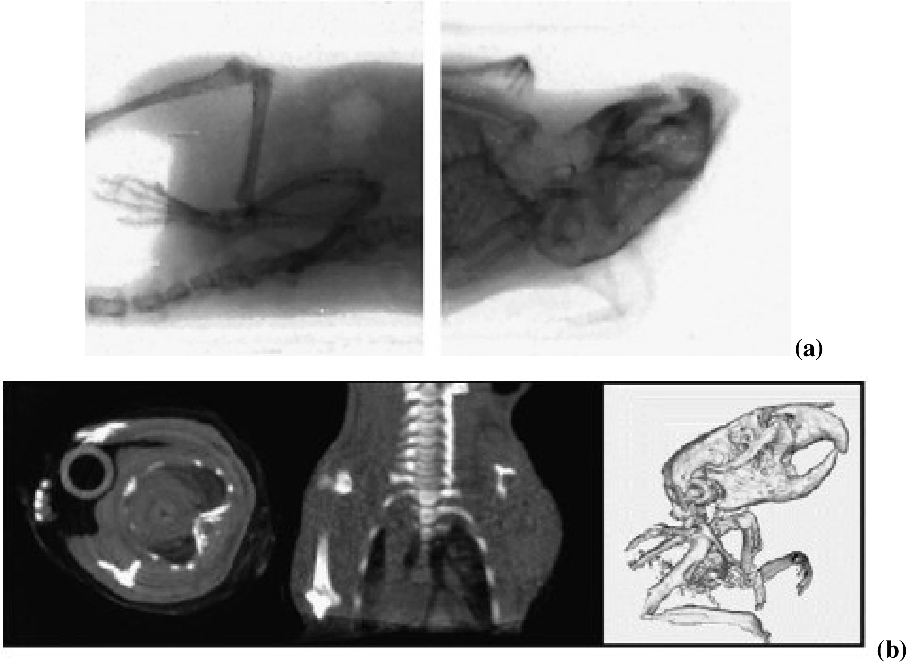

Fig. 1-11 Projection of an anesthetized mouse (a); tomographic reconstruction of mice images: horizontal slice of a mice thorax (left), coronal slice (middle), bone surface image of a mouse head and thorax (right). XPAD2 detector was employed [26]

1.3.2 Pixel Apparatus for the SLS (PILATUS) [28]

The PILATUS detector (**pi**xel appar**atu**s for the **S**LS) is a novel type of X-ray detector, which has been developed at the *Paul Scherrer Institut (PSI)* for the *Swiss Light Source (SLS)*. PILATUS detectors are two-dimensional hybrid pixel array detectors, which operate in SPC mode; they comprise a preamplifier, a comparator and a counter in each cell. The preamplifier enforces the charge generated in the sensor by the incoming X-ray; the comparator produces a digital signal if the incoming charge exceeds a predefined threshold and thus, together with the counter, one obtains a complete digital storage and read-out of the number of detected X-rays per pixel. PILATUS detectors main features include: no read-out noise, superior signal-to-noise ratio, read-out time of 5 ms, a dynamic range of 20bit, high detective quantum efficiency and the possibility to suppress fluorescence by an energy threshold that is set individually for each pixel.

The PILATUS 100k detector system has been designed for the detection of X-rays from synchrotrons or laboratory source. This hybrid pixel SPC detector has 487 x 195 pixels with a pixel size of 0.172 mm and an active area of 84 x 34 mm^2. The device has a dynamic range of 10^6 (20 bits), a read-out time of less than 3 ms and a frame rate of over 200 images/s. The quantum efficiency when the sensor is a 0.32 mm thick silicon semiconductor is suitable for experiments in the energy range of 3-12 keV, also if the detector can be used for energies of up to 30 keV or more. The counting rate higher than $2 \cdot 10^6$ photons/s/pixel allows for detection of elevated flux as from synchrotron light sources. A photo of the PILATUS SPC detector is shown in Fig. 1-12 in which the bump-bonding between chip and sensor is visible, while Tab. 1-3 reports its main features.

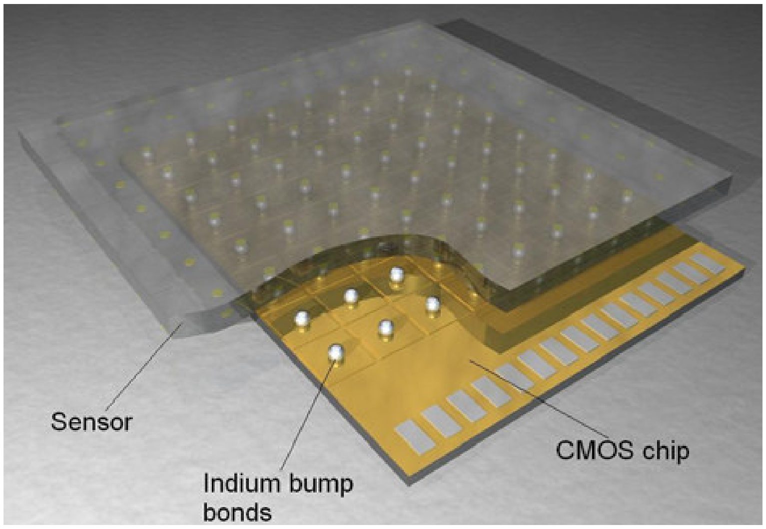

Fig. 1-12 Bump-bonded hybrid PILATUS chip [29]

Pixel size	**172 x 172 µm^2**
Format	**487 x 195 = 94 965 pixels**
Active area	**83.8 x 33.5 mm^2**
Counting rate	**> 2x10^6 counts/s/pixel**
Energy range	**3 – 30 keV**
Readout time	**< 2.7 ms**
Framing rate	**> 200 Hz**
Power consumption	**5W, air cooled**
Dimensions	**285 x 146 x 85 mm^3**
Weight	**3.9 kg**

Tab. 1-3 Main features of PILATUS SPC detector [29]

.

1.3.3 Multi-Picture Element Counters (MPEC) [30]

The MPEC read-out chip is a SPC pixel chip realized at *Bonn University, Physikalisches Institut*, with 1 MHz high-count rate capability and energy windowing. The latest version of the chip is the MPEC 2.3 for photon energy discrimination. The active area of 6.4 mm x 6.4 mm is structured into 32 x 32 pixels of 200 µm x 200 µm size. Multichip modules are built, arranged with 4 SPC MPEC chips, bump bounded to 1.3 cm x 1.3 cm large semiconductor sensor. Every pixel cell of a MPEC 2.3 chip contains a preamplifier, two independent discriminator, and two 18 bit counters. A coarse discriminator threshold is set globally and a fine adjustment can be applied dynamically for each pixel. An energy window can be set using the two independent discriminators. The hybrid nature of the chip allows to bump bond it either to a silicon (300 µm thick) or to a CdTe (500 µm thick) sensor.

1.3.4 A Large-Area Detector with Incrementor (ALADIN)

ALADIN is a read-out SPC chip solder bump bonded to a silicon pixel detector developed from the collaboration between the *Imperial College of London (UK), the Glasgow University (UK) and the Rutherford Appleton Laboratory, Chilton (UK).* It is provided with 64 x 64 pixels, 150 µm x 150 µm in size, capable of a max count-rate of 1 MHz per pixel and a read-out speed of 400 µs. Up to seven detectors have been connected together to get large area modules for X-ray diffraction studies. It has been showed that these ALADIN composed modules can image 19 keV photons at 200 kHz photons per pixel with 3 keV FWHM noise [31]. The frame-rate speed can arrive up to 1000 images per second, independently of the image size.

Finally, we report here a table (Tab. 1-4) with a list of several systems and projects for hybrid SPC detectors [32], underlying that the development of this kind of devices had as its first aim the application in the High Energy Physics (e.g. ALICE [33], ATLAS [34], CMS [35], LHCb [36]) and that, only after a while they have been exploited in the Medical Imaging Field.

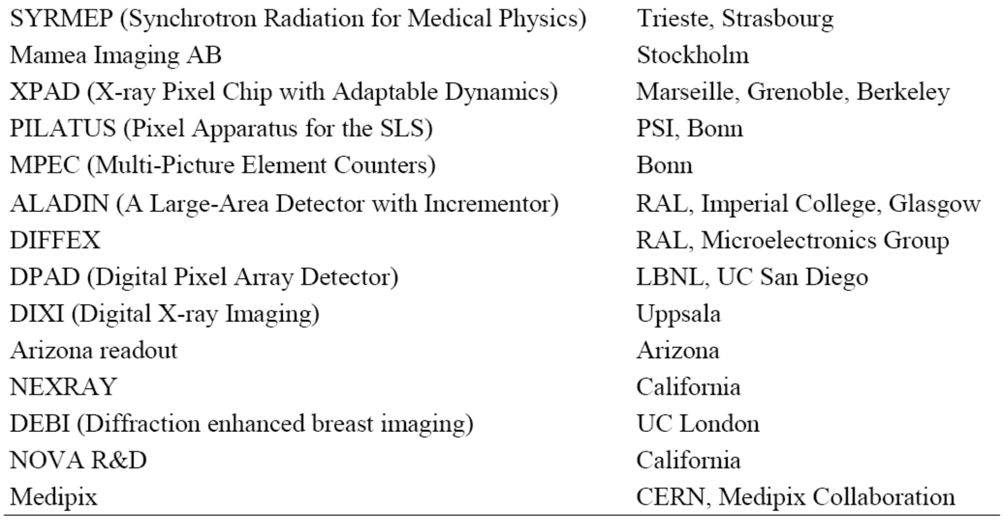

SYRMEP (Synchrotron Radiation for Medical Physics)	Trieste, Strasbourg
Mamea Imaging AB	Stockholm
XPAD (X-ray Pixel Chip with Adaptable Dynamics)	Marseille, Grenoble, Berkeley
PILATUS (Pixel Apparatus for the SLS)	PSI, Bonn
MPEC (Multi-Picture Element Counters)	Bonn
ALADIN (A Large-Area Detector with Incrementor)	RAL, Imperial College, Glasgow
DIFFEX	RAL, Microelectronics Group
DPAD (Digital Pixel Array Detector)	LBNL, UC San Diego
DIXI (Digital X-ray Imaging)	Uppsala
Arizona readout	Arizona
NEXRAY	California
DEBI (Diffraction enhanced breast imaging)	UC London
NOVA R&D	California
Medipix	CERN, Medipix Collaboration

Tab. 1-4 Systems and projects for hybrid photon counting pixel arrays [32].

1.4 References

[8] H. Bruce, “Physics of medical X-ray imaging”, Medical Physics Publishing, USA, pp. 327 (1991);

[9] http://www.aapm.org/meetings/99AM;

[10] G. P. Saha, “Basic of PET imaging – Physics, Chemistry, and Regulation”, Springer New York (2005);

[11] H. M. Hudson, R. S. Larkin, “Accelerated image reconstruction using ordered sub-sets of projection data”, IEEE Trans. on Medical Imaging, vol. 13, No. 4 (December 1994);

[12] B. Mikulec, *et al.*, "Characterization of a single photon counting pixel system for imaging of low-contrast objects”, NIM A, vol. 458, p. 352-59 (2001);

[13] J. Hsieh, *et al.*, “Investigation of a solid-state detector for advanced computed tomography”, IEEE Trans. Med. Imaging, vol. 19, pp. 930-40 (2000);

[14] M. Chmeissani, B. Mikulec, “Performance limits of a single photon counting pixel system”, NIM A, vol. 460, pp. 81-90 (2001);

[15] X. Llopart, *et al.*, “Medipix2, a 64k pixel redout chip with 55 μm square elements working in single photon counting mode”, IEEE Trans. Nucl. Sci., vol. 49, pp. 2279-83 (October 2002);

[16] L. Tlustos, “Performance and limitations of high granularity single photon counting processing X-ray imaging detectors”, Doctoral Thesis (2005);

[17] http://www.impactscan.org

[18] G. Wang, *et al.*, “An outlook on X-ray CT research and development”, Med. Phys., vol. 35 (3) (March 2008);

[19] F. Arfelli, *et al.*, “At the frontiers of digital mammography : SYRMEP”, NIM A, vol. 409, pp. 529-33 (1998) ;

[20] E. Beuville, *et al.*, “High resolution X-ray imaging using a silicon strip detector”, IEEE Trans. Nucl. Sci., vol. 45, pp. 3059-63 (1998);

[21] J. A. Heanue, *et al.*, “CdZnTe detector array for a scanning-beam digital X-ray system”, Proc. SPIE, vol. 3659, pp.718-25 (1999);

[22] T. O. Tumer, *et al.*, “Preliminary results obtained from a novel CdZnTe pad detector and read-out ASIC developed for an automatic baggage inspection system” IEEE Nucl. Sci. Symp. Conf. Rec., 1 4/36-4/41 (2000);

[23] S. Thunberg, *et al.*, “Dose reduction in mammography with photon counting imaging”, Proc. SPIE, vol. 5368, pp. 457-65 (2004);

[24] P. M. Shikhaliev, Molloi "Count rate and dynamic range of an X-ray imaging system with MCP detector", NIM A, vol. 557, pp.501-7 (2006);

[25] P. M. Shikhaliev, *et al.*, "Scanning-slit photon counting X-ray imaging using a microchannel plate detector", Med. Phys., 31, pp. 1061-71 (2004);

[26] P. Delpierre, *et al*, IEEE Trans. Nucl. Sci. NS-49 (4) 1709 (2002) ;

[27] P. Delpierre, *et al.*, "PIXSCAN: pixel detector CT-scanner for small animal imaging", IEE NSS Conf. Rec., vol. 4, pp.2381-85 (2005);

[28] http://pilatus.web.psi.ch/pilatus.htm;

[29] User Manual – PiILATUS 100k Detector System, hasylab.desy.de/e81/e3796/e32448/e41226/e41228/infoboxContent44425;

[30] P. Fischer, *et al*, "A photon counting pixel chip with energy windowing", IEEE Trans. Nucl. Sci. (2001);

[31] P. Seller, *et al.*, "Photon Counting hybrid pixel detector for X-ray imaging", NIM A, vol. 455, pp. 715-720 (2000);

[32] J. Ludwig, B. Mikulec, "Detector systems for medical diagnostics", Russian Journal, vol. 46 (6), pp. 609-14 (2003)

[33] M. Campbell, *et al.*, "The ALICE silicon pixel detector", NIM A, vol. 582 (3), pp. 728-32 (2007);

[34] http://atlas.ch

[35] A. Dominguez, "The CMS pixel detector", NIM A, vol. 581 (1-2), pp. 343-46 (2007);

[36] T. Gys, "The pixel hybrid photon detector for the LHCb-rich project", NIM A, vol. 465 (1), pp. 240-46 (2001).

Chapter 2. Experimental set-up, system characterization and elaboration data procedures

In this chapter we present the single photon counting detector used in this work and the set-ups in which it has been employed. The characterization of the set-ups is reported.

A comparison of the SPC with a commercial energy integrating flat panel (FP) device has been carried out by means of a number of image quality parameters which have been here defined. Moreover, two pixel efficiency correction methods, a commonly applied one in Medical Imaging field (the Flat Field Correction, FFC) and a novel one (the Signal-to-Thickness Calibration, STC), performed on experimental data are here described.

The chapter is divided in 3 paragraphs:

1.4 Medipix2 SPC detector
1.5 Experimental set-up
1.6 Image quality (evaluation parameters and image correction methods)

2.1 Medipix2 SPC detector [37]

Medipix2 is an experimental single photon counting (SPC) detector developed within the Medipix2 European Collaboration (designed at CERN, Geneva, Switzerland) for various imaging application with X-rays and γ-rays, including synchrotron radiation, nuclear medicine, mammography, dental radiography, and radiation monitoring in nuclear facilities.

The Medipix2 is the second improved generation [38] of a hybrid [39] Application-Specific Integrated Circuit (ASIC) consisting of a CMOS read-out chip which is bump-bonded pixel by pixel to a matching pixel semiconductor detector. The hybrid nature makes it possible to develop separately the read-out board from the sensor, giving the opportunity to choose the semiconductor material relatively to the application. The chip is design to accept either positive or negative charge input (either electrons or holes collection of the radiation induced ionization charge) in order to assure a large choice for the sensor material (Si, GaAs, CdZnTe,...). Detector leakage current gets compensate pixelwise at the input. Both the chip-board and the sensor have 256 x 256 square pixels, 55 μm pitch size, for a sensitive area of 14 mm x 14 mm. A clarifying illustration is depicted in Fig. 2-1, while a photo of the detector is shown in Fig. 2-2.

Each cell contains (Fig. 2-3)

- a charge sensitive preamplifier;
- a double threshold discriminator, with an upper and lower threshold adjustment performed with a 3-bits register in each pixel, which allows threshold adjustment in eight steps;

– a 13-bit pseudo-random counter (the counter dynamic range can reach 11810 counts with overflow for a redesigned Medipix2 version called Mpix2MXR [40]).

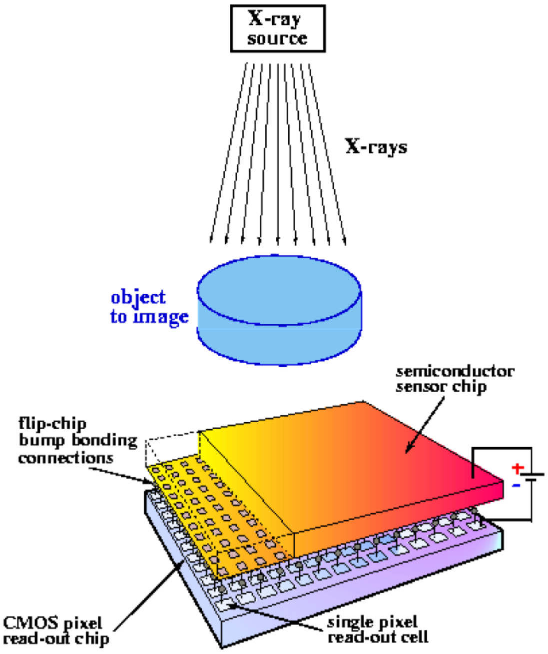

Fig. 2-1 The Medipix2 ASIC is a high spatial, high contrast resolving CMOS pixel read-out chip working in SPC mode. It can be combined with different semiconductor sensors (Si, GaAs, CdZnTe, ...) which convert the X-rays directly into detectable electric signals. This hybrid device represents a new solution for various X-ray and gamma-ray imaging applications [5].

The serial read-out can be performed either by a data acquisition card connected to the MUROS [41] serial interface circuit board (designed at NIkHEF [42]) or by a USB adapter (designed at Institute of Experimental and Applied Physics [43] of Czech Technical University in Prague, Czech Republic). The serial read-out speed is of 8.5 ms at 100 MHz with the MUROS interface, while the parallel read-out speed is of 266 µs at 100 MHz, allowing for high frame-rate real-time imaging [45] [46].

Fig. 2-2 Front and back of the Medipix2 hybrid detector.

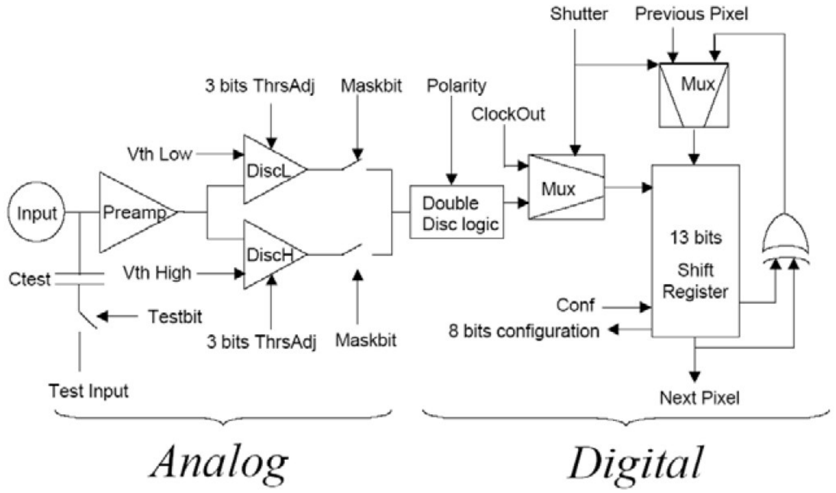

Fig. 2-3 Scheme of the Medipix2 read-out circuit for each pixel [44]

Each pixel can handle count rates up to about 100 kHz of randomly arriving particles and the exposure time can be arbitrarily set by means of the dedicate software Pixelman [43]. A summary of the main features of Medipix2 is listed in Tab. 2-1 [47].

Matrix array size	256 × 256 pixel
Square pixel size	55 μm
Sensitive area	14.08 × 14.08 mm^2
Ratio (sensitive area/total chip area)	87%
Pixel counter	13 bit
Max. count rate per pixel	1 MHz
Window threshold discrimination	High and low levels
Serial read-out bus	LVDS (>100 MHz)
Parallel read-out bus	32-bit single-ended CMOS (>100 MHz)
Charge preamplifier gain (e^-)	12.5 mV/ke$^-$
Charge preamplifier gain (h)	13.25 mV/ke$^-$
Charge preamplifier nonlinearity (e^-)	<3% to 100 ke$^-$
Charge preamplifier nonlinearity (h)	<3% to 80 ke$^-$
Charge preamplifier peaking time	<200 ns
Nominal test input capacitance	8 fF
Electronic noise (sigma)	105 e$^-$
Threshold dispersion (sigma)	500 e$^-$
Threshold dispersion after adjustment (sigma)	110 e$^-$
Configuration register	8-bit (mask, enable, 3-bit thrs. adj. for each discriminator)
No of DACs for internal voltage settings	13 (8 bit each)
R/W internal fast shift register	256 bit
Analogue & digital circuitry supply voltage	2.2 V
Total analogue power consumption	500 mW
Serial read-out time @ 100 MHz	8.5 ms
Parallel read-out time @ 100 MHz	266 μs
No of I/O pads	127
Radiation tolerance	<200 krad (10 keV x-ray)
Buttability on three sides, daisy chain connection between chips	

Tab. 2-1 Main characteristics of the Medipix2 SPC chip [47]

In this work a MUROS2 interface has been used for the serial read-out and control of the chip. The sensor material was a 300 µm thick silicon sensor. The efficiency of this semiconductor for the mean energy of about 15 keV, in which we were working, results of about 50 %. For the low energy range (0 – 40) keV exploited for biological imaging Si is the most common chosen material. Obviously, a thicker detector would have a higher absorption efficiency. Fig. 2-4 shows the absorption efficiency for different materials (GaAs 200 µm and 300 µm thick, Si 300 µm and 1 mm thick and CdTe 300 µm thick) as a function of the photon energy ranging from 5 to 100 keV [48].

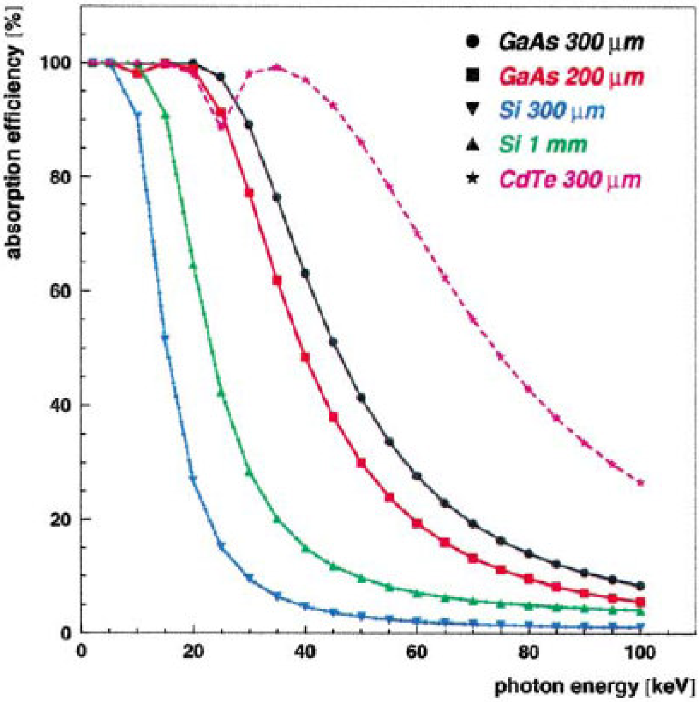

Fig. 2-4 Absorption efficiency for different materials (GaAs 200 µm and 300 µm thick, Si 300 µm and 1 mm thick and CdTe 300 µm thick) as a function of the photon energy ranging from 5 to 100 keV. [48]

2.2 Experimental set-up

The radiographic/tomographic systems for this research used alternatively the experimental SPC detector Medipix2 and a commercial energy integrating CMOS FP detector (*Hamamatsu, mod. C7942-02*). This device (photo in Fig. 2-5) is an indirect converting pixel detector provided with a scintillation layer 150 µm thick made of CsI:Tl coupled to an active photodiode array of 2240 x 2344 square pixels of 50 µm pitch (sensitive area of 120 x 120 mm^2). The whole device is covered by 1 mm thick Al alloy enclosure. The detector has about 7 lp/mm resolving power at 10 % of MTF [49]

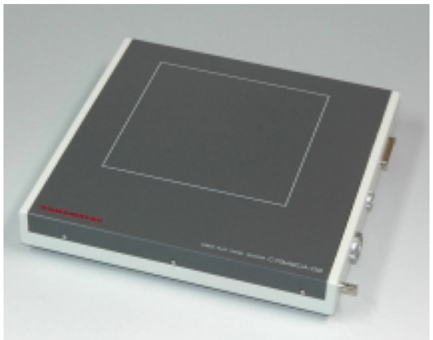

Fig. 2-5 Flat panel energy integrating indirect detector provided with a scintillation layer 150 µm thick made of CsI:Tl coupled to an active photodiode array of 2240x2344 square pixels of 50 µm pitch (sensitive area of 120 x 120 mm^2).

Two different X-ray sources have been employed in two different set-ups: an X-ray tube provided with a micro-focus of 5 µm (*Hamamatsu, mod. L8601*, max voltage 90 kVp, max current 250 µA, tungsten anode) and an X-ray tube provided with a micro-focus of 35 µm size (*Oxford Instrument, APOGEE package, series 5000*, max voltage 50 kVp, max current 1 mA, molybdenum anode). Fig. 2-7 and Fig. 2-9 show the two set-ups with the tungsten anode source and with the molybdenum anode source respectively. The first system has been developed by the Institute of Experimental and Applied Physics (IEAP) of the Czech Technical University (CTU) of Prague (Czech Republic), while the second system has been made-up in the Medical Physics Laboratory of the Physical Science Department of "Federico II" University of Napoli, Naples (Italy). The two systems are arranged in the same way: the X-ray source, the housing for the sample and the detector (either Medipix2 or the FP detector).

In the system developed at IEAP the sample and the detector can be moved along the three directions through software controlled motors. Moreover, the sample can be placed on a rotation stage so as to perform tomographic acquisitions. The tomographies have been acquired in the step-and-shoot mode: at each angular view the sample holder stops and the detector records an image. The tube voltage has been fixed at a value of 40 kVp and the mean energy of the beam for this setting has been calculated simulating the output tungsten spectrum [50] (Fig. 2-6) as $\bar{E}_{simul}$ = 15.0 keV. The source-to-detector distance ($R_1 + R_2$) has been kept fixed at 61 cm.

In the system assembled at Medical Physics Laboratory in Naples both the sample and the detector can be moved along the two x-y directions by means of manually controlled motors or via a dedicated software, to enable the system for tomographic acquisitions. The tomographies have been acquired both in the step-and-shoot mode (when the FP detector has been employed) and in the continuous mode (when Medipix2 has been employed): the sample rotates 360° while the detector (Medipix2) records images. This means that the number of angular views on 360° is recovered by dividing the time of a complete rotation of the sample for the acquisition time, t_{acq}, set for the detector. The tube voltage has been fixed at a value of 40 kVp and the mean energy of the beam for this setting has been calculated simulating the output molybdenum spectrum [50] (Fig. 2-8) as $\bar{E}_{simul} = 15.75$ keV. The source-to-detector distance has been kept fixed at 35.7 cm.

The Medipix2 detector has always been used setting only the low threshold discrimination level at a value of 5 keV.

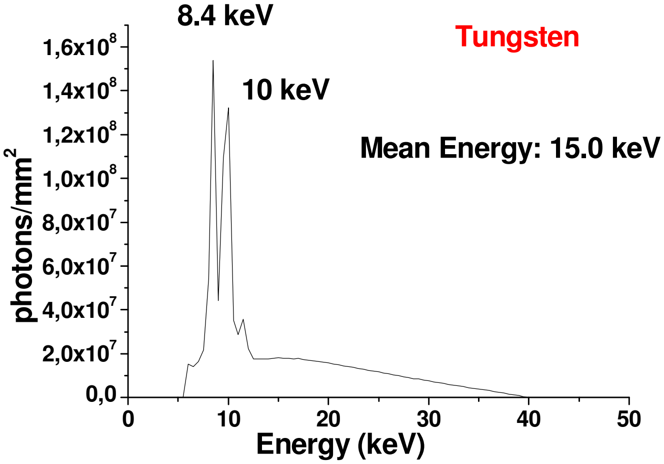

Fig. 2-6 Tungsten spectrum for a radiogen tube with a tube voltage of 40 kVp for 1 mAs exposure.

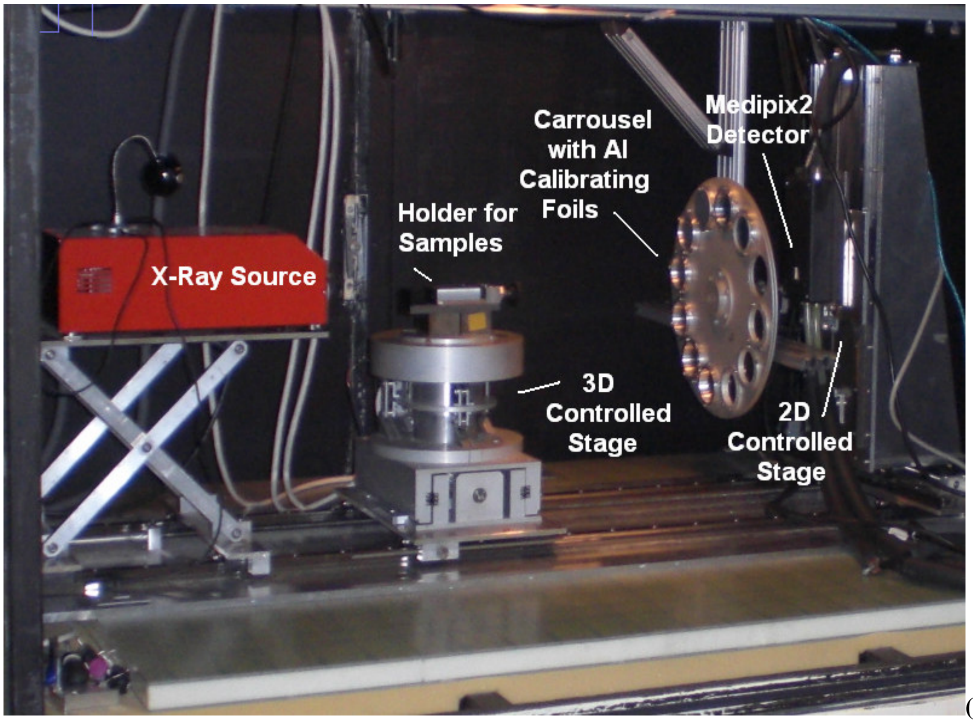

(a)

Fig. 2-7 Micro-tomographic system placed in the IEAP laboratory. The system is arranged with an X-ray tube, molybdenum anode, provided with a micro-focus spot size (5 µm), a sample-holder, a rotating wheel in which are placed aluminium foils used to perform a Signal-to-Thicknesses Calibration that equalizes the detector pixels response and the detector (Medipix2 in the photo). Sample and detector can be moved along the three directions through software controlled motors. Moreover, the sample has the possibility to rotate to perform tomographic acquisitions.

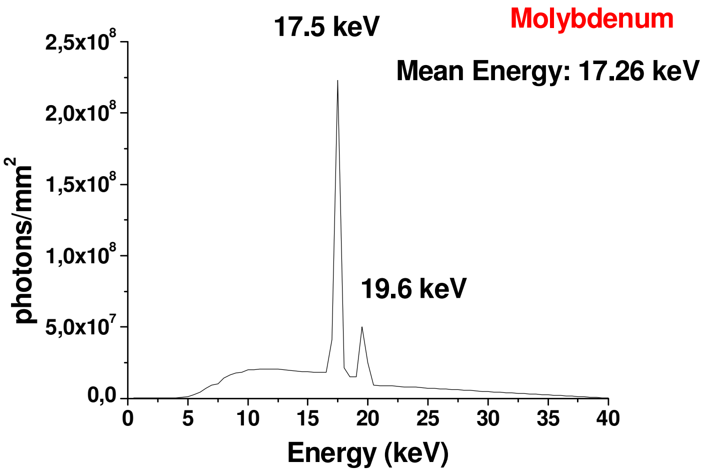

Fig. 2-8 Molybdenum spectrum for a radiogen tube with a tube voltage of 40 kVp for 1 mAs exposure.

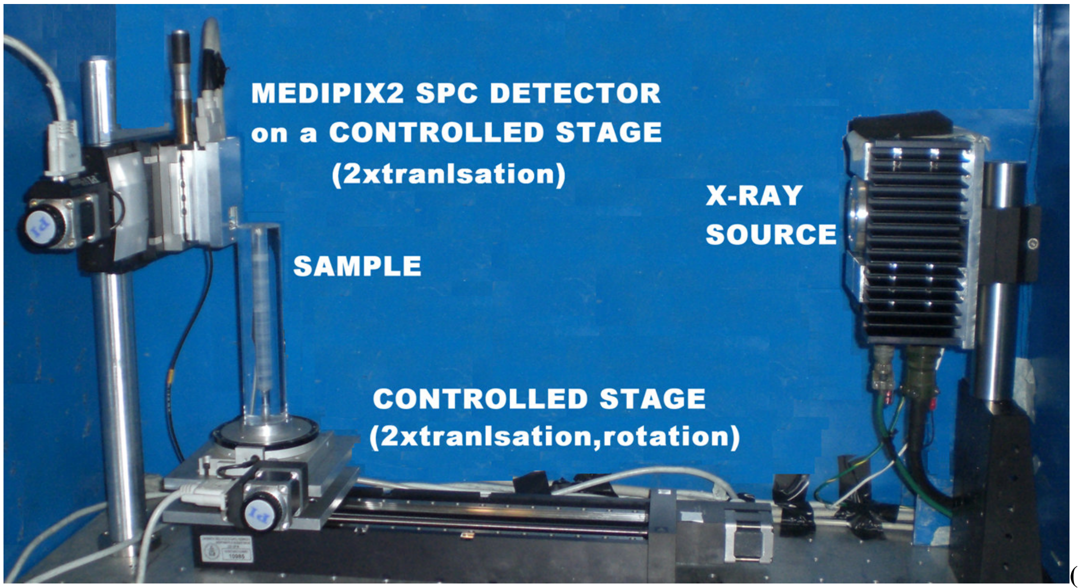

(b)

Fig. 2-9 Micro-tomographic system assembled in the Medical Physics laboratory of Physical Science Department of Napoli, composed of a radiogenic tube, tungsten anode, provided with a micro-focus (35 µm), a housing for the sample and the detector (Medipix2 in the photo). Both the sample and the detector can be moved along the two x-y directions by means of manually controlled motors or via a dedicated software, to enable the system for tomographic acquisitions.

Fig. 2-10 shows the system spatial resolution versus increasing magnification M for both Medipix2 and the FP detector when the 5 µm focal spot source is employed [51]. The resolutions have been evaluated imaging a 0.05 mm thick tilted steel edge. The edge spread function (ESF) has been fitted with the error function and the Full With at Half Maximum (FWHM) of the amplitude has been estimated. For each point, 150 acquisitions of 1 s acquisition time each have been averaged. The tube voltage was V = 40 kVp and the tube current was I = 50 µA (to keep the focal spot as small as possible).

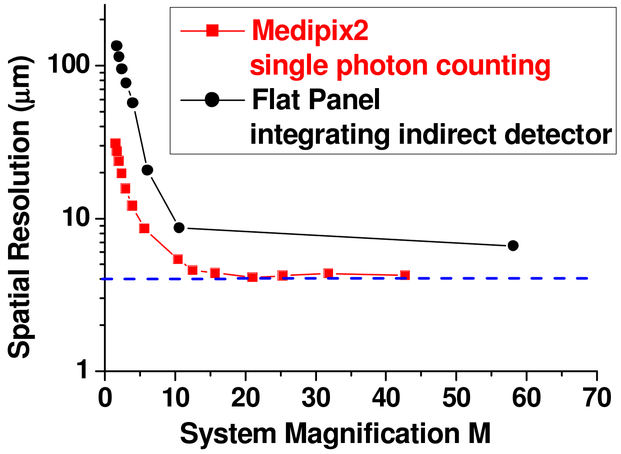

Fig. 2-10 FWHM spatial resolutions achieved with Medipix2 and the FP detector using a steel edge 0.05 mm thick at different magnifications M. V = 40 kVp; I = 50 µA. [51]

From Fig. 2-10 it is evident that the limitation to the highest achievable spatial resolution is connected with the spot size of the X-ray tube [52]; the system spatial resolution reaches the highest value when using Medipix2 (4.2 µm) rather than the FP detector (6.6 µm), although the pixels of the two detectors have almost the same size.

A measure of the exposure (in mAs unit) versus the dose in air at isocenter has been carried on for the tomographic system employing the 35 µm focal spot X-ray source; the measurements have been done both in the configuration with the Medipix2 and in the configuration with the FP detector. The geometrical source-to-detector distance has been kept the same ($R_1 + R_2 = 35.7$ cm). The plots related to the Medipix2 configuration and to the FP detector configuration are shown in Fig. 2-11a and Fig. 2-11b.

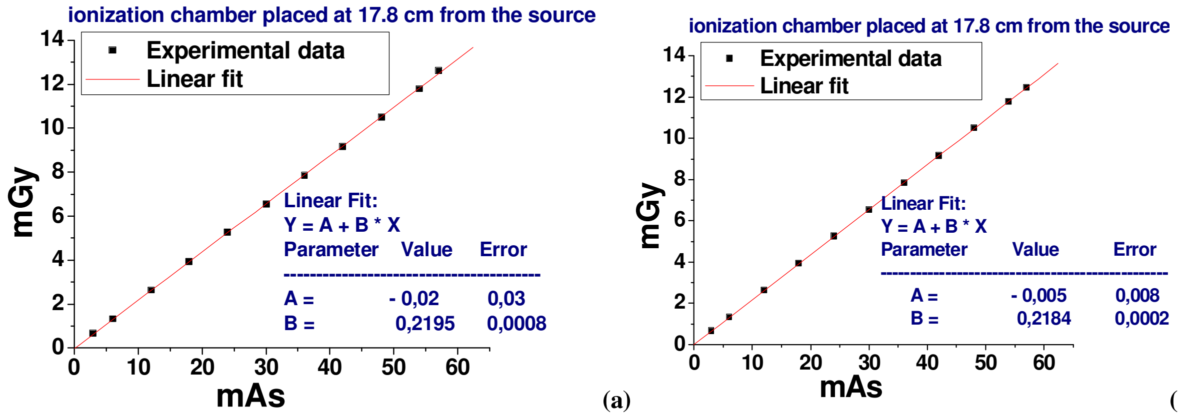

(a) (b)

Fig. 2-11 Calibration of the exposure in mAs unit into the dose in air in Gy units for the set-up utilizing the Medipix2 detector (a) and the FP detector (b) for a tube voltage of 40 kVp with the 35 µm focal spot X-ray Mo source.

The measurement of the exposure has been done by means of an ionization chamber (*Radcal Corporation, mod. 2026C, sensor 20x6-6*, volume of 6 cm^3) placed at the isocenter:

$(R_1 + R_2)/2 = R_{iscenter} = 17.8$ cm. The exposure rate per minute has been measured in Roentgen (R) unit and then converted into Gray (Gy) units.The experimental data have been fitted and the two exposure/dose-in-air-calibrations are:

Dose in air (mGy) = -0.02 + 0.2195 * Exposure (mAs) for the Medipix2 configuration;

Dose in air (mGy) = -0.005 + 0.2184 * Exposure (mAs) for the FP detector configuration.

A measure of the average counts recorded per pixel as a function of the air dose (evaluated from the exposure/dose in air calibration curve) has been done for the two detectors. The two plots are shown in Fig. 2-12a and Fig. 2-12b, respectively for Medipix2 and for the FP. The experimental data have been fitted and the parameters values of the two average counts per pixel versus dose-in-air-curves are:

Average Counts per Pixel = 7 + 345347 * Air dose (mGy) for the Medipix2 configuration;

Average Counts per Pixel = 67 + 52429 * Air dose (mGy) for the FP detector configuration.

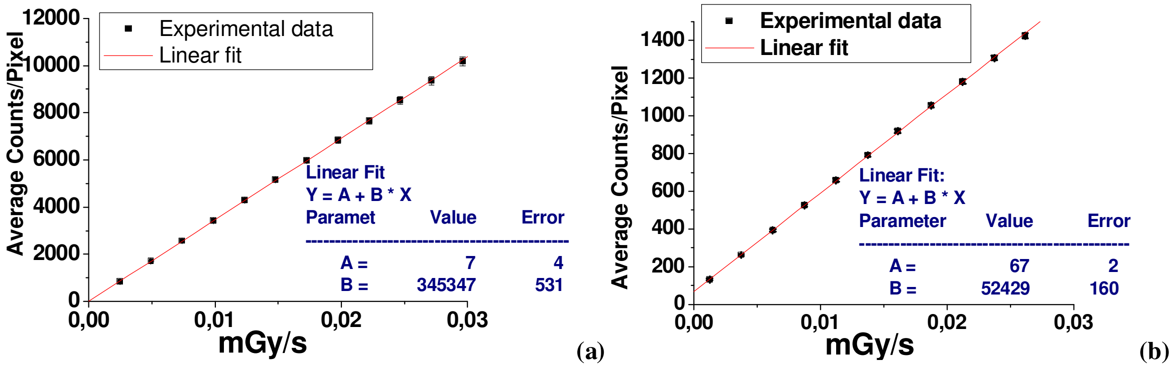

Fig. 2-12 Average counts per pixel as a function of the air dose (evaluated from the exposure/dose in air calibration for Medipix2 (a) and for the FP detector (b)

2.3 Image quality and pixel efficiency correction methods

Image quality can essentially be summarized by four main performance characteristics: first, the spatial resolution that is the ability to distinguish adjacent features, second, the contrast image resolution which measures the ability to differentiate a low-contrast feature from its background. Image noise, partly due to random fluctuations of the X-ray photon flux, partially coming from the electronics and from the environment contribution, imposes a limiting factor to this parameter. The third characteristic is the temporal resolution, determining the ability to capture structures in motion. Finally, the fourth one is the quantitative accuracy needed to relate the image pixel values to physically meaningful quantities (X-rays attenuation coefficient, CT numbers). The X-ray CT research and development aim at major improvements in image quality maximizing these four parameters. In this thesis we focus our attention on the study of the second parameter, the contrast image resolution. In fact, in medical imaging one of the main tasks for a diagnostic system is the ability to distinguish anomalies, variations and small suspected masses present in an organism from the background. In X-ray CT the main problem linked to this task is that these structures have an attenuation coefficient similar to the background. Moreover, soft tissues are little absorbing, so that they are, of themselves, difficult to be visualized.

To quantifying the contrast resolution in this thesis we have been using the following parameters:

- Signal-to-Noise Ratio

$$SNR = \frac{\mu_{obj}}{\sigma_{BG}}$$

- Contrast

$$C = \frac{|\mu_{obj} - \mu_{BG}|}{\mu_{BG}}$$

- Contrast-to-Noise Ratio

$$CNR = \frac{|\mu_{obj} - \mu_{BG}|}{\sqrt{(\sigma^2{}_{obj} + \sigma^2{}_{BG})}}$$

where

μ_{obj} and μ_{BG} are the mean signal values in a region of interest (ROI), chosen, respectively, in the imaged object and in the background;

σ_{obj} and σ_{BG} are the standard deviation of the mean pixel values μ_{obj} and μ_{BG}.

The SNR parameter compares the signal to the noise level in a ROI and it is generally higher than the value expected from the Poisson statistics of $\sqrt{N}$, where N is the mean number of detected photons. In fact, several other sources of noise additionally contribute to the inherent fluctuations of the photon beam, such as dark current in the detector, secondary quantum noise in indirect detection systems, noise generated in the read-out electronics and fixed pattern noise due to beam or detector non-homogeneities or variations in detector response. For this reason the SNR does not include information about the statistical correlation of the fluctuations. The SNR parameter depends on the size of the chosen ROI and on the number of absorbed X-rays: the higher the latter is, the better the SNR is, but, evidently, the dose increases as well. Commonly for a signal to be detectable, the SNR values must be at least higher than 5 [53]. Besides the absorption efficiency of the detector, the SNR depends on the operation mode of the system, if counting or integrating. In fact, it was shown that the ideal detector which yields the maximum SNR disregards any energy information and simply takes into account the number of photons [54]. This means that energy integrating systems can only reach maximum SNR with a mono-energetic photon beam.

The C parameter, on the opposite, is independent from the ROI size and also of the dose (incoming number of photons) but gives an evaluation of the visibility and of the detectability of the signal in a ROI compared to the background signal or, analogously, it estimates the detector ability in distinguishing between two similarly attenuating materials.

Also the CNR parameter is related to the visibility of a ROI compared to the background signal relatively to the noise. In fact, the noise is the major limiting factor in object detectability and a low noise level is therefore a prerequisite for a good image quality at reasonable doses, particularly when viewing small, low-contrast objects. The CNR value depends on the ROI size: the minimum threshold contrast, indicating the level from which the system is able to visualize, is inversely proportional to the square root of the object area and also of the number of incoming photons [55].

An evaluation of these parameters allows, at least to some extent, to asses the quality of a medical image for radiographic/tomographic studies. In Chap. 3 SNR, C and CNR were used both to evaluate an SPC detector's performances in the medical imaging field and to compare the SPC image quality to that of a commercially available charge integrating FP detector.

The low contrast resolution limit of a radiographic system is often determined using objects having a very small difference from the background. In this case, because the signal (the difference between object and background intensities) is very small, the noise is a significant factor to be evaluated.

Image noise in tomographic slices, in its most simple definition, is measured as the standard deviation of voxel values in a homogenous (typically water) phantom and it is influenced by a large number of parameters, including:

- X-ray tube voltage
- X-ray tube current
- exposure time
- focal spot to isocenter distance
- detector efficiency
- X-ray beam collimation
- reconstructed slice thickness
- reconstruction algorithm or filter

For this reason in the comparison study between the two detectors technologies 2-D and 3-D images have been obtained using the same experimental conditions both in the measurement and in the elaboration of the acquired data.

Related to the image quality, a further aspect has to be considered. In fact, if on the one hand pixel detectors show advantages over non-pixellated devices, on the other hand they have an important drawback: the single pixel response varies from one element to the other. In fact, although identical in design, non-homogeneities in the sensor material or in the integrated analog circuits (e.g. different gains or offsets of the pre-amplifiers), give raise to significant discrepancies and need to be taken into account because under uniform irradiation condition their response is not uniform. This non-uniformity lowers the contrast resolution in the radiographic images and leads to more serious artefacts in the tomographic slices.

To recover an efficiency map for the detector pixels the commonly performed procedure is the so-called "flat field correction (FFC)". A flood irradiation of the detector (without any object between the source and the detector) is recorded in the same experimental condition (geometry, tube voltage, tube flux, beam filtration, detector energy threshold) as for the subsequent image of the object that will need the correction. If <f> is the mean pixel value of this flat image matrix and f_{ij} is the value recorded in the ij_{th} pixel, then the correction coefficient for that pixel will be $c_{if} = \langle f \rangle / f_{ij}$. It is clear that this kind of correction does not take into account the theoretical exponential trend typical of the X-ray absorption, $exp(-\mu x)$ and, moreover, it does not take into account that the theoretically calculated spectrum out-coming from an attenuating object is not the same as the incident one because of the beam hardening effect. Because the detection efficiency is different from one pixel to another and it depends in a unique way on the photon energy and on the local attenuating properties of the traversed object, it is evident that the flat field correction is just an approximate way to equalize the detector response.

An alternative correction procedure consists in a per-pixel response calibration to differently attenuated X-ray spectra [6]. A set of homogenous filters of a given material but of different thicknesses is used to acquire a number of flat images in the same experimental conditions as the subsequent sample imaging. At changing thickness of the filter the spectrum changes and a given pixel records a different value. The experimental data set - filter thicknesses *versus* per-pixel recorded counts - can be locally fitted between two points with an exponential function of the form (Fig. 2-13):

$$Y = A_k \cdot \exp(a_k X) + O_k$$

where k represents the number of experimental points and the parameters A_k, a_k and O_k are evaluated for each pixel assuming that part of the photons is totally absorbed, part traverses undisturbed the sample (harder component) - O_k - and part is attenuated with the exponential trend $A \cdot \exp(aX)$. In this way one gets a calibration of the pixel response, that, for a given recorded number of counts in a pixel, returns an "equivalent thickness", that is the thickness of the calibration filter used that would have attenuated as the sample has. In the resulting radiography the map of the "equivalent thicknesses" substitutes the intensity pixel value. The filter thicknesses used for the calibration must lie in a range starting from zero (open beam), up to the filter thickness that gives an attenuation slightly higher than the maximum attenuation coming from the sample.

This Signal-to-Thickness Calibration (STC) overcomes both the pixel efficiency problem and the beam hardening effect.

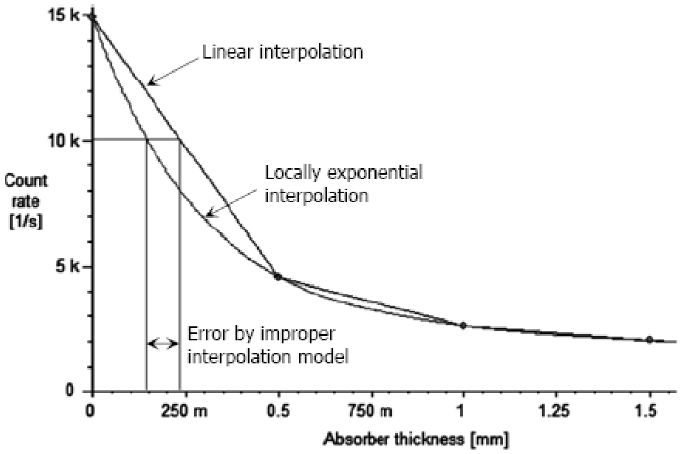

Fig. 2-13 Calibration function of a single pixel, evaluated by local interpolation of the exponential function $Y = A_k \cdot \exp(a_k X) + O_k$; in the graph it is also shown how a linear interpolation would lead to significant errors in the calibration. [6]

In Fig. 2-14 are shown two images of the same sample, a rose leaf, the raw datum (a) and the corresponding STC corrected image, in which the channels network structure is clearly visible. The image has been acquired with the Medipix2 SPC detector and with the 5 µm spot-size tungsten X-ray source with a tube voltage of 40 kVp and a tube current of 50 µA. The acquisition time was $T_{acq} = 100$ s. The STC calibration has been performed with a set of aluminium filters, starting from a minimum thickness of 50 µm (the leaf equivalent thickness results of 195 µm).

Fig. 2-15 shows images of a lentil corrected with the two equalization procedures, the FFC (a) and the STC (b). The raw image has been acquired with the Medipix2 SPC detector and with the 5 µm spot-size tungsten X-ray source with a tube voltage of 50 kVp and a tube current of 110 µA. The acquisition time was $T_{acq} = 100$ s and the magnification factor was $M = 3.7$x. The lentil has an equivalent aluminium thickness of 0.3 mm.

Because the STC corrected images shows the "equivalent thickness" as pixel values, each set of planar projections acquired for the tomographies presented in Chap. 3 have been elaborated in a different way compared to the images corrected by means of the FFC when the reconstruction algorithm used to get the 3-D slices was the FBP one. First of all, the projections have been multiplied by the factor $(-\mu_{<E>})$, where $\mu_{<E>}$ is the attenuation coefficient of the calibration filter material used, calculated [48] for the mean energy <E> of the beam. Then, the operation *(exp)* of the whole matrix pixels has been performed. In this way, the new matrix has in each pixel a value $exp\ (-\mu_{<E>}x)$, corresponding to the theoretical attenuation of an X-ray beam with mean energy <E> when passing through an homogeneous object made of the same material as the one used for the STC, with a thickness x. The beam geometry chosen for the 3-D reconstruction was the parallel-beam geometry, because, after the described elaboration, the reconstruction software has the exact information on the traversed thickness and inserting a cone-beam parameter (as for the flat field corrected images) corresponds to fake the geometry. On the contrary, in the cases when the iterative OSEM algorithm has been used, the projections have not been elaborated after the STC.

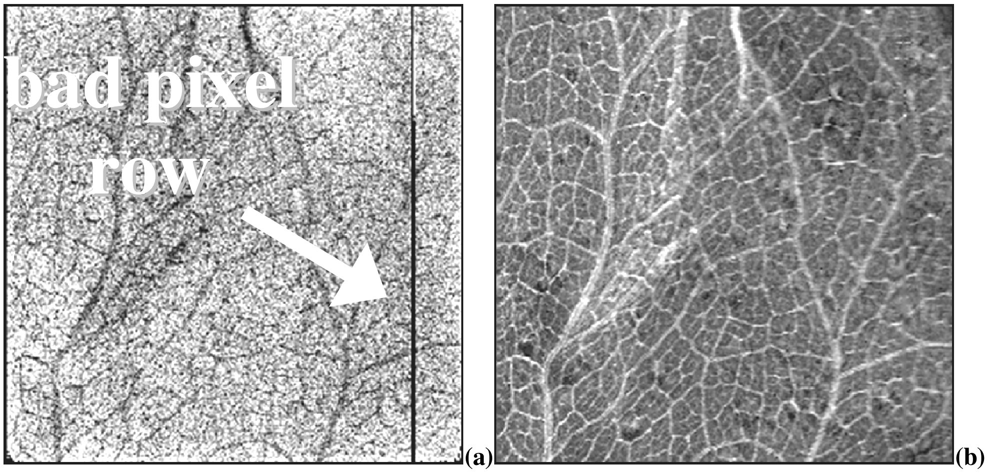

Fig. 2-14 Raw image of a rose leaf in which the vein structure is hardly distinguishable and also a bad pixel row is visible (a); STC corrected image of the leaf: the structure is clearly observable. The image has been acquired with the Medipix2 SPC detector and with a 5 µm spot-size tungsten X-ray source with a tube voltage of 40 kVp and a tube current of 50 µA for a T_{acq} = 100 s (W anode). The STC calibration has been performed with a set of aluminium filters, the thinnest one of 50 µm (the leaf mean thickness was of 195 µm).

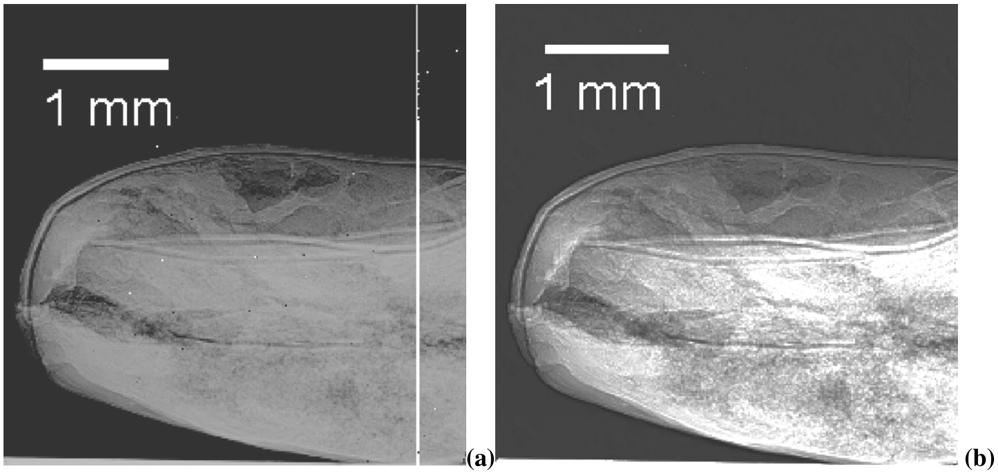

Fig. 2-15 FFC corrected image of a lentil (a bad pixel row is visible) (a); STC corrected image of the same lentil: the internal structure is more clearly observable than for the FFC image. The image has been acquired with the Medipix2 SPC detector and with a 5 µm spot-size tungsten X-ray source with a tube voltage of 50 kVp and a tube current of 110 µA for a T_{acq} = 100 s (W anode). The STC calibration has been performed with a set of aluminium filters, the thinnest one of 50 µm (the leaf mean thickness was of 300 µm).

2.4 References

[37] Medipix collaboration at *www.cern.ch/medipix*;

[38] X. Llopart, M. Campbell, R. Dinapoli, D. San Segundo, and E. Pernigotti, "Medipix2: a 64-k pixel read-out chip with 55 micron square elements working in single photon counting mode," *IEEE Trans. Nucl. Sci.*, vol. 49, no. 5, pp. 2279-2283 (Oct. 2002);

[39] P. Russo, "Hybrid semiconductor pixel detectors for low- and medium energy X- and gamma-ray single photon imaging using the Medipix read-out chip", Encyclopedia of Imaging Science and Technology, J. P. Homak, Ed. New York: Wiley Interscience (2002);

[40] X. Llopart, "Design and characterization of 64x pixels chips working in single photon processing mode", Mid Sweden University Doctoral Thesis 27, (May 2007);

[41] D. San Segundo Bello, *et al.*, "An interface board for the control and data acquisition of the Medipix2 chip", NIM A, vol. 509, 164-170 (2003);

[42] http://www.nikhef.nl/en

[43] http://www.utef.cvut.cz

[44] X. Llopart, *et al.*, "Medipix2, a 64k pixel read-out chip with 55 μm square elements working in single photon counting mode", IEEE Transaction on Nuclear Science, vol. 49, pp. 2279-83 (2002);

[45] J. Dammer, *et al.*, "Real-time X-ray μ-imaging of living organism", Amer. Inst. of Phys., V 958, 136-138 (2007);

[46] J. Dammer, *et al.*, "Real-time in vivo μ-imaging with Medipix2", NIM A, vol. 607, issue 1, pp. 205-207 (2009);

[47] G. Mettivier, *et al.*, "First images of a digital autoradiography system based on a Medipix2 hybrid silicon pixel detector", Phys. Med. Biol., vol. 48, pp. 173-181 (2003);

[48] NIST Physical Reference Data; http://physics.nist.gov/PhysRefData;

[49] S. C. Lee, *et al.*, "A flat-panel detector based micro-CT system: performance evaluation for small-animal imaging", Phys. Med. Biol., vol. 48, pp. 4173-4185 (2003);

[50] J. M. Boone, *et al.*, "Molybdenum, rhodium and tungsten anode spectral models using interpolating polynomials with application to mammography", Med. Phys., vol. 24, pp. 1863-74 (1997);

[51] P. M. Frallicciardi, *et al.*, "Comparison of single photon counting and charge integrating detectors for X-ray high resolution imaging of small biological objects", NIM A, Vol. 607, Issue 1, p. 221-222 (2009);

[52] N. Belcari, *et al.*, "Preliminary characterization of a single photon counting detection system for CT application", NIM A, vol. 576, p. 204-8 (2007);

[53] S. Webb, “The physics of Medical Imaging”, Institute of Physics Publishing (1998);

[54] M. Sandborg, G. A. Carlsson, “Influence of X-ray energy spectrum, contrasting detail and detector on the Signal-to-Noise Ratio (SNR) and Defective Quantum Efficiency (DQE) in projection radiography”, Phys. Med. Biol., vol. 37 (6), pp. 1245-63 (1992);

[55] A. Workman, D. S. Brettle, “Physical performance measures of radiographic imaging systems”, Dentomaxillofacial Radiology, vol. 26, pp. 139-46 (1997).

Chapter 3. Experiments

In this chapter we present some experimental results demonstrating the capability of the SPC detector Medipx2 for high contrast planar, real-time and tomographic micro-imaging on biological samples. We will show also a comparison, in terms of image quality, with a more commonly used FP charge integrating detector. The highest performance of the SPC technology compared to a charge integrating one in terms of image quality in the field of medical physics for high contrast micro-imaging on biological samples is here demonstrated.

For these purposes we carried on a series of tests and measurements both by means of the Medipix2 detector and using either detector in the same experimental conditions. Moreover, we compared the two flat field techniques (described in Chap. 2) for the detector pixel equalization: the standard Flat Field Correction (FFC) and the novel Signal-to-Thickness Calibration (STC).

The chapter is divided into 5 paragraphs:

3.1 2-D μ-imaging with Medipix2 SPC detector[4]
3.2 real-time μ-imaging with Medipix2 SPC detector on living biological samples[10]
3.3 3-D μ-imaging on living samples with Medipix2 SPC detector[10]
3.4 2-D image quality comparison between Medipix2 SPC and the FP detector by means of two pixels equalization techniques
3.5 3-D image quality comparison between Medipix2 SPC and the FP detector by means of two pixels equalization techniques.

For each of these topics we also present an example from the literature.

3.1 2-D μ-imaging with Medipix2 SPC detector:

The planar imaging performed with the Medipix2 and with the μ-focus X-ray source takes advantage from the phase shift effect (see Appendix A) as the phase-contrast visibility conditions are verified from the used set-up. In fact, the use of the Propagation Based Imaging (PBI) technique by means of a common X-ray tube is less common but still possible under the conditions examined in Appendix A, in particular:

- the X-ray source is partially coherent;
- the object-to-detector distance is suitable to let the refracted rays to diverge from the undeviated ones but not too large to avoid the source blurring;
- the micrometric detector spatial resolution is high enough to detect separately refracted and transmitted rays;

---

[4] All the presented images have been corrected using the STC calibration procedure described in Chap. 2 when it is not expressly differently declared.

– the chosen biological and organic samples show high spatial frequencies of details to be visualized.

Here we present some results obtained with the PBI technique with the X-ray μ-focus tube provided with a focal spot of 5μm (tungsten anode) and with the experimental detector Medipix2, based on the SPC technology.

Typical phase contrast examples are shown in Fig. 3-2a and Fig. 3-3a. The images are phase contrast radiographies (100 s acquisition time) of two insects acquired with Medipix2 SPC detector placed at a distance of 61 cm from the source (tube current I = 200 μA, tube voltage V = 40 kV, mean energy $\bar{E}$ = 15.0 keV), for a magnification factor M, respectively, of 9.1x and 4.7x. From the details pointed out (Fig. 3-2b and Fig. 3-3b) it is clearly visible how the bright and the dark fringes alternate; this phenomenon corresponds to an under-shoot followed by an over-shoot, as it is clear in the linear profile taken in that regions (Fig. 3-2c and Fig. 3-3c). The two samples shown in Fig. 3-2a and Fig. 3-3b present an attenuation to X-rays around the 15% at 15 keV mean energy, which means that in a pure attenuation regime it would be a hard task to visualize details as the anatomic tracheal tubes - forming a complex network of vessels in the whole body - in the ant's arm or the complete and clear structure of the beetle's feeler. The absorbed dose has been calculated from the simulated W spectrum [50] and knowing the equivalent thicknesses of the samples (from the STC calibration) as about 0.3 μGy. In Fig. 3-1 the photos of the two samples are shown: the ant (a) and the beetle (b).

Fig. 3-1 Photos of the biological samples imaged with Medipix2 SPC detector and X-ray source W anode, 5 μm spot size.

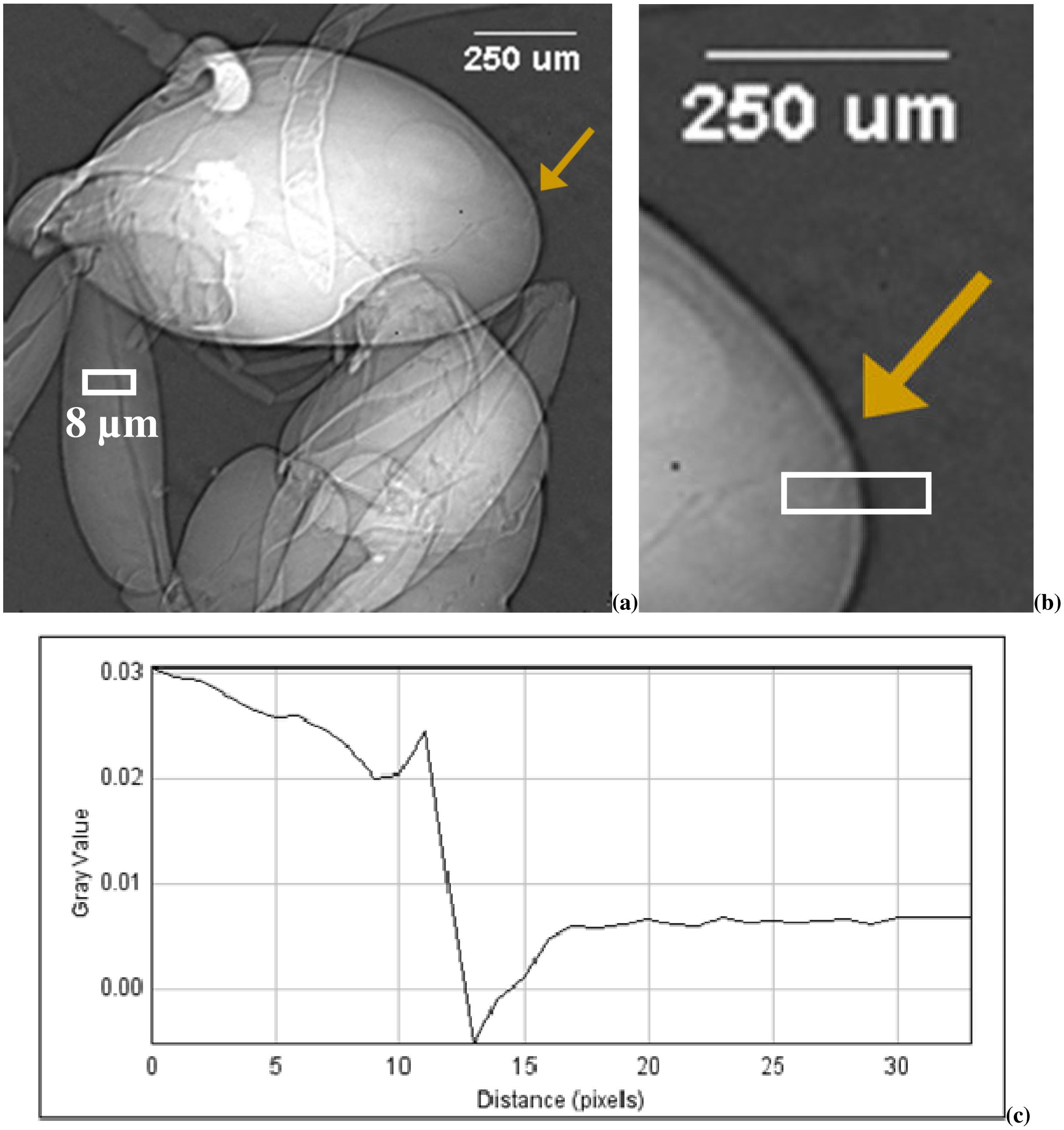

Fig. 3-2 Phase contrast radiography of an ant (a), of a head detail (b) in which the bright and dark fringes enhancing the contour are clearly visible; (c) horizontal profile taken along the region pointed out in (b). The x-axis is in equivalent Al thicknesses (mm), obtained from the Signal-to-Thickness Calibration (STC). The distance between the source and the sample is R_1 = 6.65 cm, the distance between the sample and the detector is R_2 = 54.35 cm, the magnification is M = 9.1x. I = 200 µA; V = 40 kV; focal-spot of 5 µm size, W anode; acquisition time T_{acq} = 100 s. The channel visible in (a) has been evaluated 8 µm in diameter. The calculated absorbed dose, obtained simulating the W spectrum [50], is of about 0.3 µGy.

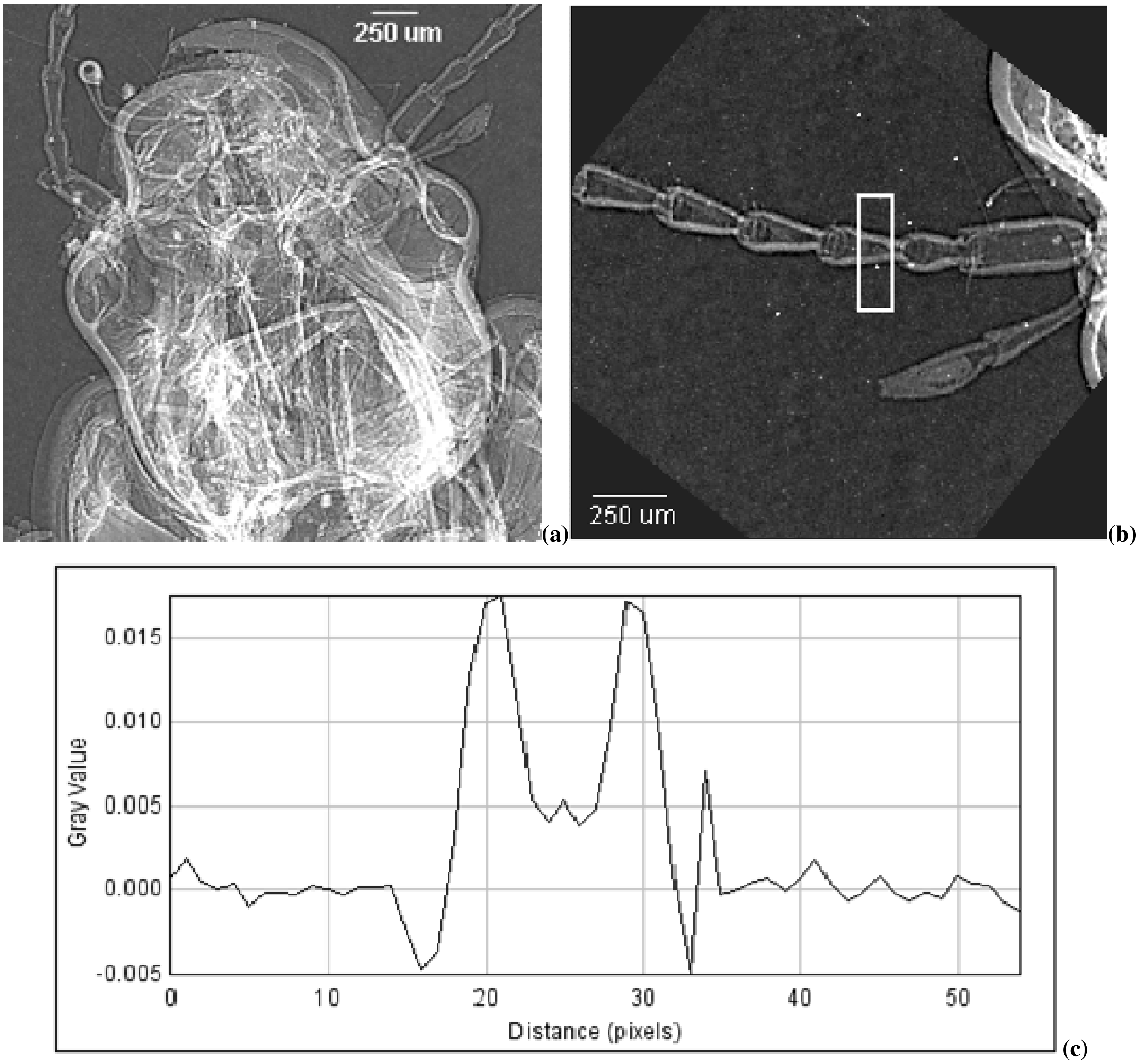

Fig. 3-3 Phase contrast radiography of an insect (a), of a feeler (b) in which the bright and dark fringes enhancing the contour are clearly visible; (c) horizontal profile taken along the region pointed out in (b). The x-axis is in equivalent Al thicknesses (mm), obtained from the Signal-to-Thickness Calibration (STC). The distance between the source and the sample is R_1 = 13.15 cm, the distance between the sample and the detector is R_2 = 48.85 cm, the magnification is M = 4.7x. I = 200 µA; V = 40 kV focal-spot of 5 µm size, W anode; acquisition time t_{acq} = 100 s. The FWHM evaluated for the left and right peaks are of $FWHM_{LEFT}$ = 20. 4 µm and $FWHM_{RIGHT}$ = 36 µm. The calculated absorbed dose, obtained simulating the W spectrum [50], is of about 0.3 µGy.

The experimental results can be compared to that of a theoretical calculation that takes into account the coherence criterion needed so that the phase shift phenomenon may be revealed (Appendix A): if one wants to reveal the bright and dark fringes, typical manifestation of the interference, the value of the following ratio [80]:

$$\frac{\mathrm{L_{shear}}}{\mathrm{L_{coh}}} = \frac{R_2 \cdot s \cdot |u|}{M \cdot R_1} = \frac{(M-1) \cdot s \cdot |u|}{M}$$

should be either much lower than 1 - to be the field completely coherent along all the sharing length - or less than 1 - for the partial coherence of the field. This criterion is always verified when applied to an X-ray source provided with a focal spot of size $s = 5 \cdot 10^{-3}$ mm to visualize 10 µm linear size details (corresponding to a spatial frequency $|u| = 50$ lp/mm) for every magnification value. Of course, for details characterized from a higher spatial frequency, e.g. $|u| = 250$ lp/mm (2 µm), a restriction on the M value appears and, for the same s only values $M < 5$ result suitable.

The phase shift effect can be quantitatively evaluated directly by measuring the upward and the downward over-shoot at different magnifications as the distance in equivalent thickness (e. t.) units (result of the STC correction procedure) between the two peaks. In Fig. 3-4 we present radiographies of the same ant's feeler detail acquired with Medipix2 in the same conditions ($I = 200\ \mu A$, $V = 40$ kV, $t_{acq} = 100$ s), but at different magnifications and R_2 distances ($M_{01} = 3.17x$, $R_{2\_01} = 41.75$ cm; $M_{02} = 5.41x$, $R_{2\_02} = 49.75$ cm; $M_{03} = 8.9x$, $R_{2\_03} = 54.15$ cm).

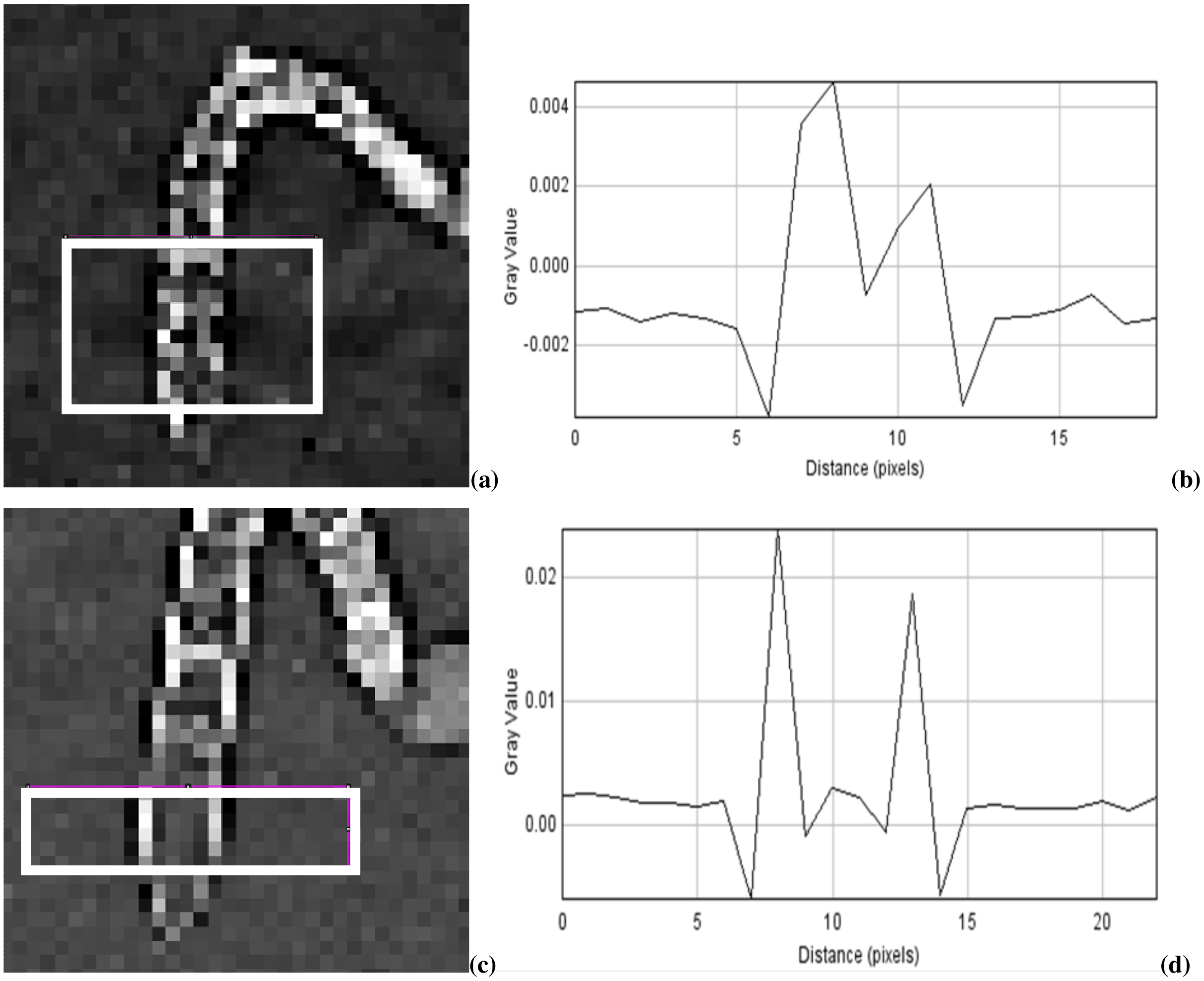

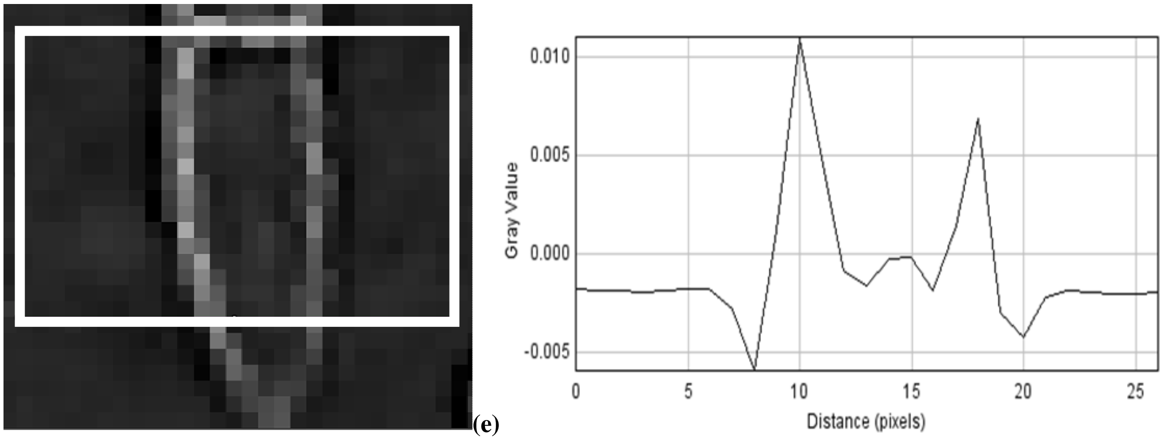

(e) (f)

Fig. 3-4 Phase contrast radiographies of an ant feeler detail for a magnification M_{01} = 3.17x and a detector-to-object distance $R_{2\text{-}01}$ = 41.75 (a); M_{02} = 5.41x, $R_{2\text{-}02}$ = 49.75 (c); M_{03} = 8.9x e $R_{2\text{-}03}$ = 54.15 (e). In correspondence plot profiles of the pointed out area are shown (Fig. b, d, f). The peak-to-peak distance values are listed in Tab. 3-1. The y-axis is in equivalent Al thicknesses - e. t. (mm), obtained from the STC.

The upward and the downward over-shoot values are listed in Tab. 3-1. In the table one can find the predicted trend of the simulations shown in Fig. A.3 of the Appendix [81]: an initial increase of the phase-contrast phenomenon with the magnification up to a certain M value, exceeded which the jump in intensity decreases again.

Image	Left Peak-to-Peak Distance (e. t.)	Right Peak-to-Peak Distance (e. t.)	Magnification M	R_2 (cm)
Fig. 3.4 (a)	8.46	5.58	3.17	41.75
Fig. 3.4 (c)	29.48	24.18	5.41	49.75
Fig. 3.4 (d)	16.92	11.15	8.9	54.15

Tab. 3-1 Values of the peak-to-peak distance between the upward and the downward over-shoot for three different magnifications M (source-Medipix2 distance = 61 cm), evaluated in correspondence of the plot profile of Fig. 3-4b, Fig. 3-4d and Fig. 3-4f.

With the SPC detector we imaged low absorbing samples selected among biological and organic object (living insects, small animals, leaves, seeds, shells, fossil, etc.) using the radiographic system of Fig. 2-7 (Chap. 2) (source-to-detector distance 61 cm). The tube voltage was set to 40 kVp (mean energy $\bar{E}$ = 15.0 keV, tungsten anode).

Fig. 3-5 and Fig. 3-6 show two radiographies of the same dead ant presented above, acquired with 20 mAs and a magnification factor of 5.5x and 9.3x respectively. The first image shows the front side of the ant body: the two feelers and their structure are clearly discernible. In the second image it is better observable the channels of the respiration system (tracheae) that form a complex network of gas-filled vessels throughout the body segments and legs.

Radiographies of Fig. 3-7a and Fig. 3-7b show the already presented beetle imaged with 2 mAs and 4 mAs at a magnification of 2.6x and 4.6x respectively. The first image shows the entire superior part of the insect's body, while in the second image two legs are visible, with also the attached hair. In particular, Fig. 3-7c shows a zoomed detail of Fig. 3-7b.

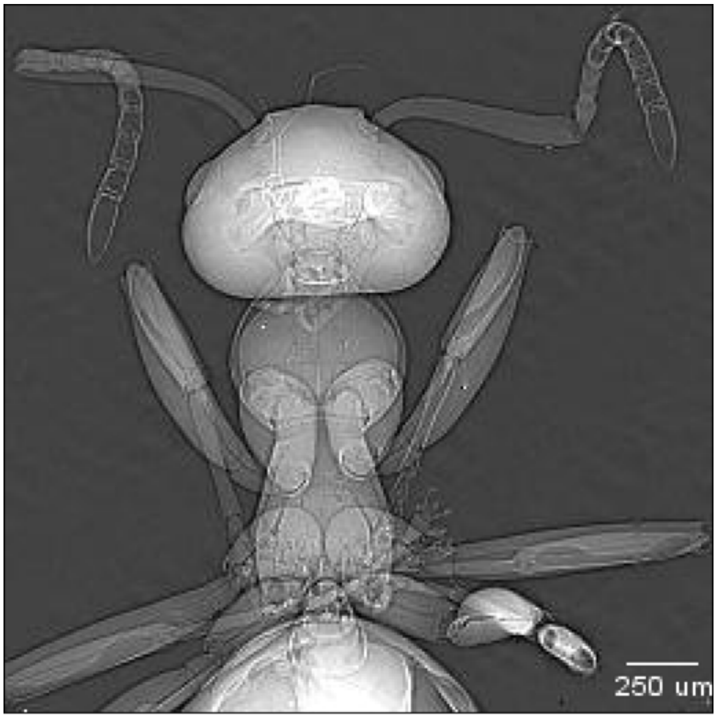

Fig. 3-5 Radiography of an ant (front side) acquired with an exposure of 20 mAs, a tube voltage of 40 kVp and a magnification factor of 5.5x. The two feelers structure is clearly distinguishable.

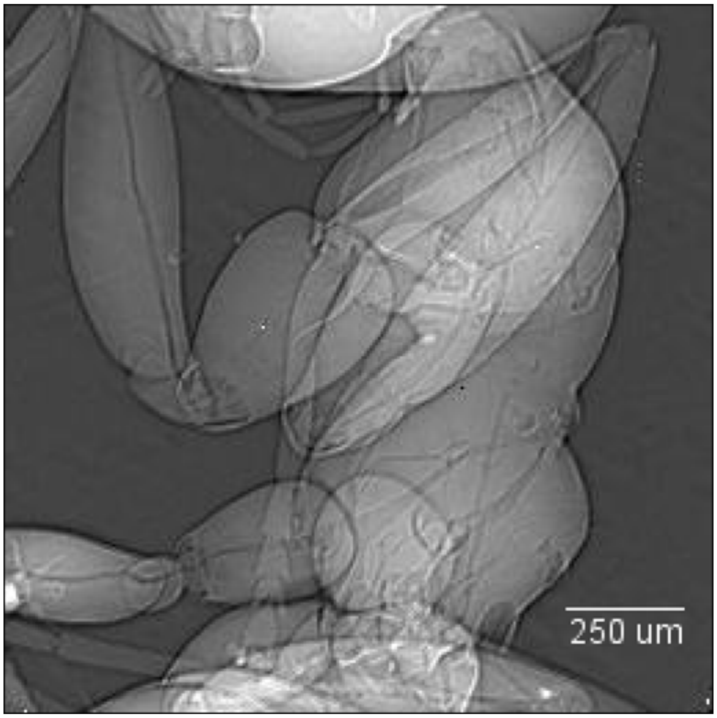

Fig. 3-6 Lateral radiography of an ant: exposure of 20 mAs, tube voltage at 40 kVp and magnification factor of 9.3x. The complex network of gas-filled vessels is clearly visible throughout the whole body.

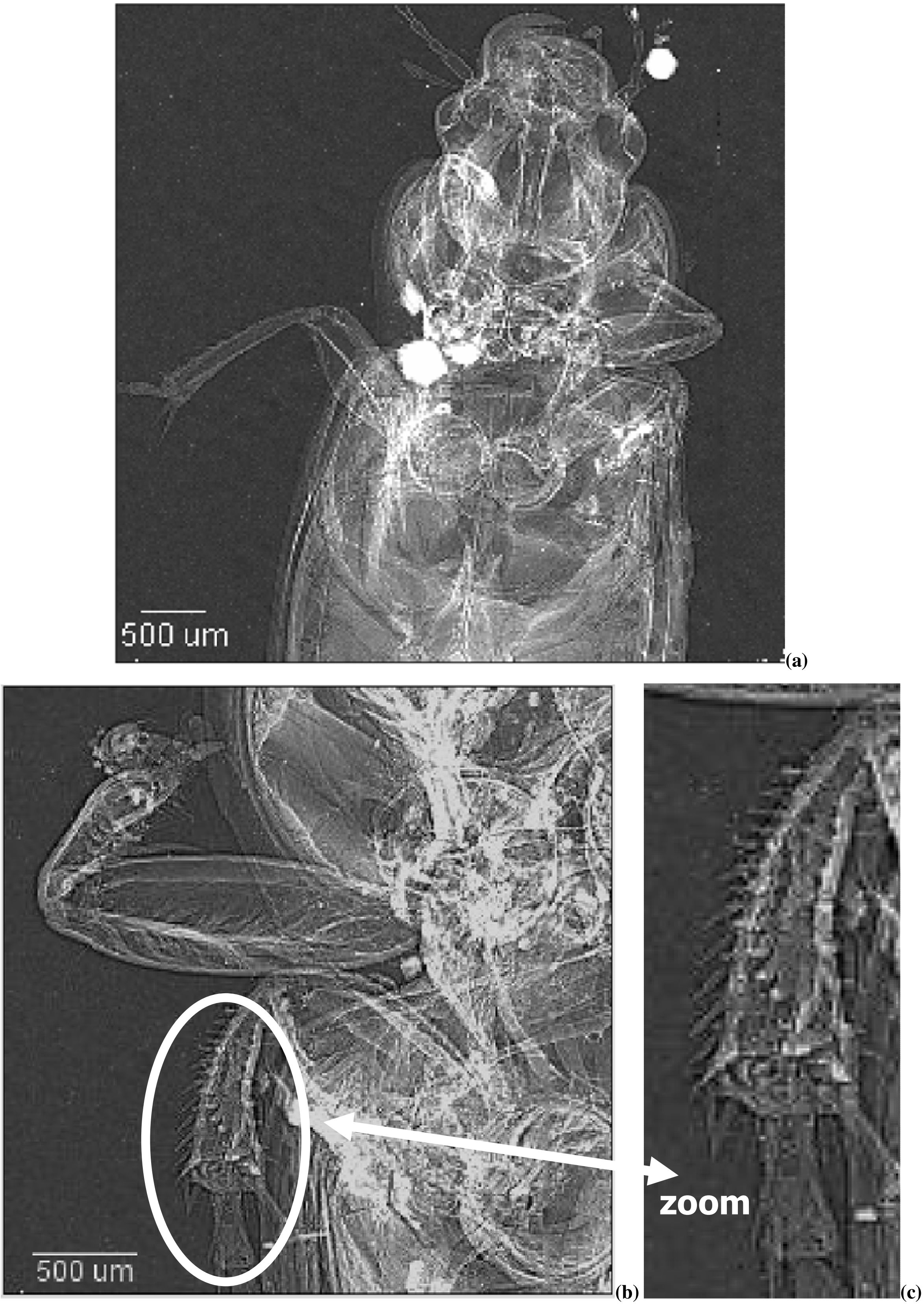

Fig. 3-7 Radiography of a beetle acquired with an exposure of 2 mAs, a tube voltage of 40 kVp and a magnification factor of 2.6x (R_1 = 23.45 cm, R_2 = 37.55 cm) (a); side part of the beetle's body, showing two legs, thanks to the 4.6x magnification factor (R_1 = 13.45 cm, R_2 = 47.85 cm); the exposure is 4 mAs (b); zoomed detail of the beetle's leg in which hair is clearly visible.

In Fig. 3-8a and Fig. 3-8b the sample is a living fly placed on a leaf, on which it is distinguishable one leaf channel (as labelled in the figure). The magnification factors are, respectively, 9.1x and 7.4x, while the exposure is of 27.5 mAs for the firs image and 11 mAs for the second one.

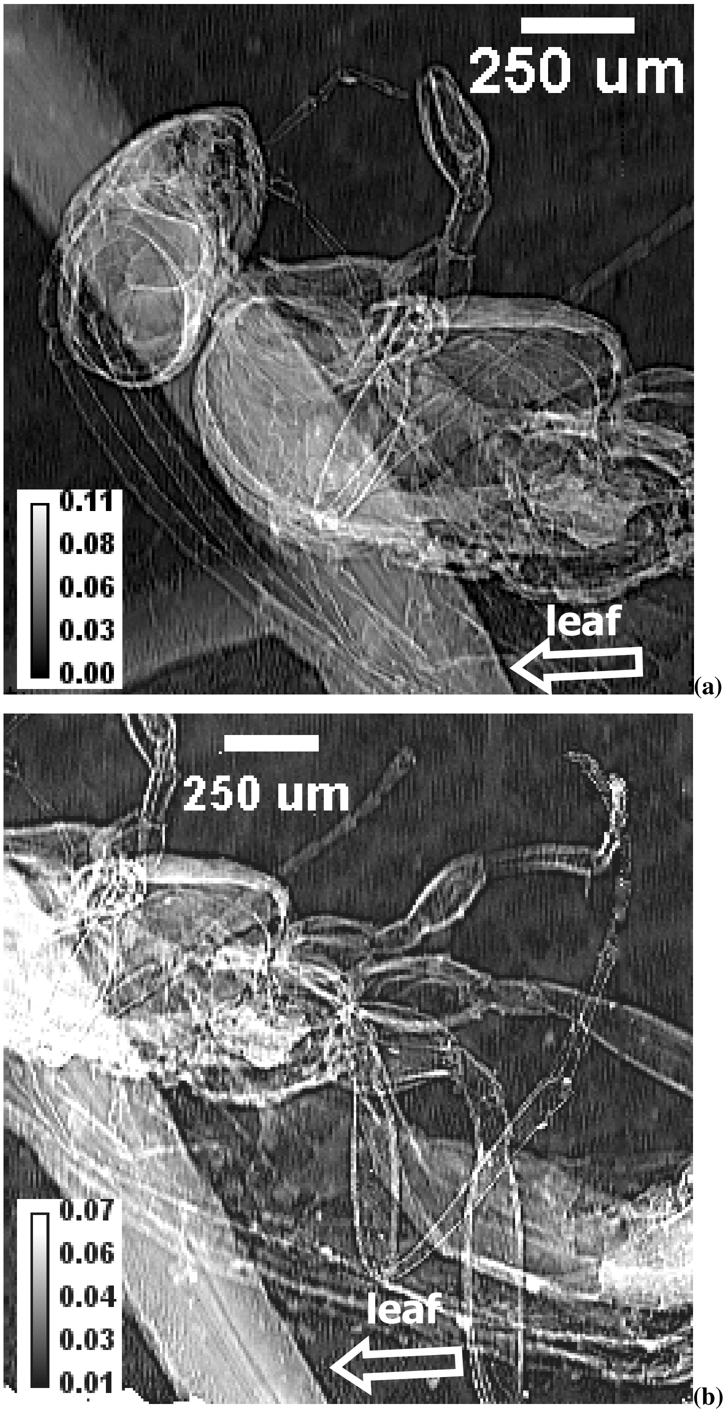

Fig. 3-8 Radiography of a living fly laying on a leaf (outlined with an arrow), acquired with an exposure of 27.5 mAs, a tube voltage of 40 kVp and a magnification factor of 9.1x (a); low part of the fly body, showing the legs, acquired with 11 mAs at M = 7.4 (b). In both radiographies the phase contrast enhancement is fundamental for the body structure visualization.

A different type of fly is the target of Fig. 3-9: in (a) the magnification factor of 12x allows to visualize the whole sample, while in (b) it is magnified (M = 33x) the back part of the body covered with hair, as indicated by the arrow. In (c) the 38x magnification factor allows the visualization of part of the body's coat and of the wing hair. In (d), one filament from the body coat is zoomed and a line profile of its section has been shown in (e): the diameter size has been evaluated as 5 μm. The sample was imaged alive.

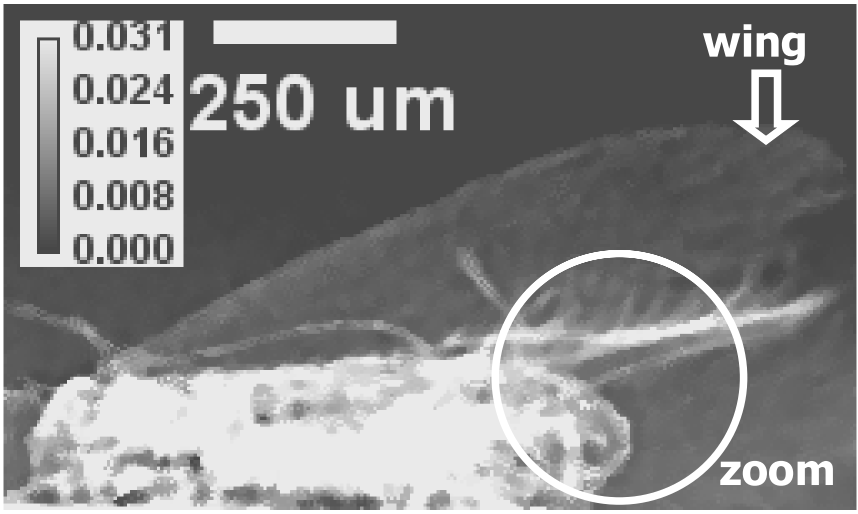

(a)

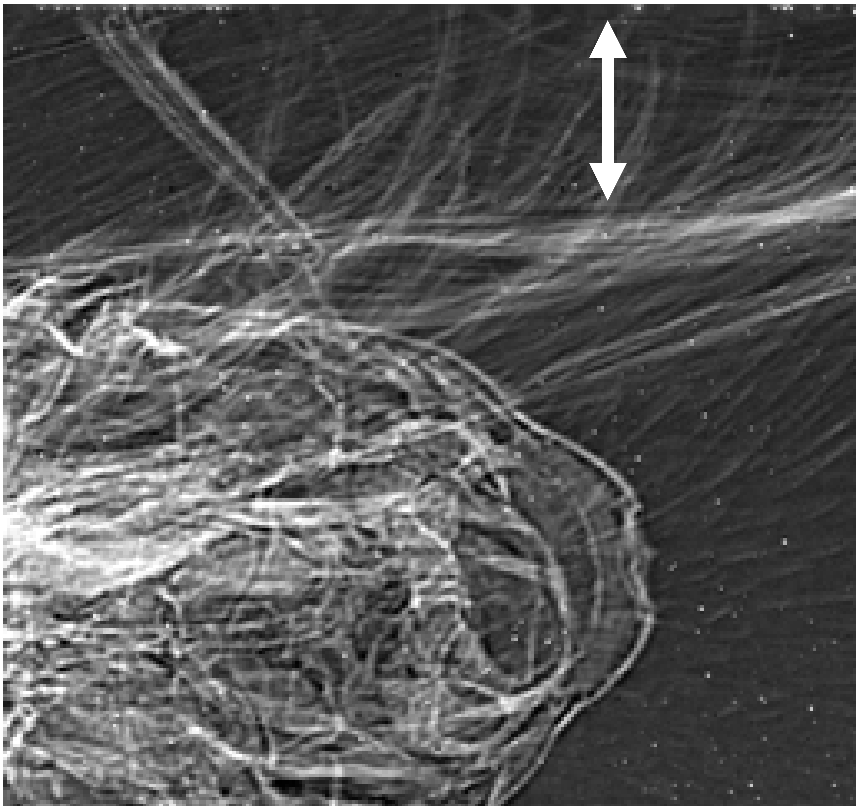

(b)

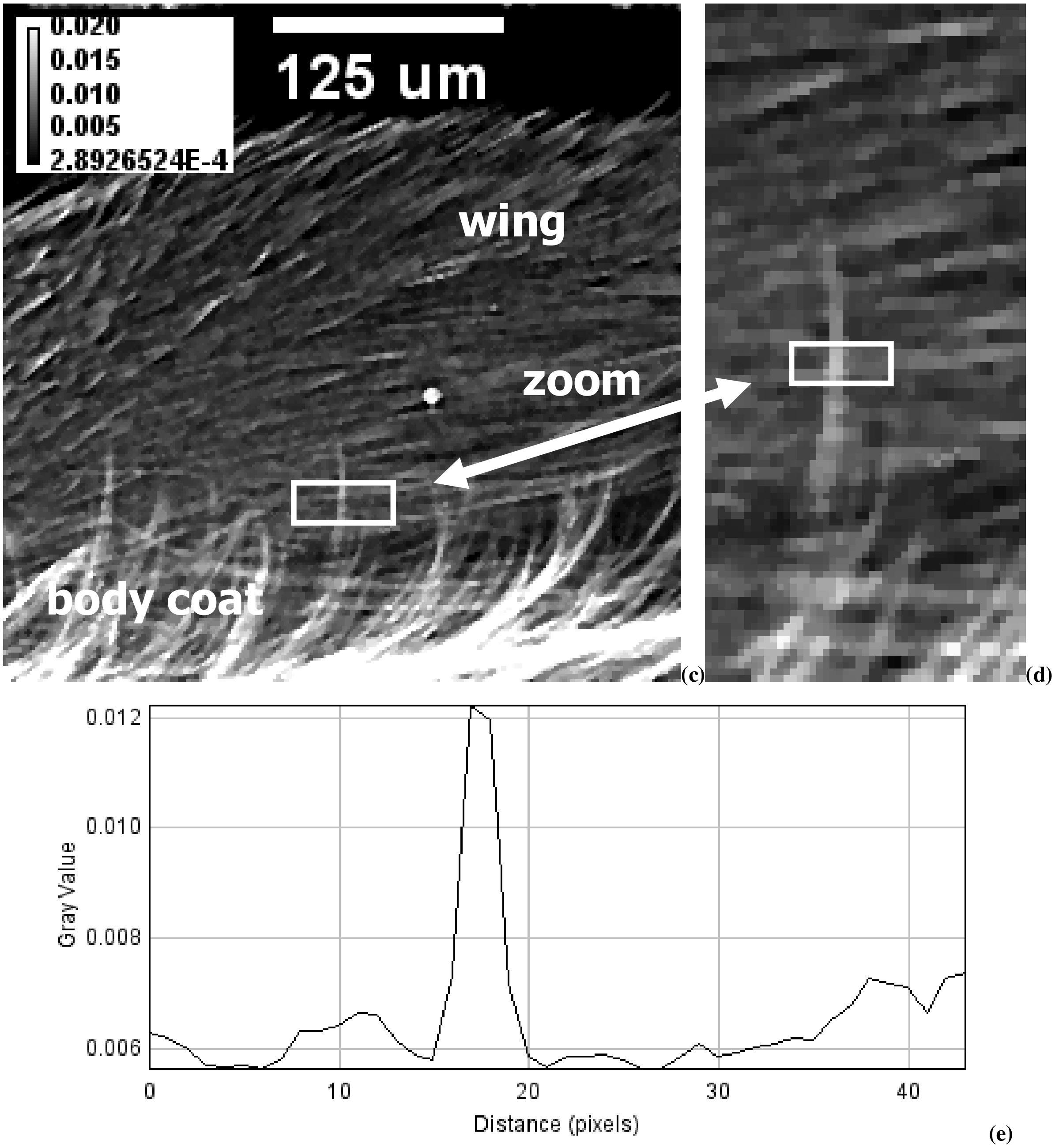

Fig. 3-9 Radiography of a fly, imaged at M = 12x (a), back side of the fly body covered with hair, as indicated from the arrow, imaged at a magnification of 33x (b). Radiogram of part of the body coat and of the wing hair, M = 38x (c); one filament from the body coat is zoomed (d) and a profile (e) of its section has been determined: the diameter size has been evaluated as 5 μm. The sample was imaged alive with an exposure of 20 mAs.

Fig. 3-10a and Fig. 3-10b show two radiographies of a rose leaf: in the first image, 5 mAs exposure, the structure of channels and of the webbed veining is visualized, while in the second one, 0.25 mAs, thanks to the higher magnification (M = 14x), one can distinguish the stomata which are pores necessary to the leaf to exchange gas (~ 40 μm diameter size).

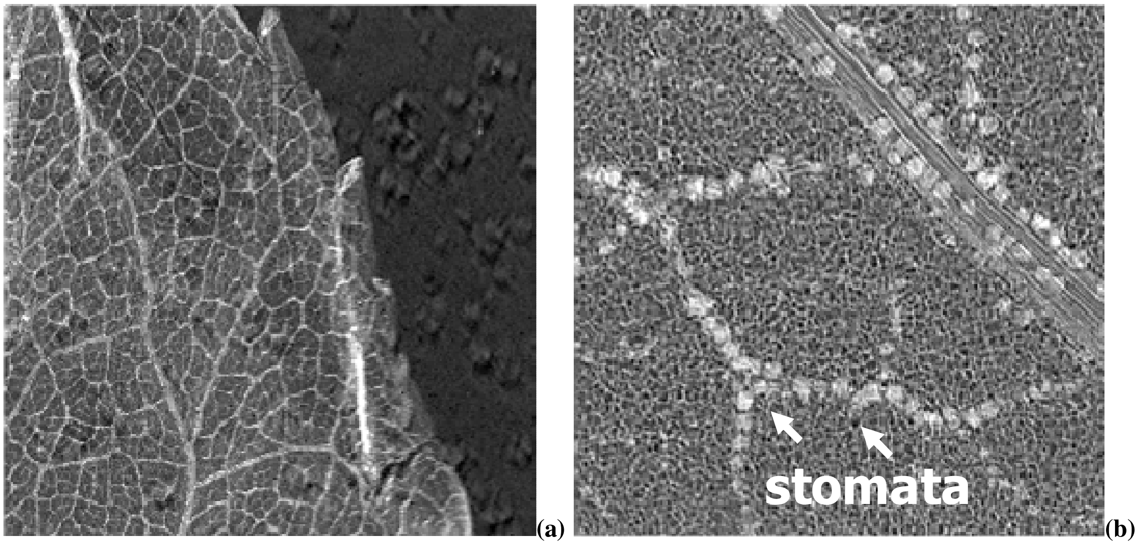

Fig. 3-10 Radiographies of a rose leaf: in (a), 5 mAs exposure, is visualized the structure of channels and of the webbed veining, while in (b), 0.25 mAs, thanks to the higher magnification (M = 14x), it is possible to distinguish the stomata which are pores necessary to the leaf to exchange gas (~ 40 μm diameter size).

To the purpose of comparing the above results with best results showed in the literature in this field, we will now briefly illustrate some examples from other groups with the use of different X-ray set-ups.

Among the published phase-contrast based works, we present here a very early result of year 1996, by the pioneer Australian group of S. W. Wilkins [58]. The paper has the merit to first present the evidence of the phase-shift phenomenon, using a conventional polychromatic X-ray source (instead of the synchrotron radiation), having a high spatial but essentially no chromatic coherence. The X-ray tube was provided with a 20 μm focal spot (*Kevex model PSX* with a Cu anode). The following images (Fig. 3-11a and Fig. 3-11b) represent two radiographies of a small aquarium fish (fantail) with the source operating at 60 keV, $R_1 = 300$ mm and $R_2 = 1$ (a) and $R_2 = 1100$ mm (b). The thickness of the fish was ~ 15 mm. The image for $R_2 = 1$ (a) corresponds essentially to an absorption-contrast-only image, while that for $R_2 = 1100$ mm should also contain some phase-contrast information. It is very evident that many more details of the weakly absorbing features of the fish anatomy are present in the Fig. 3-11b than in Fig. 3-11a. In particular, one can note the spinal cord (α), the ligament (β) and the lateral line canals (γ). The fact that the contrast at the edges of the organs is negative also points to the presence of the phase-contrast effect in the images.

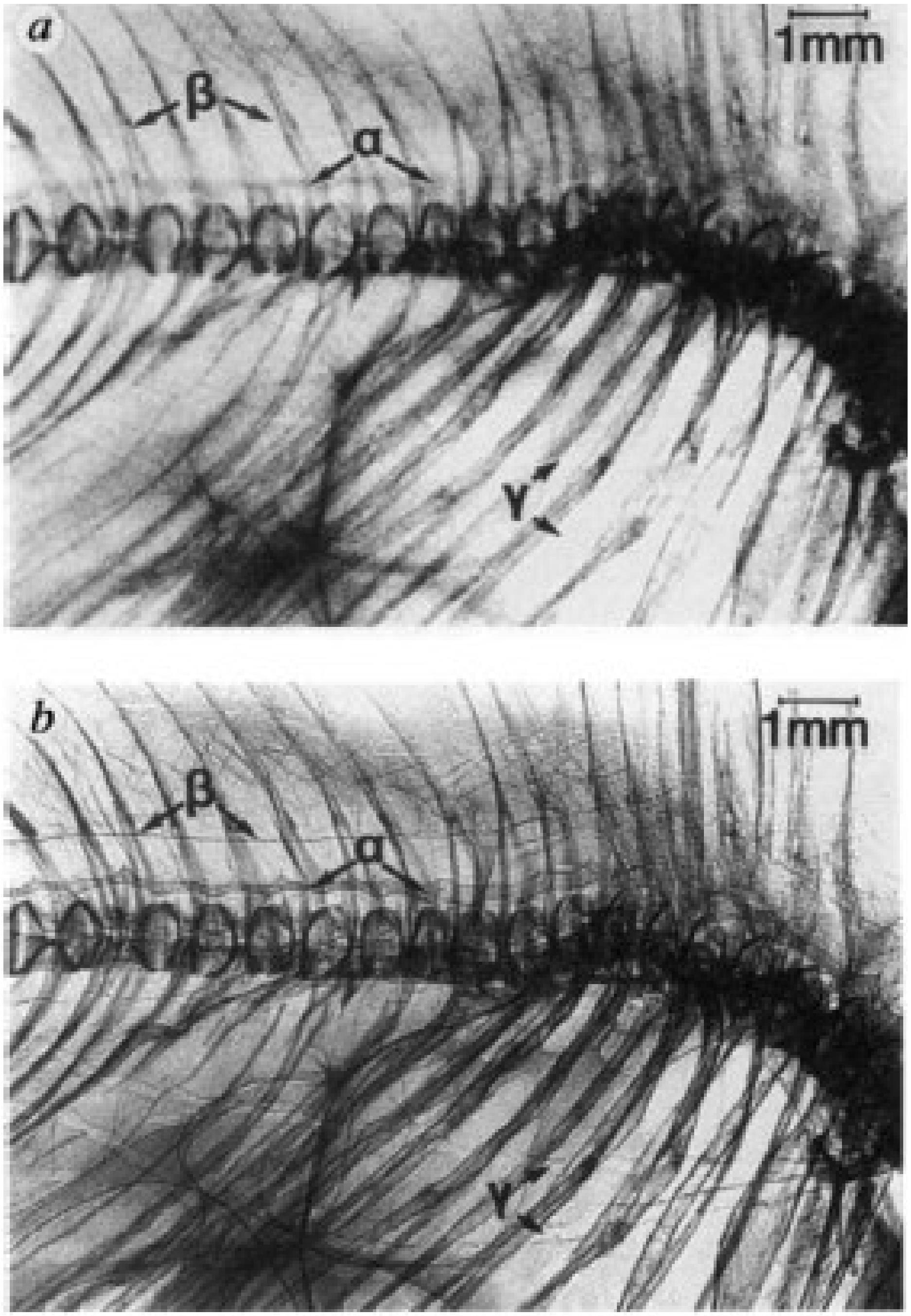

Fig. 3-11 Image of a small aquarium goldfish (fantail) recorded with a source-object distance of $R_1 = 300$ mm and an object-detector distance of $R_2 = 1$ mm (2 minutes exposure) (a) and an object-detector distance of $R_2 = 1100$ mm (110 minutes exposure). The tube voltage was V = 60 kV. [58]

A more recent example (2007) reported from literature of imaging on small biological samples exploiting the phase shift effect, comes from Gundogdu *et al.*, of University of Surrey, Guildford [59]. In their paper, they present imaging results obtained from a bench-top X-ray source employing the free space propagation method for biological samples imaging with a negligible absorption contrast. Fig. 3-12 shows a conventional absorption image (a) and the phase-enhanced image (b) of the same wasp, realized using an X-ray source with a focal spot of ~ 3 µm

(*Hamamatsu L8321*) provided with a tungsten target. The exposure time was of 1 minute, the tube voltage of 40 kVp and the tube current of 100 μA. For the phase-contrast image (b) the source-to-sample distance was $R_1 = 20$ cm, while the sample-to-detector distance was $R_2 = 65$ cm.

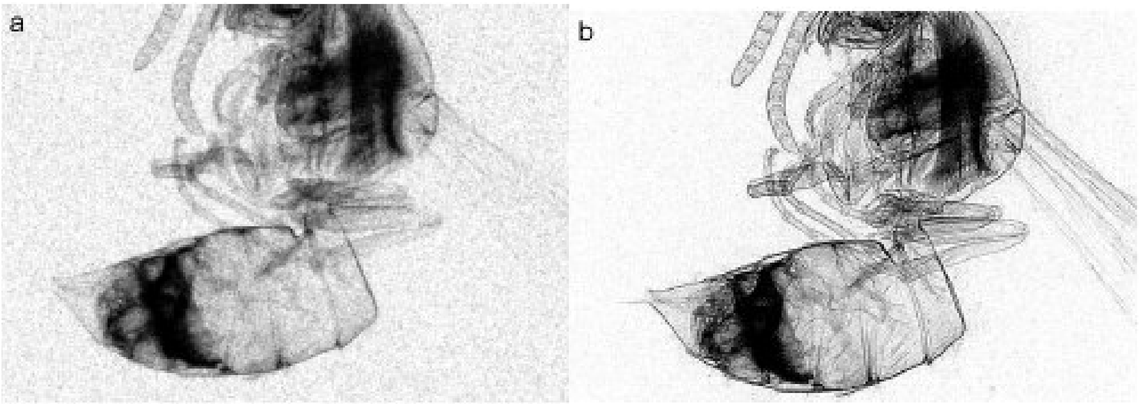

Fig. 3-12 X-ray image obtained with an X-ray tube provided with a focal spot of ~ 3 μm at 40 kV and 100 μA, with a 1minute exposure time. Absorption image (a) and phase-contrast image (b) obtained at $R_1 = 20$ cm and $R_2 = 65$ cm.[59]

All the results showed above take advantage from the phase contrast enhancement provided by the micrometric X-ray source focal spot besides the small detector pixel size. Nevertheless, in particular conditions of magnification M, tube voltage V and exposure (expressed in mAs unit) it is still possible to visualize the dark/bright Fresnel fringes also when the X-ray source has a focal spot several times bigger in size than the one used for the above images. To investigate which are the limits of the phase contrast effect manifestation, we did some tests on two polymethylmethacrylate (PMMA) slabs, one 0.5 cm thick and the other 1 cm thick with the *Oxford Instrument APOGEE package, series 5000*, X-ray source with a mini-focus of 35 μm. For the phase contrast measurement we choose to evaluate two parameters [60] [61] [62], the Edge Enhancement Index (EEI) and the Edge Enhancement to Noise ratio (EE/N) defined as follows (see also the Appendix A):

$$EEI = \frac{(P-T)/(P+T)}{(H-L)/(H+L)} \quad \text{and} \quad EE/N = \frac{(P-T)}{\sqrt{(\sigma_H^2 + \sigma_L^2)}}$$

where

P and T are the peak and through intensity values at the edge;

H and L represent the intensity average values, respectively, on the higher-intensity side of the edge and on the lower-intensity side of the edge;

σ_H and σ_L represent the standard deviations of the pixels used to calculate H and L in the EEI equation.

The two parameters EEI and EE/N have been evaluated at different exposure (in mAs unit), at different tube voltages (30 kVp, 40 kVp and 50 kVp) and at different magnifications M, since these three variables have been found to be as the crucial factors determining the extent of the phase contrast effect. Fig. 3-13a and Fig. 3-13c show, respectively, one radiography of the air/PMMA edge for the 0.5 cm thick slab and for the 1 mm thick slab at M = 1.76x (source-to-slab distance R_1 = 20 cm; source-to-detector distance (R_1 + R_2) = 35.2 cm), V = 40 kVp, I = 0.35 mA, t_{acq} = 5 s, while, Fig. 3-13b and Fig. 3-13d show the relative plot profiles taken across the edge for the two PMMA slabs. The profiles are an average of several line profile of a chosen ROI of the interface.

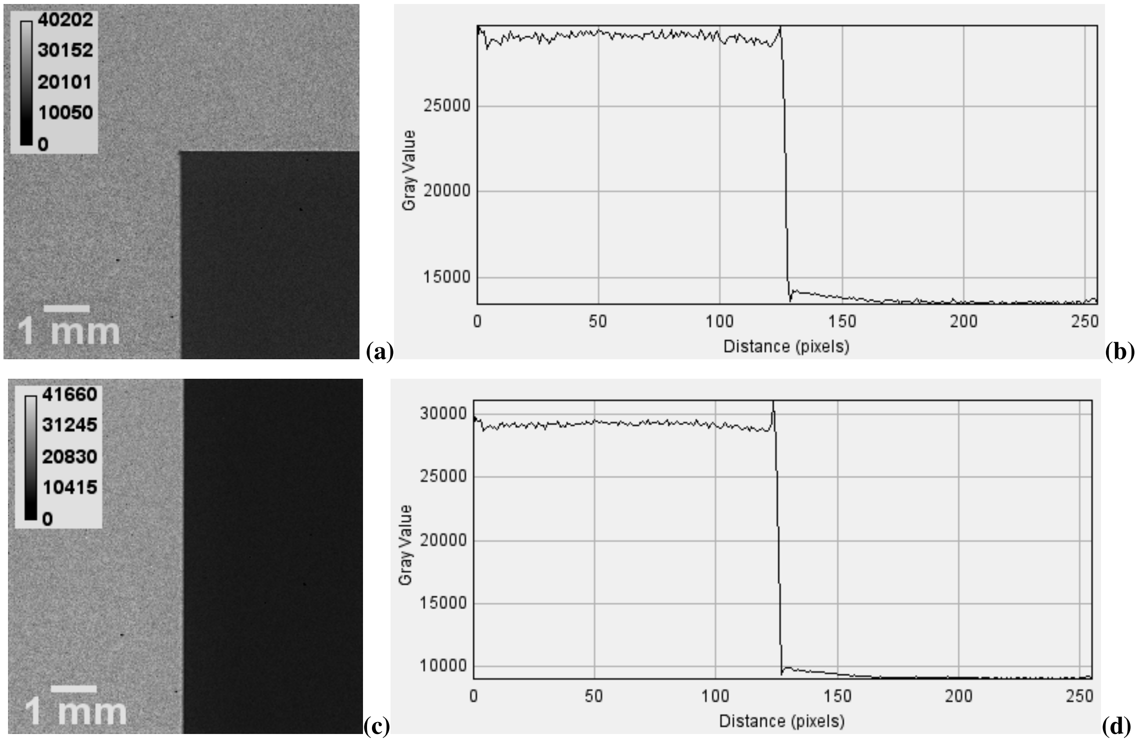

Fig. 3-13 Radiograms of two air/PMMA edges made with a PMMA slab 0.5 cm thick (a) and a PMMA slab 1 cm thick (c) at a magnification M = 1.76x (source-to-slab distance a = 20 cm; source-to-detector distance (R_1 + R_2) = 35.2 cm), with V = 40 kVp, I = 0.35 mA and t_{acq} = 5 s and the respective plot profiles taken across the interfaces (b, c). The images are corrected by means of the standard FFC. The profiles are an average of several line profile of a chosen ROI of the interface.

In the two profiles the up-ward and down-ward overshoot are clearly visible also if they are not much enhanced. In figures Fig. 3-14 (a) - (d) the results of the tests for the EEI parameter are presented.

As it is defined, the EEI value depends on both the difference (P-T) and the difference (H-L). The difference (P-T) is related to the magnitude of the phase contrast effect, while the second one depends only on the different attenuation properties of the two interfaced materials. It is reasonable to think that for thicker objects (less penetrating) the first term is higher than for thinner objects because the magnitude of the phase shift is bigger; similarly the second term is also bigger because the difference in the intensity is higher between air and a thicker material than between air and a thinner material. From these considerations, one can gather that the behaviour of Fig. 3-14a - Fig. 3-14d depends on which effect is predominant. Fig. 3-14b shows that for 40 kVp the two effects of phase shift and attenuation are balanced for the two thicknesses but, from Fig. 3-14c and Fig. 3-14d, it can be deduced that for a thicker material an increase in the transparency - gained at higher voltages - is more significant than the same increase achieved from a thinner material compared to the phase effect term (P-T). Both the results of Fig. 3-14c and Fig. 3-14d are interesting from the point of view of *in vivo* imaging, because they show that it may be possible to image tissues at higher X-ray energies than for the standard absorption imaging, resulting in a lower absorbed dose for the living organism. Moreover, because the EEI parameter does not depend on the noise, the increasing exposure (mAs unit) does not correspond to a considerable change in the EEI value. Similarly, the phase shift effect is not affected, even if, during exposure, the tube focal spot could become larger in size due to the anode heating effect, leading to a worse visibility of the phase-shift phenomenon. In any case, the reason for the different trends of EEI at high exposure values – increasing for the 1 cm thick slab and decreasing for the 0.5 cm thick slab - is not clear. On the other hand, the trend of EEI with magnitude corresponds to the theory's predictions: it grows at larger object-to-detector distance R_2, because the refracted rays have a longer pathway to diverge from the undeviated ones but, at too high magnification values the source blurring, due to the enlarged focal spot dimension, prevails.

In Fig. 3-14a - Fig. 3-14d the results of the tests for the EE/N parameter are presented.

On the contrary, the EE/N value depends on both the difference (P-T) and the noise on the H and L regions. This fact explains why the EE/N parameter raises at increasing exposures (Fig. 3-15a), since the noise decreases with increasing exposure (higher number of events recorded in H and L regions). Moreover, the higher value of EE/N for the thicker slab (Fig. 3-15a - Fig. 3-15b) can be explained with the higher phase shift effect which X-rays undergo when passing through a longer path. The EE/N vs M trend has already been explained above, even though it is not clear the reason of a successive second increase at high M values (not observable for the EEI parameter). The effect of the voltage for EE/N results reversed compared to EEI; in fact, at higher tube voltages the contribution of the standard deviations σ_H and σ_L in the denominator is superior to the one from the (P-T) term.

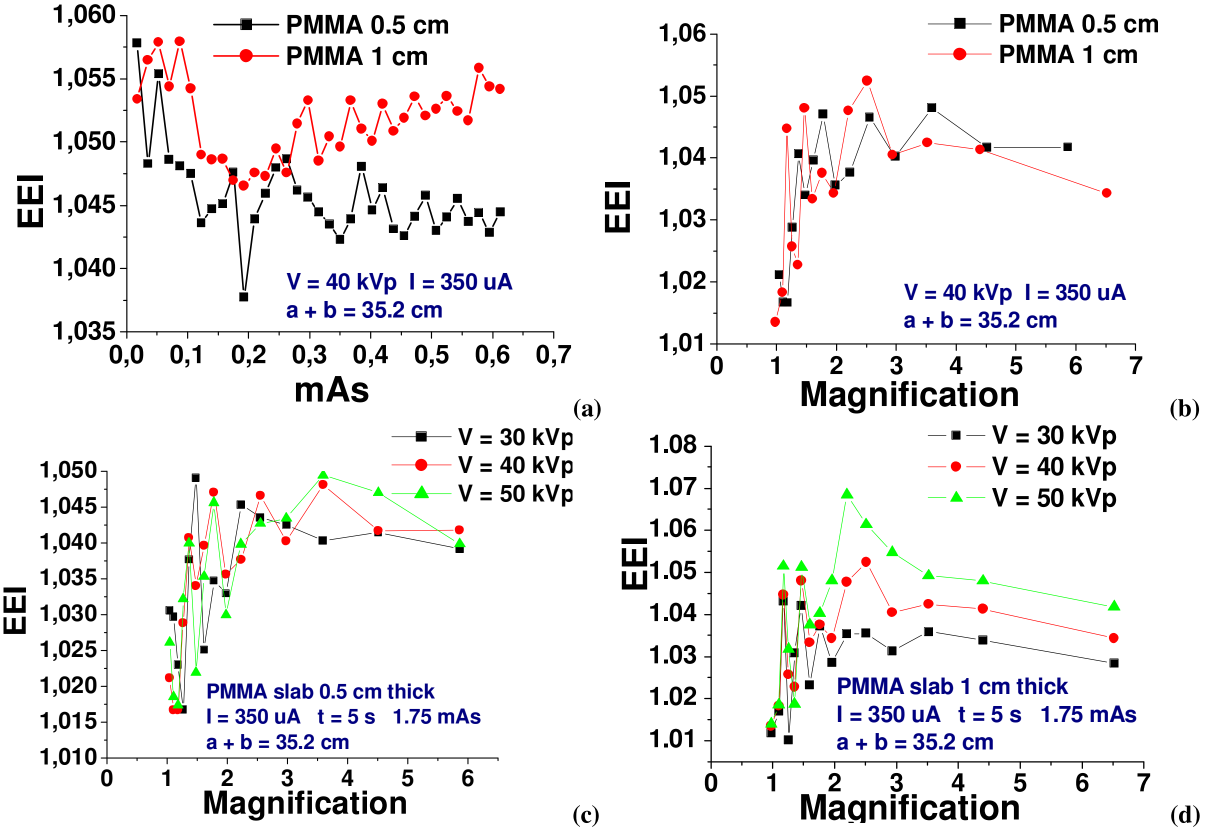

Fig. 3-14 Plots of the EEI values at different exposures (in mAs unit) for M = 2.5x (a) and at different magnifications (b) for a 5 mm thick slab and a 1 cm thick slab (V = 40 kVp; I = 350 μA); plots of the EEI values at different magnifications and different tube voltage for a 5 mm thick slab (a) and for a 1 cm thick slab (t_{acq} = 5 s; I = 350 μA). The focal spot-size is 35 μm.

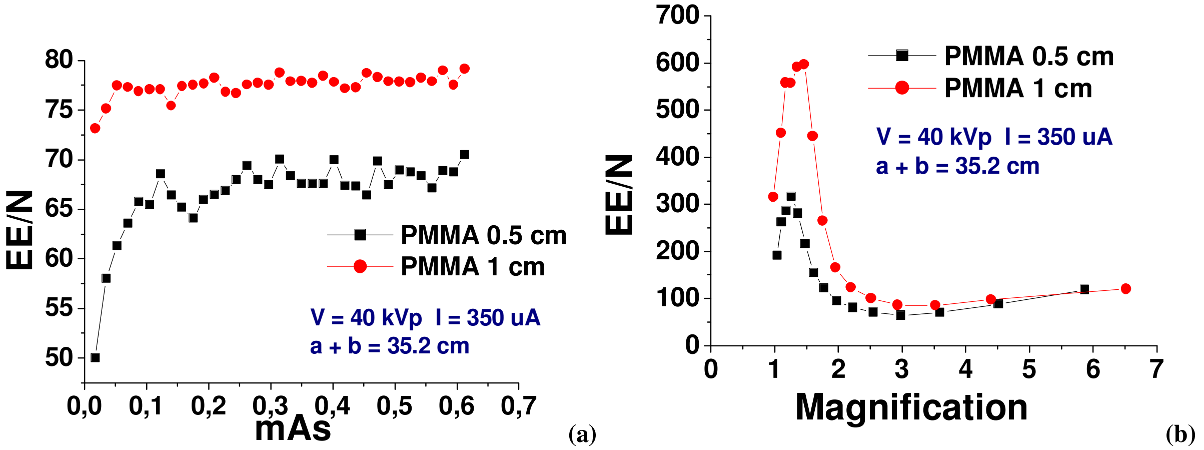

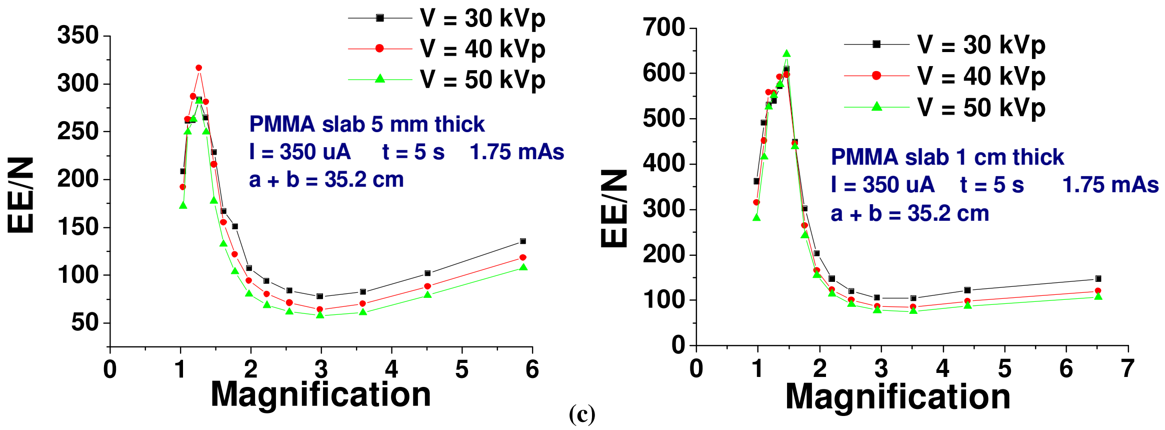

(c) (d)

Fig. 3-15 Plots of the EE/N values at different exposures (in mAs unit) for M = 2.5x (a) and at different magnifications (b) for a 5 mm thick slab and a 1 cm thick slab (V = 40 kVp; I = 350 µA); plots of the EE/N values at different magnifications and different tube voltages for a 5 mm thick slab (a) and for a 1 cm thick slab (t_{acq} = 5 s; I = 350 µA). The focal spot-size is 35 µm.

3.2 Real-time µ-imaging with Medipix2 SPC detector on living biological samples [63] [64] [65]

There are two ways of dealing with biological and organic samples, such as insects or parasites, as well as small seeds and leaves, when the aim is a morphological study: an *in vitro* or an *in vivo* investigation. The *in vitro* approach has two fundamental drawbacks: first of all, the test conditions may not correspond to the condition inside the living organism; the second aspect to take into account is the impossibility of longitudinal studies that means studies on the same sample during a period of time. The *in vivo* approach, on the other hand, allows following one sample through all the evolution processes of its life cycle, catching its morphologic changes (metamorphosis, mutation, growing processes). However, dealing with small biological samples, such as insects or parasites, is a challenging task if the aim is a non-invasive inspection that leaves the sample alive. Electron microscopes need a preparation of the sample that leads to the impossibility of *in vivo* and longitudinal studies on the same object. Nevertheless, this kind of investigation can be possible, to some extent, using X-ray imaging techniques. The requirement for this kind of study is a high spatial resolution (micrometer scale) radiographic system made up of an X-ray source and an X-ray detector [65]. By means of the SPC detector Medipix2 and the µ-focus X-ray source, a temporal study has been carried out by following an entomologic sample through its metamorphosis from the larva stage to the pupa stage using the phase contrast enhancement technique.

The chosen sample is the *Aesculus hippocastanum* (horse chestnut) tree pest *Cameraria ohridella*, a leaf miner belonging to the *Lepidopteran* family *Gracillariidae*. It is a well known plague of central and southern Europe and its name comes from the mines that it digs into the leaves, where females put their eggs. The larva penetrates from the egg directly into the internal part of the leaf, feeding between the upper and the lower surface of it and extending, in this way, the mine (up to 5 cm in length). The dimensions of leaf miners in the pupa stage are about 3.5-5 mm. A human control which reduces the leaf miner harmful spread is usually hard, but a natural control exists: in spring and in summer, nymphs of *Cameraria ohridella* are attached by a parasitic wasp that puts its eggs inside the leaf close to the larva of leaf miner. From each egg a new parasite larva emerges and develops, feeding the inner parts of its host [66].

The metamorphosis from the larva to the pupa, progressing inside the leaf miner, has been imaged during a period of several weeks' time by means of daily observations.

For all the measurements performed in this study the X-ray tube voltage was set at 40 kV to get a high soft tissues visibility (mean energy $\bar{E} = 15.0$ keV). The current was set at 200 µA to assure a high photon flux maintaining good spatial resolution. The exposure time was of 100 s for each image. The distance between the source and the detector was $(R_1 + R_2) = 62$ cm, while the magnification factor was varied from 4x up to 6x by alternations of the sample position.

Fig. 3-16a and Fig. 3-16b show, respectively, a photograph and a radiography (source-to-sample distance R1 of 15.5 cm for a magnification factor M of 4x), acquired with the radiographic set-up, of a living sample of the leaf miner *Cameraria ohridella*.

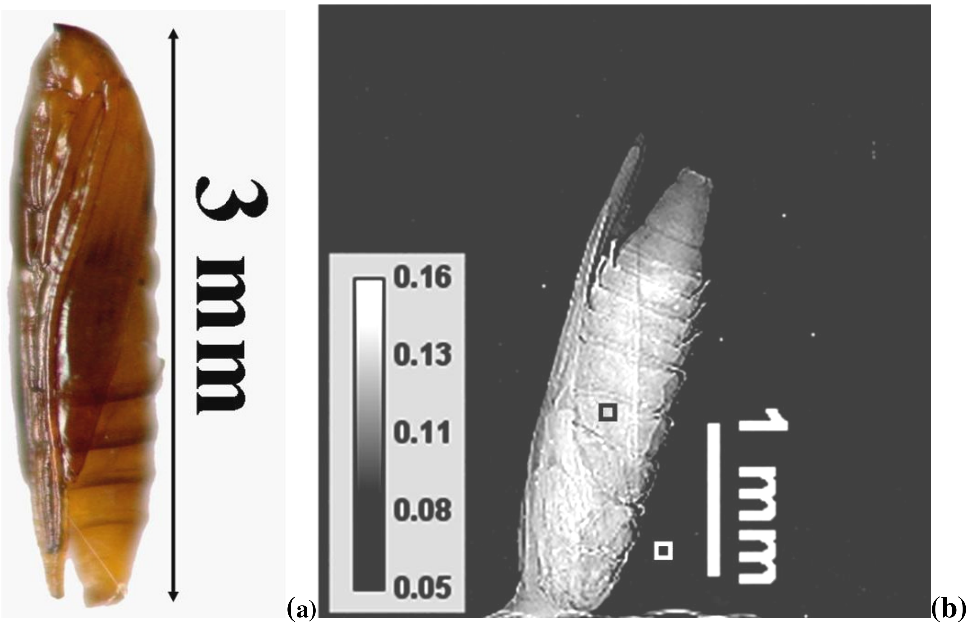

Fig. 3-16 Photograph (a) and radiography (b) of a living pupa of leaf miner. The radiography has been realized with Medipix2 SPC detector and with the micro-focus X-ray source (40 kVp tube voltage, 200 µA tube current, 100 s acquisition time). The magnification factor is M = 4x (source-to-sample distance $R_1 = 15.5$ cm). The ROIs used for the SNR evaluation are depicted (10 pixels x 10 pixels). The gray scale is in e. t. units.

The sample has a length of 3 mm. From the SNR evaluation on the radiography, a value of 47 was found. The ROI size was chosen of 10 pixels x 10 pixels (Fig. 3-16b). An estimation of a small detail size of the leaf mine body was also done for a magnification value of 7x. The size of a thin detail (Fig. 3-17b) of the living leaf miner body (Fig. 3-17a) was evaluated as 15 µm.

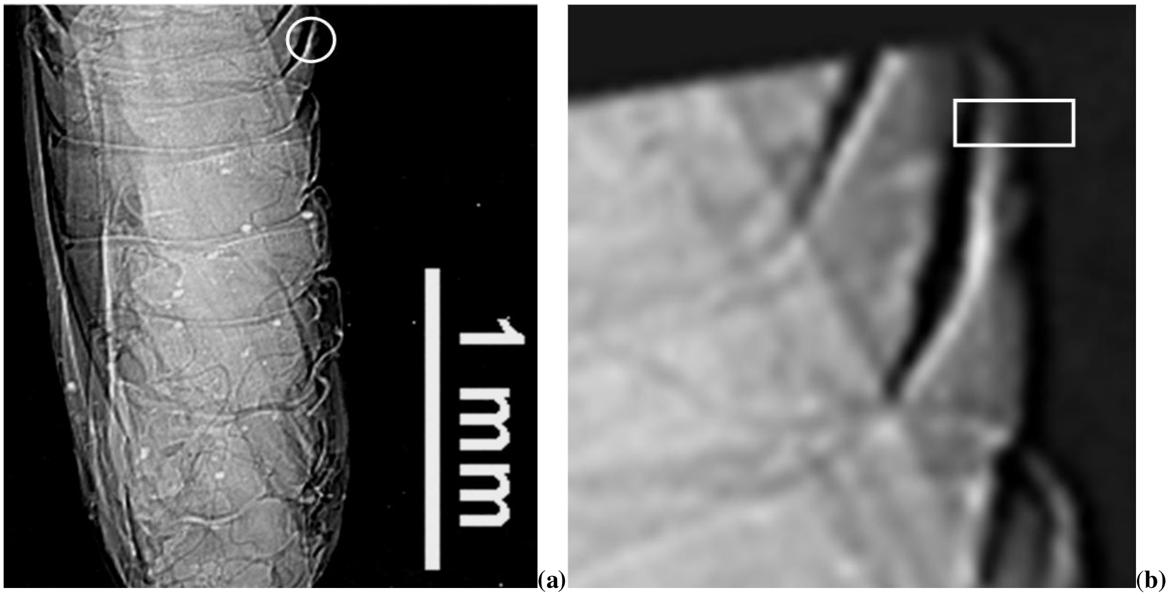

Fig. 3-17 Radiography of a living pupa of leaf miner; a circle has been drawn around a small detail of the body (a); zoom of the detail (b) for which the dimension has been evaluated as 15 µm. The magnification factor is 7x, tube voltage and tube current were, respectively, V = 40 kVp and I = 200 µA.

The target of the temporal study is the parasite vital morphological changes inside the life miner. Fig. 3-18a, Fig. 3-18b and Fig. 3-18c show, respectively, a photograph of the larva stage and two images from the scanning electron microscope of the pupa and of the imago stage.

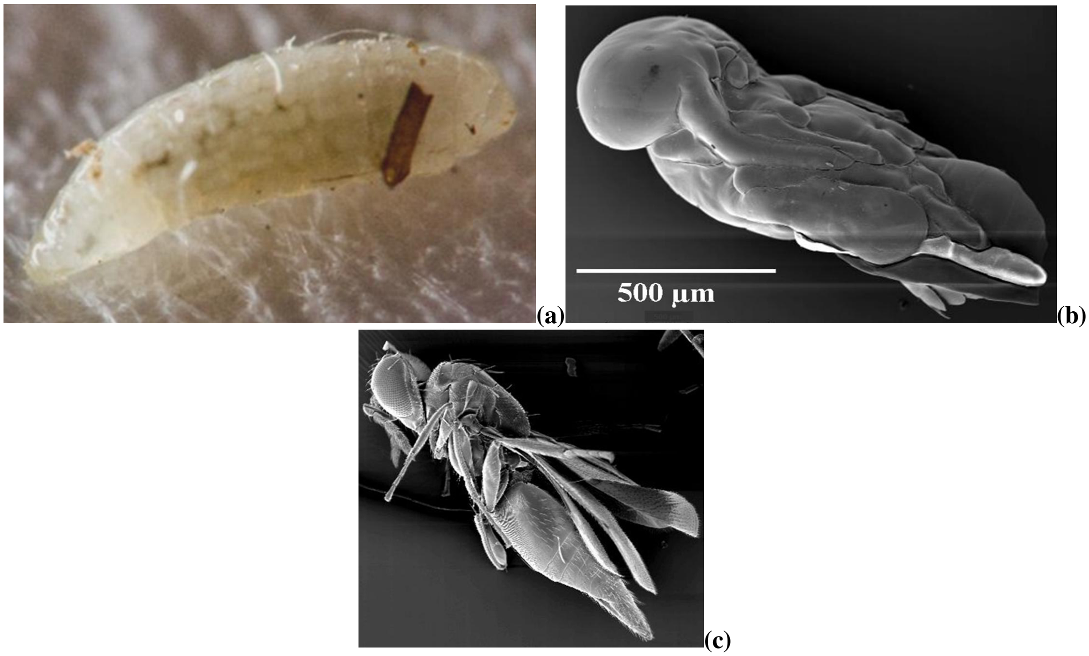

Fig. 3-18 Photograph of the larva stage of *Cameraria ohridella* parasitic wasp (a), scanning microscope image of the pupa stage (b) and scanning microscope image of the imago stage (c).

The sequence of radiograms presented in Fig. 3-19 shows the metamorphosis of the parasitic wasp of Cameraria ohridella, from the larva stage (Fig. 3-19a, Fig. 3-19b, Fig. 3-19c, Fig. 3-19d), to the pupa stage (Fig. 3-19e) and to the imago stage (Fig. 3-19f). Fig. 3-19g shows a radiography of a living imago of *Cameraria ohridella*. The magnification factor is 3.8x for the first six images and 6x for the last one.

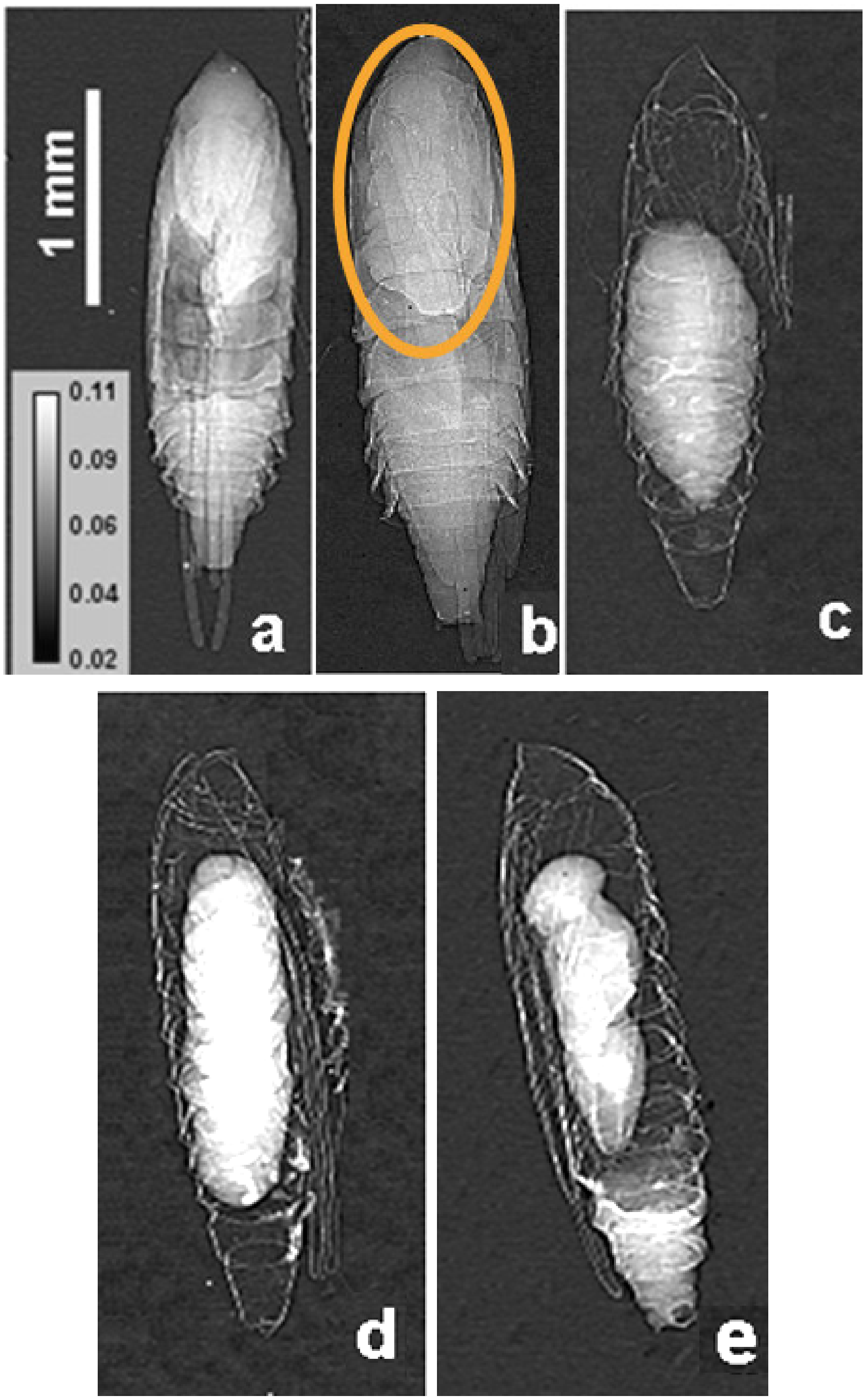

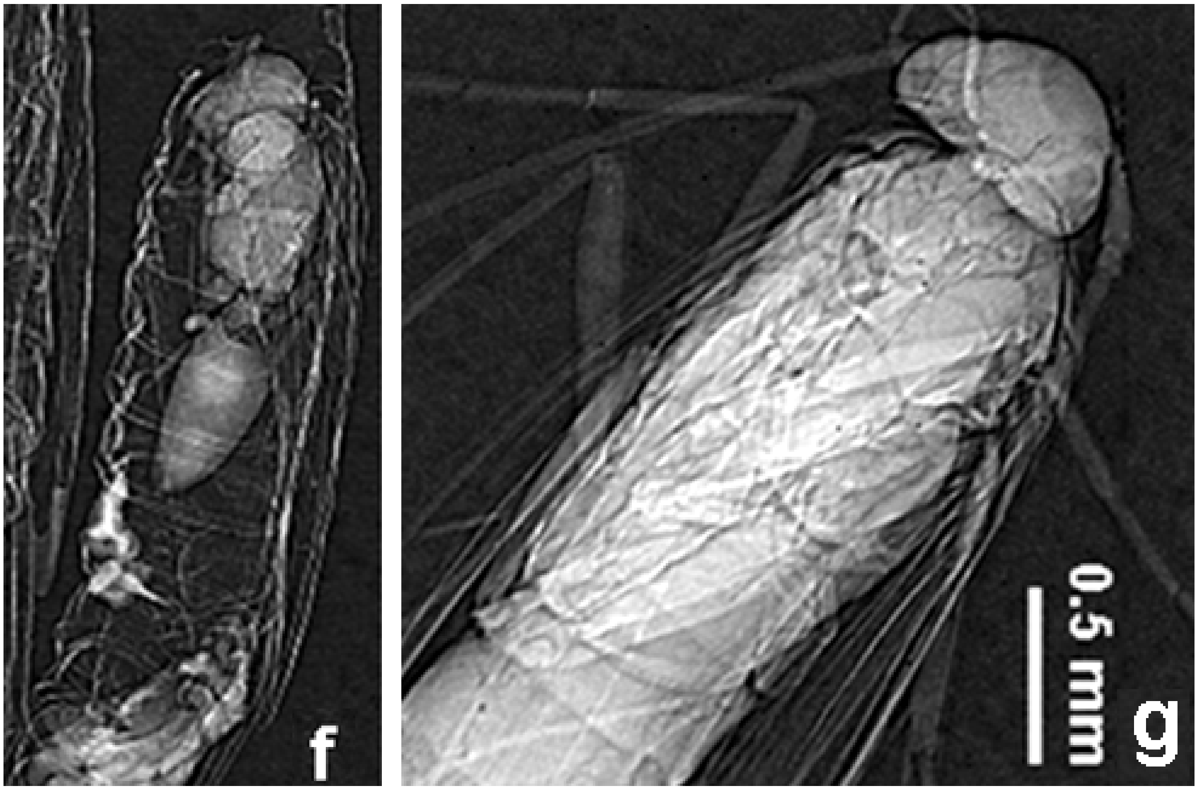

Fig. 3-19 *In-vivo* radiograms of the parasitic wasp of *Cameraria ohridella*, acquired during a period of several weeks. In (a), (b), (c) and (d) the larva is growing in length from a "ball" shape into a worm shape, eating the inner tissue of its host. In (e) it is shown the pupa stage and in (f) it is shown the imago stage. In (g) a radiography of a living imago of *Cameraria ohridella* is presented. The magnification factor is 3.8x for images a - f and 6x for image g; the acquisition time was 100 s and the tube settings were V = 40 kVp and I = 200 µA.

Fig. 3-20 shows a single radiography of six samples of leaves miner *Cameraria ohridella*: the first two samples, a and b, are alive, while c, d and e are already dead, killed by their host. It is possible to notice the inner host in three different stages of the life cycle (different length and body shape). The last sample, f, is just the outer skin of a dead *Cameraria ohridella*, empty also of the parasite that, having completed its metamorphosis, has left its host. The samples were acquired with a magnification factor of 2.9x, and the radiograph is an average of 100 frames of 1 s each.

Besides the anatomic information, entomologists and biologists are interested in observing also the target behaviour when it is still alive and placed into its natural environment. This kind of study can be carried out by acquiring photographs and movies with high resolution cameras, but with few and unsatisfactory information about the morphology and the anatomy of the sample. Combining the two goals - excellent spatial resolution and visibility of anatomic details - and following one sample not only through its life cycle, but also looking at its social life and at its real-time behaviour - can be realized by means of an X-ray imaging system, equipped with a µ-focus source, a digital X-ray detector and a high speed read-out hardware and software. The system made up with Medipix2 and the μ-focus X-ray source has the needed features to perform real-time studies for observations of time-dependent processes inside biological samples.

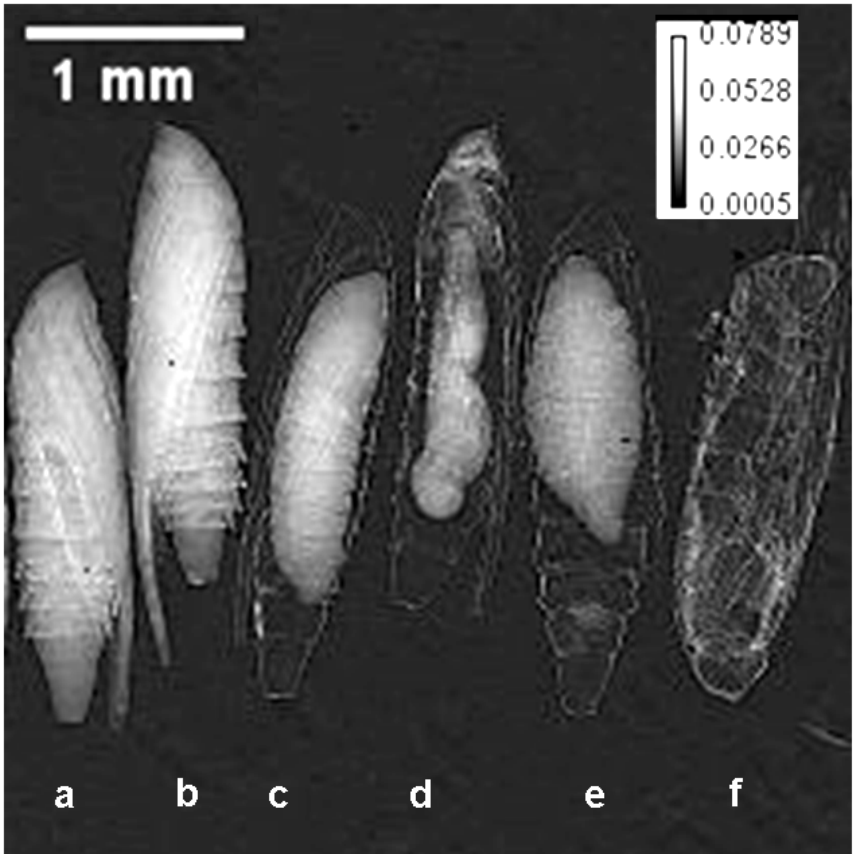

Fig. 3-20 Radiography of six samples leaf miner pupas. The radiography has been realized with Medipix2 SPC detector and with the micro-focus X-ray source (40 kVp tube voltage, 200 μA tube current, $t_{acq} = 100$ s). The magnification factor is 2.9x (source to sample distance R_1 of 21.4 cm).

The metamorphosis from the larva to the pupa stage we have presented above progresses inside the leaf miner during a period of several weeks time. During this period inside its host, the parasite is alternating moments of quick movements, mostly when eating, and moments of quietness. The behaviour of the parasite inside its host has been caught while moving in different phases of its metamorphosis by means of real-time videos: a first one, during the larva stage, while it was eating the leaf miner's inner tissue and a second one, when its metamorphosis was almost completed, during its attempt to get out from its host.

Images were acquired with a frame-rate of 2 frames/s (500 ms each), with a duty cycle of 96 %, with a tube current of 200 μA and a tube voltage of 40 kVp, for a source-to-detector distance of 62 cm and a magnification factor of 3.7x. The acquired images have been stacked together and converted into an *avi* file. Images of the larva stage and of the pupa stage are shown respectively in Fig. 3-21 and in Fig. 3-22. The significance of the presented real time X-ray μ-imaging is in the key role of the phase contrast effect; in fact, looking at the image sequence in Fig. 3-21 and Fig. 3-22 it is clear that the empty skin of the *Cameraria ohridella* presents almost no attenuation to X-rays.

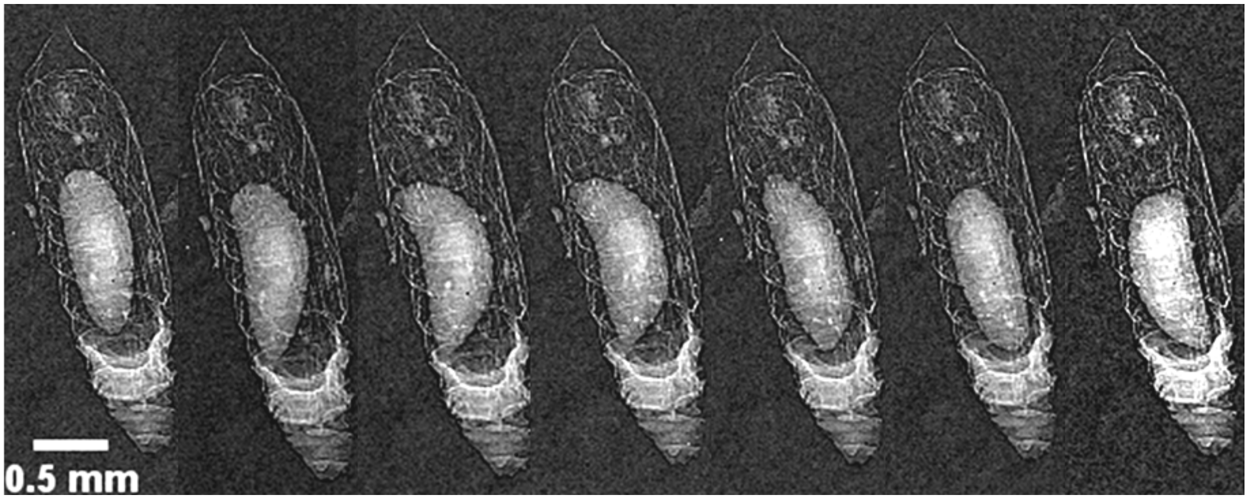

Fig. 3-21 Sequence of radiograms showing the parasite behaviour inside the leaf miner, when in the larva stage. Each image has been acquired for 500 ms corresponding to a frame rate of 2 frames/s. Tube voltage and tube current were set at 40 kV and 200 µA respectively. The magnification factor was of 3.7x.

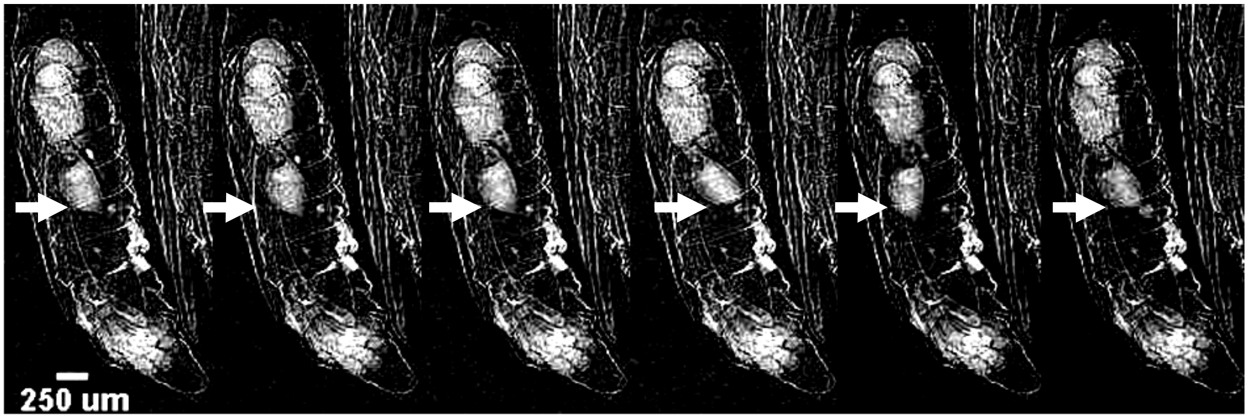

Fig. 3-22 Sequence of radiograms showing the parasite behaviour inside the leaf miner when in the pupa stage. Each image has been acquired for 500 ms corresponding to a frame rate of 2 frames/s. Tube voltage and tube current were set at 40 kVp and 200 µA respectively. The magnification factor was of 3.7x.

In fact, we observe a well defined edge separating the dead insect from the parasite: it should be clear that without the contrast enhancement at the interfaces, as a result of the interference fringes, we would not be able to visualize the living structure wrapped in the thin layer or, in other words, that in the absorption regime this kind of investigation would be not possible.

The second reason of the significance for the real-time imaging here presented is in the use of a polychromatic X-ray commercial tube. In fact, in literature it is possible to find other real-time studies on biological samples but realized with a coherent synchrotron radiation. Here we report two examples of dynamic imaging on living samples realized by means of the phase contrast in-line technique.

The first study has been carried on by M. W. Westneat *et al* [67]. The paper shows the capability of the phase contrast imaging technique to observe the previously unknown mechanism of respiration in insects, using 15-to-25 keV synchrotron radiation.

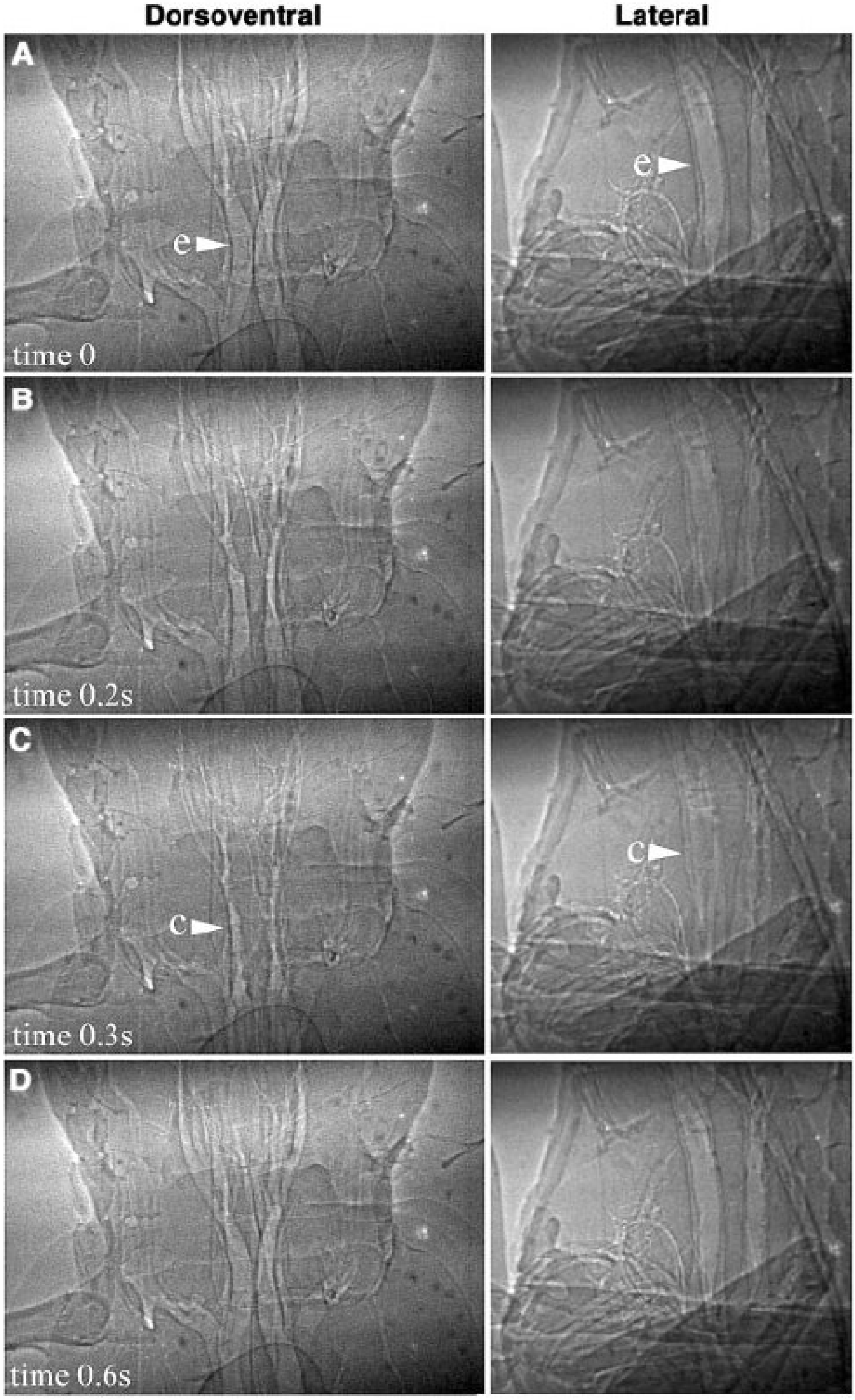

Fig. 3-23 Dorsoventral (left) and lateral (b) view of the respiration mechanism by tracheal compression in the head and in the thorax of a beetle. Tracheal tubes are expanded at rest [(A), arrowed e], and compression (B) occurs throughout the anterior region of the insect. Maximal compression [(C), arrowed c] is followed quickly by expansion of the tracheae (D). The entire respiratory cycle is completed in less than 1 s. [67]

Most insects breath through a system of tubes called tracheae which connect to the air via spiracles that can be actively opened or closed. Tracheal tubes are gas-filled vessels (the tiniest one, called "tracheoles", may be 1 μm in diameter), and their function is to exchange gas with tissues of the body. X-ray videos were recorded for different insects - ground beetles, carpenter ants and house crickets - while breathing. The respiratory frequency ranged from about 0.4 Hz to 0.7 Hz in the beetle and the duration of tracheae compression ranged from about 0.7 to 1.6 s in the three species, followed by a period of inactivity. In Fig. 3-23 we report those results on the respiration by tracheal compression in the head and thorax of the beetle, with the purpose of a qualitative comparison with our results.

A second example comes from R. A. Lewis *et al*, [68] that reports on dynamic propagation-based phase contrast imaging of lungs function. By means of the synchrotron beam, 300 mm width and 20 mm long at 25 keV energy (*SPring-8, beamline 20B2 of the Biomedical Imaging Centre*, Japan), they have gained semi-quantitative information on the rate of liquid clearance from the lung of rabbit pups. The living pups were continuously imaged at 4 s intervals, using a phosphor charge-coupled device (CCD) detector (*Hamamatsu, mod.C4742-95H*) with 5.9 μm pixels (spatial resolution of approximately 25 μm) for an active area of (24 x 15.7) mm^2. The time resolution limit was given from the read-out speed of the CCD detector and was no higher than 1.7 frames per second. Fig. 3-24 shows selected frames from an X-ray movie of the dynamic study recorded during the first hour after birth of a single live rabbit pup. At birth the lungs stop secreting liquid as when in placenta and the airways are cleared to allow the entry of air inside with the onset of ventilation. The initial images, recorded few minutes after birth, clearly reveal the major airways and the branching structures down to the tertiary bronchi because of the animal's shallow breathing. Subsequently, the inspiratory effort becomes visibly more pronounced leading to accelerated rates of aeration of the small airways and alveolar structures. It can be seen from the images that, as length and the number of inhalations increase, both the visibility and the brightness of the speckle pattern of the lungs increase dramatically.

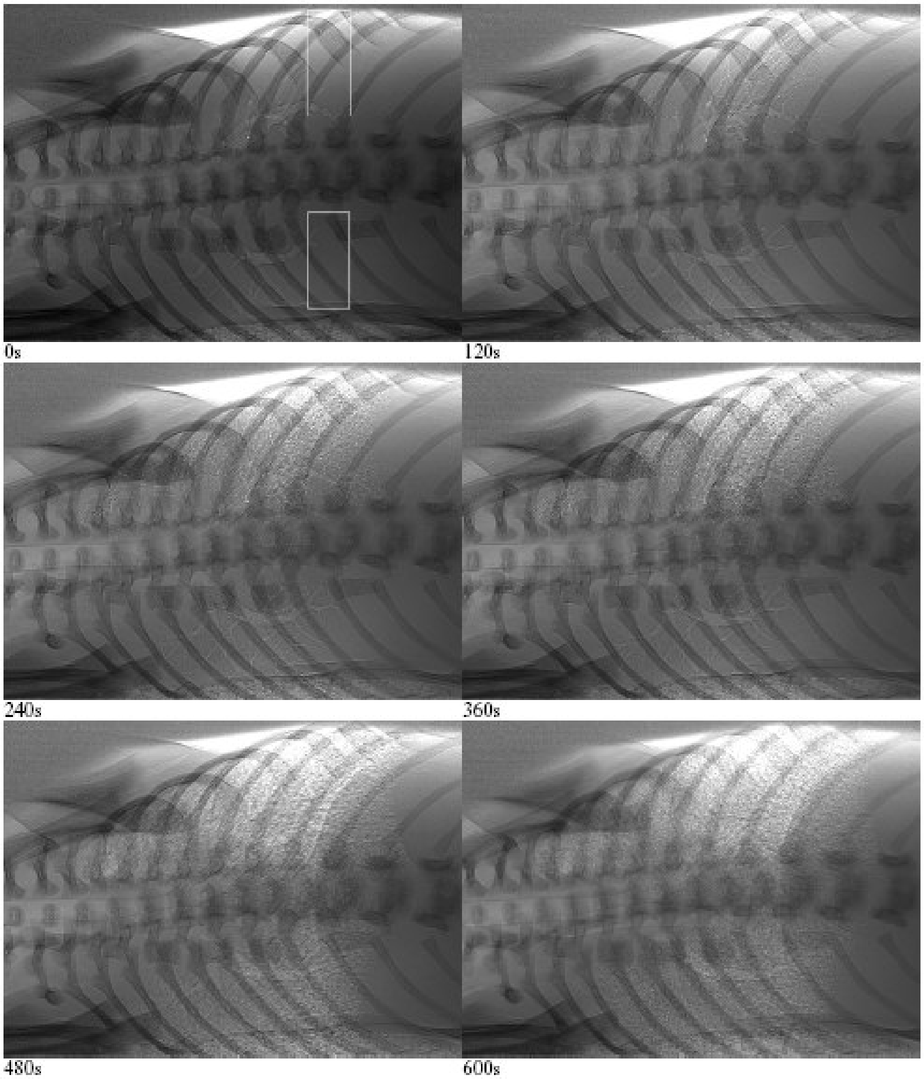

Fig. 3-24 Time series of breathing rabbit pup showing selected frames at various times after the onset of imaging. Breathing began 30 s earlier. Exposure time: 588 ms. The white boxes measure 0.72x3.30 mm^2. [68]

3.3 3-D μ-imaging on living samples with Medipix2 SPC detector

Common imaging techniques for the study of the internal structure of insects and organic objects require a mechanical sectioning of the sample that can be damaging and not fully satisfactory, because the sample can not be kept alive. In fact, shapes, compositions and functions of organs and tissues in the still state are usually different from the same in the living state. Electron and optical microscopic techniques, for example, are able to reach high spatial resolution and to detect information of small details, but the sample has to be prepared in a way that does not allow for *in vivo* and longitudinal investigations on the same sample. On the opposite, using the system set-up with Medipix2 SPC detector and an X-ray μ-source it is possible to perform *in vivo* 3-D μ-imaging. The chosen sample is, once again, a dead *Cameraria ohridella* with a living parasite inside. As we did for planar imaging, to enhance image contrast we have operated from two points of view: on one hand we provided soft X-rays (40 kVp X-ray tube voltage corresponding to a mean energy $\bar{E} = 15.0$ keV), suitable for thin biological tissues; on the other hand, we took advantage from the phase contrast technique. During the tomographic acquisition, both the source and the detector were kept fixed, while the sample is placed on a rotating stage. The μ-tomography of living sample was realized taking 180 projections over 180°, each of them with an exposure time of 10 s. The tube current was set at 250 μA to assure a high photon flux maintaining good spatial resolution and the magnification factor was 3x.

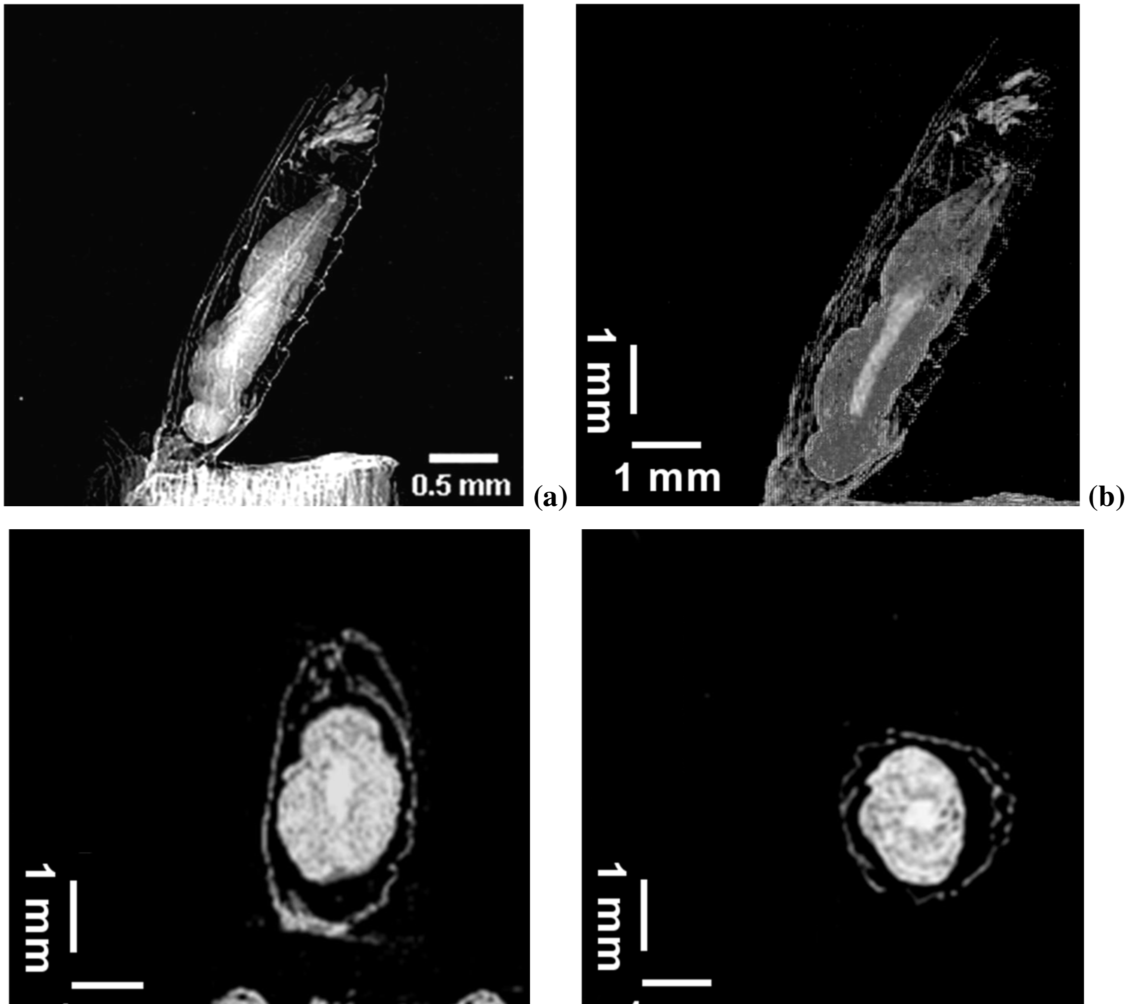

Fig. 3-25 Projection of a leaf miner killed by its parasite living inside its body (a); slices from the tomographic reconstruction obtained with the OS-EM algorithm: coronal view (b), sagital view (c), transaxial view (d). The voxel size is 17 μm x 17 μm x 21 μm and the total number of voxels is 259 x 259 x 211. The length of the dead leaf miner is 3.1 mm and the mean diameter of its body is 800 μm x 800 μm, while the length of the inner parasite is 2 mm for a thickness going from 68 μm x 170 μm, in the thinnest region, to 700 μm x 500 μm in the thickest region. The magnification factor is 3x.

The object slices have been reconstructed using the home made statistical Ordered Sub-set Expectation Maximization (OS-EM) iterative algorithm [6].

Fig. 3-25 shows one projection (a), the sagital (b), the coronal (c) and the transaxial (d) views, obtained from the 3-D reconstruction of the leaf miner with the parasite living inside its body. The tomographic reconstruction is realized by 211 planar slices of 259 x 259 pixels, for a voxel size of 17 µm x 17 µm x 21 µm. The empty body of the leaf miner pupa has been estimated as 3.1 mm long, with a mean diameter of 800 µm x 800 µm; the living parasite, in the pupa stage at the moment of the tomography, had reached a length of 2 mm, while the diameter of its body was estimated as 68 µm x 170 µm in the thinnest region and as 700 µm x 500 µm in the thickest part.

3.4 2-D image quality comparison between Medipix2 SPC and the FP detector by means of two pixels equalization techniques

In the first 3 paragraphs (3.1 - 3.3) it was showed that an SPC detector is adequate for medical imaging on both *ex vivo* and *in vivo* biological samples. Here we want to carry out a comparison of image quality, between two different technologies: an FP detector and the experimental Medipix2 detector.

The image quality is evaluated by means of two parameters: the contrast C and the contrast-to-noise ratio CNR as defined in Chap. 2. Because the interest of this study is in the performance of the two detectors for biological imaging, the experimental tests were carried out on polymethylmethacrylate (PMMA) phantoms containing inserts of materials characterized by different attenuations to X-rays as in biological tissues. In fact, in the diagnostic energy range (20 keV - 80 keV) the PMMA presents a linear attenuation coefficient close to that of water. Filling a PMMA phantom with different materials simulates the conditions for the visibility of a number of organs and tissues present in an organism having different attenuation to X-rays.

The first test [51] has been realized with a PMMA filter, 0.1 mm thick, on the X-ray tube window, so as to cover a half of it and leaving open the second half. Fig. 3-26 shows two radiograms of the filter edge, realized both with the FP (left) and with the Medipix2 (right) detector at a tube voltage of 40 kVp and a tube current of 50 µA. Each image is the average of 150 acquisitions of 1 s exposure time. The ROI chosen for the C and CNR evaluations are of 60 pixels x 60 pixels. The values found are: $C_{FP} = (0.9 \pm 0.1)$ % and $CNR_{FP} = 0.25$ for the FP detector and $C_{Mpx2} = (8.93 \pm 0.06)$ % and $CNR_{Mpx2} = 1.59$ for the Medipix2 detector, showing a higher performance of the SPC compared to the charge integrating detector in terms of image quality for 2-D imaging.

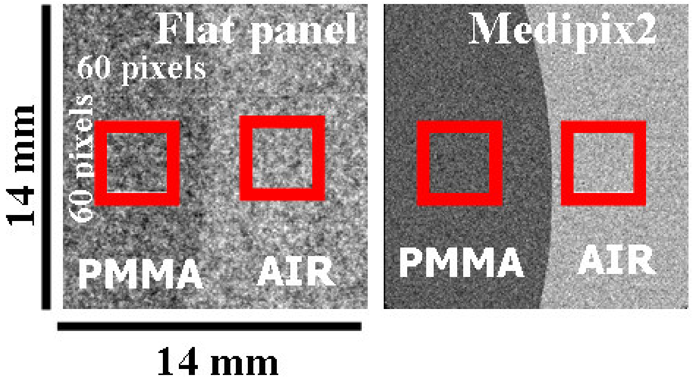

Fig. 3-26 Radiography of an air - PMMA edge realized attaching a 0.1 mm thick filter on one half of the X-ray tube window, leaving open the second half. The left image has been acquired with the FP detector while the right image with Medipix2 SPC. Each image is the average of 150 acquisitions of 1 s time (7.5 mAs). V = 40 kVp, I = 50 µA. The ROI of 60 pixels x 60 pixels chosen for the evaluation of C and CNR are pointed out. The found values are: $C_{FP} = (0.9 \pm 0.1)$ % and $CNR_{FP} = 0.25$ for the FP detector and $C_{Mpx2} = (8.93 \pm 0.06)$ % and $CNR_{Mpx2} = 1.59$ for the Medipix2 detector. [51]

A second test has been done by measuring the ratio $\bar{\mu}_{signal} / \sigma_{signal}$ *versus* time on flat field images, where $\bar{\mu}_{signal}$ is the mean signal value chosen in a region of interest (ROI) of a fixed area inside the flat field image and σ_{signal} is its standard deviation. In the presence of only Poisson noise, this quantity should increase with the square root of the exposure. Fig. 3-27 show the trends for the FP detector and for Medipix2. Unfortunately, because of the FP detector limited dynamic range, a number of flat fields of 1 second acquisition time have been acquired and summed up to get flat field images of higher acquisition times. This means that for each flat field analyzed, the noise is the sum of the noises of a number of flat fields of 1 second exposure time. For this reason the noise contribution in the plot of FP detector data results to be constant. On the other hand, the Medipix2 detector flat field have been obtained setting increasing exposure times, so for higher level of exposure the noise is increasing at. The Medipix2 curve has been fitted with the function $y = a \cdot x^b$ and the b parameter has been found to have the value $b_{Medipix2} = 0.41 \pm 0.02$, indicating that there is a further contribution other than the Poisson noise. Although the comparison is disadvantageous for the Medipix2 detector, one can see that the ratio $\bar{\mu}_{signal} / \sigma_{signal}$ is increasing for Medipix2 more than for the FP detector.

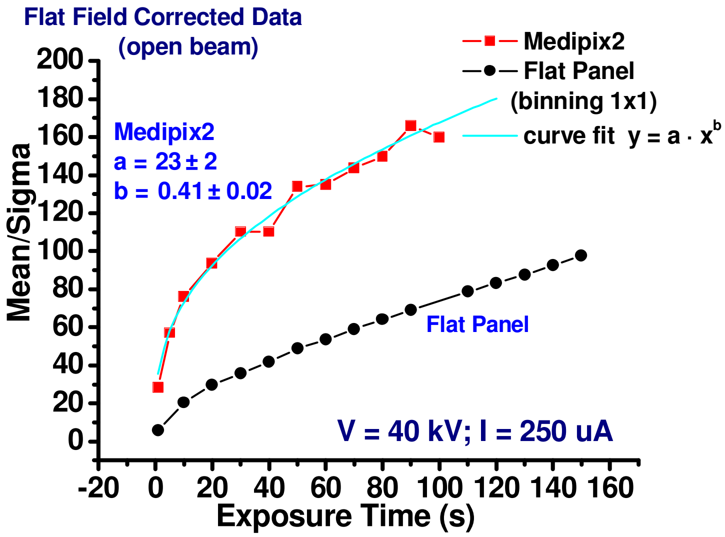

Fig. 3-27 Trends of the quantity $\overline{\mu}_{signal} / \sigma_{signal}$ evaluated on a ROI of 213x256 pixels of a flat field image at different exposures (I = 250 µA) for a tube voltage of 40 kVp, W anode, for both the FP and the Medipix2 detectors and the curve fit y = a · x^b. The detector pixels have been equalized by means of the standard flat field correction FFC.

From the plot in Fig. 3-27 it is evident that Medipix2 has a better mean/sigma ratio compared to the FP detector. The reason for this different behaviour lays in the different technologies behind the two detectors: the FP detector is a charge integration device, which means that it integrates the whole signal arriving from all the incoming events impinging on its sensitive area, both from the desired and from the undesired radiation (exactly the noise, generally speaking), so that, at increasing exposure, both the numerator and the denominator of the ratio increase. On the contrary, Medipix2 operates in single photon counting mode, which means that each incoming photon is first compared to a discrimination threshold and, only if the signal generated from the energy released is higher than this level, the photon is counted, contributing to the "good" signal $\overline{\mu}_{obj}$. This is also the reason for the highest values of the CNR parameter evaluated above.

As already explained in Chap. 2, X-ray images acquired with pixellated detectors need a post-correction that flatters the pixel response over the array in order to improve the image quality of 2-D radiograms and to avoid artefacts in the 3-D tomographic reconstruction. The most common way to perform this is the so called "Flat Field Correction" (FFC), while the novel algorithm we want to compare to the FFC is the Signal-to-Thickness Calibration (STC) that takes into account the modification of the spectrum in traversing the sample. To compare the two techniques on images acquired with both the detectors, we proceeded as follows:

- two independent flat field measurements were performed in the same conditions using a set of aluminium filters with different thicknesses with a tube voltage of 40 kVp and a tube current of 250 µA;

- one set has been used as data to be corrected, marked as "D" ("Data"), while the second one has been used to perform FFC and SCC on the first set and has been marked as "C" ("Correction data");
- each image of the first set D has been corrected by FFC, using each image of the second flat fields set, C, of different thicknesses;
- each image of the first set D has been corrected by SCC computed using data of the second set C;
- standard deviations of corrected data matrices have been computed;
- one comparison has been carried out between Medipix2 and FP detector for the same correction method;
- one comparison has been carried on between FFC and SCC methods for the same detector.

Because we were dealing with flat fields of filters images, the aluminium top cover of the FP detector has been removed to have the same experimental conditions for both detectors.

The average counts per frame for Medipix2 detector have been kept constant (~ 1500 counts/frame), changing the acquisition time at filter thickness increase; 45 frames have been summed up for each thickness value; the number of frames acquired with the FP detector has been chosen so that the sum of all of them would have the same statistics as the sum of 45 frames acquired by Medipix2 detector has.

Tab. 3-2 summarizes a detailed report of the measurements described above.

The plots in Fig. 3-28 (a - h) show four examples of trends for the average pixel standard deviation evaluated - as explained above - on flood irradiation images of Al filters (set D) when the images are corrected by means of the FFC using, at every turn, flat fields of Al filters in the range [0, 8] mm both for the FP (Fig. 3-28b, Fig. 3-28d, Fig. 3-28f and Fig. 3-28h) and for the Medipix2 (Fig. 3-28a, Fig. 3-28c, Fig. 3-28e and Fig. 3-28g) detector (read caption note for details).

Medipix2			**Flat Panel**	
filter thickness (mm)	**t_{acq} (s)**	**number of summed frames**	**t_{acq} (s)**	**number of summed frames**
0	0.2	45	0.25	24
0.05	0.3	45	0.25	25
0.1	0.4	45	-	-
0.25	0.9	45	0.25	31

0.5	1.6	45	0.25	37
1	3.3	45	0.25	52
2	7.5	45	0.25	85
4	21	45	-	-
6	42	45	-	-
8	80	45	1.5	100

Tab. 3-2 List of flat fields acquired for the FP and for theMedipix2 detector for filters of thickness in the range [0, 8] mm of aluminium. For Medipix2 45 frames acquired with different acquisition times have been summed up so as to have a fixed average number of counts per frame, while for the FP detector a number of frames of different acquisition times has been acquired and summed up so as to recover the same average number of counts reached with Medipix2.

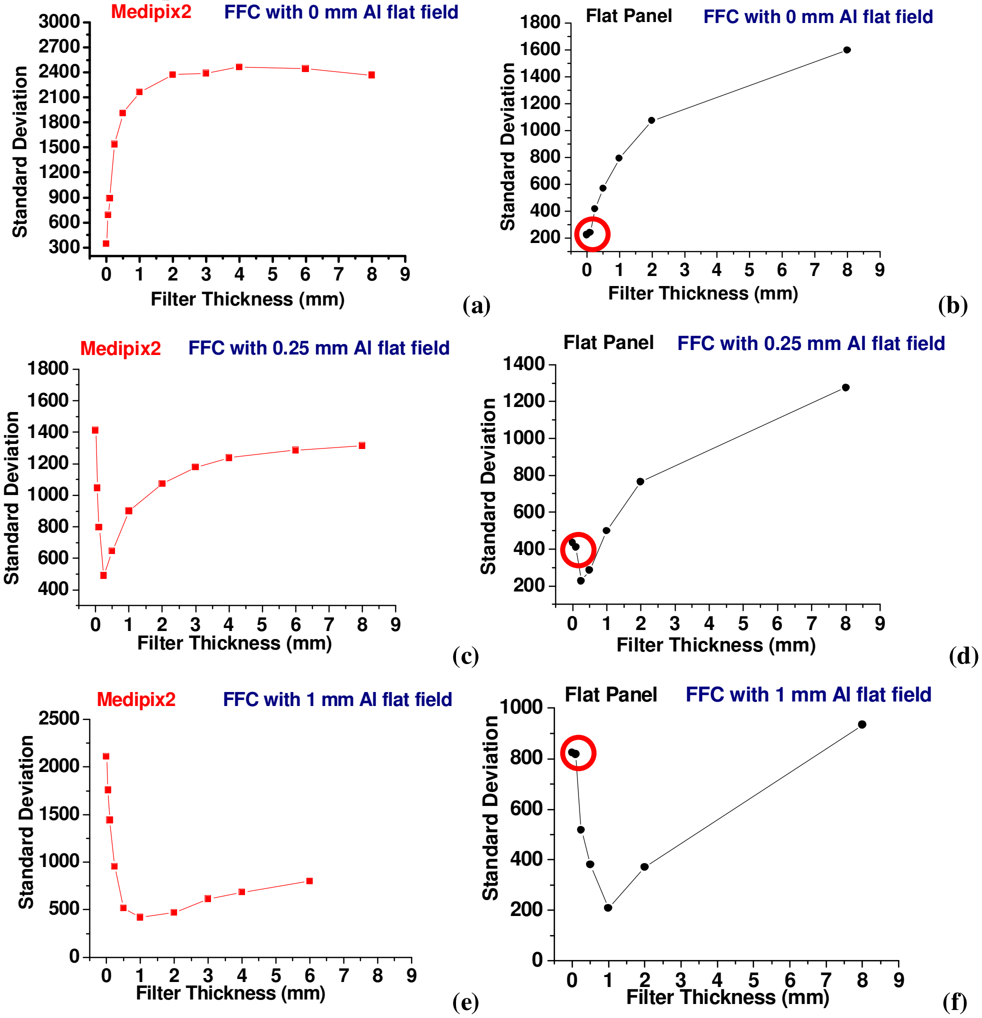

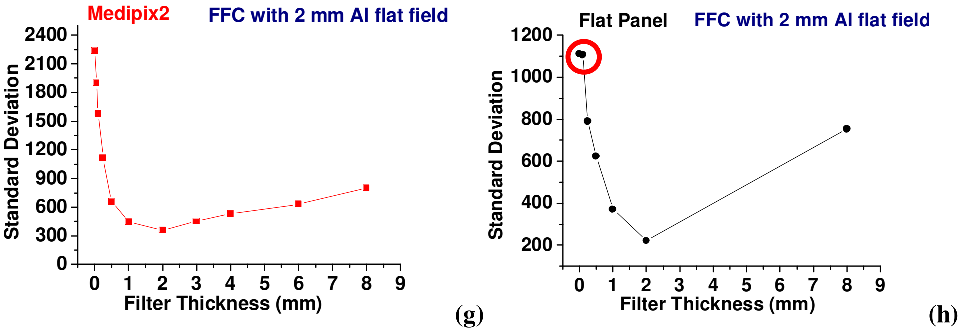

Fig. 3-28 Plots of the standard deviations of the average pixels value evaluated on flood irradiation images of aluminium filter with thicknesses in the range [0, 8] mm (data set D) when corrected with the FFC performed with different filter thicknesses (from data set C): (a) Medipix2 and (b) FP detector open beam flood irradiation, (c) Medipix2 and (d) FP detector, 0.25 mm thick Al filter flood irradiation, (e) Medipix2 and (f) FP detector, 1 mm Al thick filter flood irradiation, (g) Medipix2 and (h) FP detector, 2 mm thick Al filter flood irradiation. The circle marking the first two points in the plots relative to the FP detector points out that for this device the FFC correction performed with the open beam is almost the same as the correction with a 0.05 mm filter.

The minimum value of the average pixel values standard deviation is reached when a filter of thickness *t* is corrected with a flat field obtained from a flood irradiation of a filter of the same thickness *t*; this result could have been predicted because this correction well takes into account the beam hardening effect, related to the traversed thickness. This trend confirms the inadequacy of the FFC when an open beam irradiation is used to correct a sample of a thickness *t*. In fact, it does not take into account the change of the spectrum in traversing the sample that gives rise to a different pixel response (pixel efficiency is energy-dependent so it changes as the incoming spectrum is modified by the beam hardening effect).

From the plots it is possible to notice that for the FP detector the standard deviations in correspondence of the open beam (0 mm Al filter) and of the 0.05 mm thick filter have always the same values: this indicate that this device has not the capability to appreciate the change in attenuation coming from thin objects, or, in other words, the fluctuations in the pixel values are higher than the difference in attenuation (and thus in the recorded counts) due to the two thicknesses (0 mm and 0.05 mm). This means that it makes no difference to correct an image by means of the FFC made with either the open beam or the 0.05 mm thick filter. On the other hand, the standard deviation values of FP detector data always result to be lower than the Medipix2 ones. To explain this phenomenon it is worth observing two radiographies, acquired with the two detectors and corrected by means of the FFC.

In Fig. 3-29 the radiograms of the 0.25 mm thick filter, corrected with a flat field of the same filter, show the difference between the FP (Fig. 3-29 left) and Medipix2 (Fig. 3-29 right) detector. While the first is a uniform flat image, the latter exhibits a non-homogenous structure that can be interpreted as the texture of the surface roughness of the Al foil. In fact, the 0.25 mm thick filter has been realized overlapping five 0.05 mm thick filters, so that the texture of all the filters can be distinguished. This explanation proves, once again, the detection superiority of a single photon counting, provided with an energy discrimination threshold, to the charge integrating technology of an FP detector.

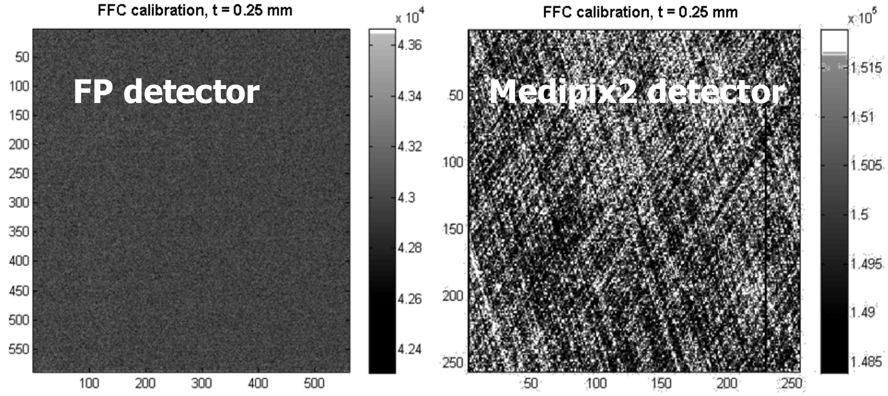

Fig. 3-29 On the left: a radiography of a 0.25 mm thick aluminium filter acquired with the FP: the image is uniform and flat thanks to the flat field correction (with a flat field of the same 0.25 mm thick Al filter); on the right: a radiography of the same 0.25 mm Al filter, acquired in the same conditions and corrected in the same way as the left image, but realized with Medipix2 SPC detector. It is possible to distinguish the texture of the five 0.05 mm thick filters overlapped to make the 0.25 mm thick filter.

The two plots showed in Fig. 3-30 report the average pixels value standard deviations for the FP (Fig. 3-30a) and for the Mdipix2 detector (Fig. 3-30b) when the experimental data set D is corrected with the STC and when the correction is performed by means of the FFC using a flat field of a filter with the same thickness used for the data (best correction condition for the FFC). In other words, the graphs are comparing the best FFC correction (the one that gives the standard deviation minima) with the STC correction. In both cases the STC performs better that the FFC, even if, for the FP detector the difference between the two correction methods appears much more evident.

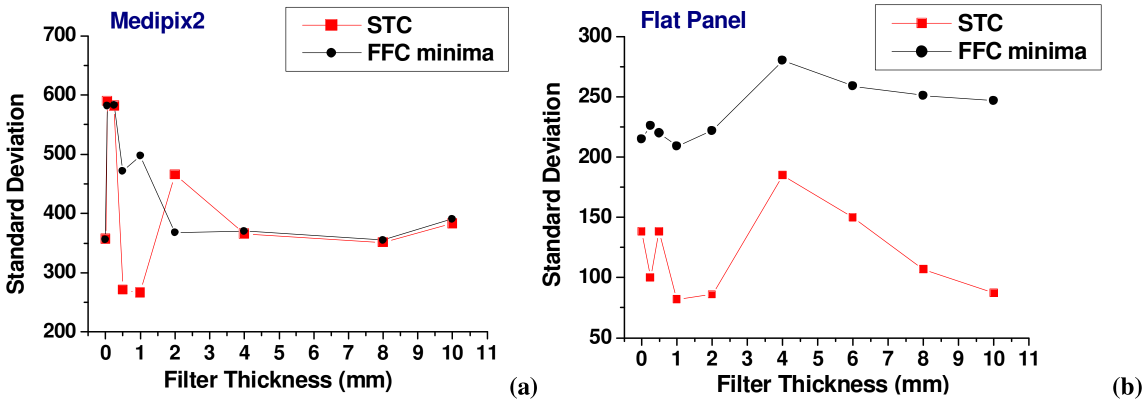

Fig. 3-30 Plots comparing the standard deviation values evaluated on FP detector (a) and Medipix2 detector (b) experimental data D corrected either with the STC or with the FFC performed using a flat field of the same thickness as the datum thickness. STC performs better than FFC for both the FP and the Medipix2 detector.

The standard deviations evaluated on STC data recorded with the charge integrating device are lower than the standard deviations at STC data recorded with the Medipix2. The STC corrected data acquired with the two detectors show the same phenomenon seen for the FFC corrected data: the FP detector returns an uniform image of the filter imaged, while the Medipix2 is able to detect the surface structure of the overlapped filters used to reach the desired thickness, giving rise to a non-homogenous image with a higher standard deviation. Images of two filters are presented in Fig. 3-31 (FP detector image on the left, Medipix2 detector image on the right).

A comparison that takes into account both the two detectors performances and the two corrections effectiveness has been done evaluating the contrast C for planar images of a PMMA cylinder provided with a 10 mm diameter size channel filled with a rod of polytetrafluoroethylene (PTFE) 6 mm in diameter. The PTFE simulates the same attenuation to X-rays as the trabecular bones has. A photo of the PMMA cylinder is shown in Fig. 3-32.

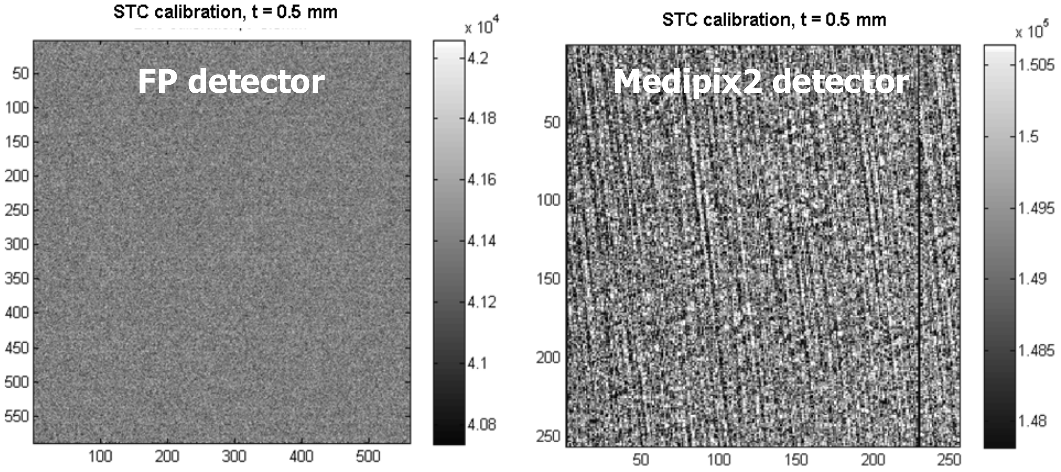

Fig. 3-31 On the left: a radiography of a 0.5 mm thick aluminium filter acquired with the FP: the image is uniform and flat thanks to the Signal-to-Counts Correction; on the right: a radiography of the same 0.5 mm Al filter, acquired in the same conditions and corrected in the same way as the left image, but obtained with Medipix2 SPC detector. It is possible to distinguish the surface texture of the ten filters 0.05 mm thick overlapped to make the 0.5 mm thick filter.

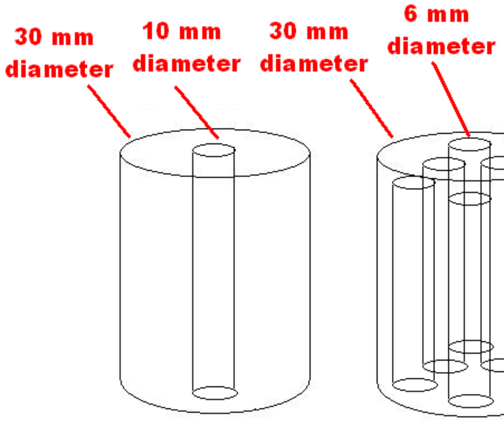

Fig. 3-32 A set of polymethylmethacrylate cylinders has been used for the 2-D and 3-D image quality tests. The dimension chosen - 30 mm in diameter – corresponds to the width of a common laboratory mouse and the material simulates the attenuation to X-rays of the water in the diagnostic energy rage (20 - 80) keV. Each cylinder is provided with either one (10 mm diameter size) or five (6 mm diameter size) empty channels along all its length, filled with different materials and substances simulating the attenuation to X-rays of a number of organs and tissues, from the softer ones to the more opaque ones.

The comparison has been carried by imaging the object with both the FP and the Medipix2 detector and correcting the two radiograms by means of either the FFC or the STC. The four images have been compared by evaluating the CNR between the PTFE rod and the external PMMA. The four radiographies are showed in Fig. 3-33, while Tab. 3-3 reports the results.

The images have been acquired for 0.5 seconds with a tube current of 0.91 mA and a tube voltage of 40 kVp. The image magnification factor is 1.07x. To evaluate the CNR two ROIs of 50 x 100 pixels have been chosen both in the PTFE area and in the PMMA area and the mean values have been averaged to get, respectively, μ_{PTFE} and μ_{PMMA} and their standard deviations.

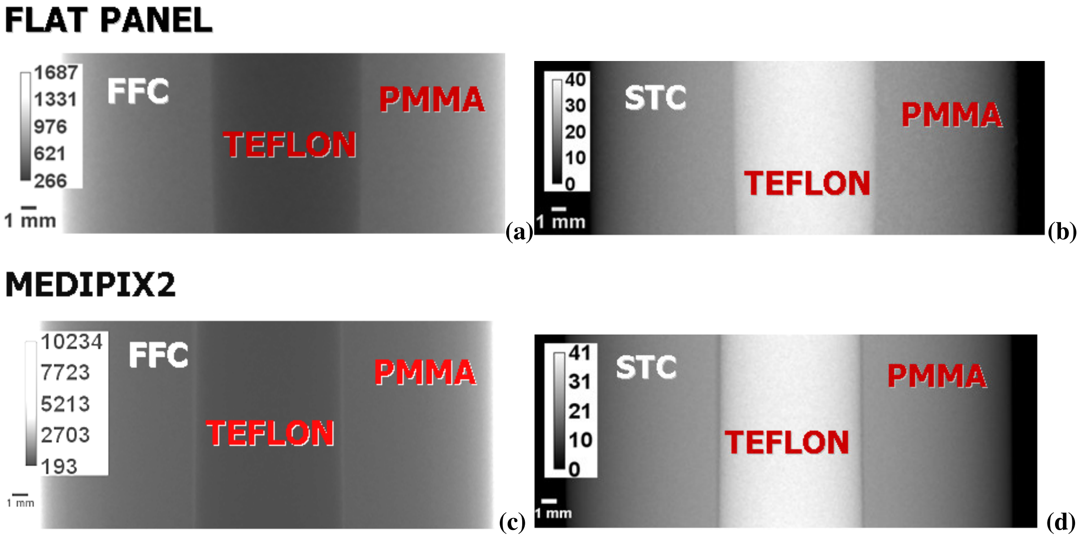

Fig. 3-33 Radiographies of a polymethylmethacrylate cylindrical phantom (60 mm diameter) containing a PTFE rod of 10 mm size in diameter in an internal channel. The four radiographies have been acquired with the FP detector (a and b) and with the Medipix2 detector (c and d) and then corrected by means of the two flat field corrections, the FFC (a and c) and the STC (b and d).

CNR	**FP**	**Medipix2**
FFC	6.3	6.7
STC	8.5	**11.9**

Tab. 3-3 Table of the CNR values estimated for the PTFE rod enclosed in a PMMA cylinder. The highest value of the CNR is achieved using Medipix2 SPC detector and by correcting the raw image with the STC algorithm. Also for the FP detector images the STC correction performs better than the FFC one.

A comparison between the two detectors has been made on biological samples, as well as on phantoms. The radiographies proposed below have been made with the *Hamamatsu* X-ray source provided with the 5 µm focal spot. In our experimental conditions, phase contrast effects have been observed. What we can compare here is the phase contrast visibility of the single photon counting and the FP detector. The comparison has been carried by evaluating the intensity jump across the interface between air and a detail of a biological sample body. Fig. 3-34 shows the *ex vivo* insect used for the study (a specie of beetle), while Fig. 3-35a and Fig. 3-35b show a detail of the sample acquired respectively with the FP and with Medipix2 detector in the same experimental conditions (tube voltage, geometry, pixel size) except the exposure which is of 20 mAs for the FP detector and of 50 mAs for the Medpix2 detector (0.3 µGy absorbed dose).

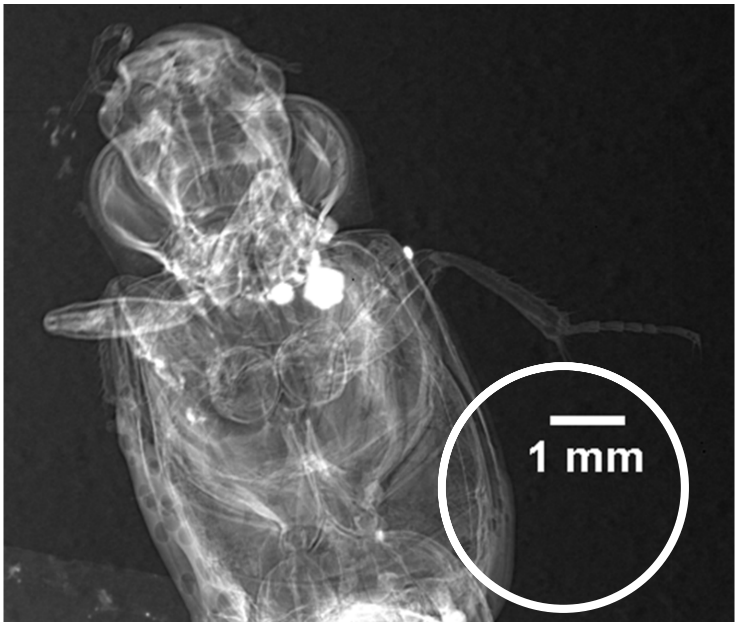

Fig. 3-34 Radiography of a beetle acquired with the FP detector (without the 1 mm thick Al top cover). $R_1 = 13.05$, $R_2 = 48.95$, $M = 4.75x$, $V = 40$ kVp, $I = 200$ µA, $t_{exp} = 100$ s (20 mAs). The calculated absorbed dose, obtained simulating the W spectrum [50], is of about 0.3 µGy.

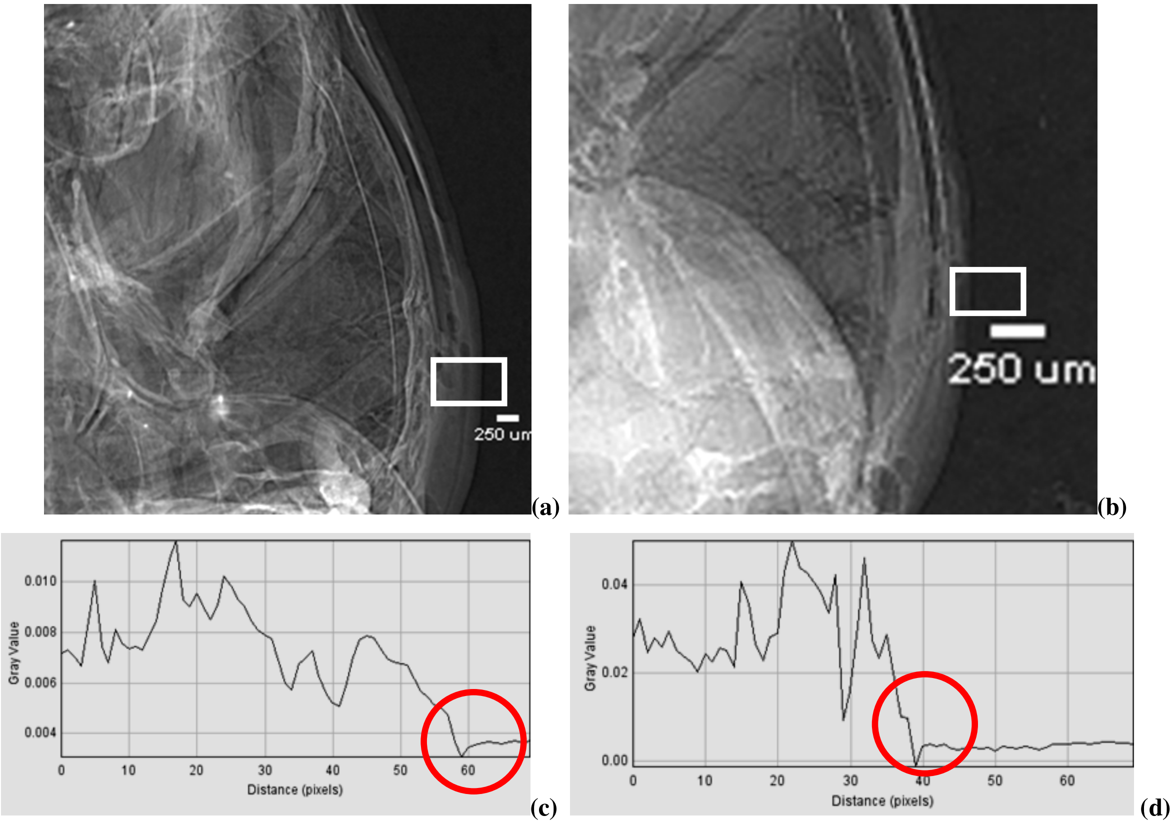

Fig. 3-35 Radiographic detail of an insect body acquired with the FP detector (a) and with the Medipix2 (b) in the same geometrical conditions ($R_1 = 13.05$, $R_2 = 48.95$, $M = 4.75x$), with a tube voltage of $V = 40$ kVp, but at different exposure levels: $I = 200$ µA, $t_{exp} = 100$ s for the FP detector and $I = 50$ µA, $t_{exp} = 100$ s for Medipix2. The rectangles illustrate the ROI to evaluate the plot profiles showed in (c) - for the FP detector – and in (d) – for Medipix2. The circles on the plots point out the jump due to the interference fringes, resulting from the phase shift. The jump for the FP detector is of $4.4 \cdot 10^{-4}$, while the jump recorded with Medipix2 is of $5.7 \cdot 10^{-3}$, that is one order of magnitude bigger.

The phase contrast effect has been evaluated in the indicated regions as the difference between the downward peak due to the dark fringe and the average pixels values in the air region. The values found result of $4.4 \cdot 10^{-4}$ for the FP detector and $5.7 \cdot 10^{-3}$ for Medipx2 detector, indicating a superior detection ability of the Medipix2 for the phase shift phenomenon.

3.5 3-D image quality comparison between Medipix2 SPC and the FP detector by means of two pixels equalization techniques

In comparing the two presented detectors we performed tomographic imaging with the Molybdenum anode X-ray source, 35 µm focal-spot size. Here we present some tests on 3-D imaging on phantoms. The CT scans have been done for a given object by acquiring the projections with both the FP detector and the Medipix2 and correcting them, before the reconstruction, either with the FFC or the STC. Finally, we get for each sample four CT slices on which the Contrast-to-Noise Ratio (CNR) has been evaluated.

The test objects are – as already explained in the note to Fig. 3-32 – a set of polymethylmethacrylate cylinders, 30 mm in diameter size. Each cylinder is provided, along its whole length, with either one single channel (10 mm diameter) or five empty channels (6 mm diameter each), filled with different materials and substances simulating the attenuation to X-rays of a gamut of organs and tissues, from the softer ones to the more radiopaque ones.

At a given X-ray tube voltage energy one can associate to each material a so called "CT number" that is the effective linear attenuation coefficient of that substance related to that of the water, at the same energy. In this way, it is possible to create a scale of units – the Hounsfield units – in a range starting from the value -1000, corresponding to the air, up to ~ 4000 for bones and metal inserts. The Hounsfield units, or CT numbers, are defined as:

$$\mathbf{CT_{\#}} = \frac{\bar{\mu} - \mu_{water}}{\mu_{water}} \cdot 1000$$

where $\bar{\mu}$ and μ_{water} are defined, respectively, as the effective linear attenuation coefficient for a given material and for water. Then, the CT number of water is zero.

In Tab. 3-4 a number of organs' and tissues' substitute materials and their constituents and composition are listed [69].

All the CT scans, realized with the FP, have been done with the same parameters: 720 projections acquired on over 360°, with an angular step of 0.5° (2 frames/s), for an exposure time per view $t_{acq} = 0.5$ s, with a tube voltage V = 40 kVp ($\bar{E}_{simul} = 15.75$ keV) and a tube current I = 0.91 mA. The source-to-sample distance was $R_1 = 33.4$ cm, while the tube-to-detector distance was $(R_1 + R_2) = 35.8$ cm, for a magnification factor of M = 1.072x. All the projections have a size of 768 x 256 pixels, while the tomographic slices have a voxel size of 47 μm x 47 μm x 47 μm.

All the tomographies realized with the Medipix2 detector were realized at a tube voltage V = 40 kVp ($\bar{E}_{simul} = 15.75$ keV) and a tube current I = 0.91 mA; the tube-to-sample distance was $R_1 = 32.4$ cm and the tube-to-detector distance was $(R_1 + R_2) = 35.2$ cm, for a magnification factor of M = 1.086x. All the tomographic slices have a voxel size of 51 μm x 51 μm x 51 μm. The number and the acquisition time t_{acq} of the projections acquired on 360° is slightly different from one tomography to another and so also the angular step is not always the same. These parameters will be specified for every measurement presented below.

The complete series of tomographies, from FP detector acquisitions and for Medipix2 acquisition have been reconstructed by the commercial software "Cobra" [70] which uses the Felkamp FBK algorithm [71]. FFC data have bean reconstructed using the fan beam geometry while STC data have been reconstructed using the parallel-beam geometry as explained in Chap.2.

For the first test we chose a number of different materials approximately in the CT numbers range of [550 - 1800]: olive oil, water, a solution 1 mg/ml of iodixanol[5] and PTFE, filling four of the five channels in a PMMA phantom and leaving the fifth one empty (air). For all these materials we evaluated the CNR compared to the surrounding PMMA. The number of projections acquired on 360° for Medipix2 is 683 for an angular step of 0.53° and an acquisition time of 0.8 s per projection. Because of the small Medipix2 sensitive area, to image the entire PMMA cylinder the detector has been translated laterally by 11 mm two times for each angular step and, successively, the three images have been stacked together to recover a projection of 658 pixel x 256 pixels.

It is worth remembering here that the pixel efficiency corrections have been performed on each planar projection before the tomographic reconstruction.

Tab. 3-5 reports the CT numbers, from the reconstruction procedure, for the four materials, while Fig. 3-36 shows the plots of the CNR *versus* CT numbers for the four materials, evaluated, respectively, on the images recorded (a) with the FP detector and corrected by means of either the FFC or the STC correction, and (b) with the Medipix2 detector and corrected by means of either the FFC or the STC correction. From these figures we conclude that the STC algorithm provides a higher CNR than the FFC and that the results are more evident for the highest absolute CT numbers. Moreover, the Medipix2 SPC detector gives higher CNR values compared to the charge integrating device, demonstrating, also in 3-D imaging the superiority, in terms of image quality, of the single photon counting technology.

---

[5] The iodixanol is a commonly used contrast medium for CT because of the high atomic number of the iodine. We used the commercial solution *Visipaque*, *GE Healthcare*, 320 mg I/ml, active principle: iodixanol.

Substitute or tissue	Constituents (w/o) or formula synonyms, tradenames	Elemental composition (w/o)
Adipose		H(12.00); C(64.00); N(0.8); O(22.90); Na(0.05); Mg(0.002); P(0.016); S(0.07); Cl(0.12); K(0.03); Ca(0.002); Fe(0.002)
AP6	Epoxy CB4(79.00); phenolic microspheres(4.96); polyethylene(12.00); teflon(4.04)	H(8.36); C(69.14); N(2.36); O(16.94); F(3.07); Cl(0.14)
Ethoxyethanol	$C_4H_{10}O_2$ (Ethylene glycol monoethyl ether)	H(11.18); C(53.31); O(35.51)
Polyethylene	$(C_2H_4)_n$	H(14.37); C(85.63)
Polystyrene	$(C_8H_8)_n$	H(7.74); C(92.26)
Cortical bone		H(3.39); C(15.50); N(3.97); O(44.10); Na(0.06); Mg(0.21 P(10.20); S(0.31); Ca(22.20)
Aluminium	Al(100)	Al(100)
Cameron wax	Paraffin wax(58); calcium carbonate(42)	H(8.62); C(54.42); O(20.14); Ca(16.82)
Facey liquid	Water(45); calcium chloride(55)	H(5.04); O(39.96); Cl(35.14); Ca(19.86)
Magnesium	Mg(100)	Mg(100)
Plaster of Paris	$CaSO_4 \cdot 2H_2O$ (natural gypsum)	H(2.34); O(55.76); S(18.62); Ca(23.28)
Poll resin	Epoxy AYHZ18(22.66); calcium hydrogen orthophosphate(77.34)	H(4.09); C(16.38); N(0.51); O(47.09); P(13.92); Ca(18.01
P.V.C.	$(C_2H_3Cl)_n$[poly(vinyl chloride)]	H(4.84); C(38.44); Cl(56.73)
Pyrex	Glass-Corning No. 7740	B(4.01); O(53.96); Na(2.82); Al(1.16); Si(37.72); K(0.33)
SB3	Epoxy CB2(32.51); calcium carbonate(67.49)	H(3.10); C(31.26); N(0.99); O(37.57); Cl(0.05); Ca(27.03
Shonka plastic (B100)	Nylon(21.60); polyethylene(30.00); carbon(14.00); calcium fluoride(34.40)	H(6.51); C(54.24); N(2.26); O(2.59); F(16.74); Ca(17.66)
Spiers' liquid	Water(50); calcium bromide(50)	H(5.60); O(44.41); Ca(10.03); Br(39.98)
Sulphur	S(100)	S(100)
Teflon	$(C_2F_4)_n$ (p.t.f.e.)	C(24.02); F(75.98)
White's powder	Polyethylene(32.40); calcium sulphate(67.60)	H(4.66); C(27.74); O(31.78); S(15.92); Ca(19.90)
Witt liquid	Water(38.46); dipotassium hydrogen orthophosphate(61.54)	H(4.70); O(56.80); P(10.90); K(27.90)
Fat		H(12.21); C(76.08); O(11.71)
Alderson fat	Polyethylene/wax/antimony trioxide	H(14.37); C(85.61); O(0.004); Sb(0.02)
FT1	TPX(81.42); lithium carbonate(18.58)	H(11.70); Li(3.48); C(72.74); O(12.07)
FT2	EVA-28(100)	H(12.31); C(77.28); O(10.41)
Glycerol trioleate	$C_{57}H_{104}O_6$ (triolein)	H(11.84); C(77.32); O(10.84)
Lithium palmitate	$LiC_{16}H_{31}O_2$	H(11.91); Li(2.64); C(73.25); O(12.20)
Lung		H(9.90); C(10.00); N(2.80); O(74.00); Na(0.18); Mg(0.007); Al(0.001); P(0.08); S(0.22); Cl(0.26); K(0.19); Ca(0.01); Fe(0.04); Zn(0.001)
Alderson lung	Epoxy system/phenolic microspheres/antimony trioxide	H(5.74); C(73.94); N(2.01); O(18.14); Sb(0.16)
Gelatin	Protein	H(7.00); C(52.00); N(16.0); O(23.00)
LN1	Polyurethane (PU1)(85.73); aluminium oxide(14.27)	H(6.00); C(51.44); N(4.29); O(30.72); Al(7.55)
Rogers adiprene	Adiprene(81.97); Moca(15.98); silicone(1.64); adipic acid(0.41)	H(13.95); C(40.89); N(8.79); O(30.79); Si(1.14); Cl(4.44)
Stacey latex	Latex/boron carbide/sulphur/zinc oxide/other fillers	H(10.10); B(8.00); C(79.20); O(0.12); S(1.91); Zn(0.67)
Muscle		H(10.20); C(12.30); N(3.50); O(72.893); Na(0.08); Mg(0.02); P(0.2); S(0.5); K(0.3); Ca(0.007)
Akagi liquid	Water(68.05); sucrose(22.41); urea(8.59); cresol(0.95)	H(9.71); C(11.89); N(4.00); O(74.39)
Alderson muscle (1)	Isocyanate rubber/phenolic microspheres/antimony trioxide	H(8.83); C(64.45); N(4.05); O(20.35); Cl(2.24); Sb(0.08)
Alderson muscle (2)	Isocyanate rubber/phenolic microspheres/antimony trioxide	H(8.87); C(66.81); N(3.10); O(21.13); Sb(0.08)
Aluminium butoxide	$Al(C_4H_9O)_3$	H(11.05); C(58.51); O(19.49); Al(10.95)

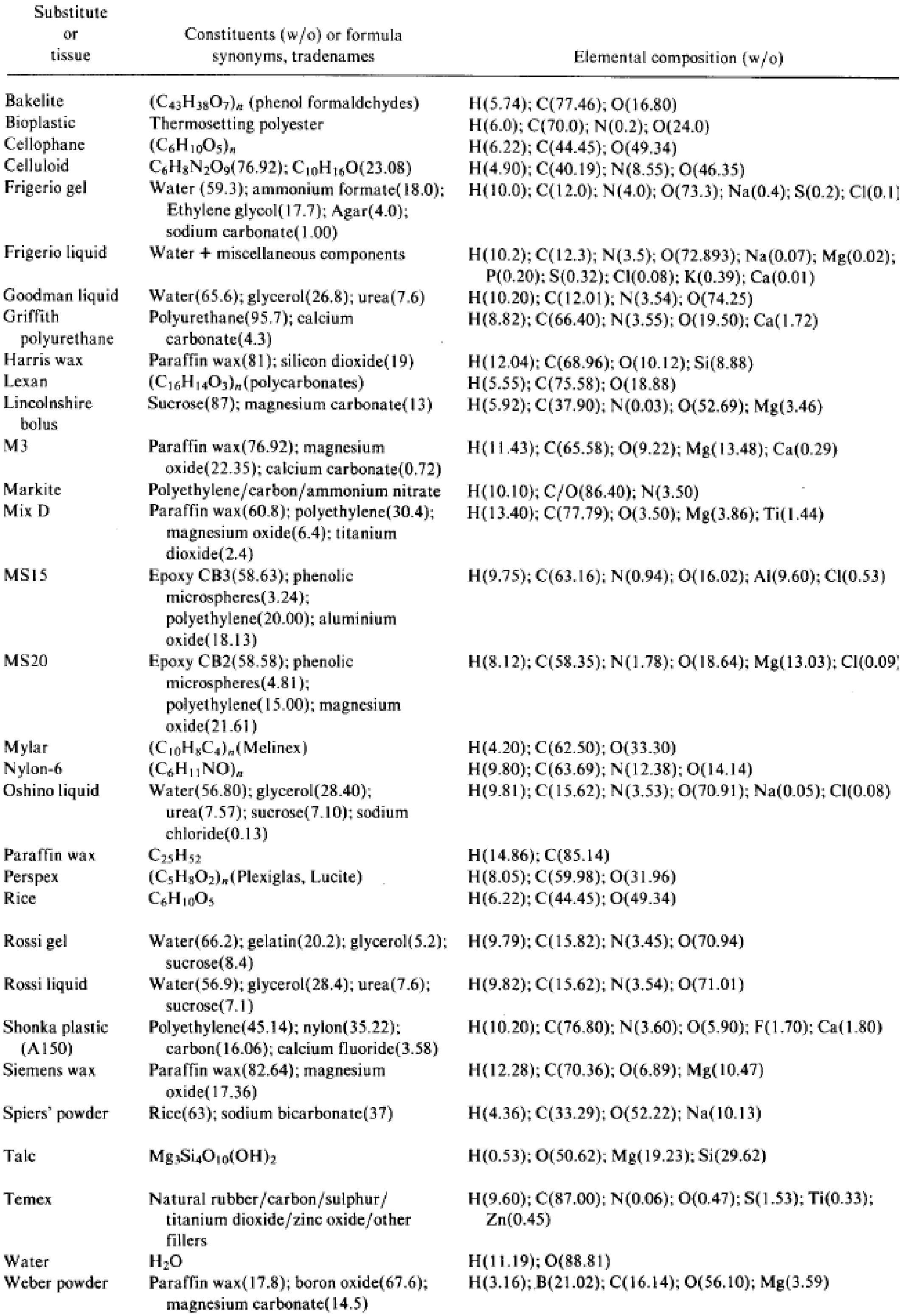

Substitute or tissue	Constituents (w/o) or formula synonyms, tradenames	Elemental composition (w/o)
Bakelite	$(C_{43}H_{38}O_7)_n$ (phenol formaldehydes)	H(5.74); C(77.46); O(16.80)
Bioplastic	Thermosetting polyester	H(6.0); C(70.0); N(0.2); O(24.0)
Cellophane	$(C_6H_{10}O_5)_n$	H(6.22); C(44.45); O(49.34)
Celluloid	$C_6H_8N_2O_9$(76.92); $C_{10}H_{16}O$(23.08)	H(4.90); C(40.19); N(8.55); O(46.35)
Frigerio gel	Water (59.3); ammonium formate(18.0); Ethylene glycol(17.7); Agar(4.0); sodium carbonate(1.00)	H(10.0); C(12.0); N(4.0); O(73.3); Na(0.4); S(0.2); Cl(0.1
Frigerio liquid	Water + miscellaneous components	H(10.2); C(12.3); N(3.5); O(72.893); Na(0.07); Mg(0.02); P(0.20); S(0.32); Cl(0.08); K(0.39); Ca(0.01)
Goodman liquid	Water(65.6); glycerol(26.8); urea(7.6)	H(10.20); C(12.01); N(3.54); O(74.25)
Griffith polyurethane	Polyurethane(95.7); calcium carbonate(4.3)	H(8.82); C(66.40); N(3.55); O(19.50); Ca(1.72)
Harris wax	Paraffin wax(81); silicon dioxide(19)	H(12.04); C(68.96); O(10.12); Si(8.88)
Lexan	$(C_{16}H_{14}O_3)_n$(polycarbonates)	H(5.55); C(75.58); O(18.88)
Lincolnshire bolus	Sucrose(87); magnesium carbonate(13)	H(5.92); C(37.90); N(0.03); O(52.69); Mg(3.46)
M3	Paraffin wax(76.92); magnesium oxide(22.35); calcium carbonate(0.72)	H(11.43); C(65.58); O(9.22); Mg(13.48); Ca(0.29)
Markite	Polyethylene/carbon/ammonium nitrate	H(10.10); C/O(86.40); N(3.50)
Mix D	Paraffin wax(60.8); polyethylene(30.4); magnesium oxide(6.4); titanium dioxide(2.4)	H(13.40); C(77.79); O(3.50); Mg(3.86); Ti(1.44)
MS15	Epoxy CB3(58.63); phenolic microspheres(3.24); polyethylene(20.00); aluminium oxide(18.13)	H(9.75); C(63.16); N(0.94); O(16.02); Al(9.60); Cl(0.53)
MS20	Epoxy CB2(58.58); phenolic microspheres(4.81); polyethylene(15.00); magnesium oxide(21.61)	H(8.12); C(58.35); N(1.78); O(18.64); Mg(13.03); Cl(0.09
Mylar	$(C_{10}H_8C_4)_n$(Melinex)	H(4.20); C(62.50); O(33.30)
Nylon-6	$(C_6H_{11}NO)_n$	H(9.80); C(63.69); N(12.38); O(14.14)
Oshino liquid	Water(56.80); glycerol(28.40); urea(7.57); sucrose(7.10); sodium chloride(0.13)	H(9.81); C(15.62); N(3.53); O(70.91); Na(0.05); Cl(0.08)
Paraffin wax	$C_{25}H_{52}$	H(14.86); C(85.14)
Perspex	$(C_5H_8O_2)_n$(Plexiglas, Lucite)	H(8.05); C(59.98); O(31.96)
Rice	$C_6H_{10}O_5$	H(6.22); C(44.45); O(49.34)
Rossi gel	Water(66.2); gelatin(20.2); glycerol(5.2); sucrose(8.4)	H(9.79); C(15.82); N(3.45); O(70.94)
Rossi liquid	Water(56.9); glycerol(28.4); urea(7.6); sucrose(7.1)	H(9.82); C(15.62); N(3.54); O(71.01)
Shonka plastic (A150)	Polyethylene(45.14); nylon(35.22); carbon(16.06); calcium fluoride(3.58)	H(10.20); C(76.80); N(3.60); O(5.90); F(1.70); Ca(1.80)
Siemens wax	Paraffin wax(82.64); magnesium oxide(17.36)	H(12.28); C(70.36); O(6.89); Mg(10.47)
Spiers' powder	Rice(63); sodium bicarbonate(37)	H(4.36); C(33.29); O(52.22); Na(10.13)
Talc	$Mg_3Si_4O_{10}(OH)_2$	H(0.53); O(50.62); Mg(19.23); Si(29.62)
Temex	Natural rubber/carbon/sulphur/titanium dioxide/zinc oxide/other fillers	H(9.60); C(87.00); N(0.06); O(0.47); S(1.53); Ti(0.33); Zn(0.45)
Water	H_2O	H(11.19); O(88.81)
Weber powder	Paraffin wax(17.8); boron oxide(67.6); magnesium carbonate(14.5)	H(3.16); B(21.02); C(16.14); O(56.10); Mg(3.59)

Tab. 3-4 Constituents and composition of biological tissues' substitutes. [69]

$\text{CT}_{\text{numbers}}$	Flat Panel		Medipix2	
	FFC	STC	FFC	STC
OIL	-545 ± 39	-346 ± 17	-446 ± 5	-468 ± 5
WATER	6 ± 30	22 ± 16	4 ± 16	1 ± 10
IODIXANOL (1 mg/ml)	81 ± 28	67 ± 18	24 ± 13	25 ± 15
PTFE (TEFLON)	1811 ± 54	1212 ± 24	488 ± 19	1135 ± 15

Tab. 3-5 CT numbers derived from the tomographic reconstruction of the cylindrical phantom for four substances simulating the attenuation of different organs and tissues present in a body. Tube current I = 0.91 mA, V = 40 kVp, Mo anode.

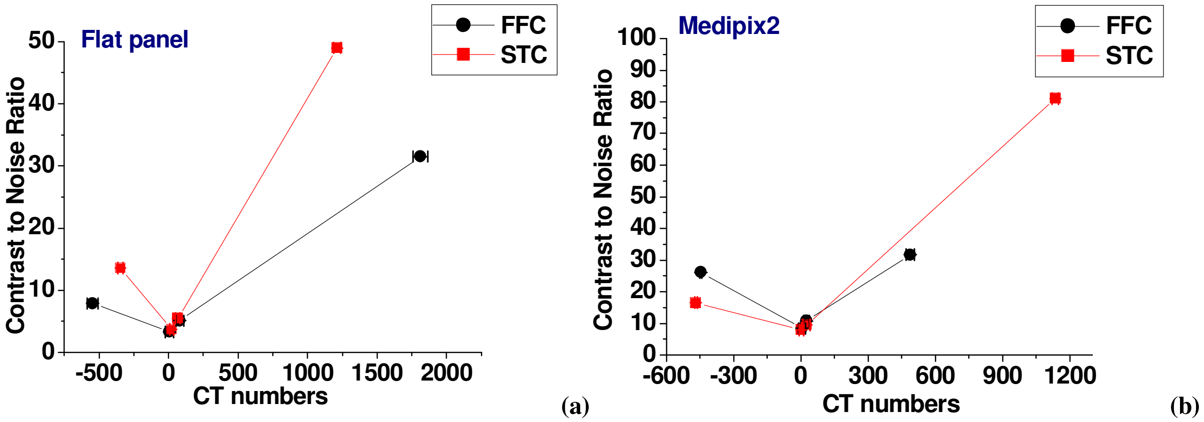

Fig. 3-36 Values of the CNR for different materials - oil, water, 1 mg/ml of iodixanol solution, PTFE (listed in increasing order of CT number) – compared to the PMMA. The four substances fill channels hollowed in a PMMA cylinder, 30 mm in diameter. Tube current I = 0.91 mA, V = 40 kVp.

Similarly, other two tests have been done by filling the five channels of the PMMA cylinder with different concentrations of the iodixanol solution with increasing CT numbers. The first phantom was filled with the following iodixanol concentrations: 1 mg/ml, 2 mg/ml, 5 mg/ml, 8 mg/ml and water, while the second phantom was filled with: 8 mg/ml, 15 mg/ml, 25 mg/ml, 30 mg/ml and water.

Fig. 3-37 shows the four tomographic slices, average of 233 slices, obtained, respectively, with the FP detector and the FFC correction (a), the FP detector and the STC correction (b), the Medipix2 and the FFC correction (c) and the Medipix2 and the STC correction, with the first set of iodixanol concentrations [1 - 8] mg/ml.

The number of projections acquired over 360° for Medipix2 is 685 for an angular step of 0.52° and an acquisition time of 0.8 s.

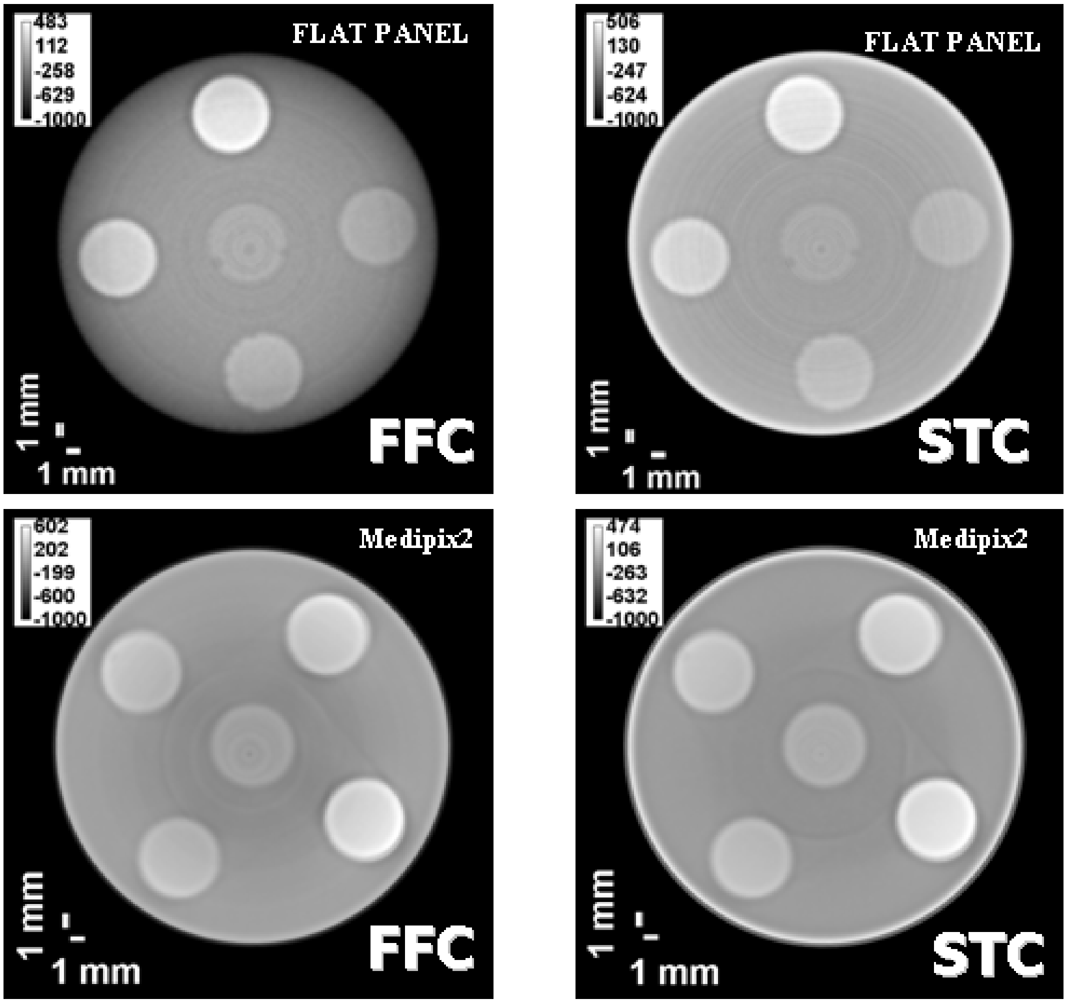

Fig. 3-37 Average image of 233 tomographic slices of a cylindrical phantom (30 mm in diameter) provided with five channels (6 mm in diameter) filled with water and with a solution of iodixanol at different concentrations: 1 mg/ml, 2 mg/ml, 5 mg/ml and 8 mg/ml. The voxel size is 47 µm x 47 µm x 47 µm for the FP detector recorded slices and 51 µm x 51 µm x 51 µm for the Medipix2 images. The top images have been acquired with the FP detector and have been corrected by means of either the FFC (left image) or the STC (right image). Analogously, the bottom images have been acquired with the Meipix2 detector and have been corrected by means of either the FFC (left image) or the STC (right image) algorithm, respectively.

The CNR evaluation results are in Fig. 3-38 (iodixanol concentration range [1 - 8] mg/ml) and in Fig. 3-39 (iodixanol concentrations [8 - 30] mg/ml): the plots of the CNR values versus the iodixanol concentration for the two phantoms are relative to the FP detector (Fig. 3-38a and Fig. 3-39a) and to the Medipix2 (Fig. 3-38b and Fig. 3-39b) detector.

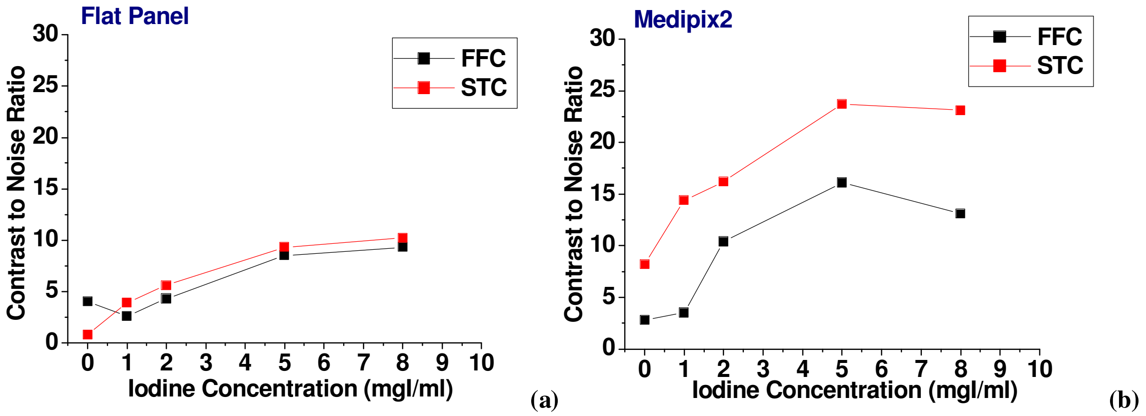

Fig. 3-38 Values of the CNR for different concentrations of a iodixanol solution – 1 mg/ml, 2 mg/ml, 5 mg/ml, 8 mg/ml and water - compared to the PMMA. The five substances fill 6 mm diameter channels hollowed in a PMMA cylinder, 30 mm in diameter. The CNR values have been evaluated for FFC and STC corrected data acquired with the FP (a) and the Medipix2 (b) detector.

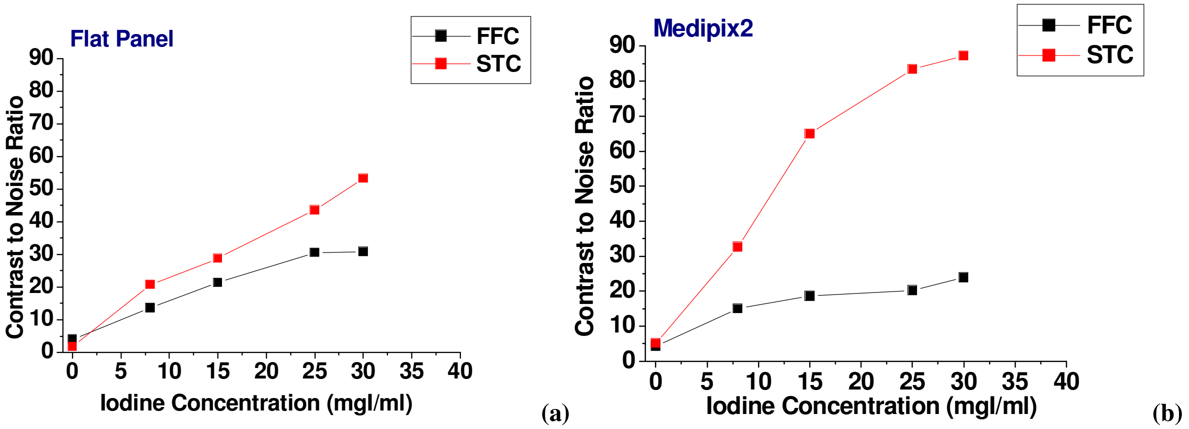

Fig. 3-39 Values of the CNR for different concentrations of a iodixanol solution – 8 mg/ml, 15 mg/ml, 25 mg/ml, 30 mg/ml and water - compared to the PMMA. The five substances fill 6 mm diameter channels hollowed in a PMMA cylinder, 30 mm in diameter. The CNR values have been evaluated for FFC and STC corrected data acquired with the FP (a) and the Medipix2 (b) detector.

From these figures we deduced that the STC algorithm provides a higher visibility than the FFC and the results are more evident for the highest CT number values (with exception of Fig. 3-38a in which seems there is any increasing discrepancy at increasing CT number values). Moreover, the Medipix2 SPC detector gives, generally, CNR values higher compared to the charge integrator device (with exception of Fig. 3-39), confirming, also in 3-D imaging, the superiority, in terms of image quality, of the single photon counting technology.

Two more examples of 3-D imaging on phantoms are here presented to show the effect of beam hardening on the images taken with the two detectors and by the two equalization corrections. The hardening of the spectrum traversing the sample results in the so called “cupping effect”, that causes the lowering of the CT numbers in the centre of the reconstructed sample image compared to the periphery.

The first example demonstrates the quality of the already discussed computer simulation in ref. [4]. In the mentioned article, CT images acquired with photon counting, charge integrating and energy weighting detectors were simulated to perform a quantitative comparison for beam hardening artefacts. It was found that the magnitude of cupping effect was lower by 1% for charge integrating and higher by 6.1% for energy weighting acquisition as compared to photon counting. Here we show the experimental validation of this simulation by means of the FP detector and of Medipix2 SPC: two tomographies of a homogenous cylindrical phantom made of PMMA were realized using either of the two detectors and on the averages of 229 CT slices it has been evaluated the cupping artefact from the line profile values.

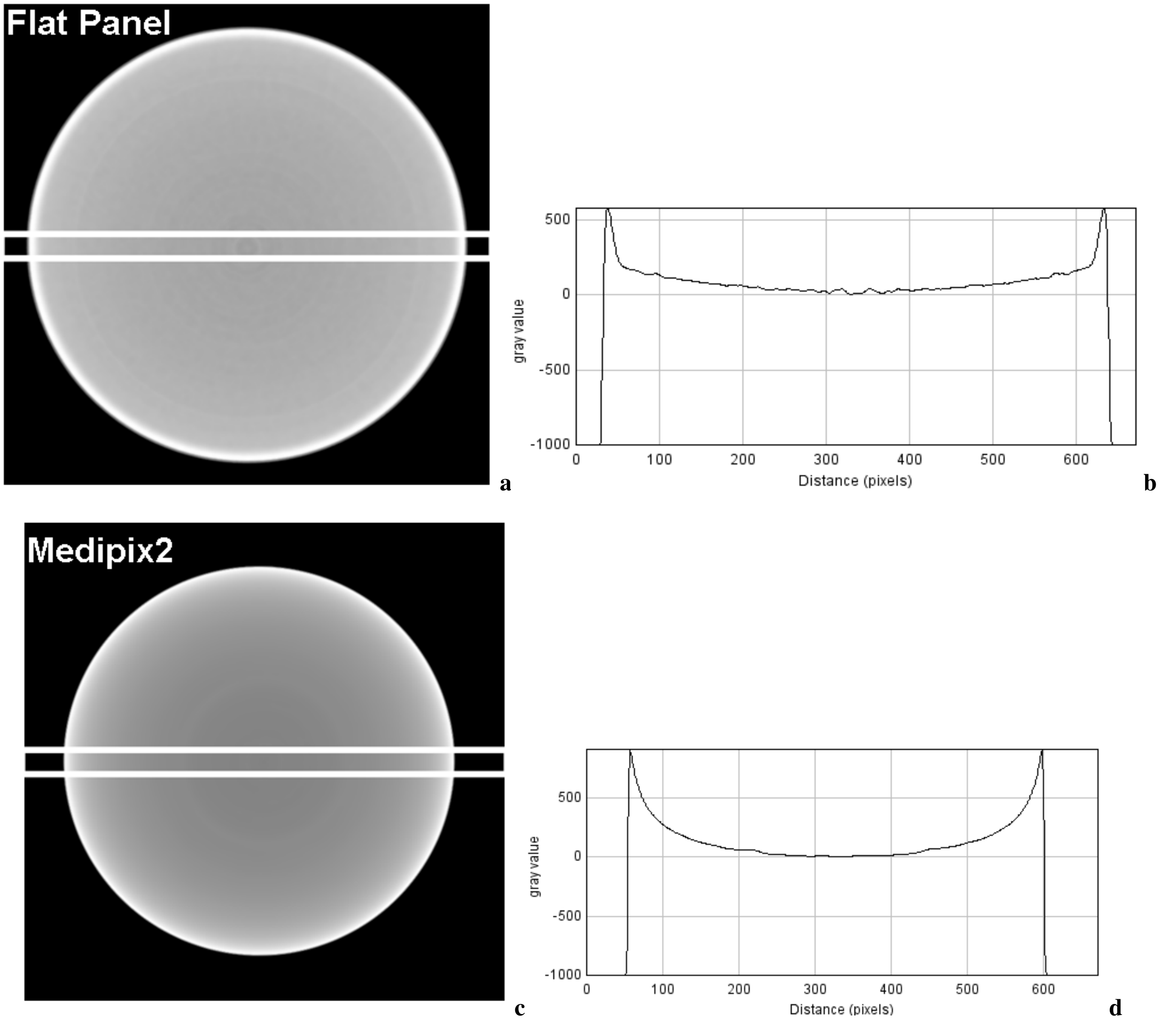

Fig. 3-40 Average images of 229 tomographic slices of a homogenous cylindrical phantom (30 mm in diameter) made of PMMA. The planar projections used for the tomographic reconstruction have been acquired with the FP (a) and with the Medipix2 SPC detector (b) detector and then corrected by means of the FFC. The voxel sizes are 50 µm x 50 µm x 50 µm (a) and 55 µm x 55 µm x 55 µm (b). In (c) and (d) there are shown the plot profiles relative to the rectangular selection depicted across the slices: the Medipix2 shows a cupping effect 1.9% higher compared to the charge integrating detector. Tube voltage was 40 kVp and tube current was 0.91 mA. Each projection has been acquired for 0.5 seconds in the case of the FP detector and for 0.8 s for the Medipix2.

The number of projections acquired on 360° for Medipix2 is of 685 for an angular step of 0.52° and an acquisition time of 0.8 s. The projection image size were of 652 pixel x 256 pixels, while the tomographic slices were reconstructed with 672 x 672 x 672 voxels of 55 µm. Fig. 3-40b and Fig. 3-40d show the line profiles relative to the rectangular selection depicted across the slices for the two detectors. The Medipix2 detector results in 1.9% higher cupping artefact compared to the charge integrating detector. This has been explained reflecting on the fact that, differently from the charge integrating, the SPC detector provides an accurate representation of the beam hardening effect due to its flat energy weighting.

The second example shows the ability of the STC correction in removing the cupping artefact. Fig. 3-41 shows two averages of 256 tomographic slices of a PMMA phantom, 30 mm in diameter, with a polyethylene rod (10 mm in diameter) inserted in an internal channel [72]. The slices are relative to a 3-D tomographic reconstruction from a set of projections acquired with Medipix2 and corrected with the FFC (a) and with the STC (b).

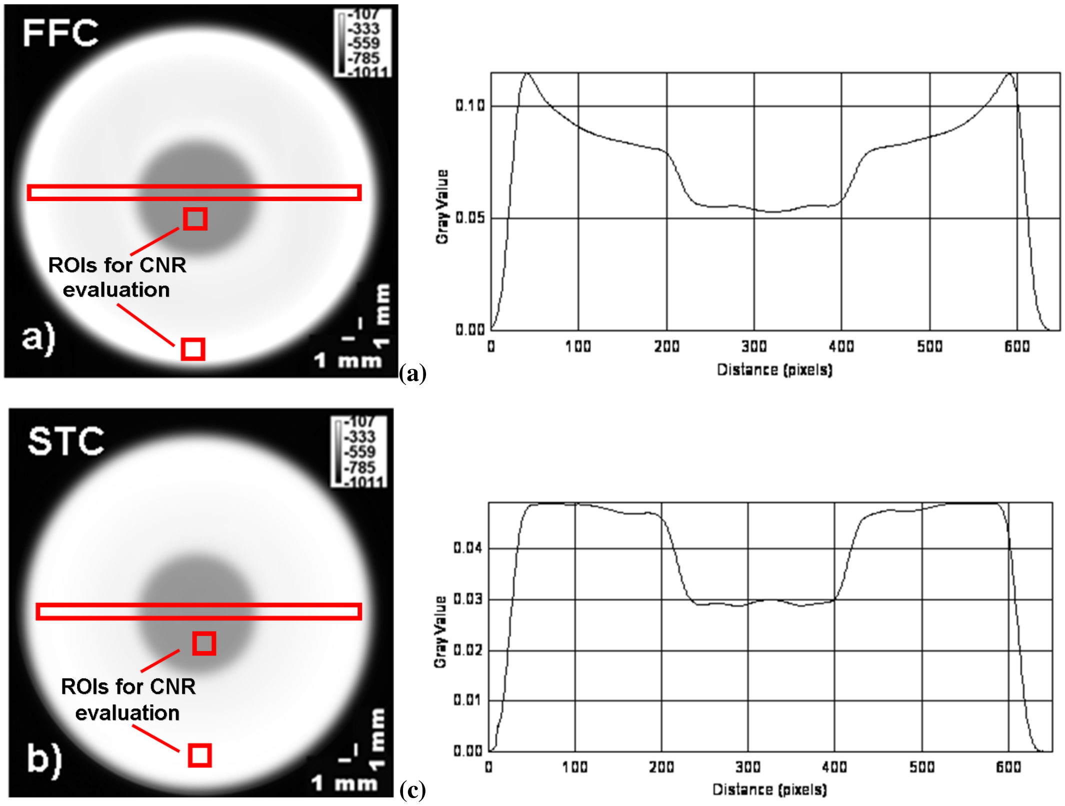

(a) (b)

(c) (d)

Fig. 3-41 Average images of 256 tomographic slices of a cylindrical phantom (30 mm in diameter) provided with a channel (10 mm in diameter) filled with a polyethylene rod. The planar projections used for the tomographic reconstruction have been acquired with the Medipix2 SPC detector and then corrected with the two algorithms: the FFC (a) and the STC (c). The voxel size is 50 µm x 50 µm x 50 µm. (b) and (d) show the line profiles relative to the rectangular selection depicted across the slices: the STC provides for the complete removal of the cupping effect (4.3 %), differently from the FFC (29 %) that requires a further image correction for the beam hardening. Also the contrast has been evaluated, using the ROIs depicted in the images, giving the values of 64 for the FFC and 117 for the STC. The tube voltage was 40 kVp and the tube current was 0.91 mA. Each projection has been acquired for 0.5 seconds. [72]

The voxel size is 50 µm x 50 µm x 50 µm. Fig. 3-41b and Fig. 3-41d show the line profiles relative to the rectangular selection depicted across the slices: the STC provides an almost complete removal of the cupping effect that results to be only 4.3 %, differently from the FFC resulting in a cupping effect level of 29 %. Thus, the FFC requires a further image correction for the beam hardening artefact. Also the contrast C has been evaluated, using the ROIs depicted in the images, giving the values C = 64 for the FFC and C = 117 for the STC. The reconstruction voxel has a size of 50 µm x 50 µm x 50 µm.

As for the 2-D imaging, a comparison between the two detectors has been done on biological samples. We have imaged *post mortem* the head of a mouse using both devices and correcting the data with both corrections. The mouse has been put into a PMMA cylinder with a diameter of 30 mm.

The tomographic reconstruction realized with the FP projections have 416 x 416 x 128 voxels of 100 µm x 100 µm x 100 µm isotropic resolution; the air dose at the sample position for the 720 projections is 1.05 Gy. The reconstruction of the Medipix2 projections (angular step 0.53) has been done with 416 x 416 x 128 voxels of size 110 µm x 110 µm x 110 µm; the air dose for the 682 projections is of 1.50 Gy. Fig. 3-42 and Fig. 3-43 show projections of the mouse head at 0°, 45°, 65° and 85° acquired with the FP detector, on which the FFC and the STC algorithm was respectively applied. Fig. 3-44 and Fig. 3-45 show four projections acquired with the Medipix2 detector, on which the FFC and the STC algorithm was respectively applied, chosen so to have a correspondence of the mouse head position compared to figures Fig. 3-42 and Fig. 3-43.

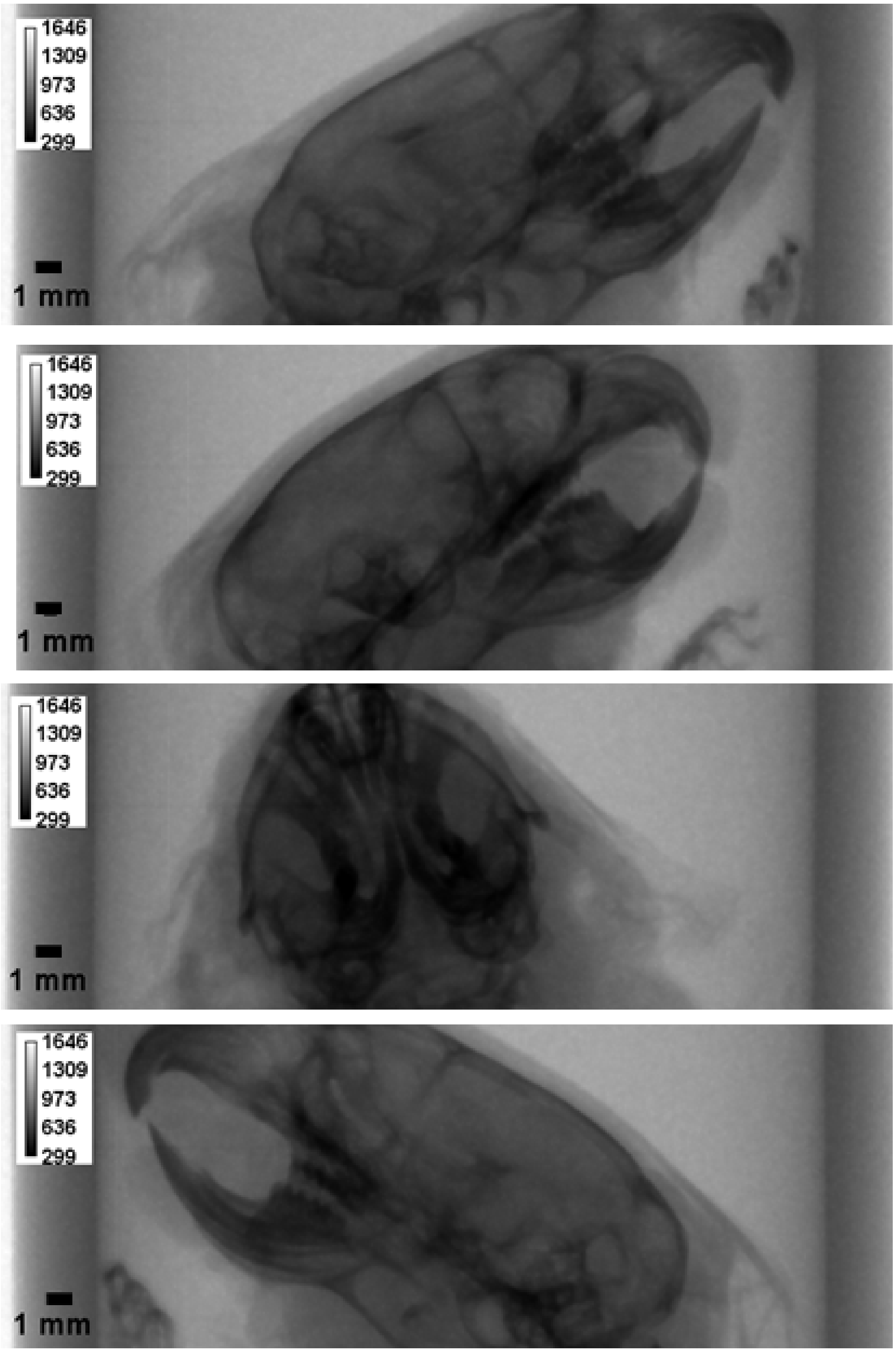

Fig. 3-42 Projections at different angular positions of a mouse head acquired with the FP detector and corrected by means of the FFC.

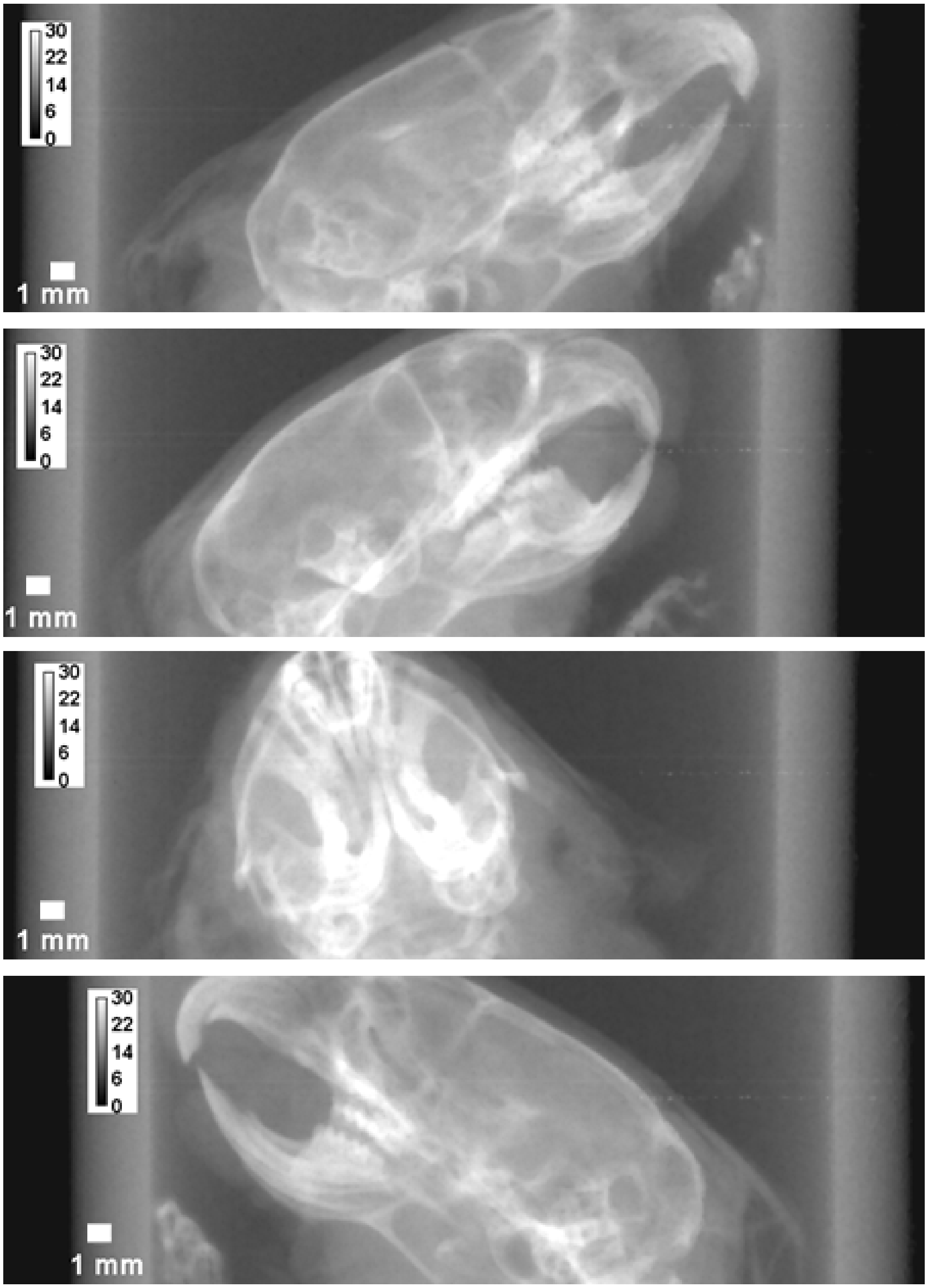

Fig. 3-43 Projections at different angular positions of a mouse head acquired with the FP detector and corrected by means of the STC.

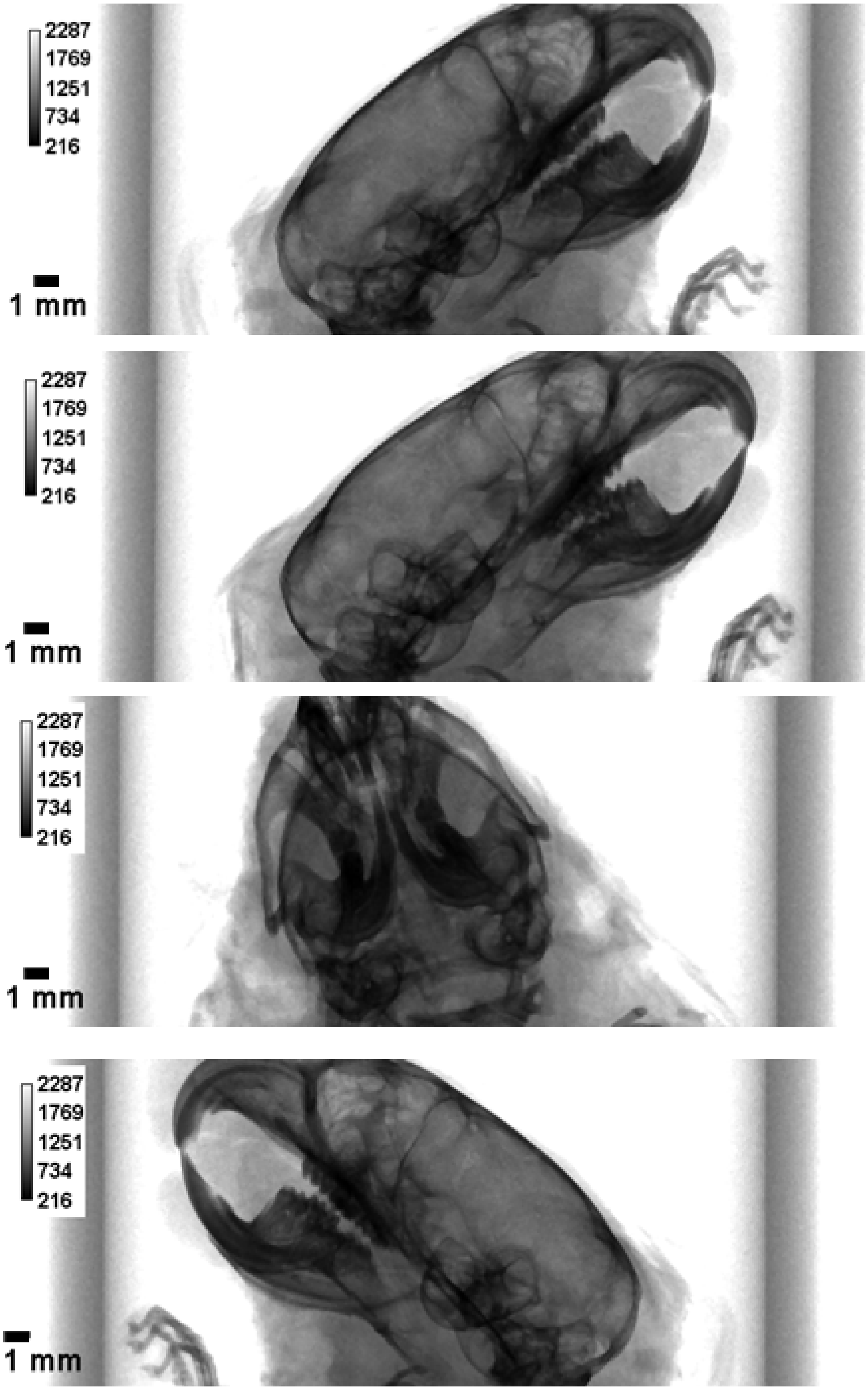

Fig. 3-44 Projections at different angular positions of a mouse head acquired with the Medipix2 detector and corrected by means of the FFC.

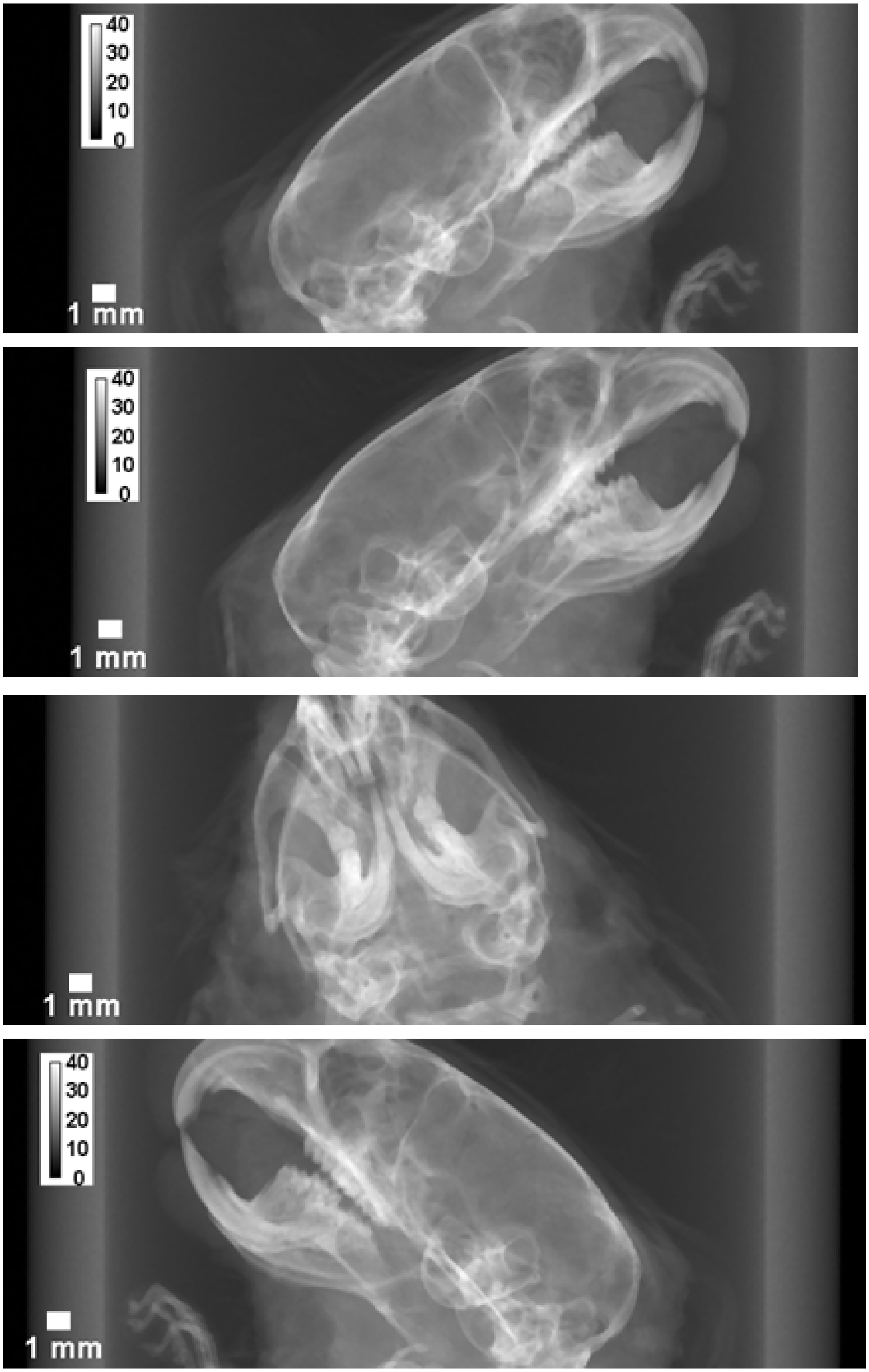

Fig. 3-45 Projections at different angular positions of a mouse head acquired with the FP detector and corrected by means of the STC.

In Fig. 3-46 a selected tomographic slice has been chosen which visualizes an anatomic detail of the head. The four images have been acquired with the FP detector (a and b) and with the Medipix2 (c and d) and corrected by means of the FFC (a and c) and of the STC (b and d).

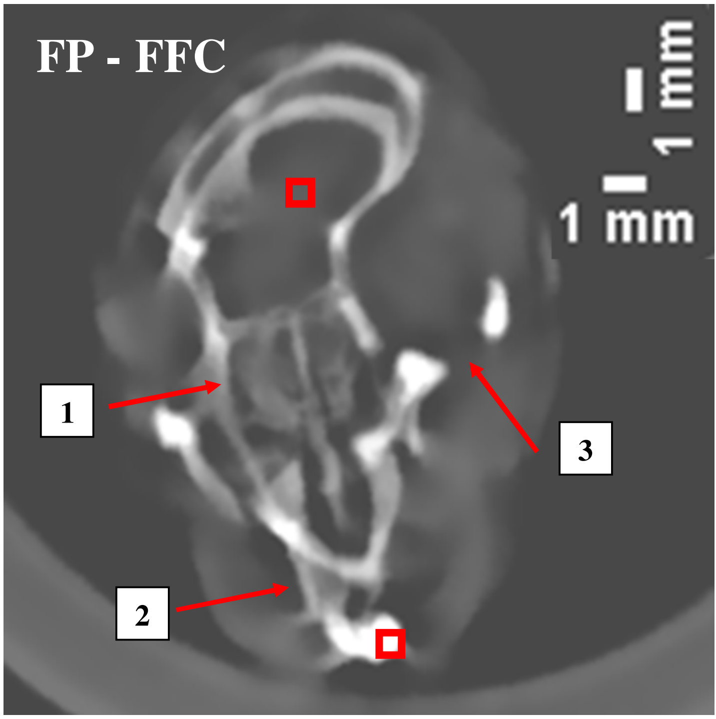

(a)

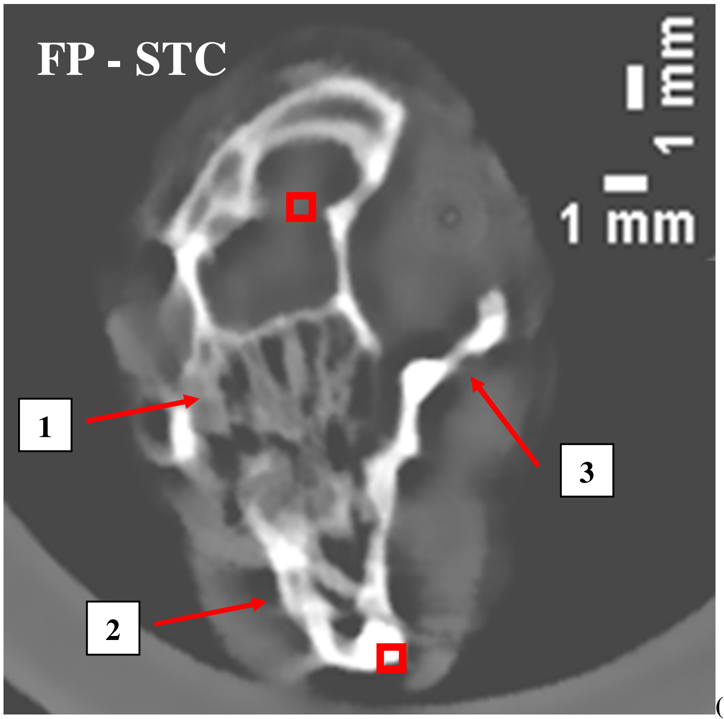

(b)

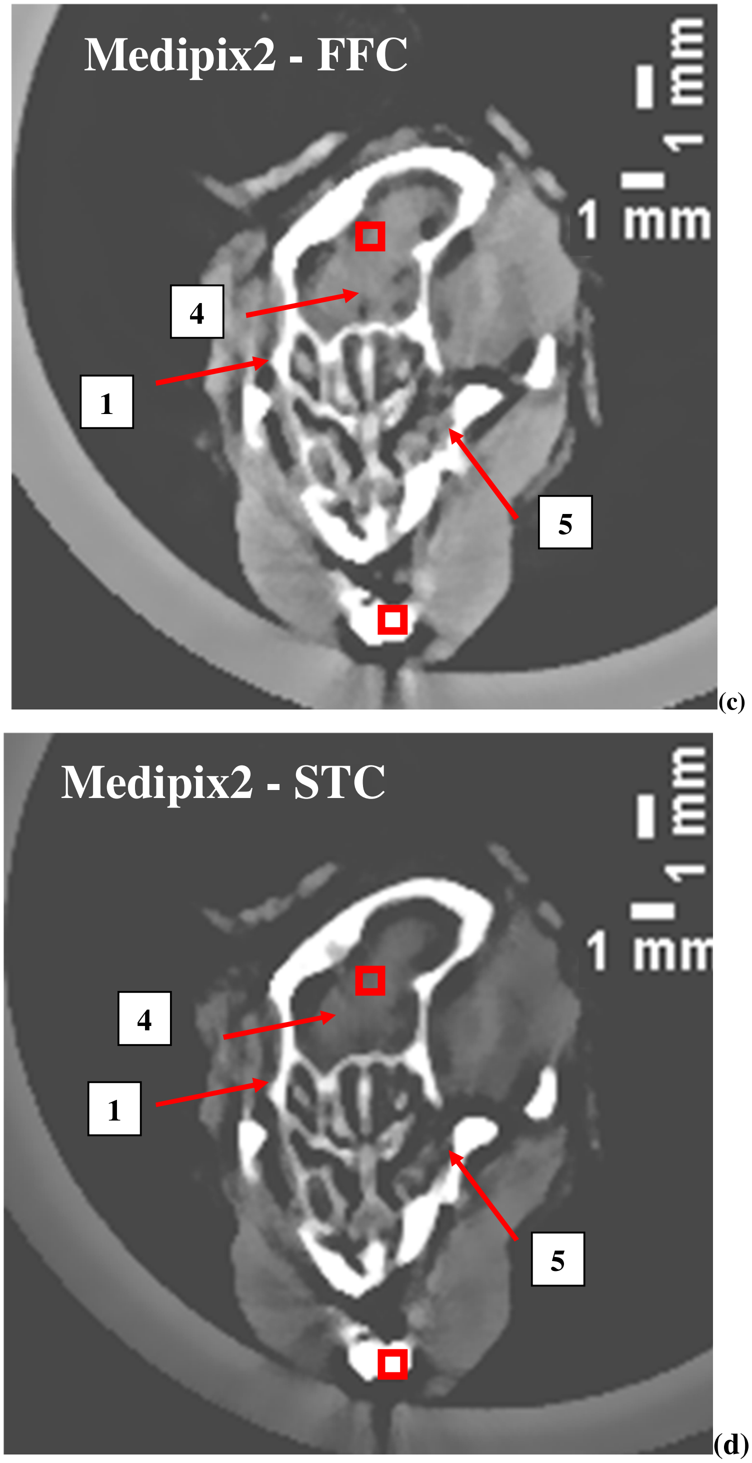

Fig. 3-46 Axial slices of the mouse head acquired with the FP detector (a, b) and with the Medipix2 (c, d) and corrected either by means of the FFC (a, c) or by means of the STC (b, d).

Qualitatively speaking, in the case of the FP detector the STC algorithm gives a more detailed image compared to the FFC, as one can see from the pointed out features labelled with 1, 2 and 3 in Fig. 3-46 (a) and (b). Also when looking at Medipix2 detector data, if focusing at detailed 1, 4 and 5, one can notice more clear and detailed visualizations coming from the STC algorithm rather than from the FFC one. Comparing the structure arrowed with 1 in all the four slices, one can state that the clearer result is obtained with the Medipix2 detector when the STC algorithm is applied (d), followed by the slice obtained with the Medipix2 when the projections have been corrected by means of the FFC (C).

Evaluating the CNR in the four slices of Fig. 3-46 both for the soft tissue (top rectangle in the images) and for the hard tissue (bottom rectangle in the images) compared to PMMA of the wall of the cylinder containing the mouse one can find the results reported in Tab. 3-6. The chosen ROIs are of 5 x 5 pixels. Differently from the tomographic tests on phantoms, both for soft tissues and for hard tissues the FP detector shows higher CNR values. Moreover, in the case of hard tissue the FFC algorithm gives better results compared to the FFC one for both detectors. The reason why, in the case of this biological sample, it is difficult to declare which detector and which correction performs better in terms of the image quality could be related to the non-real homogeneity of the ROIs into the animal body, influencing the standard deviation's values. In other words it could happen that, paradoxically, the detector that is able to achieve a higher resolution (that means Medipix2 detector) in the chosen ROIs has to face with non-homogeneities that are invisible to the detector with the worst resolution.

The contrast C has been evaluated as the difference in CT numbers of the average pixel value of a ROI in the mouse head and in the PMMA and the results are summarized in Tab. 3-7. Analogously, it is not clear how interpret the results. In the case of soft tissue, once again the FP detector shows the highest contrast value when coupled with the FFC, while in the hard tissue case the Medipix2 detector, coupled with the FFC algorithm performs better.

CNR	**Fat Panel**		**Medipix2**	
	FFC	**STC**	**FFC**	**STC**
Soft tissue	6.9	**18.9**	3.4	1.4
Hard tissue	**7.0**	4.9	5.0	4.7

Tab. 3-6 CNR values for the tomographic slices of Fig. 3-46 of soft and hard tissues compared to PMMA evaluated on ROIs of 5 x 5 pixels.

C	**Fat Panel**		**Medipix2**	
	FFC	**STC**	**FFC**	**STC**
Soft tissue	139	**186**	95	54
Hard tissue	2223	2317	**7467**	4664

Tab. 3-7 C values for the tomographic slices of Fig. 3-46 of soft and hard tissues compared to PMMA evaluated on ROIs of 5 x 5 pixels.

Fig. 3-47 shows sagittal views reconstructed from projections acquired with the FP detector (a and b) and with the Medipix2 detector (c and d) and corrected by means of the FFC (a and c) and of the STC (b and d).

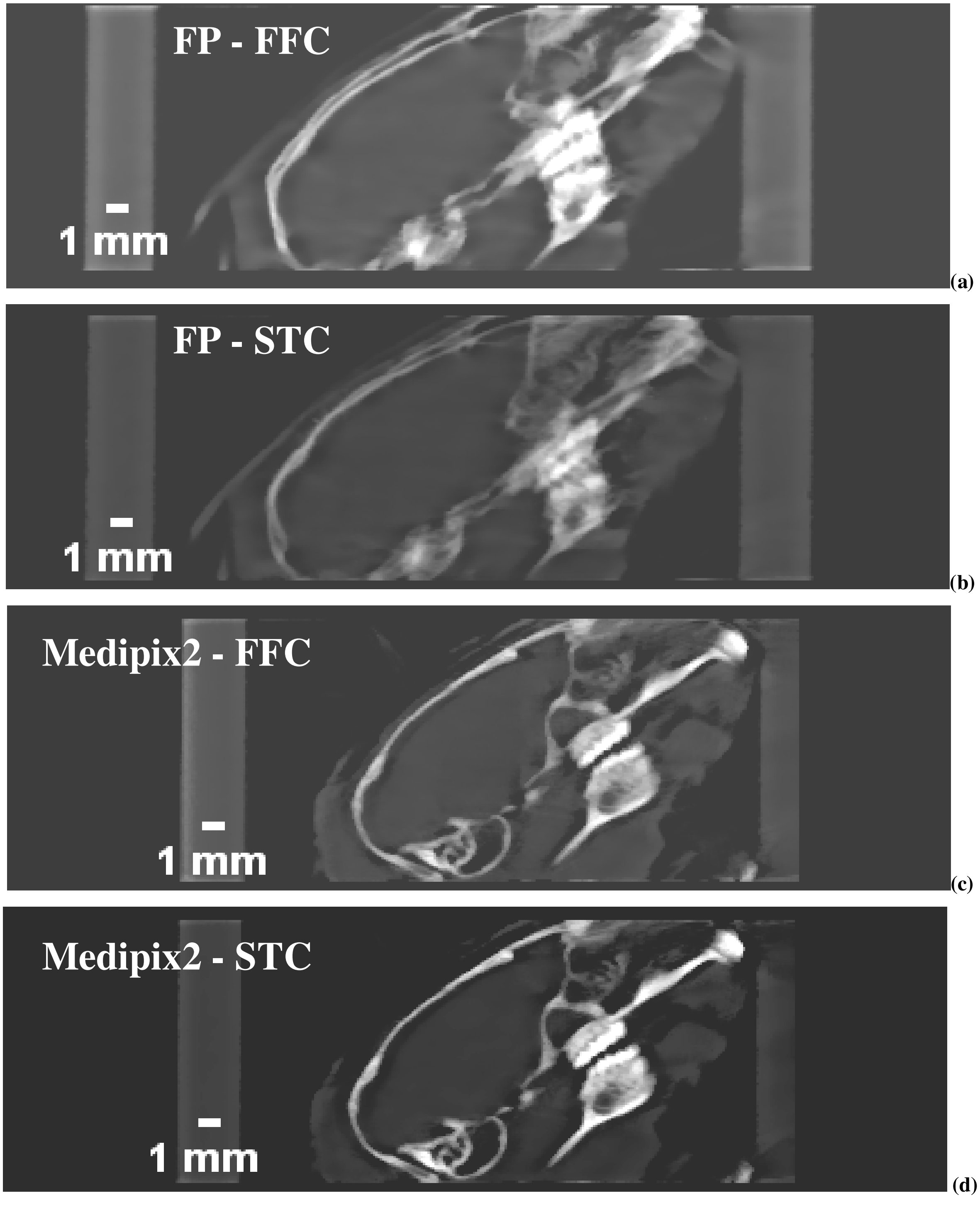

Fig. 3-47 Sagittal slices of the mouse head acquired with the FP detector (a, b) and with the Medipix2 (c, d) and corrected either by means of the FFC (a, c) or by means of the STC (b, d).

3.6 References

[56] X. Wu, H. Liu, “Clarification of aspects in in-line phase-sensitive X-ray imaging”, Med. Phys., vol. 34 (2), pp. 737-743 (2007);

[57] X. Wu, H. Liu, “ A new theory of phase-contrast X-ray imaging based on Wigner distributions”, Med. Phys. 31 (9), 2378-2384 (2004);

[58] S. W. Wilkins, *et al.*, “Phase-Contrast Imaging Using Hard X-Rays”, Nature, vol. 384, p. 335-338 (1996).

[59] O. Gundogdu, *et al.*, “Benchtop phase-contrast X-ray imaging”, Applied Radiation and Isotopes, vol. 65, p. 1337-1344 (2007);

[60] E. F. Donnelly, R. R. Price, “Quantification of the effect of kVp on edge-enhancement index in phase-contrast radiography”, Med. Phys. 29, 999-1002 (2002);

[61] E. F. Donnelly, *et al.*, “Experimental validation of the Wigner distributions theory of phase-contrast imaging”, Med. Phys. 32 (4), 928-931 (2005);

[62] E. F. Donnelly, *et al.*, “Characterization of the phase-contrast radiography edge-enhancement effect in a cabinet x-ray system”, Phys. Med. Biol. 51, 21-30 (2005);

[63] P. Frallicciardi, *et al.*, "Real-Time X-Ray 2-D and 3-D Micro-Imaging of Living Animals with Medipix2 Single Photon Counting Detector", Conf. Proc. IEEE NSS/MIC 2008, M10-112 (2008);

[64] J. Dammer, *et al.*, “Real-time in vivo µ-imaging with Medipix2”, NIM A, Vol. 607, Issue 1, p. 205-207 (2009);

[65] J. Dammer, *et al.*, “Real-time X-ray µ-imaging of living organism”*, Amer. Inst. of Phys.*, V 958, 136-138 (2007);

[66] R. Zemek, E. Prenerova, L. Volter, F. Weyda, V. Skuhravy, “Perspectives for the biological control of *Cameraria ohridella*”, Comm. Appl. Sci, 72/3, 521-526, (2007);

[67] M. W. Westneat, *et al*, “Tracheal respiration in insects visualized with synchrotron radiation X-ray imaging”, Science, vol. 299 (2003;

[68] R. A. Lewis, *et al.*, “ Dynamic imaging of the lungs using X-Ray phase contrast”, Phys. Med. Biol., vol. 50, p. 5031-5040;

[69] D. R. White, “Tissue substitutes in experimental radiation physics”, Med. Phys., vol. 5, No. 6 (1978);

[70] http://www.exxim-cc.com;

[71] L. A. Feldkamp, *et al.*, “Practical cone-beam algorithm”, J. Opt. Soc. Am. A, vol. 1, No. 6 (1984);

[72] P. Frallicciardi, *et al.*, "An Image Quality Study of Medipix2 Single Photon Counting Detector Based on Two Kinds of Flat Field Corrections for Breast Computed Tomography Application", Conf. Proc. World Congress 2009 (2009).

Conclusions

In this thesis we have used a Single Photon Counting (SPC) silicon pixel detector (Medipix2) for X-ray planar, real-time and tomographic imaging, with special interest for small biological samples, both *in vivo* and *post-mortem*. Noise suppression and the assignment of the same weight for low and high energy photons make the SPC technique extremely promising for the detectability and for the visualization of low attenuating objects such as organic and biological samples. The thesis work benefited of collaboration between the group of Medical Physics at Federico II University, and the group at Czech Technical University in Prague, Institute of Experimental and Applied Physics, with financial support from INFN and from Federico II University. The work has been done in the framework of the European Medipix2 Collaboration.

Planar images of insects, plants, seeds have been acquired at a resolution level of about 4 μm with high image quality. Small anatomical and organic structures as insect respiratory system, insects' feelers details, leaf stoma and webbed veining features have been visualized in great detail, also taking advantage of phase contrast enhancement effects. In fact, thanks to the favourable experimental conditions - micrometric focal spot size, suitable source-to-sample and sample-to-detector distances and SPC detector pixel size (55 μm) - the X-ray phase shift has been exploited jointly with the X-ray absorption, allowing the visualization of low-attenuating samples.

The Medipix2 detector read-out time, the high acquisition rate (100 kHz count-rate per pixel) and the possibility of arbitrarily setting the exposure time, make Medipix2 suitable for real-time imaging of moving objects at a reasonable frame-rate of few frames per second. This detector represents a non-invasive tool for *in vivo* investigations of small insects' life and allows entomologists to follow a biological sample through all its evolutional processes for longitudinal studies.

As an example of live X-ray imaging, X-ray planar images of a living parasite, while moving in its natural environment (its host's body), have been acquired with a frame rate of 2 frames/s, with high contrast resolution. A series of planar images of the same sample, acquired in different periods of time, show the living object in several stages of its natural biological evolution, making clearly visible the morphological changes in the animal's body anatomy. 3D X-ray micro-imaging of the living parasite inside its host has been done with a voxel resolution of 17 μm x 17 μm x 21 μm. After the study the sample was still alive for further investigations.

The achieved spatial and contrast resolutions, both in 2D and in 3D images, can be regarded as adequate to detect the main morphogenetic changes in outer anatomy, as well as for observation of inner anatomy features of small insects and organic samples. The dynamics of biological processes, as well as of biological growth and changes can also been satisfactorily followed. The possibility of tomographic imaging enables either to virtually cut the specimen into 2D slices or to have a comprehensive visualization of its 3D model for a non-invasive investigation.

The results obtained are comparable to those achieved with modern integrating systems that use large facilities as a synchrotron light source but, in addition, allow for routine and highly sensitive investigations in laboratories.

A comparison study has also been carried on between the experimental SPC detector and a commercially available Flat Panel integrating detector (CsI:Tl scintillator coupled to a CMOS flat panel), in terms of image quality for planar and tomographic imaging. The two detection technologies have been compared on 2D and 3D imaging of both phantoms and biological samples. Image quality parameters have been evaluated on images acquired with the two detectors in the same experimental conditions (geometry, X-ray tube energy, exposure, etc.), showing in all the investigated cases a higher performance of the SPC technology. We observed that the SPC technique decreases significantly the fluctuations in the signal noise, permitting a higher image quality in a large attenuation range and for low X-ray energies (40 kVp tube voltage), as used for micro-imaging on biological samples.

Two pixel efficiency correction methods have been compared: the standard Flat Field Correction (FFC) and the novel Signal-to-Thickness Calibration (STC). A correction procedure on raw data is important to account for the non-uniform pixel response. The STC calibration results in a more uniform and well contrasted planar and tomographic imaging compared to the FFC correction. Moreover, when tomographic projections are corrected by means of the STC, the beam hardening cupping artefact is almost recovered.

To sum up our results, we believe that an SPC detector, when associated to the STC technique, permits for high quality X-ray imaging. Moreover, its image quality performance is higher when compared to the charge integrating FP detector one, as far as both planar and tomographic images are concerned.

APPENDIX:

Phase Contrast Effect: outline of theory

A special remark has to be done on a phenomenon which X-rays undergo when passing through an object under certain conditions of coherence of the beam: the phase shift.

The X-rays propagation through an object can be described by the complex refractive index:

$$n = 1 - \delta + i\beta ,$$

where β is the imaginary part describing the absorption and δ is the refractive index decrement, responsible for the phase shift ϕ, caused by the radiation-matter interaction; β and ϕ are defined as:

$$\beta = \frac{\mu / \rho \cdot \lambda \cdot \rho}{4\pi}; \qquad \phi = -\frac{2\pi}{<\lambda>} \int \delta(x) dx ,$$

where the integral is calculated on the X-ray path, μ/ρ is the mass attenuation coefficient of the traversed medium, $<\lambda>$ is the mean X-ray wavelength and ρ the traversed material density.

For the image formation the conventional radiography exploits the differences in the X-ray attenuation depending on composition and thickness of the traversed medium and on the different covered distance. Low attenuating objects are visualized with low contrast, which hampers a clear interpretation of the image. On the other hand, detectors record not only X-rays absorption into an object, but also the phase shift effects occurred in the X-rays diffracted from the encountered object. Waves with different phase ϕ, travelling from the object to the detector, under coherence conditions can interfere creating bright and dark fringes in the recorded image, as shown in Fig. A. 1.

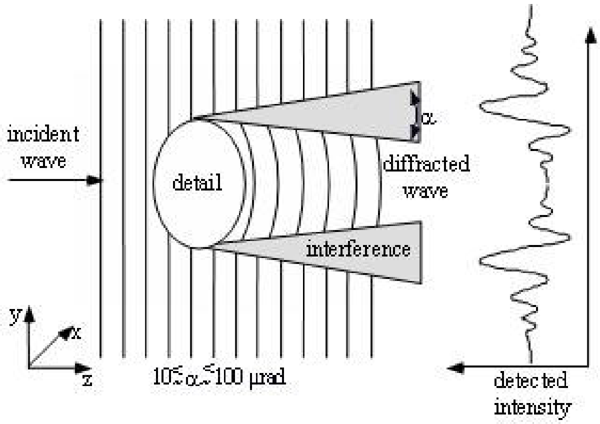

Fig. A. 1 Scheme representing the phase effect formation: a wave impinging on an object is diffracted; the diffracted waves, travelling from the object to the detector, when coherent, can interfere giving rise to intensity jumps recognisable as bright and dark fringes.

The fringes appear in the zones in which the change of refractive index is sudden, that means on edges and interfaces between objects which are different in thickness or compositions, resulting in an enhanced image contrast. The “phase contrast imaging” (PCI), when exploited in the medical imaging field, results in an appreciable gain in the visualization of tissues and structures with a similar attenuation coefficients. Among the most interesting biological objects, commonly not visible or not distinguishable from the surrounding background with a conventional radiography, one can mention:

- soft breast tissues (with similar attenuation coefficients);
- articular cartilages (normally not visible);
- blood vessels (normally visible only with contrast medium);
- small and incomplete bone fractures.

The advantage of this imaging technique can be appreciated by comparing the imaginary and the real part values of the refractive index n (Fig. A.2): in the diagnostic energy range of (10-100 keV), δ values are generally three orders of magnitude higher than β values; besides, at increasing energy, δ decreases less than β.

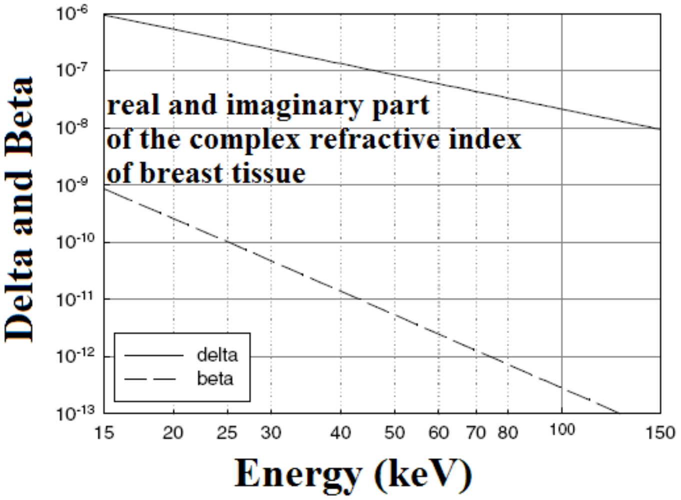

Fig. A.2 The real and the imaginary parts, δ [73] and β [74] of the complex refractive index for breast tissue.

From this datum it is possible to get two important remarks: first, the phase contrast can be much higher than the attenuation contrast in a radiographic image; a second observation is that it is possible to work at higher energies compared to the conventional radiographies energies, still keeping a more elevated contrast, which means that the absorbed dose from the organism will be lower.

The physical/geometric conditions necessary for the phase shift phenomenon manifestation can be summarized as follows:

- the X-rays source must present a high spatial coherence degree to give raise to the interference phenomenon;

- the detector-to-object distance, R_2, must be long enough to let diffracted rays diverge from undeviated ones to a sufficient extent to be separately detected (refractive angles are of few arcseconds). At the same time, the distance R_2 has to be kept not too long to avoid the blurring effect due to the focal spot contribution;
- the detector resolution must be high enough to separately detect the refracted rays from the undeviated ones;
- high frequencies details are preferably detected.

Typically, the phase enhanced contrast imaging is realized by means of the totally coherent synchrotron light. There are several studies based on this monochromatic radiation making use, basically, of two techniques: the diffraction enhanced imaging (DEI) also called the analyzer-based imaging (ABI) and the propagation-based imaging (PBI), alternatively called the refraction-enhanced imaging (REI). These techniques are often exploited for medical imaging, in particular for all the biological samples showing a low attenuation to X-rays as insects [75] or for mammographic studies on breast phantoms and excised tissue samples [76] [77], for investigation of degenerative joint diseases (bone is clearly visualized in conventional radiography, while cartilage is not) and lung imaging [78] [79]. In the latter case, because of the difference in X-ray phase shift caused by blood and soft tissues, blood vessels can be revealed with phase-contrast image without the use of any contrast agent. Both techniques, therefore, improve the image quality over absorption contrast radiography.

The use of the PBI technique by means of an X-ray tube is less common but still it is possible under the partial coherence conditions. In fact, typically, in a clinical radiographic system the source is a polychromatic X-ray tube (almost total absence of temporal coherence) with a spatial coherence degree. The smaller the focal spot is the higher the coherence degree is. The partial coherence of the waves emitted by a source of finite size s can be described in terms of lateral coherence length, L_{coh}, defined as [80]:

$$L_{coh} = \frac{<\lambda> \cdot R_2 \, |u|}{s},$$

where $<\lambda>$ represents the mean wavelength of the beam, as above, and R_1 is the source-to-object distance. The lateral coherence length is the linear size of a region over which the wavefield is strongly correlated, and it is roughly the maximal separation of two points for which the interference occurs. Besides the coherence length, what determines the phase contrast visibility is the modulus of the coherence degree for a certain structural component of spatial frequency u. This parameter is difficult to calculate, so that an alternative criterion to evaluate the coherence level reached in certain experimental conditions involves the so-called "shearing length", L_{sheear} [79].

This latter quantity represents the linear dimension necessary to the waves superposition, *conditio sine qua non* for the phase contrast phenomenon to manifest:

$$\mathrm{L}_{\mathrm{shear}} = \frac{<\lambda> \cdot R_2 \, |u|}{M},$$

where M is the geometrical magnification factor defined as:

$$\mathrm{M} = \frac{R_1 + R_2}{R_1},$$

and R_1 is the source-to-object distance. Finally, the criterion for the coherence conditions for the phase contrast effect is the value of the ratio:

$$\frac{\mathrm{L}_{\mathrm{shear}}}{\mathrm{L}_{\mathrm{coh}}} = \frac{R_2 \cdot s \cdot |u|}{M \cdot R_1} = \frac{(M-1) \cdot s \cdot |u|}{M}$$

This ratio does not depend on the X-ray wavelength λ. For $\frac{\mathrm{L}_{\mathrm{shear}}}{\mathrm{L}_{\mathrm{coh}}} << 1$ values the wavefield is almost fully coherent over the sharing length and that the phase contrast is clearly visible. For $\frac{\mathrm{L}_{\mathrm{shear}}}{\mathrm{L}_{\mathrm{coh}}} \geq 1$, the wavefield is totally incoherent and the phase contrast can not manifest itself. In intermediate cases, ($\frac{\mathrm{L}_{\mathrm{shear}}}{\mathrm{L}_{\mathrm{coh}}} < 1$), the wavefield is partially coherent and the phase contrast visibility increases with decreasing $\mathrm{L}_{\mathrm{shear}}$.

The phase shift effect can be evaluated quantitatively. From Wu and Liu work [81] the expected trend is shown in Fig. A.3, where the RPF (Relative Phase contrast Factor) parameter is defined as:

$$RPF(u) = c^2 h^2 \tilde{\mu}_{in}(\frac{\lambda R_2 u}{M}) OTF_{\mathrm{det}}(\frac{u}{M}) \cdot [\int \frac{\pi R_2 u^2}{ME^2} S_{Exit}(E) dE],$$

where

c: light speed;

h: Planck constant;

λ, R_2, M, $\boldsymbol{u}$**:** defined as before;

E: beam energy;

$\bar{\mu}_{in}(\frac{\lambda R_2 u}{\mathrm{M}}) = \mathrm{OTF}_{\mathrm{G.U.}}(\frac{u}{M})$, that is the complex degree of partial coherence that corresponds to the *Optical Transfer Function* (OTF) of the geometric unsharpness associated with a small focal spot;

$\mathrm{OTF}_{\mathrm{det}}$: detector *Optical Transfer Function*, the module of which represents the *Modulation Transfer Function* (MTF);

$\mathrm{S}_{\mathrm{Exit}}$: the spectrum outgoing from the object.

The |RPF| parameter represents a quantitative measure of the coherence and visibility of the phase-contrast phenomenon for a fixed spatial frequency **u** (20 lp/mm for the simulations of Fig. A.3), for a given spectrum (molybdenum anode with 30 μm inherent filtration in Fig. A.3). The larger this parameter is, the more the phase-shift manifests. In correspondence, the overshoot of the profile across an edge where the fringes appear will be more visible.

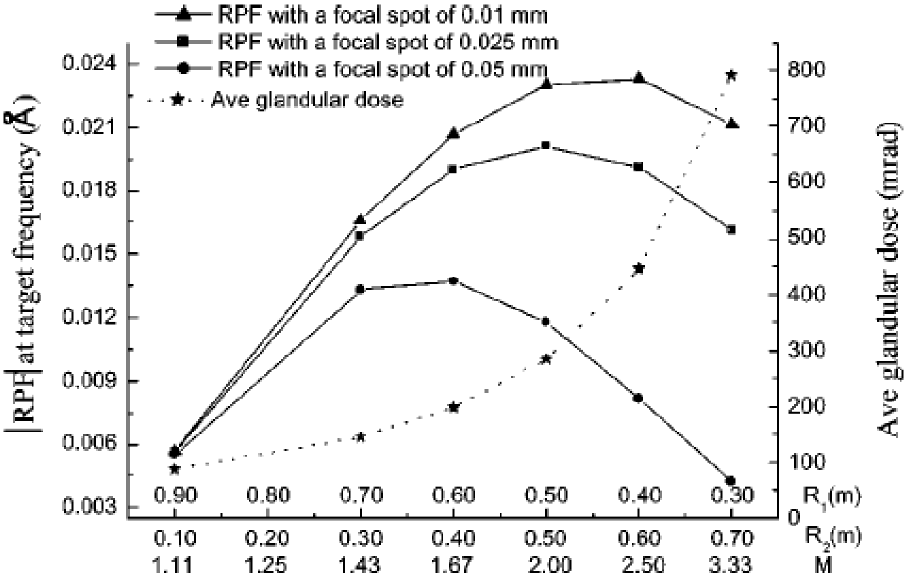

Fig. A.3 Simulated trend of the |RPF(u)| value at increasing M, for a system composed of an X-ray source provided with a focal spot of 25 μm or 50 μm and a detector with 25 μm or 40 μm pixel size. The spatial frequency is set to 20 lp/mm and the spectrum has been simulated for a molybdenum anode with 30 μm inherent filtration [81]

Similarly it can be directly evaluated the upward and the downward overshoot due to the presence of the dark and bright fringes as the distance between the two peaks. For the phase contrast extent evaluation two parameters can be defined [82][83][84] the Edge Enhancement Index (EEI) and the Edge Enhancement to Noise ratio (EE/N) defined as follows:

$$EEI = \frac{(P-T)/(P+T)}{(H-L)/(H+L)} \quad \text{and} \quad EE/N = \frac{(P-T)}{\sqrt{(\sigma_H^2 + \sigma_L^2)}}$$

where

P and T are the peak and trough intensity values at the edge;

H and L represent the intensity average values, respectively, on the higher-intensity side of the edge and on the lower-intensity side of the edge;

σ_H and σ_L represent the standard deviations of the pixels used to calculate H and L in the EEI equation.

A clarification drawing is depicted in Fig. A.4.

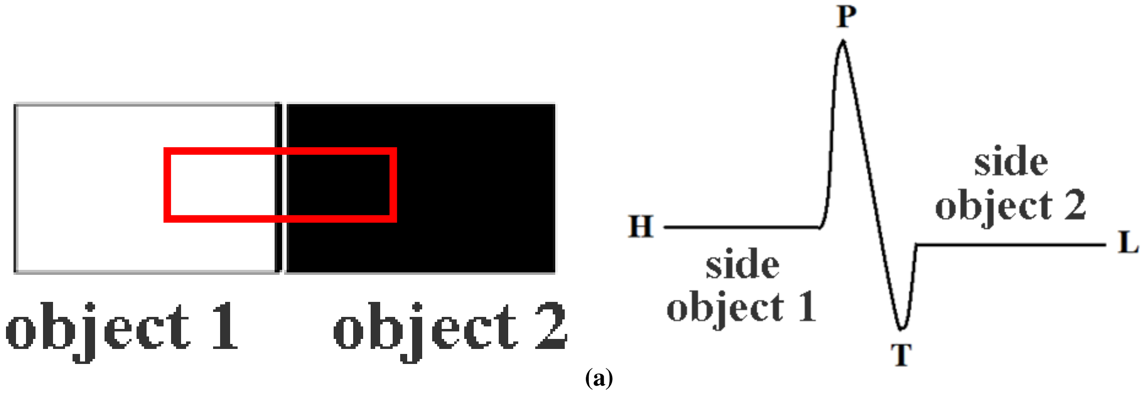

(a) (b)

Fig. A.4 Dark and bright fringes along an interface between two different materials - object 1 and object 2 – as a result of the interference of the diffracted waves, averaged by the finite detector resolution (a); correspondingly, the intensity profile across the edge demonstrates an upward (P) and a downward (T) overshooting. H and L represent, respectively, the higher and the lower intensity sides of the edge.

EEI measures the relationship of the edge-enhancement effect relative to the absolute change in intensity from absorption differences across the edge between two interfaces, while EE/N measures the magnitude of the edge enhancement effect relative to the presence of noise within the image. It should be made clear that the EEI and EE/N parameters are conceptually different from the RPF factor defined above. In fact, while the first two parameters can only provide information relative to the degree of absorption contrast in an image and quantify an observable effect, the RPF is a figure of merit that indicates which parameters for a given imaging system will maximize the degree of phase contrast.

References

[73] M. Sanchez-del-Rio, R. J. Dejus, R J XOP www.ersf.fr/computing/scientific/xop (2003);

[74] C. T. Chantler, *et al.*, “X-ray Form Factor, Attenuation and Scattering Tables”, version 2.0, D S, http://physics.nist.gov/ffast (National Institute of Standards and Technology, Gaithersburg, MD) (2003);

[75] J. Jakubek, *et al.*, "Phase Contrast Enhanced High Resolution X-Ray Imaging and Tomography of Soft Tissue”, NIM A, vol. 571, p. 69-72 (2007);

[76] S. Fiedler, *et al.*, “evaluation of two phase contrast techniques: diffraction enhanced imaging and propagation”, Proc. SPIE, 5030, p. 266-273 (2003);

[77] E. Pagot, *et al.*, “Quantitative comparison between two phase contrast techniques: diffraction enhanced imaging and phase propagation imaging”, Phys. Med. Biol., 50, p. 709-724 (2005);

[78] M. J. Kitchen, *et al*, “Phase contrast X-ray imaging of mice and rabit lungs: a comparative study”, Br. J. Radiol., vol.78, p. 1018-1027 (2005);

[79] N. Yagi, *et al*, “Refraction-enhanced X-ray imaging of mouse lung using synchrotron radiation source”, Med. Phys., vol. 26, p. 2190-2193 (1999);

[80] X. Wu, H. Liu, “Clarification of aspects in in-line phase-sensitive X-ray imaging”, Med. Phys., vol. 34 (2), pp. 737-743 (2007);

[81] X. Wu, H. Liu, “ A new theory of phase-contrast X-ray imaging based on Wigner distributions”, Med. Phys. 31 (9), 2378-2384 (2004);

[82] E. F. Donnelly, R. R. Price, “Quantification of the effect of kVp on edge-enhancement index in phase-contrast radiography”, Med. Phys. 29, 999-1002 (2002);

[83] E. F. Donnelly, *et al.*, “Experimental validation of the Wigner distributions theory of phase-contrast imaging”, Med. Phys. 32 (4), 928-931 (2005);

[84] E. F. Donnelly, *et al.*, “Characterization of the phase-contrast radiography edge-enhancement effect in a cabinet X-ray system”, Phys. Med. Biol. 51, 21-30 (2005).

List of Selected Figures

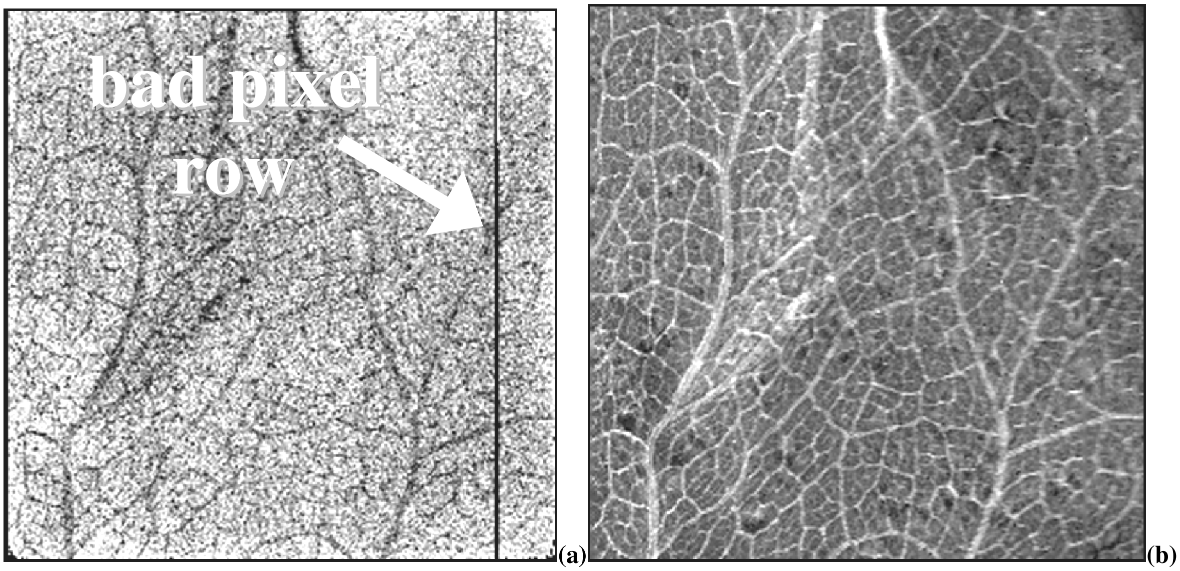

Fig. 2-14 Raw image of a rose leaf in which the vein structure is hardly distinguishable and also a bad pixel row is visible (a); STC corrected image of the leaf: the structure is clearly observable. The image has been acquired with the Medipix2 SPC detector and with a 5 µm spot-size tungsten X-ray source with a tube voltage of 40 kVp and a tube current of 50 µA for a Tacq = 100 s (W anode). The STC calibration has been performed with a set of aluminium filters, the thinnest one of 50 µm (the leaf mean thickness was of 195 µm).

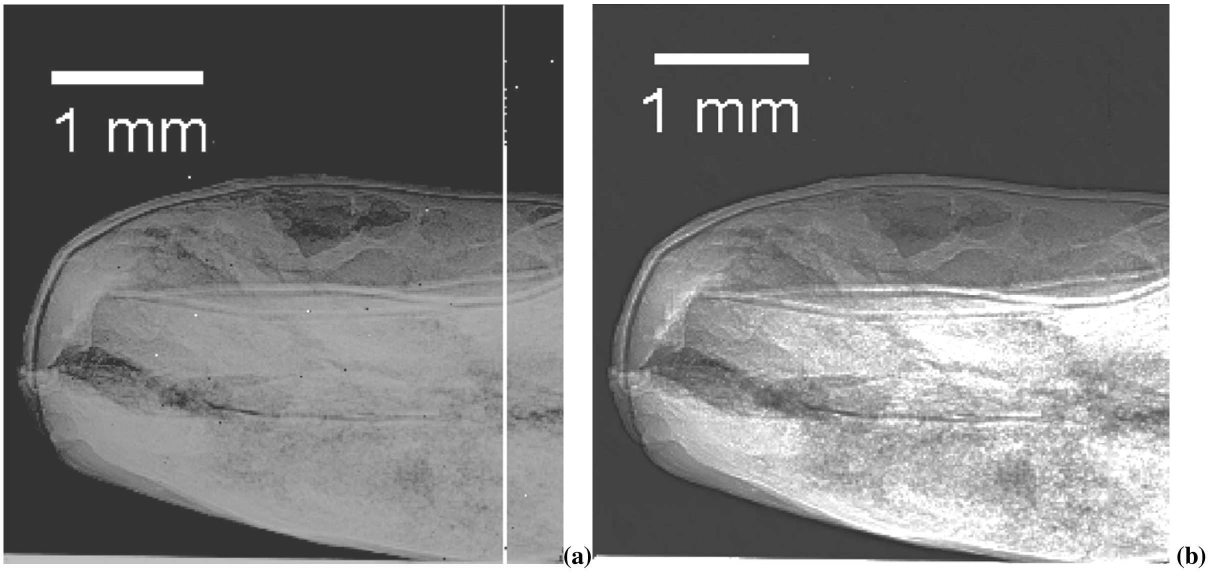

Fig. 2-15 FFC corrected image of a lentil (a bad pixel row is visible) (a); STC corrected image of the same lentil: the internal structure is more clearly observable than for the FFC image. The image has been acquired with the Medipix2 SPC detector and with a 5 µm spot-size tungsten X-ray source with a tube voltage of 50 kVp and a tube current of 110 µA for a Tacq = 100 s (W anode). The STC calibration has been performed with a set of aluminium filters, the thinnest one of 50 µm (the leaf mean thickness was of 300 µm).

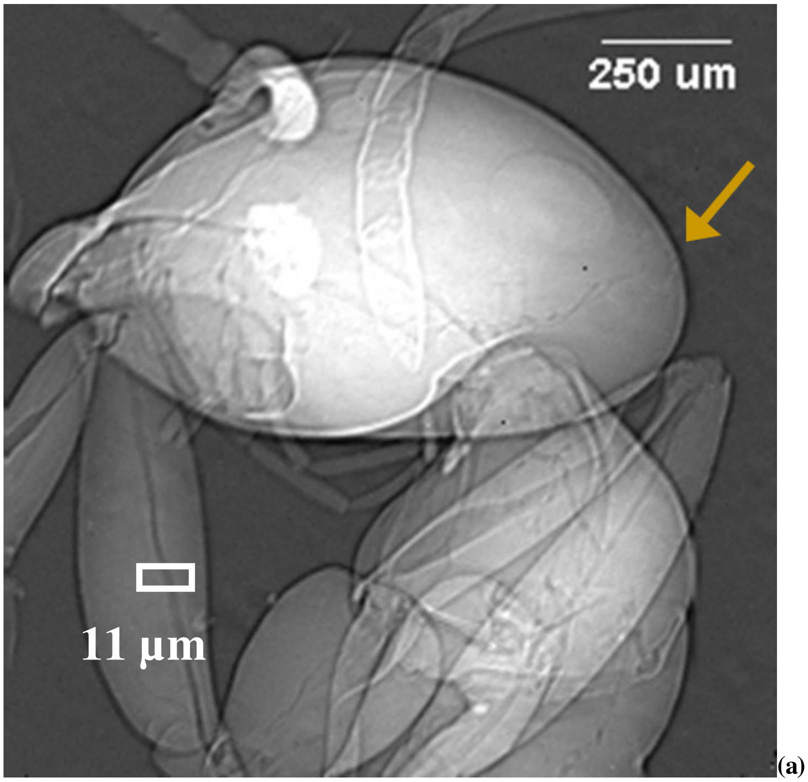

Fig. 3-2 Phase contrast radiography of an ant (a), of a head detail (b) in which the bright and dark fringes enhancing the contour are clearly visible; (c) horizontal profile taken along the region pointed out in (b). The x-axis is in equivalent Al thicknesses (mm), obtained from the Signal-to-Thickness Calibration (STC). The distance between the source and the sample is R1 = 6.65 cm, the distance between the sample and the detector is R2 = 54.35 cm, the magnification is M = 9.1x. I = 200 µA; V = 40 kV; focal-spot of 5 µm size, W anode; acquisition time Tacq = 100 s. The channel visible in (a) has been evaluated 8 µm in diameter.

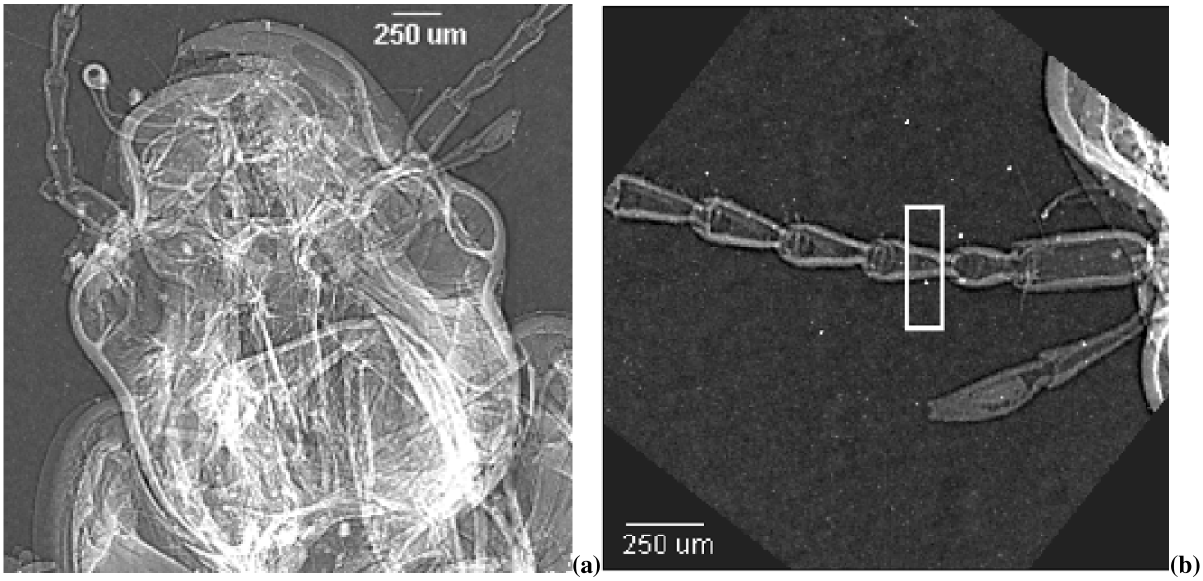

Fig. 3-3 Phase contrast radiography of an insect (a), of a feeler (b) in which the bright and dark fringes enhancing the contour are clearly visible; (c) horizontal profile taken along the region pointed out in (b). The x-axis is in equivalent Al thicknesses (mm), obtained from the Signal-to-Thickness Calibration (STC). The distance between the source and the sample is R1 = 13.15 cm, the distance between the sample and the detector is R2 = 48.85 cm, the magnification is M = 4.7x. I = 200 µA; V = 40 kV focal-spot of 5 µm size, W anode; acquisition time tacq = 100 s. The FWHM evaluated for the left and right peaks are of FWHMLEFT = 20. 4 µm and FWHMRIGHT = 36 µm.

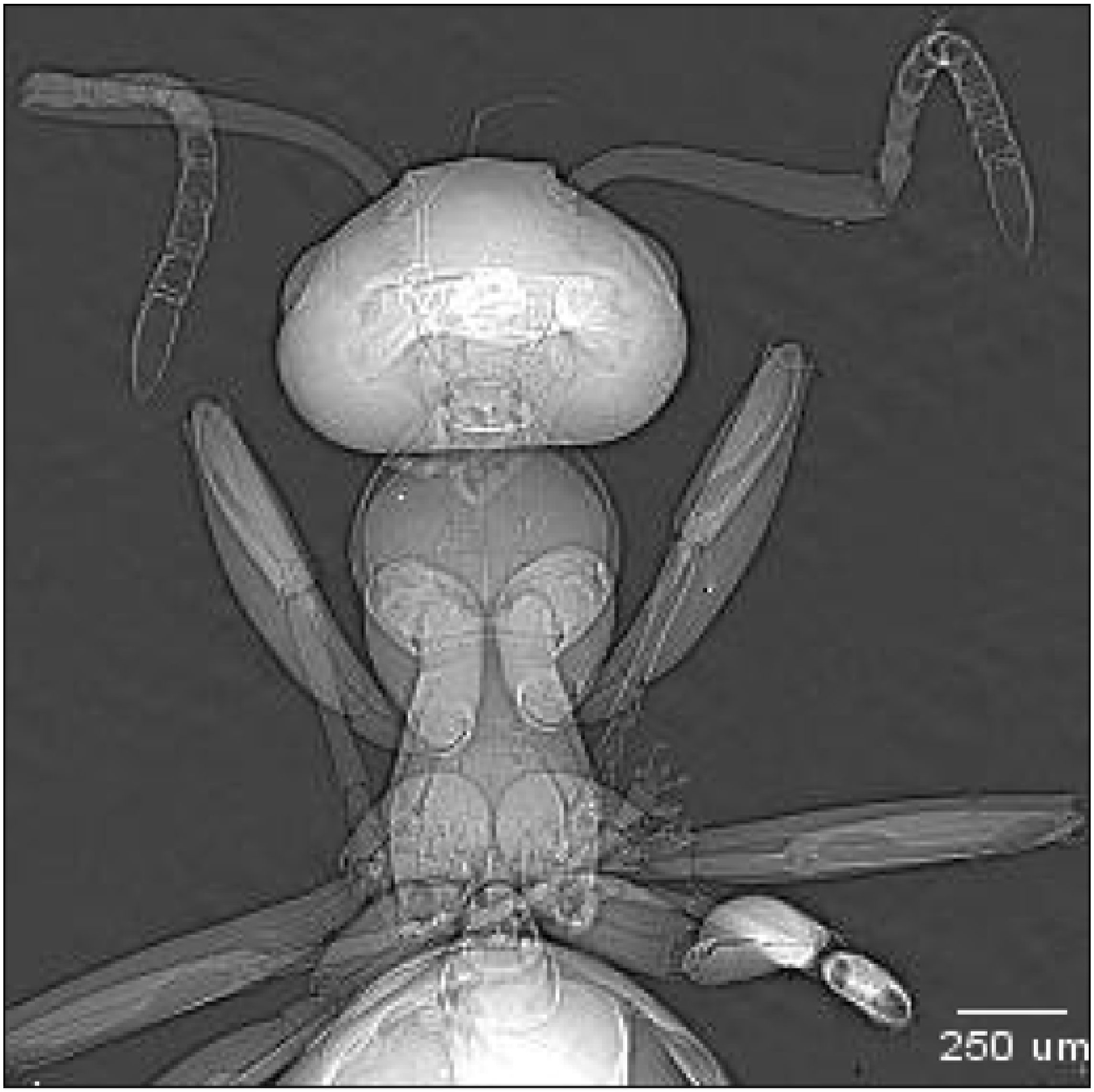

Fig. 3-5 Radiography of an ant (front side) acquired with an exposure of 20 mAs, a tube voltage of 40 kVp and a magnification factor of 5.5x. The two feelers structure is clearly distinguishable.

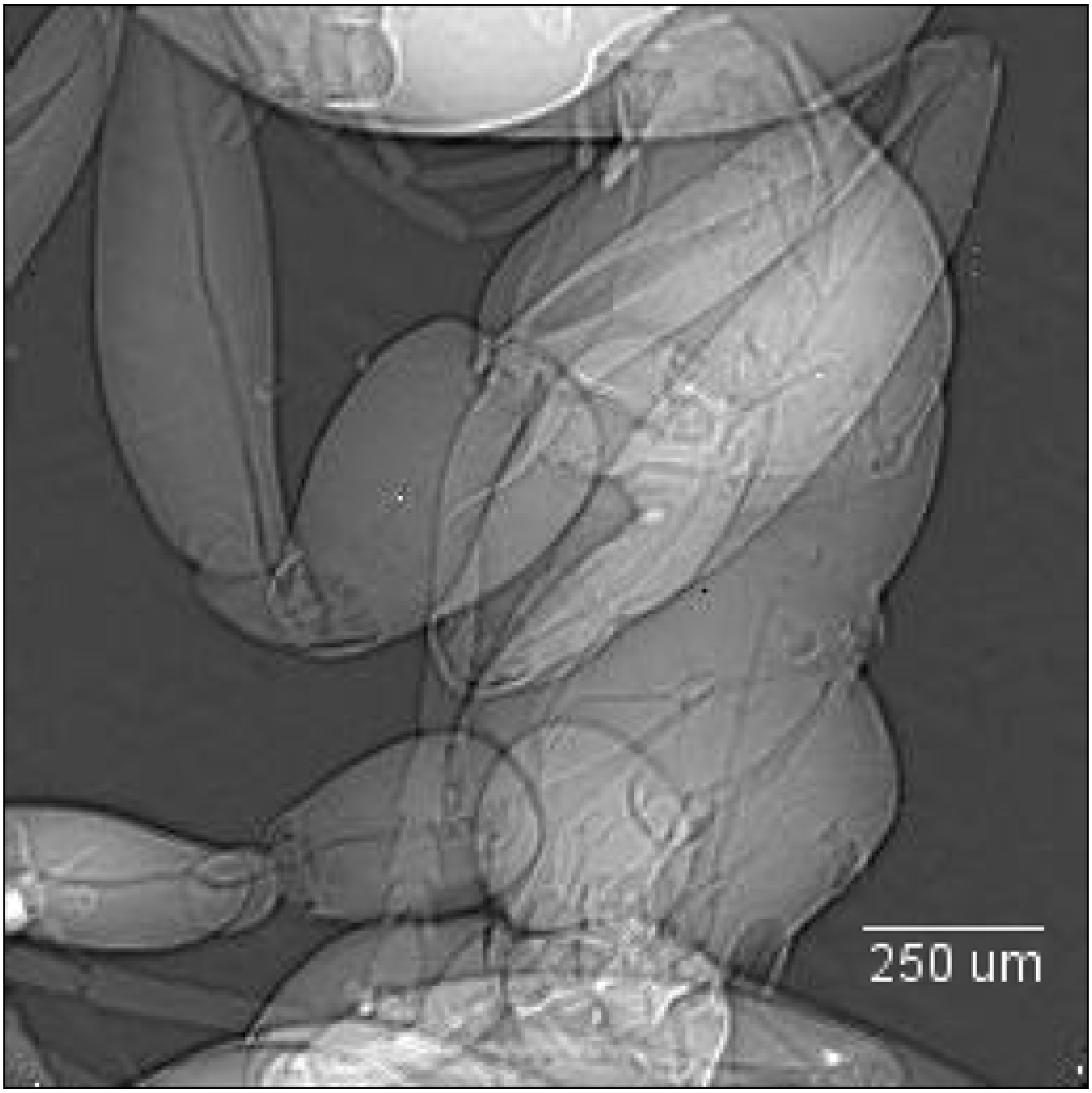

Fig. 3-6 Lateral radiography of an ant: exposure of 20 mAs, tube voltage at 40 kVp and magnification factor of 9.3x. The complex network of gas-filled vessels is clearly visible throughout the whole body.

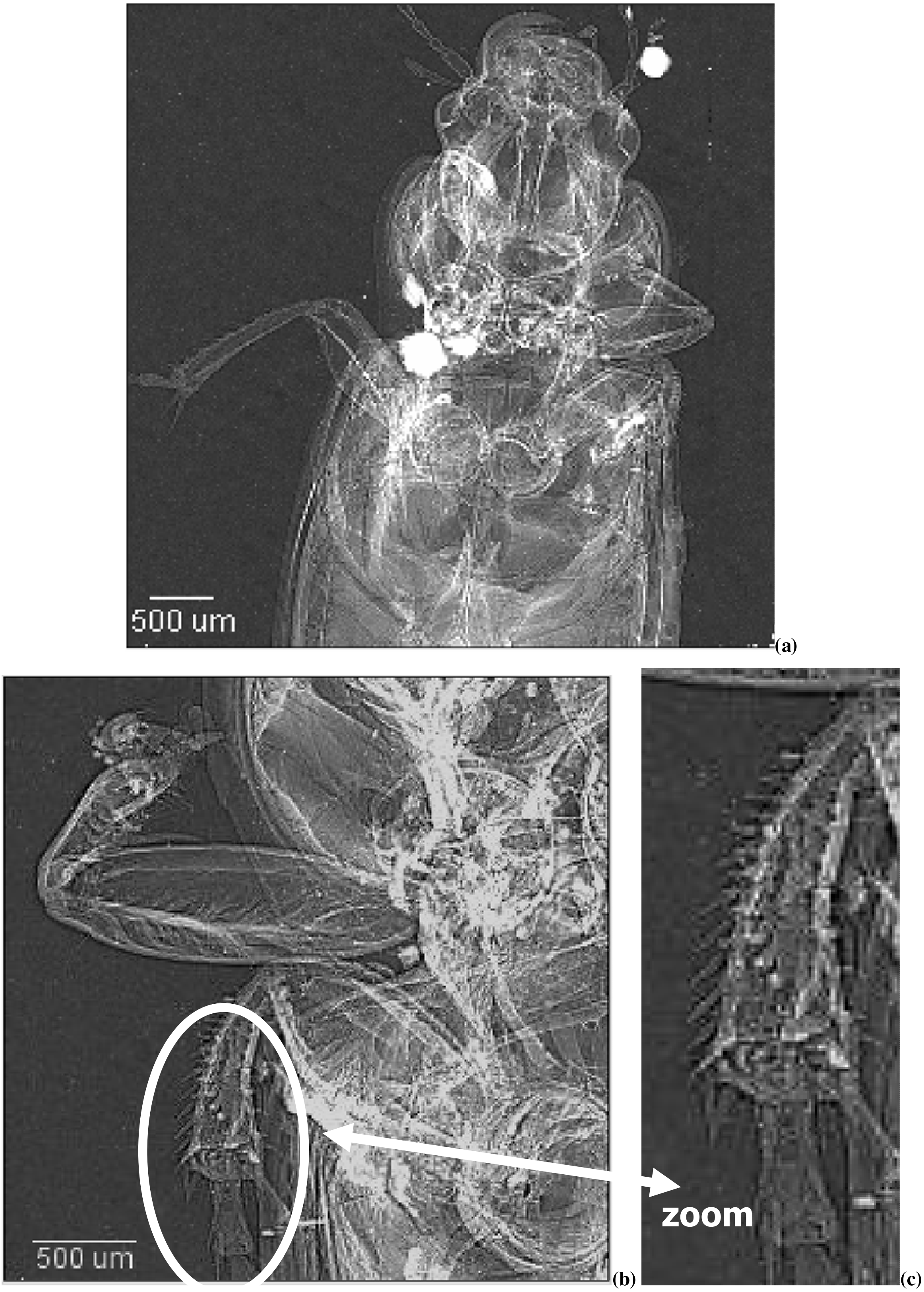

Fig. 3-7 Radiography of a beetle acquired with an exposure of 2 mAs, a tube voltage of 40 kVp and a magnification factor of 2.6x (R1 = 23.45 cm, R2 = 37.55 cm) (a); side part of the beetle's body, showing two legs, thanks to the 4.6x magnification factor (R1 = 13.45 cm, R2 = 47.85 cm); the exposure is 4 mAs (b); zoomed detail of the beetle's leg in which hair is clearly visible.

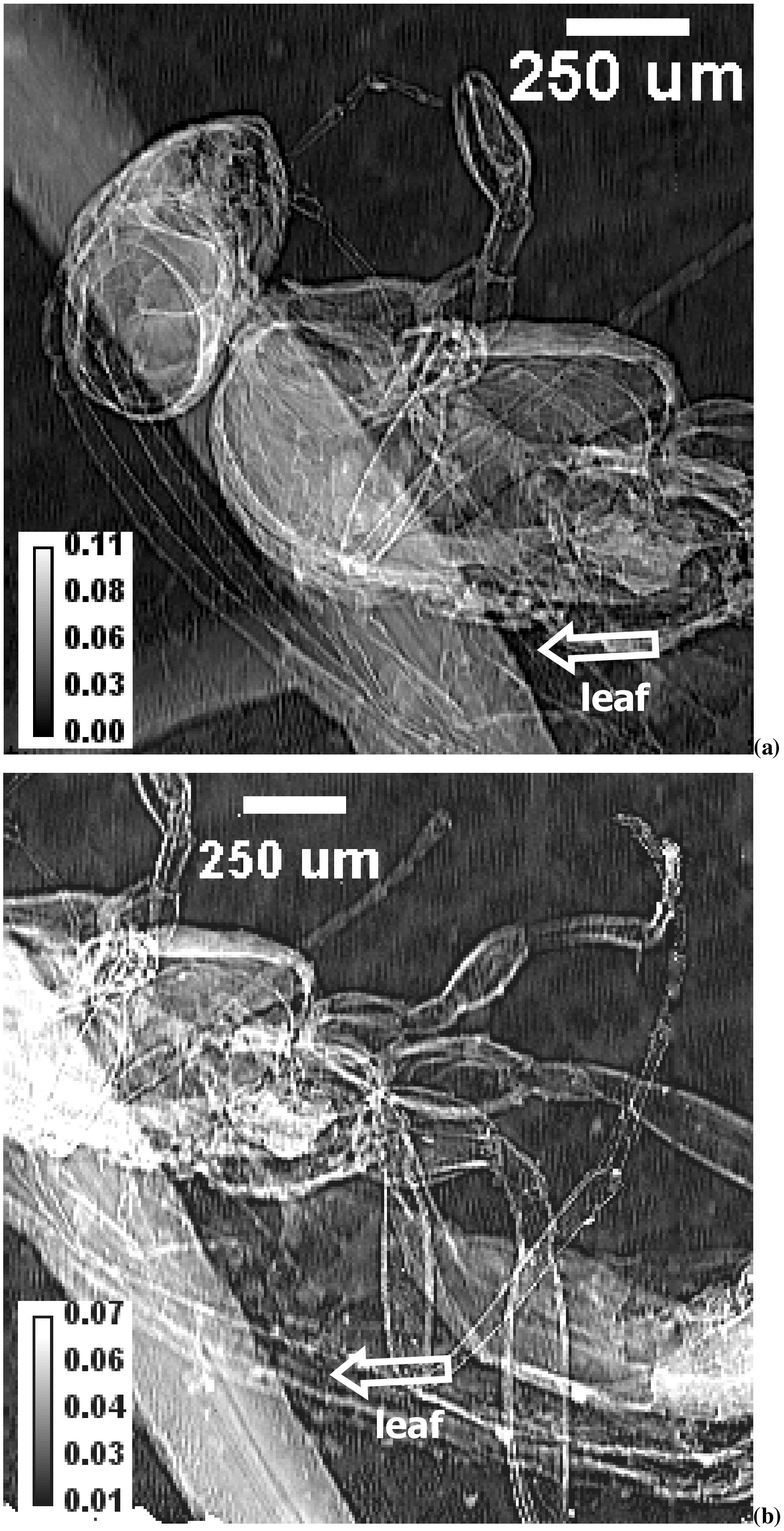

Fig. 3-8 Radiography of a living fly laying on a leaf (outlined with an arrow), acquired with an exposure of 27.5 mAs, a tube voltage of 40 kVp and a magnification factor of 9.1x (a); low part of the fly body, showing the legs, acquired with 11 mAs at M = 7.4 (b). In both radiographies the phase contrast enhancement is fundamental for the body structure visualization.

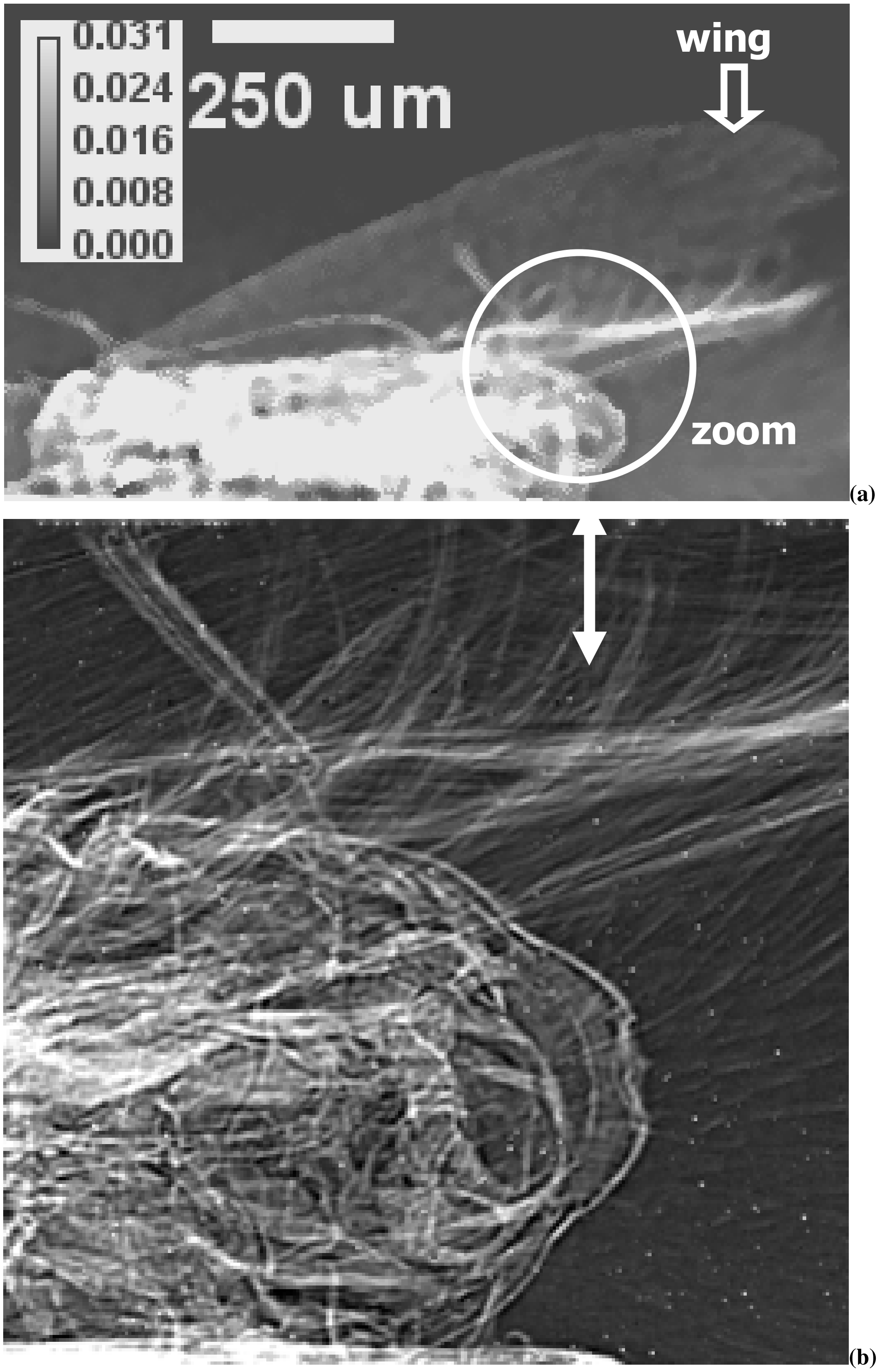
0.031
0.024
0.016
0.008
0.000
250 um
wing
zoom
(a)
(b)

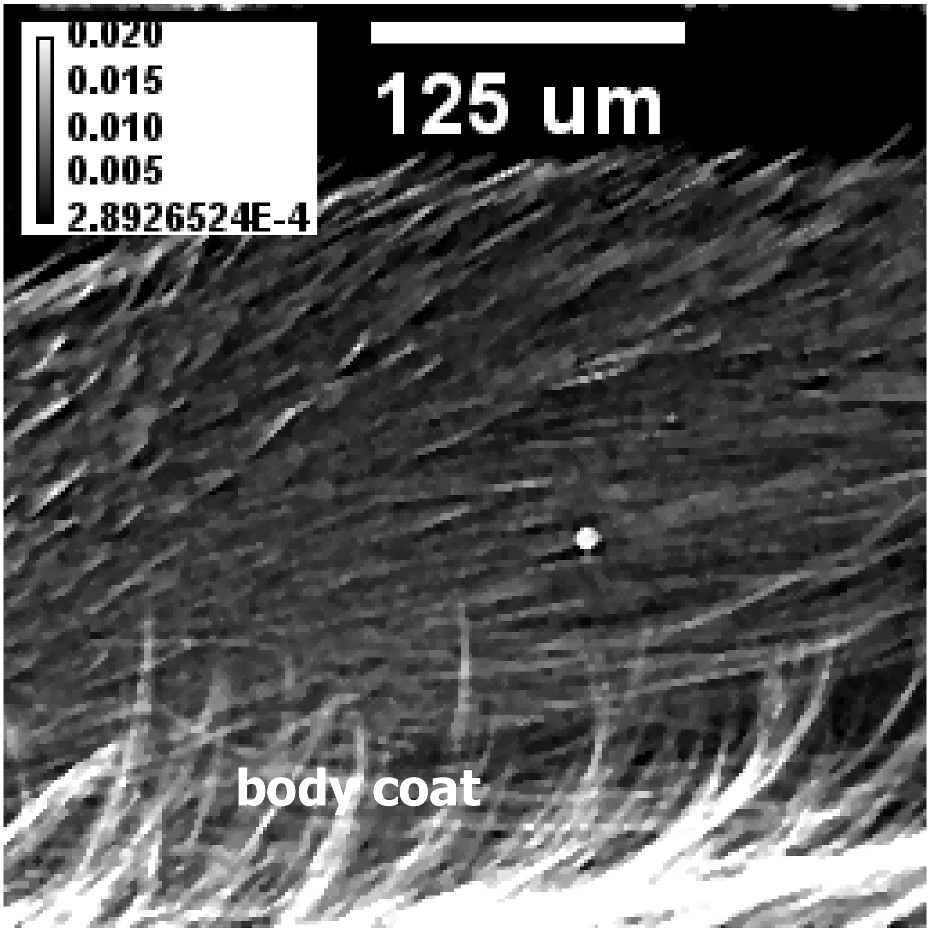

Fig. 3-9 Radiography of a fly, imaged at M = 12x (a), back side of the fly body covered with hair, as indicated from the arrow, imaged at a magnification of 33x (b). Radiogram of part of the body coat and of the wing hair, M = 38x (c); one filament from the body coat is zoomed (d) and a profile (e) of its section has been determined: the diameter size has been evaluated as 5 µm. The sample was imaged alive with an exposure of 20 mAs.

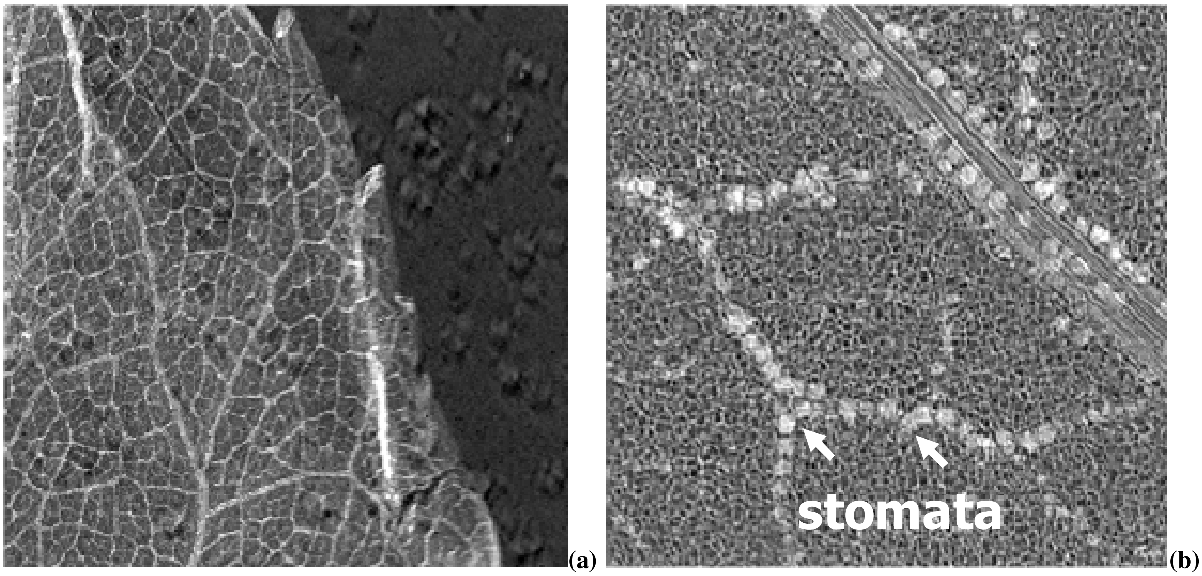

Fig. 3-10 Radiographies of a rose leaf: in (a), 5 mAs exposure, is visualized the structure of channels and of the webbed veining, while in (b), 0.25 mAs, thanks to the higher magnification (M = 14x), it is possible to distinguish the stomata which are pores necessary to the leaf to exchange gas (~ 40 µm diameter size).

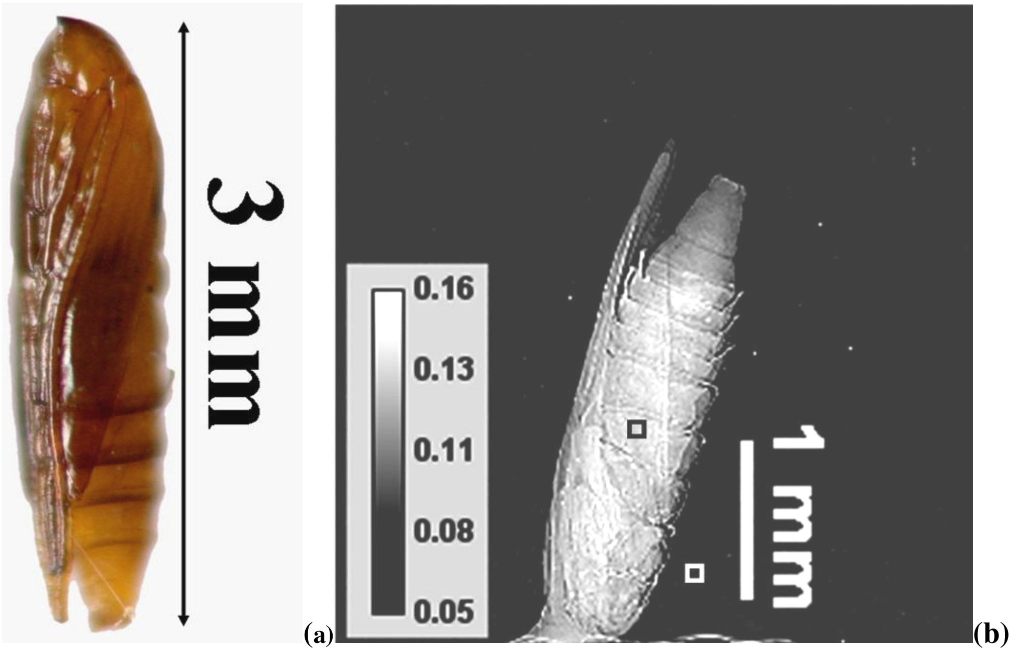

Fig. 3-16 Photograph (a) and radiography (b) of a living pupa of leaf miner. The radiography has been realized with Medipix2 SPC detector and with the micro-focus X-ray source (40 kVp tube voltage, 200 µA tube current, 100 s acquisition time). The magnification factor is M = 4x (source-to-sample distance R1 = 15.5 cm). The ROIs used for the SNR evaluation are depicted (10 pixels x 10 pixels). The gray scale is in e. t. units.

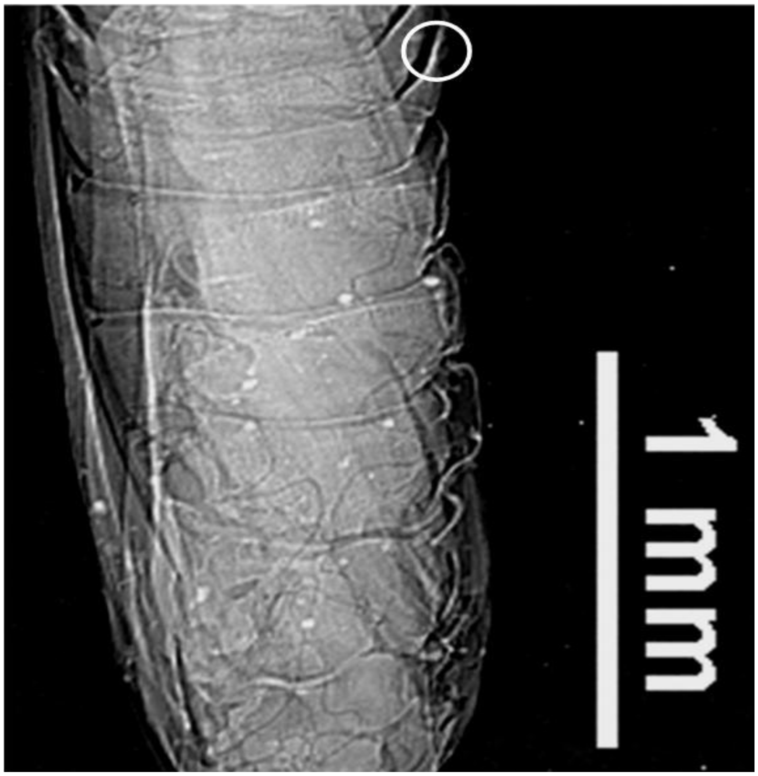

Fig. 3-17 Radiography of a living pupa of leaf miner; a circle has been drawn around a small detail of the body (a); zoom of the detail (b) for which the dimension has been evaluated as 15 µm. The magnification factor is 7x, tube voltage and tube current were, respectively, V = 40 kVp and I = 200 µA.

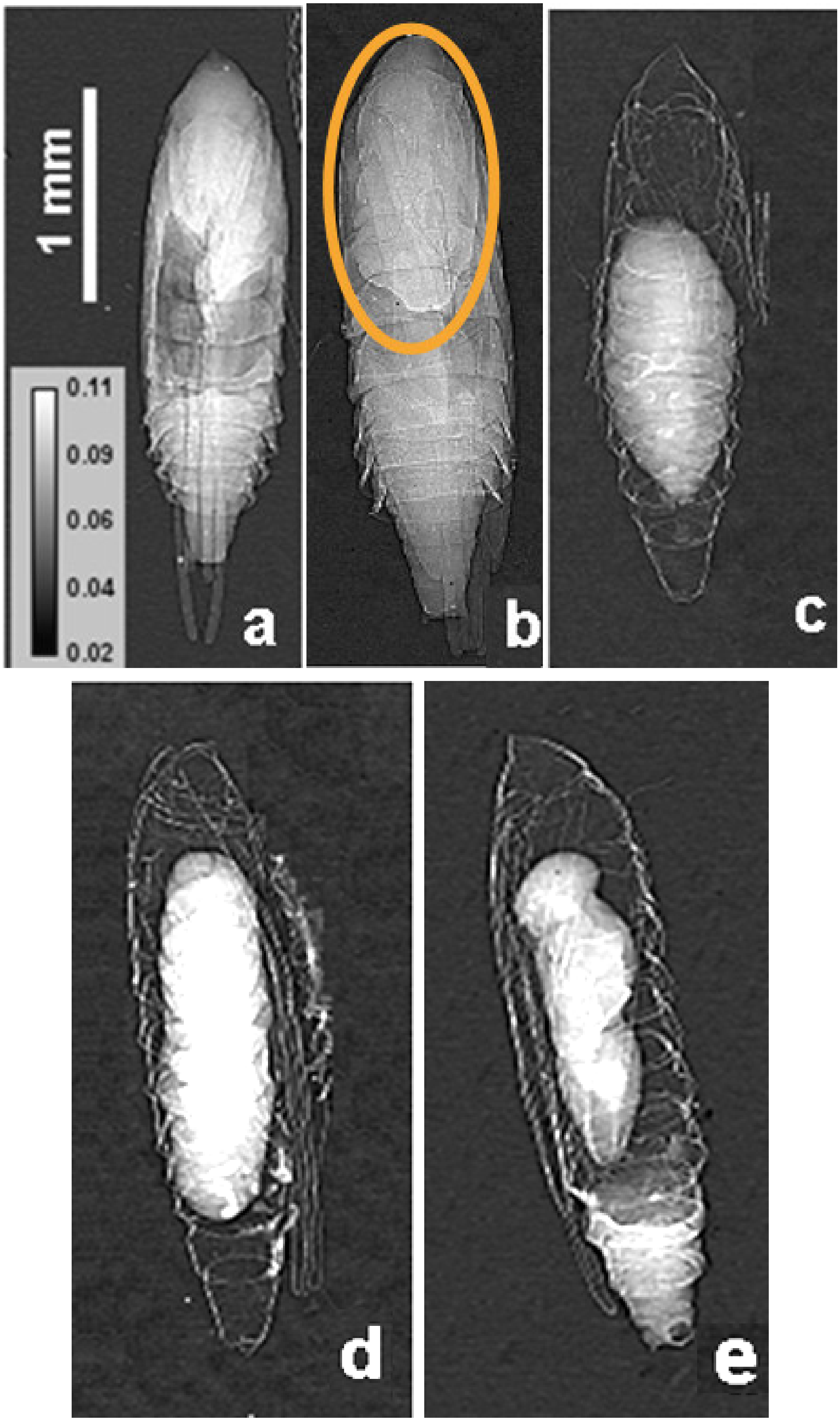
1 mm
0.11
0.09
0.06
0.04
0.02
a
b
c
d
e

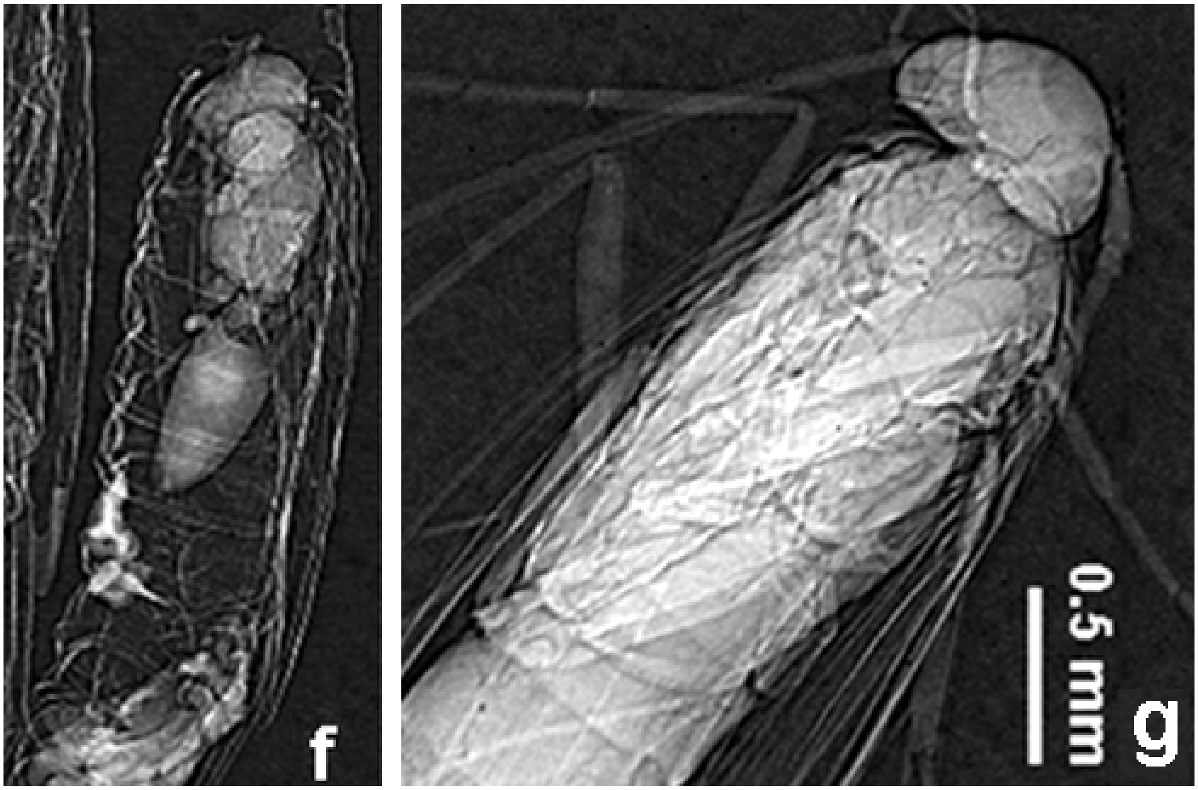

Fig. 3-19 ***In-vivo*** **radiograms of the parasitic wasp of** ***Cameraria ohridella,*** **acquired during a period of several weeks. In (a), (b), (c) and (d) the larva is growing in length from a "ball" shape into a worm shape, eating the inner tissue of its host. In (e) it is shown the pupa stage and in (f) it is shown the imago stage. In (g) a radiography of a living imago of Cameraria ohridella is** ***presented. The*** **magnification factor is 3.8x for images a - f and 6x for image g; the acquisition time was 100 s and the tube settings were V = 40 kVp and I = 200 µA.**

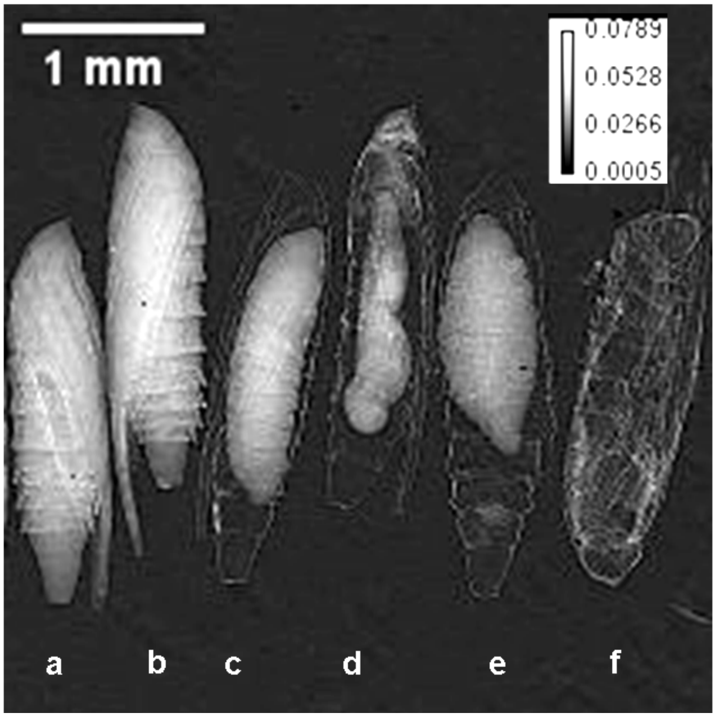

Fig. 3-20 Radiography of six samples leaf miner pupas. The radiography has been realized with Medipix2 SPC detector and with the micro-focus X-ray source (40 kVp tube voltage, 200 µA tube current, tacq = 100 s). The magnification factor is 2.9x (source to sample distance R1 of 21.4 cm).

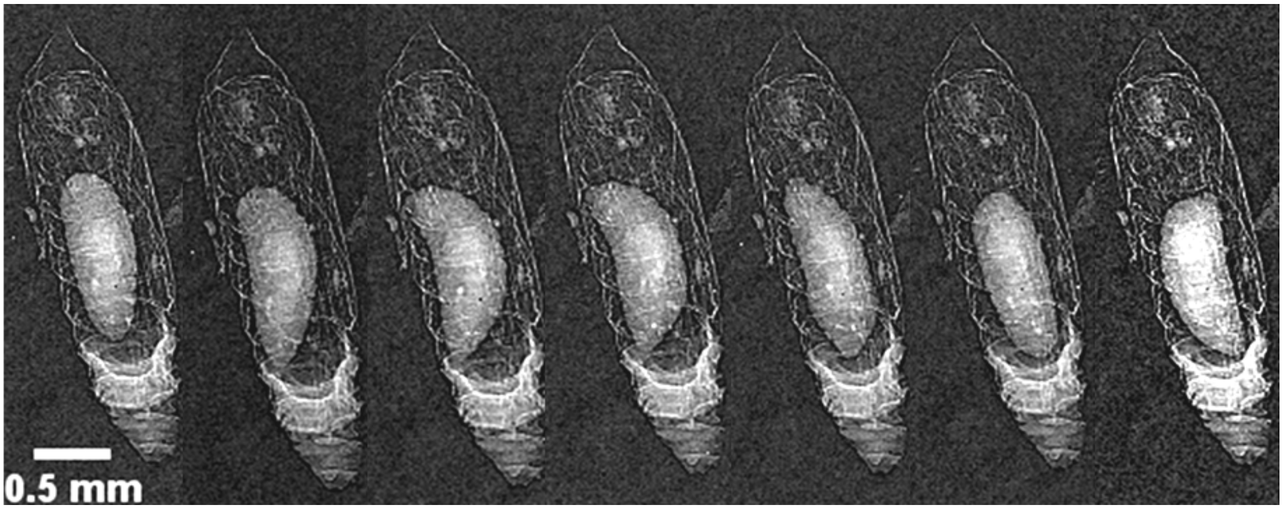

Fig. 3-21 Sequence of radiograms showing the parasite behaviour inside the leaf miner, when in the larva stage. Each image has been acquired for 500 ms corresponding to a frame rate of 2 frames/s. Tube voltage and tube current were set at 40 kV and 200 µA respectively. The magnification factor was of 3.7x.

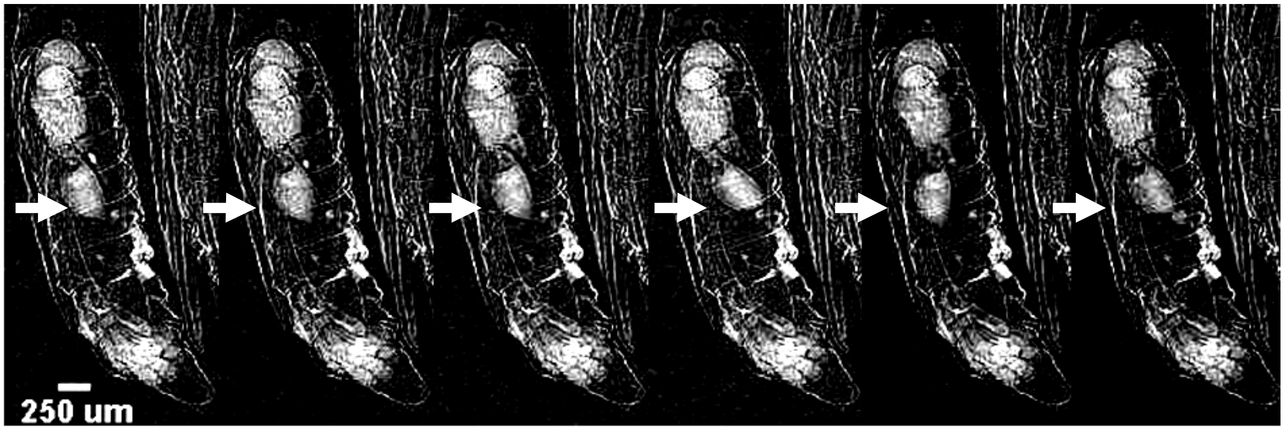

Fig. 3-22 Sequence of radiograms showing the parasite behaviour inside the leaf miner when in the pupa stage. Each image has been acquired for 500 ms corresponding to a frame rate of 2 frames/s. Tube voltage and tube current were set at 40 kVp and 200 µA respectively. The magnification factor was of 3.7x.

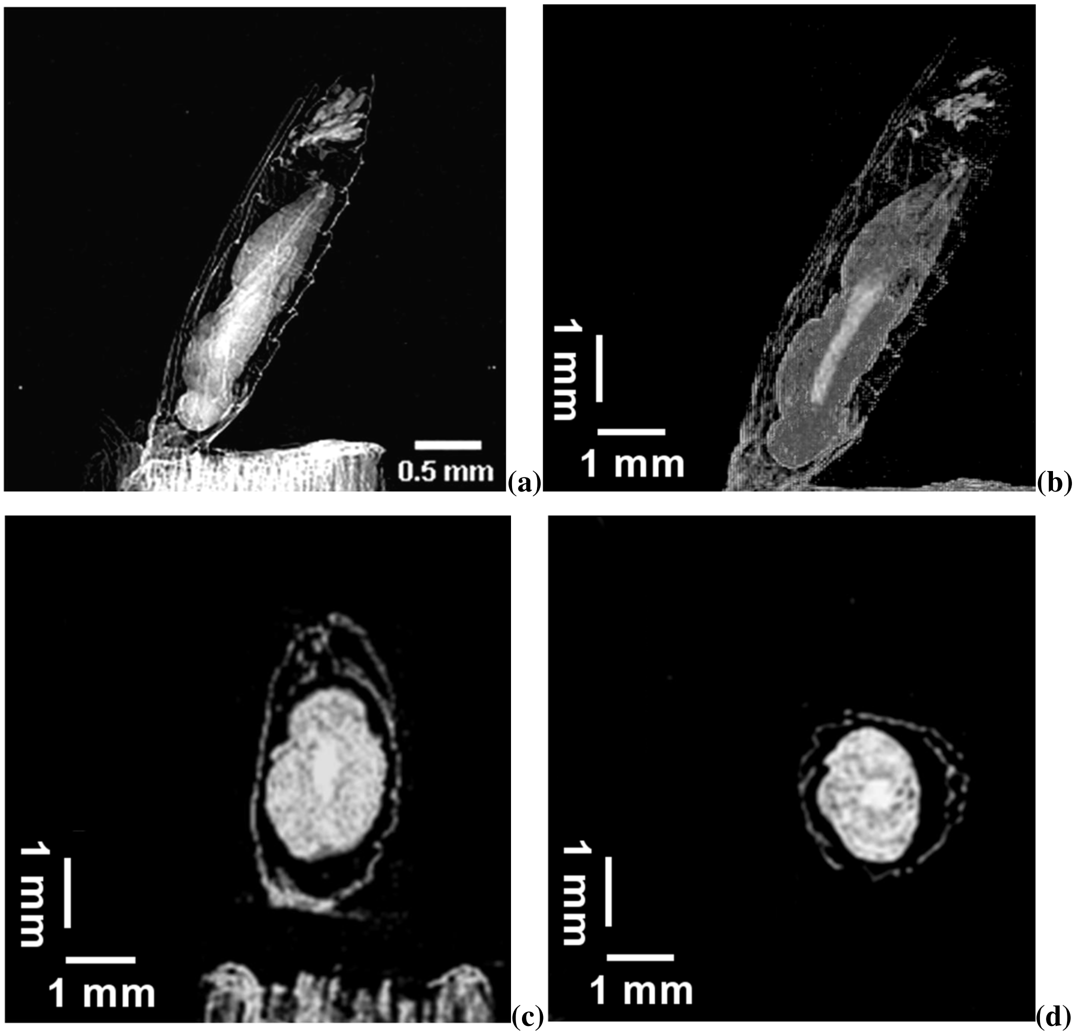

Fig. 3-25 Projection of a leaf miner killed by its parasite living inside its body (a); slices from the tomographic reconstruction obtained with the OS-EM algorithm: coronal view (b), sagital view (c), transaxial view (d). The voxel size is 17 µm x 17 µm x 21 µm and the total number of voxels is 259 x 259 x 211. The length of the dead leaf miner is 3.1 mm and the mean diameter of its body is 800 µm x 800 µm, while the length of the inner parasite is 2 mm for a thickness going from 68 µm x 170 µm, in the thinnest region, to 700 µm x 500 µm in the thickest region. The magnification factor is 3x.

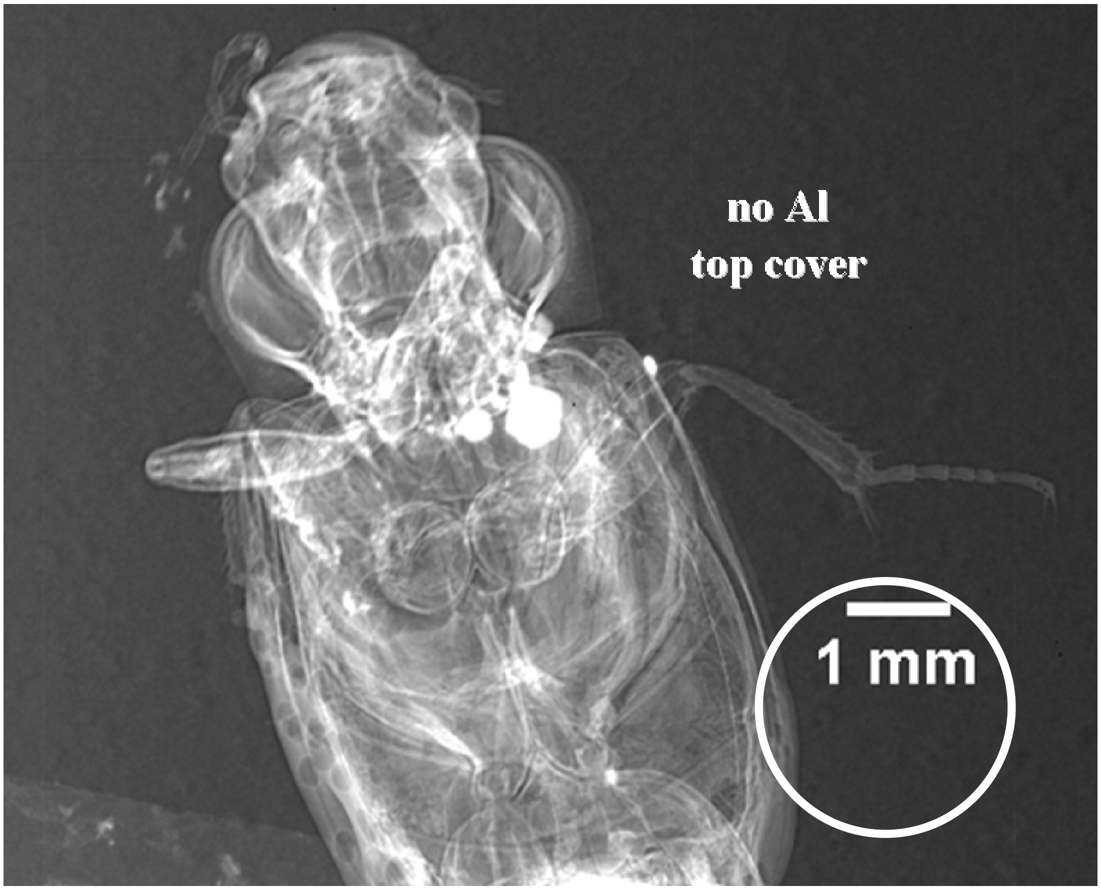

Fig. 3-34 Radiography of a beetle acquired with the FP detector (without the 1 mm thick Al top cover). R1 = 13.05, R2 = 48.95, M = 4.75x, V = 40 kVp, I = 200 µA, texp = 100 s (20 mAs).

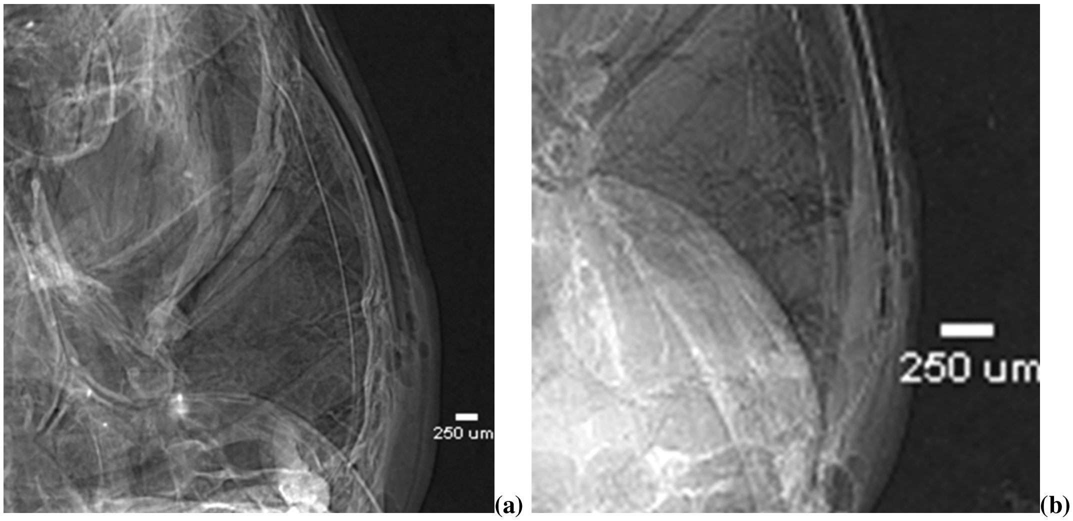

(a) (b)

Fig. 3-35 Radiographic detail of an insect body acquired with the FP detector (a) and with the Medipix2 (b) in the same geometrical conditions (R1 = 13.05, R2 = 48.95, M = 4.75x), with a tube voltage of V = 40 kVp, but at different exposure levels: I = 200 µA, texp = 100 s for the FP detector and I = 50 µA, texp = 100 s for Medipix2. The rectangles illustrate the ROI to evaluate the plot profiles showed in (c) - for the FP detector – and in (d) – for Medipix2. The circles on the plots point out the jump due to the interference fringes, resulting from the phase shift. The jump for the FP detector is of 4.4 · 10-4, while the jump recorded with Medipix2 is of 5.7 · 10-3, that is one order of magnitude bigger.

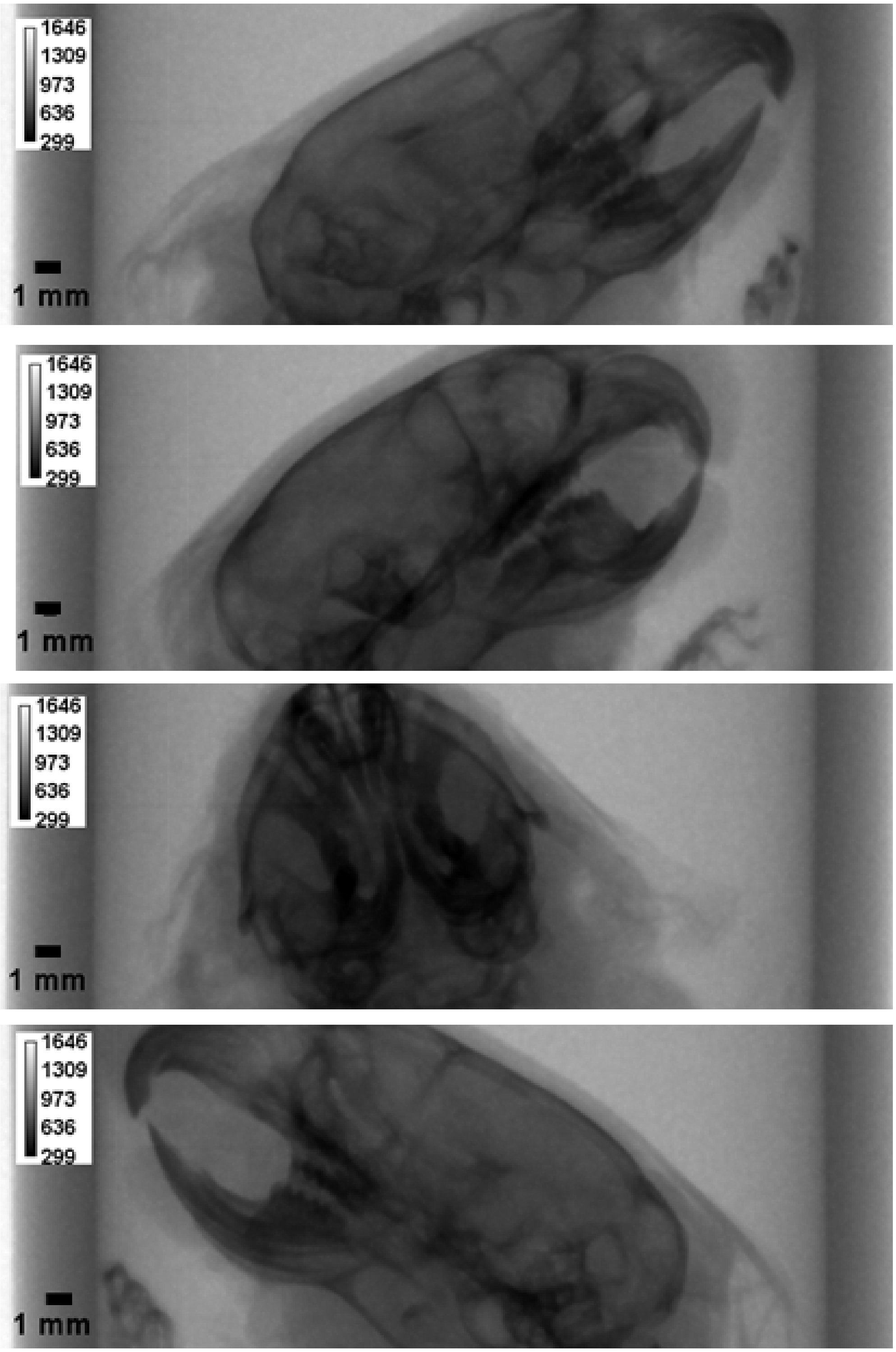

Fig. 3-42 Projections at different angular positions of a mouse head acquired with the FP detector and corrected by means of the FFC.

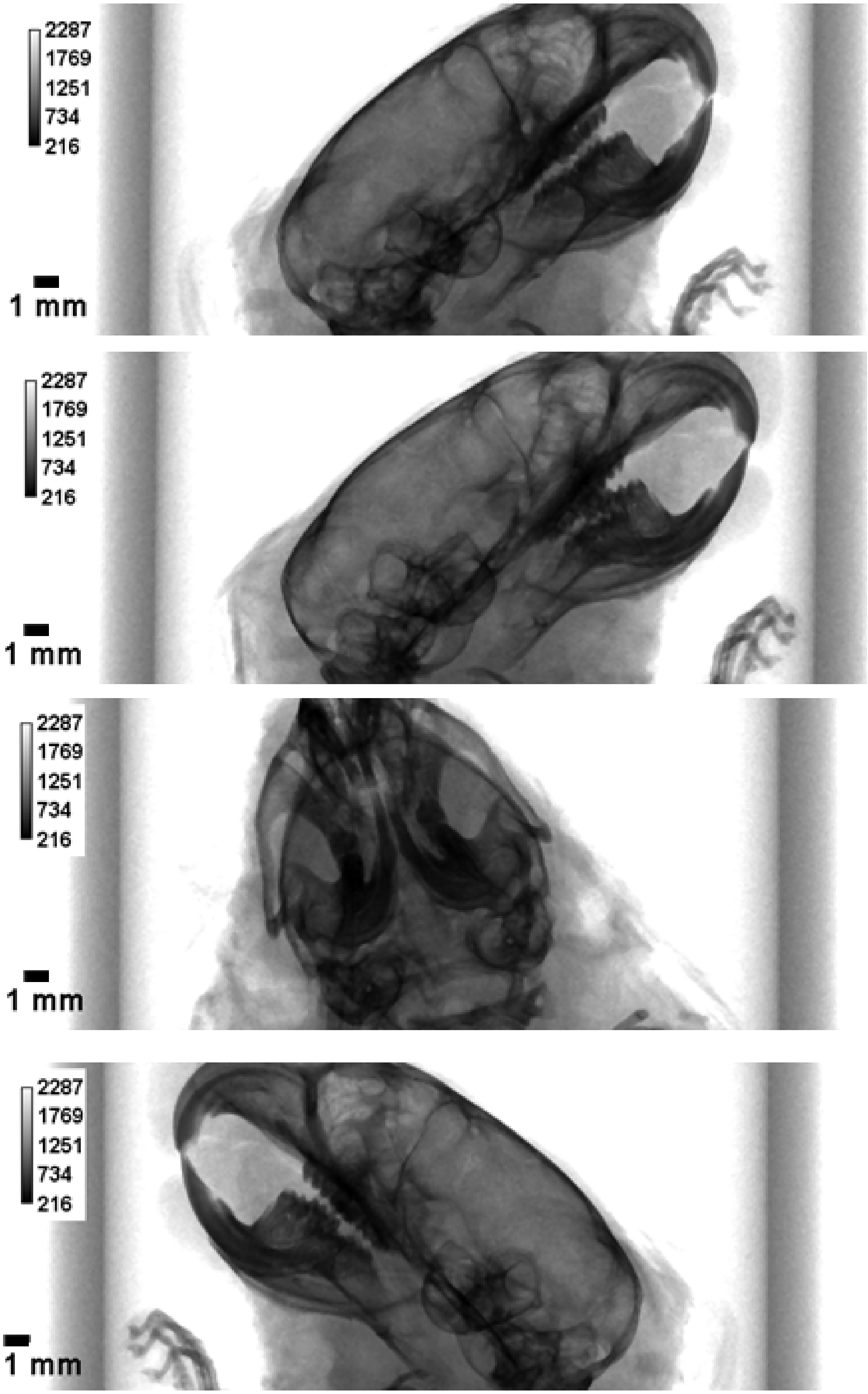

Fig. 3-44 Projections at different angular positions of a mouse head acquired with the Medipix2 detector and corrected by means of the FFC.

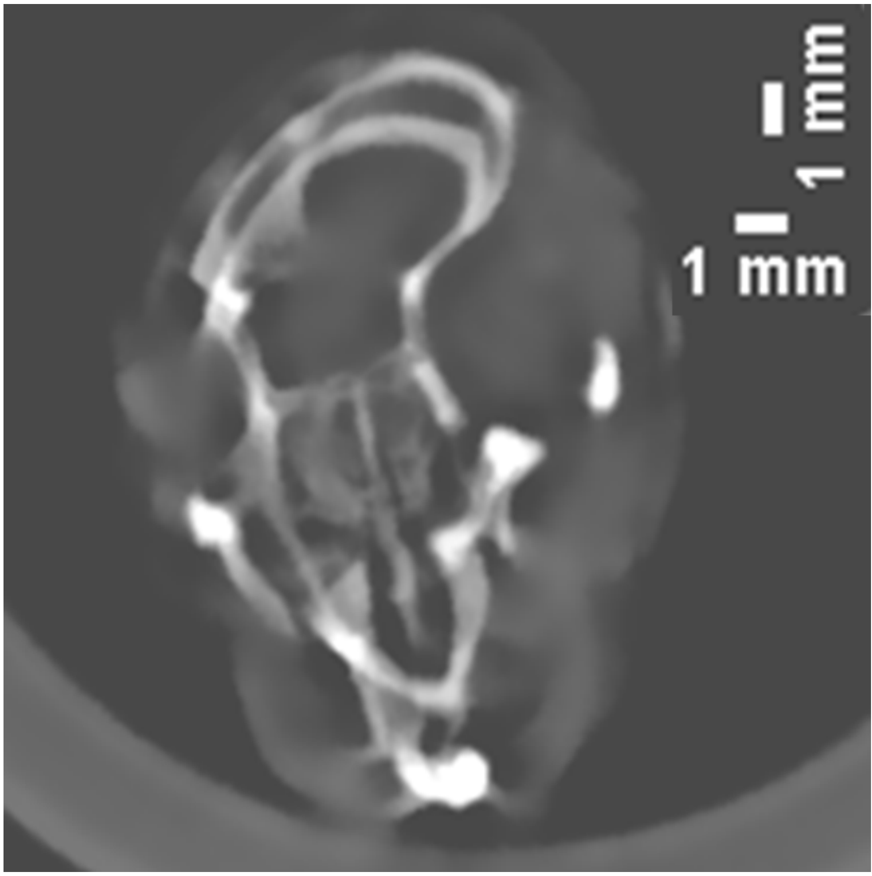

(a)

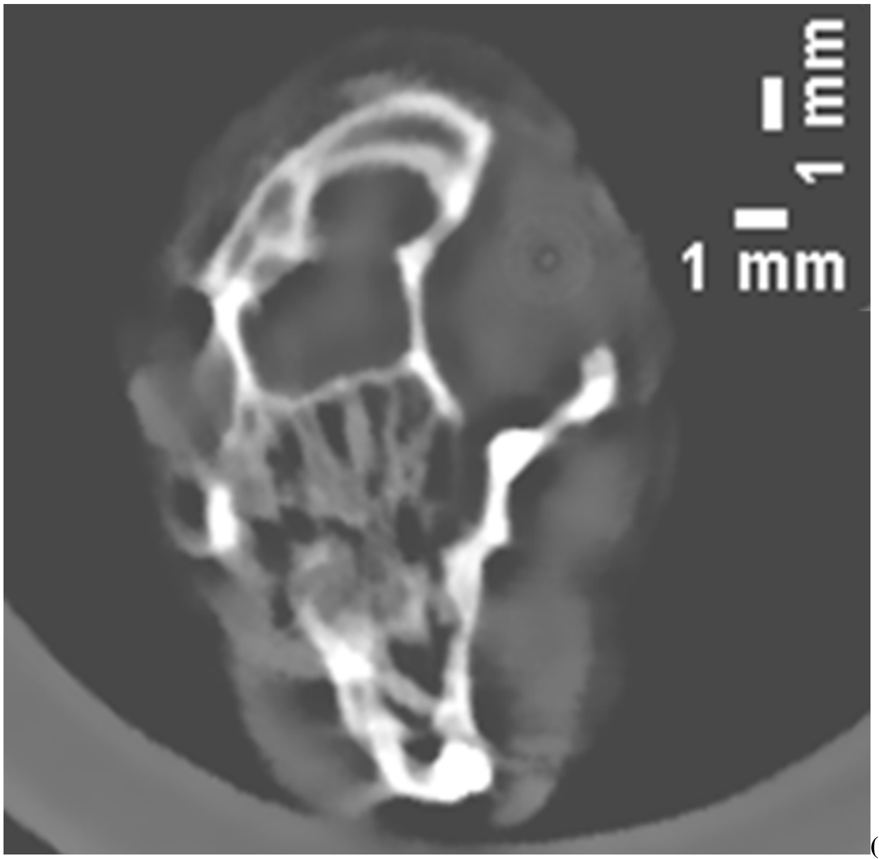

(b)

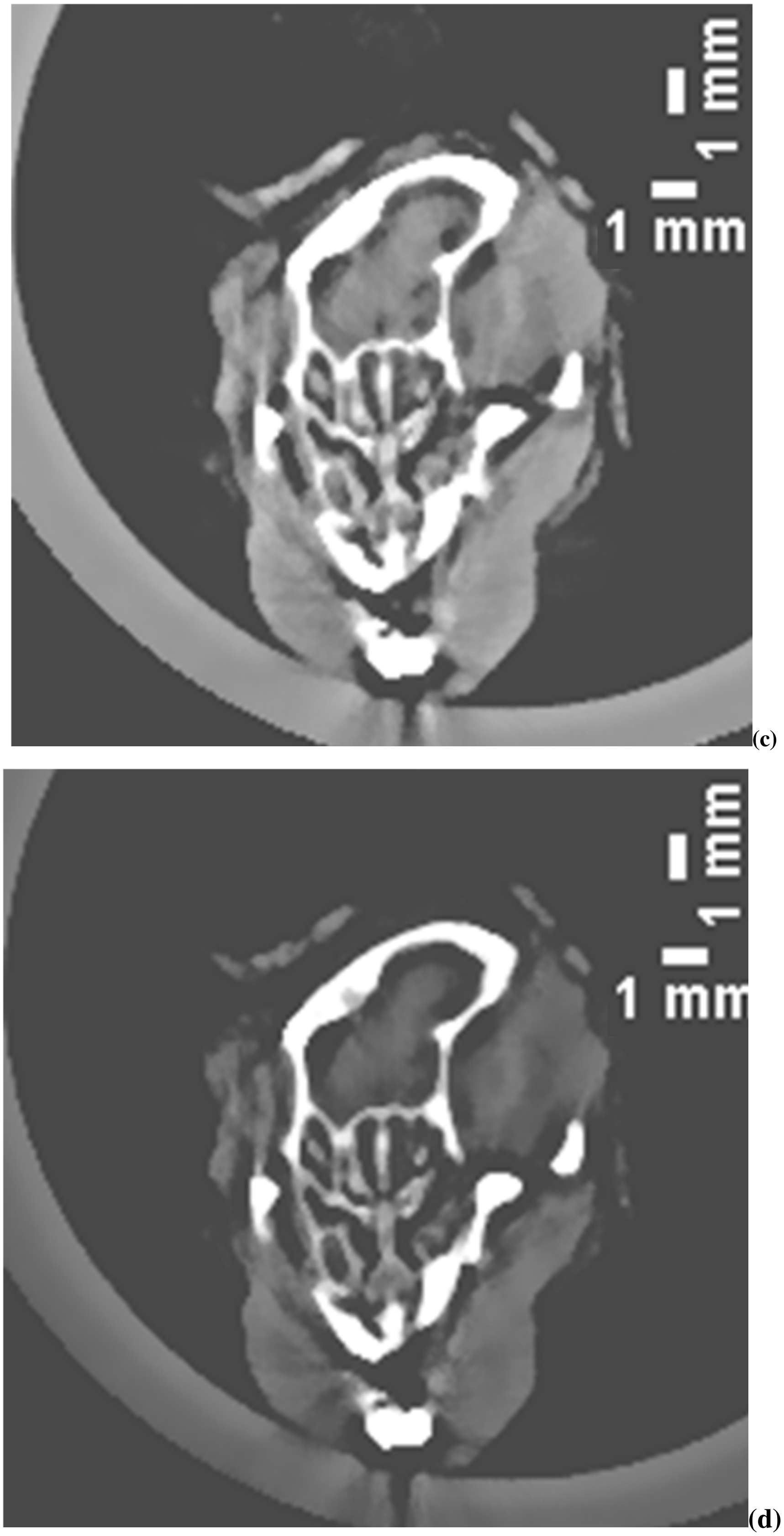

Fig. 3-46 Axial slices of the mouse head acquired with the FP detector (a, b) and with the Medipix2 (c, d) and corrected either by means of the FFC (a, c) or by means of the STC (b, d).

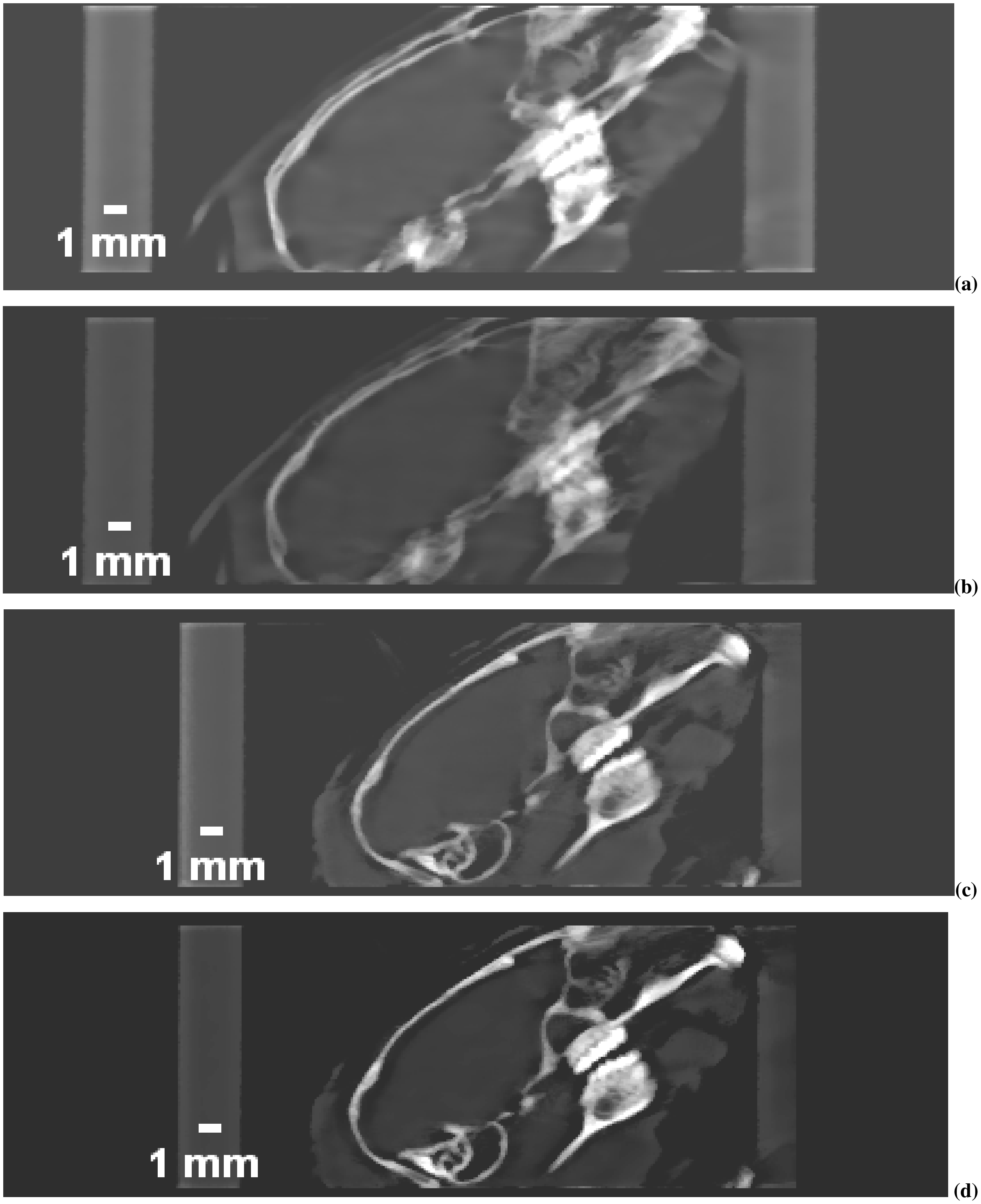

Fig. 3-47 Sagittal slices of the mouse head acquired with the FP detector (a, b) and with the Medipix2 (c, d) and corrected either by means of the FFC (a, c) or by means of the STC (b, d).

Acknowledgements

I'm here, in front of the last page of my thesis and a huge number of people come to my mind, who have contributed to let me arrive as far as here. I should like to dedicate to each of them some words, just a small recompense for the help they gave me in these 3-years.

Professor Paolo Russo, my Teacher, with capital "T": he has been guiding me for four years, first during my degree thesis and now leading me during this exciting journey that was the PhD. I have to thank him for the opportunity he gave me to approach the world of the research world.

Thanks to Professor Russo's Medical Physics staff: Dr. Maria Cristina Montesi, for the self-sacrifice that represents her main merit: she helped me also when her mind was somewhere else, she never let me perceive it; Dr Adele Lauria, always ready to give me a helping hand whatever I asked, Dr. Giovanni Mettivier, my point of reference for all kinds of questions and practical troubles I ran into during my work. Thanks to Teresa Coppola and Michela Esposito, who work in my same laboratory and share with me joys and pains: without their company everything would have been much more boring!

A huge "thank you" goes to the two staffs of the Physics Department design office - Dr. Giuseppe Passeggio, Mr. Lorenzo Roscilli and Mr. Emanuele Vanzanella - and Physics Department workshop - Mr. Raffaele Rocco, Mr. Gianluca Borriello, Mr. Ciro Cassese, Mr. Franco Cassese, Mr. Bruno d'Aquino, Mr. Benedetto De Fazio and Mr. Andrea Esposito: they professionally and patiently followed me through the building of my set-up placed in the Medical Physics Laboratory, from the starting abstract through to the concrete realization of it, always ready to give me bright hints and to optimize my work.

A (thank you)$^{\infty}$ to Mr. Guido Celentano: he solved for me all the bureaucratic (and not only!!) troubles I'm used to cause continuously!! He has a divine patience, a refined sense of humour and a big heart, which is his only defect!

During my Ph.D., I spent 6 month at the Institute of Experimental and Applied Physics of the Czech Technical University of Prague; for this opportunity, besides the already mentioned Prof. Paolo Russo, I have to thank Prof. Stanislav Pospíšil, for his generosity and for the warm welcoming of his group: he and his staff offered me the availability of the whole laboratory, making me feel comfortable working in that environment. Thanks to Dr. Jan Jakůbek, my unquestionable scientific guide when I was in Prague. Thanks to Dr. Daniel Vavřík: it was a pleasure working together as well as going together for a beer after a full day of work! Thanks to Dr. Jiří Dammer: he taught me all his secrets! Thanks to Professor FrantiseK Weyda: without him I should never have found such nice biological samples to image! He was always smiling and optimistic: an old child! Thanks to Dr. Tomáš Holý, *alias* Mr. Pixelman: he was for a period my patient and tolerant

desk-neighbour. Thanks to Dr. Zdeněk Vykydal: he was my Medipix2 chip problem solver and thanks to Dr. Martin Jakůbek, my motor problem solver!

I would like to thank all the nice Czech scientists I met in IEAP who have been my family when I was in Prague, helping me in all the small and big thing one has to solve when lives in a foreign country and always making me feel at home: Dr. Petra Kovacikova,Dr. Petr Pridal, Dr. Jaroslav Smeikal, Dr. Karel Smolek, Dr. Ivan Stekl, Dr. Ladislav Vala. And thank you to my Italian colleague Dr. Paolo Gabor who shared with me this wonderful Czech experience!

And now the biggest acknowledgements, the acknowledgements to the person that were fundamental not only for my research work, but also for my life:

Gianluca: he is slowly convincing me that the form is as important as the substance...sometimes...and this is way he is in this list...

Mr. Giuseppe Pontoriere: I can not even try to count how many times he has sacrificed his time for me: for me he did in these years 10 times more work than he would have done if he had not had me around! He was for me like a father and I will always be grateful to him for everything.

Salvatore and Mrs. Angela Savo: they adopted me since the first year of my Ph.D and I will bring them in my heart forever.

Pavel Cěrmák and all his marvellous family: it is extremely difficult for me to express my feelings for you. I like to think that somehow, somewhere, one day we will meet again...

Simona Curion: ok, just one thing: she helped me so much and to such extent that I would say she is my co-author!! I care about you...also if....!!!

My sister, Gabriella: she is part of me, she is my joy, my life, she is the smile I bring everyday hidden in my heart. My little ladybird!

My father, Vito: I know that your Love will always be the strongest one, I know all the pains, the thoughts, the sacrifices you did for me and I will repay all this the best I can...starting with this thesis.

My mother, Annamaria: she is what I want to become: a strong and determined woman knowing how to face life. As I always said to you, you represent my model and I will always try to make you feel proud of me! I love you, Mummy!

A special thanks to my mother also because she was the firs reader of this thesis: she is really brave!!

To all of you I have not named just because I risk to make longer acknowledgements than the thesis: thank you for being close to me during these last three years!